Cranfield University

College of Aeronautics

PhD Thesis

1999-2000

Abdullah M Alkhozam

The Effect of an End Plate Boundary Layer on Half Delta Wing Flows at Low Reynolds Number

Supervisor : Dr. K. P. Garry

August 2000

Abstract

An experimental investigation has been carried out to study and understand the influence of an end plate boundary layer on half delta wing models at low Reynolds Number. The programme involved measurements in two facilities: a vertical water tunnel which was used for flow visualisation studies and a conventional closed working section wind tunnel for both flow visualisation and surface static pressure measurements. In both facilities dynamic and steady state or static measurements were made on half delta wing models with 55° and 70° sweep and varying thickness/chord ratio under the influence of a number of artificially generated end plate boundary layers.

In both facilities, of all model configurations tested, for both dynamic and static test conditions, vortex burst was seen to move upstream, inboard and away from the wing surface as the angle of attack is increased and vortex core trajectory is seen to move towards the wing root, which is consistent with the findings of previous researchers. Vortex breakdown position is seen to move upstream, inboard toward the wing root and away from the wing surface as the end plate boundary layer thickness is increased. This is attributed to the influence of the interaction between the horseshoe vortex and the half delta wing leading edge vortex as a result of changes in the wall boundary layer thickness.

In terms of vortex core trajectory, increases in end plate boundary layer thickness are seen to displace the vortex core towards the wing root. During dynamic tests an increase in wall boundary layer thickness is seen to suppress the hysteric behaviour of the vortex trajectory. Surface static pressure measurements at Reynolds Number of 479,000, during both static and dynamic tests, make it possible to see that the influence of changes in wall boundary layer thickness are small, often insignificant, at (x/c) locations greater than 0.45. This is consistent with an increase in wall boundary layer thickness promoting earlier vortex breakdown.

Correlation between smoke flow visualisation (of both vortex breakdown and trajectory) and surface static pressure measurements, using the half-width of the suction peak as a parameter, was good. Differences between vortex characteristics in the water tunnel and wind tunnel were consistent with the influence of Reynolds Number.

Acknowledgement

Firstly, I would like to express my thanks to my supervisor Dr. Kevin Garry for his invaluable enthusiasms, helpfulness and patience during the course of this work. Many thanks to all member staff of the College of Aeronautics, in particular, Professor John Stollery for his moral discussion with me.

Thanks also go to the College of Aeronautics technical staff, Mr. Malcolm Goodridge and his staff with the experimental work and models construction.

Finally, I would like to thank my wife for her patience and encouragement with the little two girls throughout my study.

Dedicated to my Father

TABLE OF CONTENTS

List of Tables

List of Figures

List of Figures in Appendices

Notation

c	Wing root chord length
b	Wing span
Cp	Pressure coefficient
Re	Reynolds Number
U	Free stream velocity
u	Local free stream velocity
p_1	Static ring pressure, far
p_2	Static ring pressure, close
p_0	Total pressure
q	Dynamic pressure
q_{local}	Local dynamic pressure
K	Wind tunnel calibration factor = 0.997
ρ	Density of air
ρ_w	Density of water
ν	Kinematic viscosity = μ/ρ
μ	viscosity
x	Chord wise distance
y	Span wise distance
z	Distance away from the surface
s	Semi-span length
δ	Boundary layer thickness
δ^*	Boundary layer displacement thickness

AoA	Angle of attack
Δ	Sweep angle
2D	Two dimensional
3D	Three dimensional
k	Non-dimensional Reduced pitch rate = $\alpha^{\bullet}$ c/U
$\alpha\bullet$	Pitch rate in (rad /sec.) = (π /180^0)α
α	Pitch rate in (°/sec.)
Γ	Strength of circulation
L	Lift force
T.I.	Turbulence intensity = (u^2)$^{0.5}$ / U
u	Instantaneous velocity
$\bar{U}$	Mean flow velocity
z_o	Probe initial distance from the wall
Δz	Correction of wall deflection
d	Width diameter of pitot tube
h	Height diameter of pitot tube
$\partial p/\partial x$	Pressure gradient
v	Reduced frequency, $v = \pi f c/ U$
f	frequency, Hz

Acronyms

CFD	Computational fluid dynamic
CSV	Comma separate value
ASCII	American standard code for information interchange

DVM	Digital voltmeter
ADC	Analogue to digital converter
FFPA	Fibre-Film Probe Anemometer

Chapter 1 Introduction

The vortex lift generated by sharp edge slender wings at moderate to high angle of attack is a well known phenomenon that has been utilised in aircraft and missile design for a considerable time. In recent years attempts have been made to improve these vortex lift characteristics by employing canards or fore body strakes, which have led to: higher vortex lift, better breakdown characteristics and improved interaction between the vortices and the after body / tail surface. The lack of reliable theoretical prediction techniques suitable for the highly complicated flow field generated by such configurations has required extensive wind tunnel testing programs, in which both the load distribution on the lifting surfaces is measured, along with measurement and visualisation of the vortex path.

1.1 Boundary Layer

A wall-bounded fluid flow's ''boundary layer '' is the region where the flow varies from zero velocity (relative to the wall) at the wall's surface, to the free stream or ''edge'' velocity away from the wall. This region is typically very thin compared to the entire region of interest, such as the flow around an aircraft wing at high speed. However, the boundary layer's small size belies its importance, and it is of great engineering interest for primarily two reasons. First, this viscous region is directly responsible for a flow's skin friction drag.

Second, when a boundary layer becomes detached, or separated, from its bounding surface, the entire flow field is changed dramatically. The characteristics of an aircraft's boundary layer influence its speed, range, manoeuvrability, minimum landing speed, and many other aspects of its performance. If the flow separation can be controlled, aircraft lift can be enhanced and form drag can be decreased.

1.2 End-Plate

End plates are sometimes used during wind tunnel testing of wing models to simulate reflection planes at the root. Sometimes two end plates are used, one at each end of a rectangular section of a wing, so that essentially 2-D aerofoil data can be obtained. Also, with the use of a single end plate, half models of delta wings can be tested. The introduction of an end plate may itself be responsible for interference effects. The two of most concern are: (a) the possibility of generating downwash if the plate were aligned at incidence to the freestream flow and (b) the boundary layer on the plate, although certainly likely to be thinner than that on the wind tunnel wall, interfering with the flow over the model.

In the case of a 'half delta' wing test, there is relatively little known about the influence of the end plate or wall boundary layer on the flow field. Since the interaction with the wall boundary layer is likely to influence the wing vortex strength and trajectory, a good understanding of this interaction is important.

Mendelson et al[123] carried out a two-dimensional span-loading test in wind tunnel to determine tunnel-wall boundary-layer effects and found that the load at the tunnel-wall may be as much as 10% lower than that at the centre of the working section. Changes in boundary layer thickness produce small changes in load, and at high angle of attack, average pitching moment for the wing may differ from the centre of the tunnel because of non uniform stall.

Galbraith[135] has observed that the corner boundary layer separates before the main aerofoil separation, as a result of which the corner flow is enhanced and results in a strong standing vortex at Re = 610000. The effect of this is to decrease the lift on the aerofoil model close to the end plate. Furthermore, trailing vortices resulting from such a change in lift would have an effect on the lift distribution on the aerofoil model.

Verhaagen, et al [110] investigated the effect of the reflection end-plate boundary layer on the leading edge vortex flow over a delta wing. Their test results indicate that near the apex of the delta wing the vortex flow is strongly affected by the boundary layer on the reflection end-plate.

1.3 Aim of the Thesis

Thin slender wings with highly swept leading edges are used by several modern aircraft. At moderate and high angles of attack the flow over this type of wing separates at the leading edges, resulting in a steady and stable leading edge vortex flow. Experimental data is available from many investigations carried out mainly on flat sharp edge delta and double delta wings.

This data has resulted in a better understanding of the structure of leading edge vortices and has been used for validation of numerical codes[5,57,188] that predict the flow over delta-type wing configurations. Modern versions of these codes are also capable of predicting reasonably well the main features of the effect of a tunnel wall or endplate boundary layer, the leading edge vortex flow behaviour and the pressure distribution induced on the half delta wing surface. However they tend to under predict some of the core and behaviour characteristics of a leading edge vortex.

A precise solution for the flow in the core behaviour may be of importance to accurately predict vortex core bursting and characteristics and in the case of an aircraft, the interaction of the leading edge vortex flow with wing and tail surfaces located downstream.

The amount of experimental data available from the literature on the effect of an endplate boundary layer on the leading edge vortex behaviour of half-span delta wing is rather limited. A more detailed study is needed that includes a range of configurations of boundary layers and wing angle of attack including the effects of dynamic pitch-up and pitch-down.

The aim of the present investigation is to help extend the experimental database on the flow in this region, by investigating the interaction between the wall boundary layer and its influence on the development of the vortex flow and trajectory over the delta wing, by gathering data on this effect, of surveying the vortex trajectory and breakdown location from flow visualisation in the water tunnel, surface static pressure measurements in the wind tunnel and flow visualisation by using the smoke technique and to establish a correlation between the water tunnel and the wind tunnel results.

1.4 Outline of the Thesis

An outline of the research programme detailed in this report is as follows: The experimental apparatus and techniques for acquiring the relevant data are described in Chapter 3 for the water tunnel and Chapter 4 for the wind tunnel. Chapter 5 covers the wall boundary layer measurement (this chapter focuses on the data analysis from the - Film Probe - measurement technique and the boundary layer profile analysis). Chapter 6 covers the flow visualisation, qualitative data and close analysis of the leading edge vortex behaviour, for the water tunnel. Chapter 7 covers the results and analysis of the wind tunnel measurements. Chapter 8 covers the flow visualisation in the wind tunnel using the smoke technique, Chapter 9 concludes the work and in Chapter 10 possibilities for future work are outlined.

Chapter 2 Literature Overview

The literature overview chapter discusses the characteristics of wall boundary layer and its influence on the vortex flow behaviour, development and breakdown location on the delta wing. It also discusses the previous investigations on the factors affecting vortex characteristics, working section interference effect including the wall boundary layer thickness effect and other parameters.

2.1 Boundary Layer

Ludwig Prandtl in 1904 provided a justification for applying the results of perfect fluid analyses to viscous flows. He postulated that for fluids of small viscosity, the effects of viscosity on the flow around streamline bodies are concentrated in a *thin* boundary layer. The boundary layer is defined as the layer adjacent to a body within which the major effects of viscosity are concentrated. Intuitively, the alteration to the flow caused by the no-slip condition will decrease as we move out from the surface, and hence the effect will not be detectable beyond a certain distance. In other words, outside of the boundary layer, the flow of a viscous fluid will resemble closely that of an inviscid fluid. The limitation of Prandtl's hypothesis to fluids of small viscosity is broad enough to include gases as well as liquids.

2.1.1 Horseshoe Vortex

Prandtl developed the first practical theory for predicting the aerodynamic properties of a finite wing as follows. A vortex filament, of strength Γ, which represents the circulation around the wing (bound vortex), will experience a force $L = \rho U \Gamma$ from Kutta-Joukowski theorem. Replacing a finite wing of span b with a bound vortex, (extending from $y = -b/2$ to $y = b/2$, in Figure 2.1). The vortex filament continues as two free vortices trailing downstream from the wing tips to infinity. This vortex (the bound plus the two free) is in the shape of a horseshoe, and is called a horseshoe vortex.

When a boundary layer on a surface encounters an obstruction, (such a cylinder or wing), a complex three – dimensional flow field develops in the vicinity of the obstacle, Figure 2.2. The approach flow encounters a strong adverse stream wise pressure gradient , which coupled with the cross-stream pressure gradients generated by curvature of the external flow around the obstruction , results in a concentration of the boundary - layer vorticity into a discrete vortex near the end wall juncture. Extension of this vortex engirdle the obstruction to form "horseshoe" vortex, with the "leg" of the vortex extending downstream.

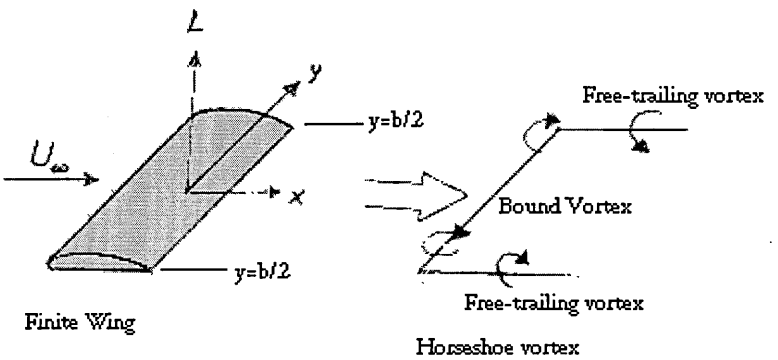

Figure 2.1 Replacement of the finite wing with a bound vortex

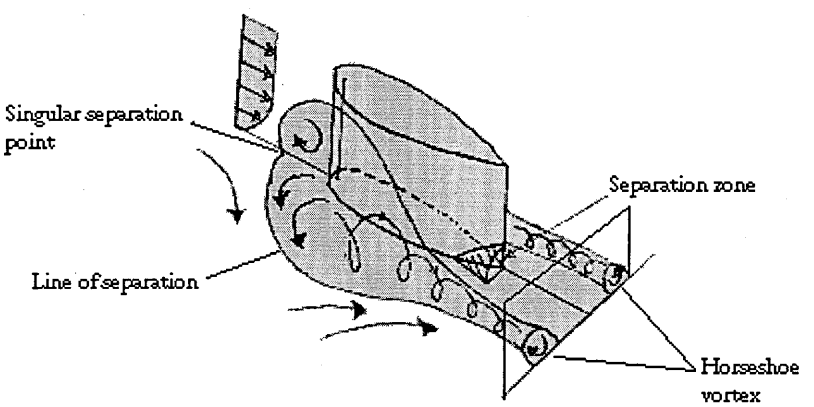

Figure 2.2 Flat plate boundary layer interaction with the junction of a symmetric aerofoil

Examples of such flows are varied, and span a range of flow scales, occurring at : wing / body junction on aircraft : control – surface junctions on submarines and ships and base flows near buildings. Junction flows have been extensively examined for laminar and turbulent flows, Baker[36,191], Barber[192], Kubendran et al[193] Shabaka et al[194], and horseshoe vortex behaviour can be categorised into several regimes of steady and unsteady behaviour that are often described in terms of Reynolds Numbers based on a length characteristic of the obstacle and /or the approach boundary layer .

2.2 Delta Wing Vortex Flow

Studies of the unsteady aerodynamic characteristics of delta planform wings at high angle of attack are encouraged by the interest in enhanced combat aircraft super-manoeuvrability, and development of post-stall capability in order to gain tactical superiority. Since the 1950's most combat aircraft have a delta wing design, a significant feature of which is a leading edge vortex flow. Two smooth suction peaks inward of the leading edges are produced. As a result of a pair of stationary leading edge vortices formed by separated flow on the low pressure side of the delta wing. The lift on a delta wing is due to these separated vortical structures. The lift increases with increasing angle of attack until vortex breakdown occurs, often not until a relatively high angle of attack. Hence, a delta planform is an effective means of obtaining high lift at high angle of attack. (see section 2.3 vortex breakdown).

2.3 Vortex Breakdown

Vortex breakdown remains a problem of major importance in many situations covering both aeronautical and extra-aeronautical applications. Since the early 1950s, a large quantity of results has been obtained on vortex breakdown, mainly in incompressible flows. Carefully executed visualisations and field measurements with LDV systems have provided a clear description of the phenomenon and a thorough identification of the parameters influencing it. It is thus well established that breakdown occurs under the action of an adverse pressure gradient which can induce a rapid deceleration in the axial motion until a stagnation point forms on the centre-line of the vortical structure.

Squire[3,40] has suggested that vortex breakdown corresponds to the formation of long standing waves in a vortex flow. Vortex breakdown (an abrupt change in the structure of the core of a swirling flow) has been observed to occur over delta wings at large angle of attack . Its occurrence is marked by rapid flow deceleration, deformation and/or expansion of the vortex core , flow reversal , and changes in the velocity and pressure distribution in the surrounding swirling flow. The spectacular character of breakdown, Hebbar et al[61] , is shown in (Figure 2.3), which shows flow visualisation, in a water tunnel, for a simple double delta wing planform.

During water tunnel experiments, the two primary vortices, originating at the wing apex, can be made apparent by the concentration of dye in their core. When breakdown takes place, the core suddenly expands, the dye traces becoming first distorted and then diffuse due to a rapid generation of turbulence. This type of visualisation gives the impression of a brutal transition – or jump – between two states with well-defined and distinct properties.

Vortex breakdown poses severe limitations on the aircraft performance where the stability and control are impacted by the sudden effects on the aerodynamic forces and moments. The onset of vortex breakdown of a manoeuvring delta wing results in dynamic hysteresis and lags in the vortex development and aerodynamic loads. In fact the coherent fluctuations within the breakdown region can promote a structural response in aircraft surfaces immersed in the vortex path. An example of this is the tail buffet in twin-tailed fighter aircraft where the fluid /structure interaction may result in significant reduction of the service life of structural components, Thompson[84].

Vortex breakdown is of importance in a large number of practical situations. With the advent of fighter aircraft manoeuvring at very high incidence, the breakdown of the primary vortex coming from the wing apex is more likely to occur over the wing itself, thus affecting its performance through the interaction of the burst structure with the wing aerodynamic field. In addition, as breakdown often takes place at a different location over the two wings, the resulting asymmetry may induce an undesired roll moment.

The same kind of problem may affect the fuselage of a missile or an aircraft, although for the classical cylindrical shape, vortex asymmetry tends to appear before breakdown except if the field is influenced by an adverse pressure gradient. Also, in some situations, the breakdown points oscillate along the axis of the vortices, the motion being in opposite phase in each wing. There results a periodic roll moment, which can be at the origin of a phenomenon similar to the wing rock due to an unsteady interaction of the two primary vortices of the wing. Also, the breakdown can interfere with the wing rock phenomenon itself, Terry Ng [73].

In some circumstances, vortex breakdown is considered beneficial. Thus, breakdown can be a means to 'kill' the large size vortices emanating from transport aircraft wings, which constitute a hazard for smaller aircraft, Chodhuri et al[33]. Also, the breakdown of the swirling jet at the exit of an injector can be used to improve the air-fuel mixing in a combustion chamber. The location of the vortex breakdown is affected by wing sweep angle , angle of attack , the slope of the leading edge of delta wing and the upstream disturbance and other factors, which will be discussed later in section 2.6.

As interest in the unsteady aerodynamic characteristics of delta wings is increasing, vortex breakdown remains a challenging aspect of vortical flow fields. Since highly manoeuvrable aircraft are designed to operate at high angle of attack , the vortex breakdown location may move on the wing and affect the stability of aircraft . Therefore, it is important to know how the location of vortex breakdown changes during manoeuvre. The basic mechanism responsible for the movement of vortex breakdown location, its influence on performance and stability , and its control continue to be explored in detail.

Extensive reviews of experimental , numerical and theoretical work on vortex breakdown are given by Visbal[5], Leibovich[7] , Lambourne et al [8] and others. These reviews show that despite significant progress, a comprehensive theory explaining the phenomenon has not yet been established . However these are some of the three major theoretical frame works that have been adopted in the explanation of vortex breakdown, Delery[133] :

a) hydrodynamic instability.
b) vortex wave theories.
c) boundary – layer separation analogy.

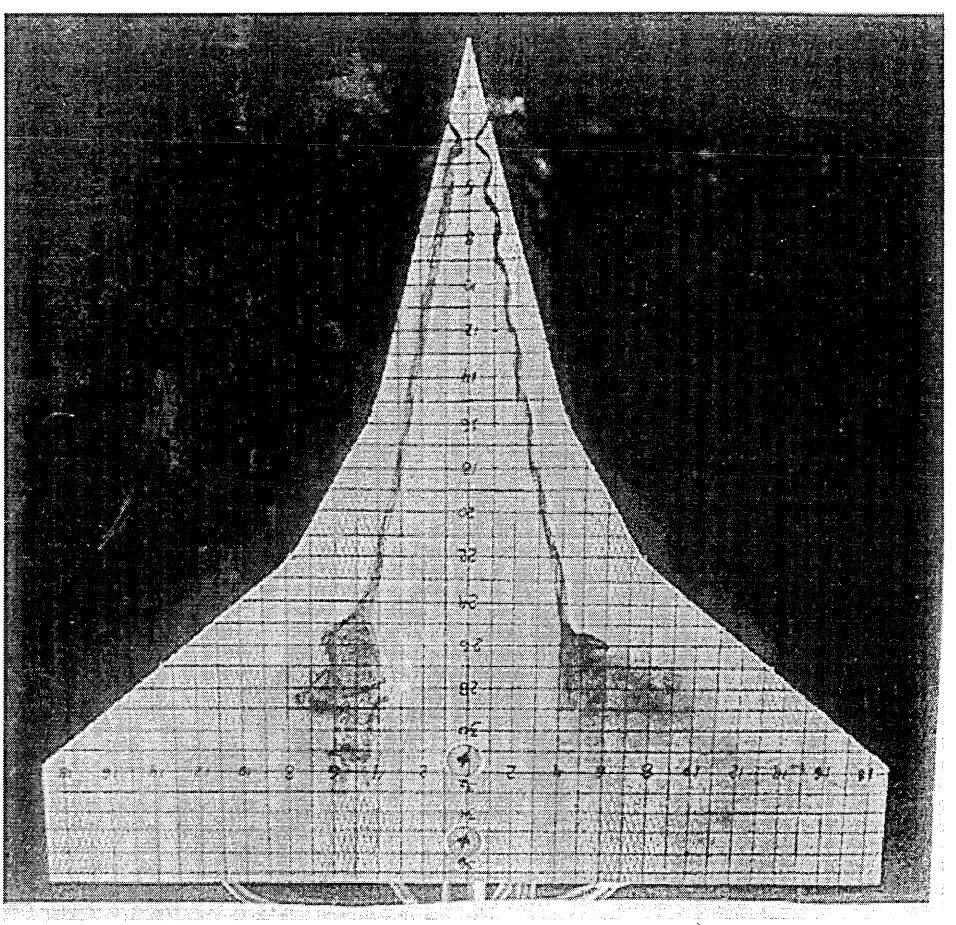

(Figure 2.3) Vortex breakdown over double delta wing, water tunnel, AOA = 20°, Re = 24,000 reproduced from Hebbar[61]

Delery[133] describes vortex breakdown as a rapid dilatation of the vortex structure. When breakdown occurs, the core of the vortex undergoes rapid expansion, and flow visualisation of the vortex gives the impression of a large jump between two well-defined flow types. Experiments by Sarpkaya[4] have suggested that there are three types of vortex breakdown, which depend on the swirl intensity of the vortex. However, Delery suggests that there is even some doubt if even some of Sarpkaya's classifications of vortex breakdown actually exist, as some of the different classifications could be different observations of the same phenomenon. Vortex breakdown does not tend to occur in vortices embedded in a turbulent boundary layer. Either the pressure gradients which cause the core deceleration do not tend to occur, or the vortices tend to be decayed by the presence of the wall before the natural burst point.

In terms of structure there are two major types of vortex breakdown (Figure 2.4 and 2.5) – denoted as bubble and spiral – are found from visualisation both in tube devices and over delta wings, Lowson[12]. An important aspect of spiral breakdown is its quasi – periodic unsteady structure.

In bubble breakdown, a stagnation point develops on the vortex axis followed by an oval-shaped recirculation zone. As described by Lambourne et al [8], the upstream half of the recirculation zone can be nearly axisymmetrical with the flow passing smoothly around it; however, the downstream half is usually open and irregular with the flow shedding from the aft end as if from an imaginary bluff body. The length of the bubble is usually two or three (upstream) 'core' diameters. Downstream of the bubble the now-diffused vortex is turbulent and continues to diffuse rapidly with distance.

Spiral breakdown is characterised by a rapid deceleration of the core flow followed by an abrupt kink at which point the vortex core takes the form of a spiral, which persists for approximately three turns before breaking into large scale turbulence. Gordnier[13] explained that one distinguishing characteristic between the bubble and spiral breakdown is the existence of a three-dimensional stagnation point at the head of the bubble breakdown. This three-dimensional stagnation point provides the distinctive change in appearance between the bubble and spiral breakdown.

The different appearance in flow visualisations of spiral and bubble modes of breakdown can therefore be viewed as the result of a change in topology (associated with the pitch of the spiral) and does not necessarily imply inherently different flow disturbances. It is suggested that the fluctuating of breakdown on delta wings reported more of a bubble character when moving upstream and a corresponding spiral appearance when moving down stream, Payne et al [15].

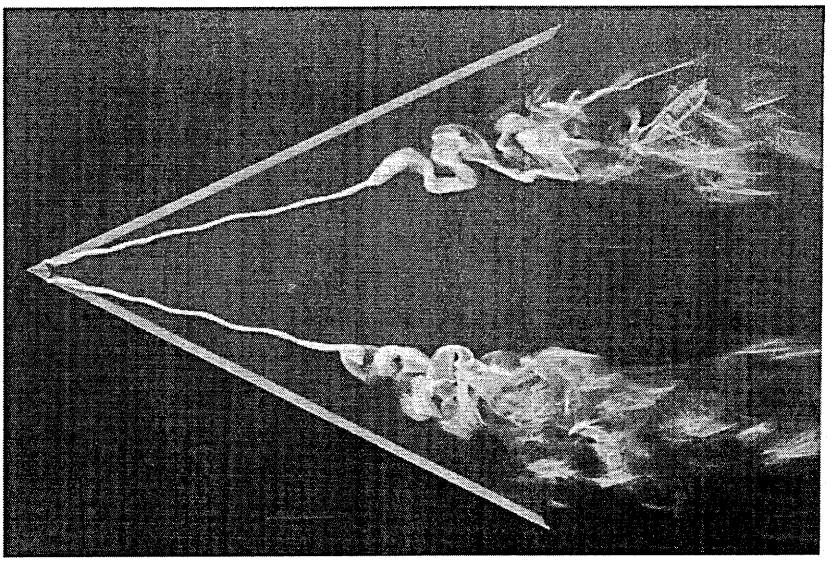

(Figure 2.4) 60° swept delta wing with a spiral type vortex reproduced from, Werle[137]

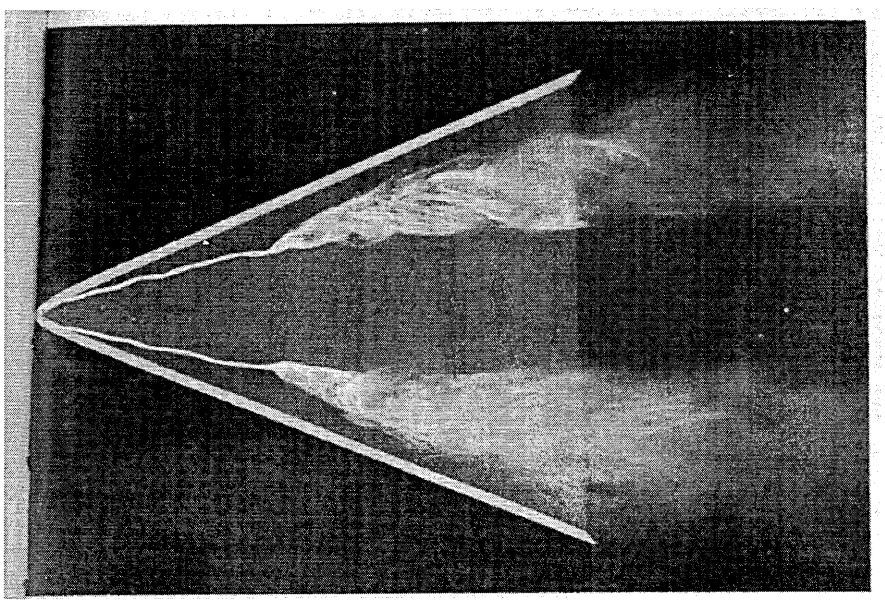

(Figure 2.5) 60° swept delta wing with a bubble type vortex reproduced from, Werle[137]

The physical mechanism responsible for breakdown is not well understood even in a steady free stream. Several experimental studies have been conducted in order to understand the nature of breakdown, Lambourne et al [8] . The early studies of vortex breakdown used flow visualisation extensively and were carried out to observe the effects of geometric parameters such as angle of attack, sweep and yaw angle.

Vortex breakdown strongly depends on the magnitude of the swirl motion, Jones[3]. The circumstances of breakdown are practically insensitive to the Reynolds Number and the local turbulent properties. However, these two factors have a strong influence on the readiness of a vortex to breakdown through their influence on the development of the vortex before it enters the breakdown region. Also, important theoretical work has been done to predict and to understand the breakdown of a vortex, most of their conclusions have been confirmed by experimental observations[4,12,16,17,18,19,23] .

2.4 Shear Layer Structure

The transverse pressure gradients (in most general cases) are responsible for the formation of vorticity. Typical cases are (a) wing tip flow; (b) delta wing at incidence; and (c) axi-symmetric bodies at incidence. In the case of a wing tip, vortex filaments created by this spanwise pressure gradient and are oriented in a streamwise direction. Due to their rotational nature, they roll-up behind the wing tip as each one interacts with the next, i.e. as in Prandtl's lifting line model. Due to the large strength of the pressure gradient close to the wing tip, it is logical to suggest that the strength of the vortex filament close to the tip will be stronger than that further inboard, and will induce the other vortex filaments to roll around it.

One of the important elements of the delta wing flow field is the feeding sheet from which the leading edge vortex arises. The 3D shear layer has been found experimentally to support several forms of coherent sub – structures which are super imposed on the primary vortex core and which presumably arise due to shear – layer instability.

Most often, several vortical structures appear on the same configuration, associated with a complex surface flow pattern, which may contain more than one separation line. However, as a general rule, the dominant intense structure comes from the so-called primary separation line at the origin of the most extended separation process. Such a separation can occur, for example, along the leading edge of swept wing.

When the flow of a delta wing separates at the sharp leading edge the shear layer rolls up into two primary vortices (Figure 2.6). These vortices induce velocities on the upper surface of the wing, which increase the suction pressure, as the flow rolls over the primary vortices and downward it impacts the surface along the primary attachment line and then flows outward. Because of the steep adverse pressure gradient outboard of the primary vortex, the boundary layer separates and forms small secondary vortices of opposite sense .

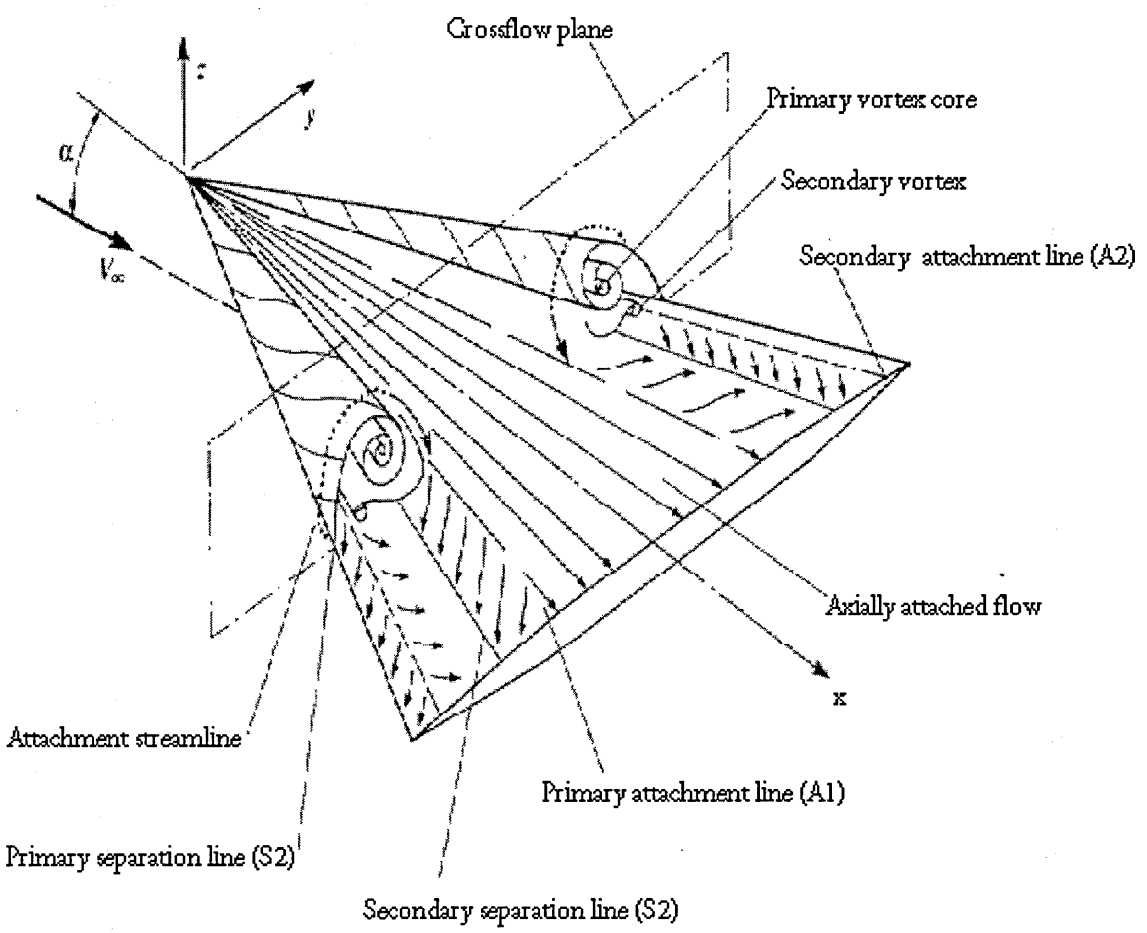

(Figure 2.6)Schematic of the flow field over the top of a delta wing at angle of attack, reproduced from Anderson[183]

Gad-el-Hak[23] observed, in flow visualisation studies of delta wings at low Reynolds Number, that the vortex sheet emanating from the leading edge rolls up periodically into discrete vortical sub – structures which under go a pairing process similar to that encountered in plane mixing layers. He attributed this phenomenon to the inviscid Kelvin – Helmholtz type instability of the shear layer.

Payne[15] reported, from smoke flow visualisation, the formation of sub – structures along the periphery of the primary vortex . These structures are stationary and do not rotate with the vortex . Lowson[12] observed two different types of vortex sheet instability coexisting in the leading edge vortex , he suggests that the first unsteady type is that found by Gad – el – Hak , where as the second stationary type corresponds to the observation of Payne .

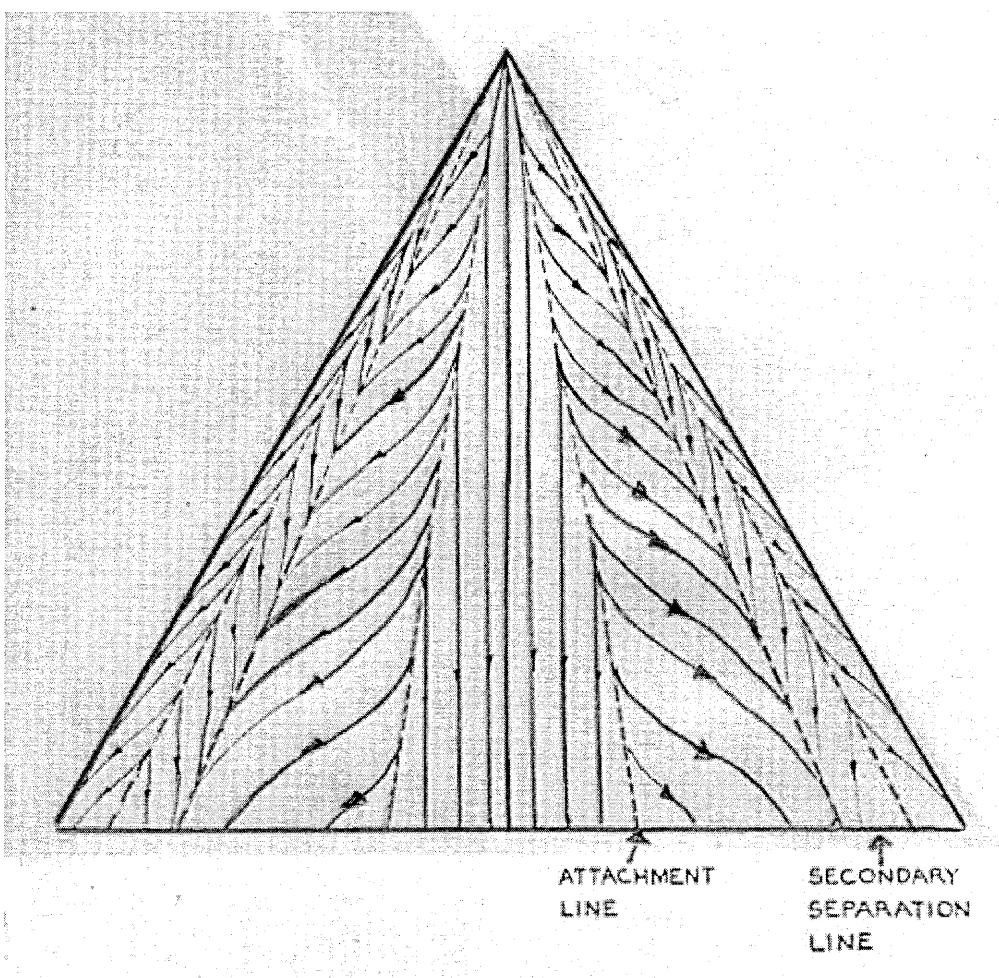

(Figure 2.7) Typical Flow over a Delta Wing at moderate incidence reproduced from Earnshaw and Lawford[95]

The flow pattern on the upper surface of a delta wing is characterised by three distinct regions (Figure 2.7) : a central region with attached stream wise flow, a region between the attachment lines and the secondary separation and a region between the secondary separation and the leading edge , where the flow pattern is produced by the secondary vortices . As the boundary changes from laminar to turbulent , the secondary separation line moves abruptly toward the leading edge of the wing this is because the turbulent boundary layer is better able to withstand the adverse pressure gradient in the spanwise direction . The secondary vortex is displaced outward toward the leading edge and its size is reduced . The surface flow patterns show the wall shear stress direction , which is a reference for the amount of the cross flow in the vortex .

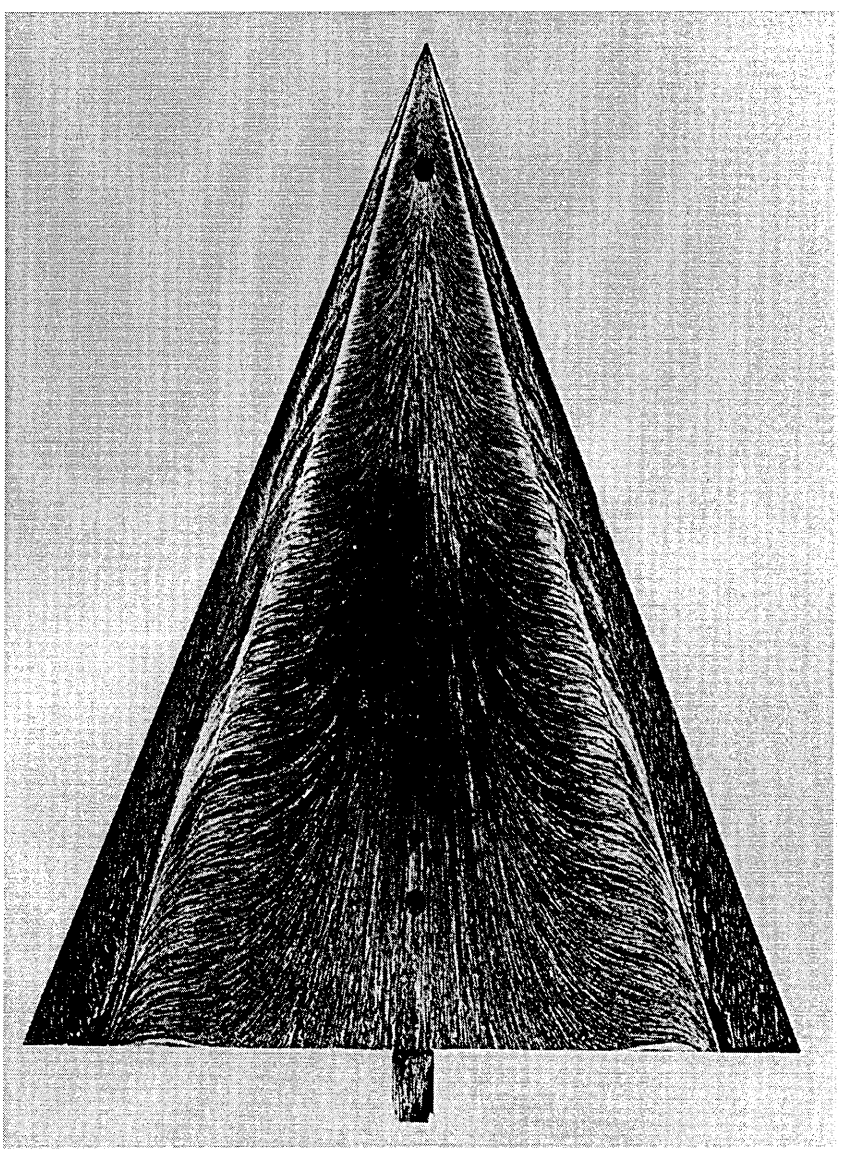

(Figure 2.8) 65° swept delta wing, flat upper surface, oil-flow pattern at AOA=20°, reproduced from Lawford[94]

The streak lines under the primary vortex thus provide an indication of the vortex strength . A stronger vortex has a greater spanwise velocity component which results in a sharper turn of the flow towards the leading edge after attachment.

Lawford [94], (Figure 2.8), measured the flow velocity through the leading edge vortex, and noted three flows regions: the free shear layer, the rotational core, and the viscous subcore. Within the subcore Lawford found axial velocities as high as three times the free stream velocity.

Another feature is the secondary separation of the boundary layer developing along the wing surface and the resulting upward ejection of vorticity . The importance of this effect was examined by Gordnier et al [187] using CFD, who found that the vortex / surface interaction characteristics depend on the vortex strength and its proximity to the wing surface , therefore it is expected that in the delta wing configuration increasing the Reynolds Number and angle of attack and reducing leading edge sweep will promote unsteady boundary layer separation and shear layer roll – up.

2.5 Vortex Dynamics

The investigation of the unsteady aerodynamics of delta wings at high angle of attack is motivated by current interest in enhanced aircraft manoeuvrability . Verhaagen et al[16] reviewed experimental and a CFD work on 76°/40° sweep double delta wing pitching to high incidence. This work shows that during transient high-angle-of-attack manoeuvres, a lag on the onset of the leading edge vortex breakdown occurs as compared with the stationary wing, this lag is also accompanied by over shoots in the wing aerodynamic loads. The initiation and unsteady behaviour of vortex breakdown represent therefore one of the central issues in high angle of attack aerodynamics

The dynamics of a pitching delta wing, Gad-el-Hak[23] , were considered as early as 1958. However the bulk of the contributions on this topic appeared only in the past few years[17→26] . The flow over a delta wing at a fixed angle of attack is dominated by two leading – edge vortices. The circumferential velocity component along a plane normal to such a vortex is reminiscent of a potential vortex with a viscous core , where as the axial component resembles a jet . The structure is symmetric about the symmetry plane of the wing.

A large number of researchers have studied this steady flow problem, and many reviews have appeared. Recent investigators reported on the use of powerful experimental techniques, like Laser – Doppler Velocimetry (LDV), Double Cross Wires , or Particle Image Velocimetry (PIV) and documented quantitatively the complex vortical flow fields over delta wings[27→38].

The three dimensional vortex – dominated flow field responsible for dynamic separation during pitch – up have been examined experimentally[25→33]. Vortices are generated and transiently reside on the upper surface of wings dynamically pitch up through the static stall angle of attack. These vortices radically alter the upper surface pressure distributions on a wing and produce greatly amplified aerodynamic forces and moments. Mutual interaction between vortices and accumulations of vorticity deform the vortex, disrupting vortex spanwise uniformity. This yields unsteady surface pressure distributions and spanwise aerodynamic loads that are highly three dimensional.

Complete control of systems that exploit unsteady aerodynamic effects will also demand understanding of three – dimensional dynamic reattachment. Ahmed et al [30] involved in an experiment of an oscillating airfoil and found that dynamic reattachment initiated near the airfoil leading edge progressed afterward over the chord , and completed with disappearance of a separation bubble .

The dominant direction of the mean flow changes due to dynamic pitch-up and pitch-down. This aspect of the flow is bound to influence both the development of the vortex as well as its breakdown characteristics. Visbal[21] noted that the angular delay and onset of breakdown are strongly linked to the pressure gradient prevailing along the vortex axis. This pressure gradient, which depends on the wing angle of attack and pitching motion, plays a dominant role in the initiation of vortex burst .

Rediniotis et al [22] investigated the transient flow field over a 75° sweep delta wing during pitch – up motion to very large angle of attack. They noted that earlier qualitative evidence of hysteresis in the development of the flow and significant differences of vorticity content between the steady and the unsteady motions for a low reduced frequencies, (Figure 2.9). Gad-el-Hak[23], investigated the flow fields, in a water tunnel, around two pitching delta wings (45° and 60° sweep) for various reduced frequencies ranging from v = 0.05 to 3.0 , (see notation for reduced frequency), and found that the evolution of the separation vortex revealed a hysteresis loop that is a strong function of the reduced frequency. At low reduced frequencies, the separation region on the suction side at the downstroke was visually thicker than that at the upstroke, (separation was assisted in terms of the dye concentration at this location) at high angle of attack.

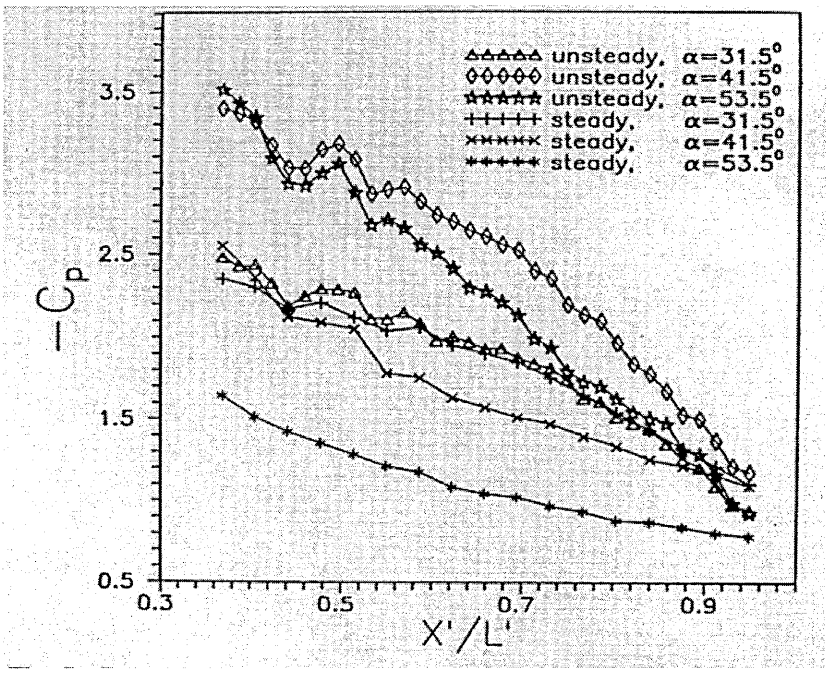

(Figure 2.9) Pressure distributions for steady and unsteady flow along the chord of a 75° swept delta wing model, reproduced from Rediniotis and Telionis[22]

Atta et al [24] experimented in water tunnel 52° sweep delta wing and noted that at low reduced frequencies, the vortex core develops in the upstream direction (towards the apex), at high reduced frequencies, there is ejection of the leading edge of the vortex core from the apex in the down stream direction. Correspondingly, the direction of the dynamic hysteresis loop of vortex breakdown location v.s. angle of attack is determined by the type of vortex development . During unsteady development of the vortex core , the axial velocity on the centre line of the vortex is essentially constant with distance along the core. At the onset of vortex breakdown, there is an abrupt deceleration, the velocity variations in this region exhibit a similar form for a range of angle of attack and reduced frequency.

Guglieri et al [102] investigated the vortex dynamics on a 65° delta wing in side slip and showed that the phase lag between dynamic vortex breakdown position and primary motion is a linear function of reduced frequency. Also, in side slip, the vortex core incident varies linearly with the angle of attack.

2.6 Factors Affecting Vortex Characteristics

Understanding the physics of vortex breakdown, either in an isolated vortex or a leading-edge one, and modelling it, have been key issues for decades. In the case of a flat delta wing with a sharp leading edge, it has been found that the angle of attack and the sweep angle have the largest impact on the breakdown location. Huang et al[101] investigated the effect on leading-edge vortex breakdown of geometry modifications on slender flat delta wings ranging from 55° to 75° sweep by means of water-tunnel flow visualisation experiments and found that the effectiveness of the leading edge bevel, (the angle geometry of the leading edge, see Figure 3.3), in delaying breakdown appears to be related to the ratio between leading edge width and pre-separation boundary layer thickness. (See section 6.3).

Kegelman et al [105] also presented results of 70° sweep half span delta wings with a different leading edge shapes ranging from blunt rounded edges to leeward and windward bevels, which show that breakdown is influenced by the leading edge geometry of the wing. In addition the trailing edge geometry might also have some influence on the location of vortex breakdown, since it might affect the adverse pressure gradient at the trailing edge. This adverse pressure gradient is believed to affect breakdown.

Pelletier et al [129] investigated both static and dynamic vortex breakdown on a slender delta wing with a centre body and found that the centre body delays the propagation of breakdown, especially at lower angles of attack where breakdown was seen to be closer to the trailing edge. For dynamic motions, both in pitch and roll, breakdown is affected by the reduced frequency increasing the reduced frequency of oscillation increases the width of the hysteresis loop and the time lag increases.

Payne et al [106] investigated vortex breakdown on a thin delta wings of 70°, 75°, 80° and 85° sweep and showed that at a given angle of attack, as the sweep angle increased, the location of breakdown moves aft. Also, the velocity profiles in the vortex core obtained with a Laser Doppler Anemometer showed the development of a jet-like core flow, which reached three times the freestream velocity before breaking down. After the breakdown the velocity profiles became wake-like in nature.

Yang et al [103] investigated a variable sweep delta wings and noted that the variation of the vortex breakdown location for harmonic variations of sweep angle between 60° to 70° showed hysteresis loops and phase lags that depend on the reduced frequency, and suggested that the external pressure gradient plays a major role in the dynamic response of breakdown location.

The effect of pitch rate has been previously investigated by Ericsson[49] with emphasis on the lag of vortex breakdown and on the overshoot in the wing aerodynamic loads as compared to the static situation, and noted that in order to explain the observed lag in the onset of bursting, further quantitative and qualitative information is required on the vortex core development at various instants during the pitch motion which can help explain, for instance, the role of the axial pressure gradient imposed on the vortex by the wing motion .

The pitch-axis location plays an important role for a delta wing in a ramp-type manoeuvre experiment, the pitch-axis location is of importance when correlating experiments performed with different pitch-axis locations ranging from the wing apex to the trailing edge . In addition , this parameter would be expected to be important when considering canard/wing configurations or double-delta wings manoeuvring at sufficiently high pitch rates. Features of the vortex development and breakdown on a wing oscillating in pitch are reported by Atta et al [46] as well as Ericsson[49]. Visbal et al [47] who investigated, using CFD, the onset of vortex breakdown above a 75 deg. sweep delta wing (subject to a ramp-type pitch manoeuvre to high angle of attack) showed that:

1. Increasing the pitch rate produced a further angular delay in the onset of breakdown

2. For a fixed pitch rate, moving the pitch-axis from the wing apex to the trailing edge resulted in an additional delay of breakdown characterised by a shift in angle of attack, but without significant alternation of the flow structure.

Thomson[50] investigated a series of delta wings and modified delta wings in a water tunnel and concluded that :

1. The vortex burst moves upstream with increasing incidence and/or decreasing leading edge sweep.

2. The sweep back of the trailing edge displaces the burst slightly Upstream, sweeping the trailing edge forward has a more noticeable effect in the downstream direction.

Ekaterinaris et al [51] investigated, using CFD, the structure of the vortical flow field over delta wings at high angle of attack for a 75-deg and 63-deg sweep delta wing and concluded that, as the angle of attack was increased , a progression from no breakdown to steady bubble-type break down to unsteady spiral-type breakdown was seen in the computed results and a decrease of the sweep angle resulted in increased suction peaks at the leeward side .

Poll[52] studied the formation and development of spiral vortex flow over a swept-back wing of three alternative leading edge shapes and found that the incidence necessary for the onset of spiral vortex flow depended strongly upon leading edge radius, and that dependence upon Reynolds Number increased with increasing leading edge radius. For the sharp leading edges tested here it is expected that the effect of Reynolds Number will be small.

Parameters like angle of attack, sweep angle and yaw angle also affect vortex breakdown, Gursul et al [103] suggested that the velocity component in the streamwise direction and the sweep angle of the leading edge determine the swirl angle $\phi = \tan(v/u)^{-1}$, where v and u are swirl and axial components of velocity respectively). An increase in the angle of attack, a decrease in the sweep angle or an increase in the yaw would increase the ratio between circumferential and axial flow, and thus make the breakdown location move toward the apex. The breakdown position will move forward during flow acceleration and remain so until the steady speed condition is reached. At this steady speed, the position will return to its normal breakdown location. Also placing an object on the axis will cause an earlier breakdown.

Traub et al [139] investigated the influence of Reynolds Number on delta wing aerodynamics and noted that for a 60° delta wing, the vortex breakdown at a given angle of attack was delayed as the Reynolds Number decreased. The vortices and secondary separation line are further inboard than at the higher Reynolds Number. Increasing the Reynolds Number is gradually associated with a gradual decrease in the peak pressure coefficient.

2.7 Working Section Interference Effects

It is desirable to use full-span models in experiments whenever possible, but some wind tunnel constraints, or the need to utilise certain experimental equipment, make the use of half-span models a necessity. The use of half-span models is accompanied by a number of problems related to the basic half-span model geometry. A half-span model requires a wall or splitter plate to lie in the vertical plane of symmetry. The size and placement of this solid surface influences the boundary layer development along the working section wall and the resulting ''corner'' regions can alter the delta wing flow field. For certain types of tests, the model must be mechanically isolated from the splitter plate and therefore, a gap must exist between the model and the plate. The influence of such a gap has been the focus of much of the concern related to half-span model testing, see for example Cunningham[107]. A further concern is the restriction associated with the symmetry imposed by the splitter plate for those conditions for which the full-span flow field would be naturally asymmetric.

It should also be noted that full-span model testing is also accompanied by certain limitations. Full-span models must be supported by either sting or strut mounts. Strut mounts are usually affixed to the bottom side of the models and their influence on the vortex development or interaction between the strut wake and the vortex dominated flow field is not well understood. Aft mounted stings present similar problems, particularly at angles of attack where the vortex breakdown approaches the trailing edge of the wing.

In order to obtain high quality, reliable wind tunnel test data, factors related to wall interference, flow angularity, local variations in velocity and support interference, etc., must be evaluated and corrected. One of these factors is the wall interference effect. Because of the presence of the solid working section wall, the flow conditions around the model are usually different from those in the free – air condition. These differences may result in:

1. A reduction in the average down wash experienced by the model.

2. A change in the stream line curvature about the model.

3. An alteration to the local angle of attack along the span of the model.

4. A change in dynamic pressure about the model because of both the solid and wake blockage.

5. An increase in the axial local on the model as a result of the axial pressure gradient in the working section – normally referred to as 'horizontal buoyancy'.

Wall interference can be a very important effect particularly for relatively large models at high angle of attack with significant amounts of separated flow.

There are differences between sidewall effects on 2D and 3D wings. In the case of 2D wings methods to account for the sidewall effects have been primarily based on two different considerations. First by, as proposed by Preston[170], it is assumed that trailing vorticity is shed due to loss of lift in the wall boundary layer and a consequent change in the effective angle of incidence. The second approach, proposed independently by Barnwell[91] , assumes the changes in the wall boundary layer thickness due to model – induced pressure field to have a significant effect on the flow over the aerofoil . Using the small disturbance equation and accounting for the changes in the width of the flow passage , Barnwell presented a simplified Prandtl – Glauet rule to account for the attached sidewall boundary layer effects .

Murthy[89] investigated a correction to account for the sidewall boundary layer effects on a two – dimensional aerofoil by taking into consideration the non linear variation of the cross flow velocity across the width of the tunnel, and showed a significant reduction in sidewall boundary layer effects on airfoil mid span measurements with increasing aspect ratio of the model.

In the case of 3D wings: Katz an et al [90] investigated the effects of blockage ratios between 7% and 20% projected frontal area ratio, so that the changes in the aerodynamic coefficients under these extreme conditions can be estimated. It was concluded that, as the blockage ratio increases , wall interference effects may become quite large. As a result the wall – pressure distribution signature varies in a similar manner and most likely can be used for engineering corrections , even when the blockage ratio reaches levels of 20%.

Pass[115] looked at wake blockage in a wind tunnel and correction methods available to simulate free-air conditions and take into account the flow acceleration around the body. After reviewing several correction techniques, a method for small subsonic wind tunnels based upon experimental data obtained with a rectangular planform of different sizes is given which utilised a correction factor, which varied with angle of attack.

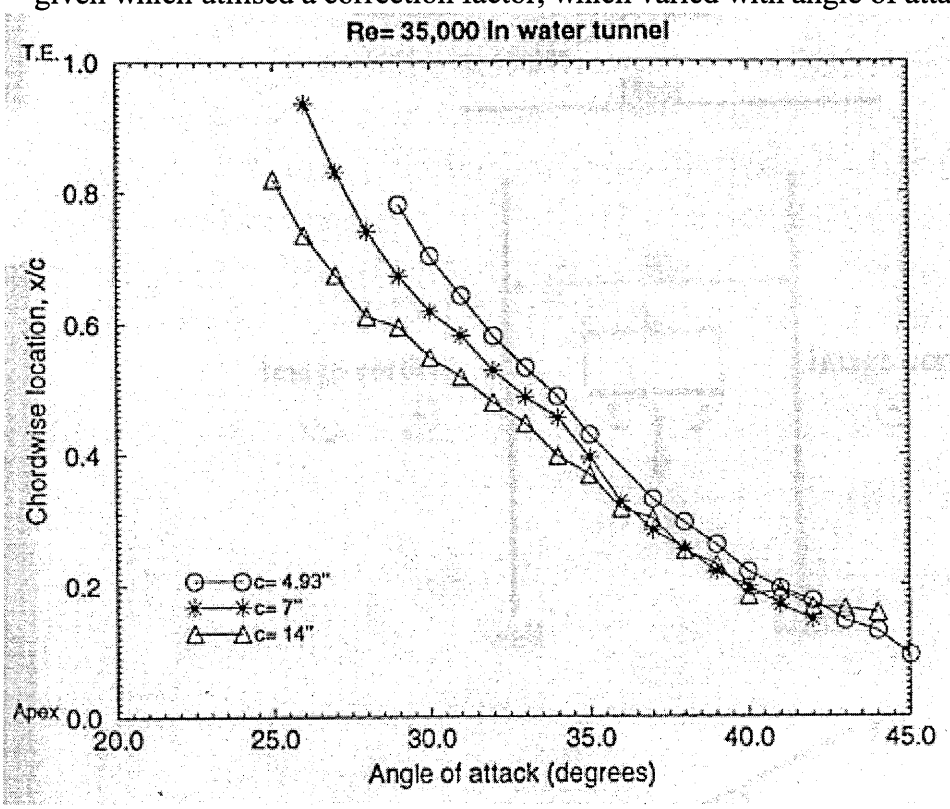

(Figure 2.10) Blockage effect of a 70° swept delta wing model of 3 type of chord length, reproduced from Nelson and Pelletier[128]

Pelletier et al [128] conducted an experimental study to investigate the effect of blockage on the chord wise location of vortex breakdown on flat-plate delta wings, where an attempt was made to explain the effect of wall interference of vortex breakdown location using the method of images to represent the walls of the test section.(Figure 2.10).

They showed that an analysis using image vortices to represent the working section walls indicated that the presence of the walls caused the effective angle of attack of the wing to increase. Consequently the vortex breakdown location was shown to move upstream with increasing wing size for a given angle of attack.

Karou[132] investigated theoretically and experimentally the interaction between the leading edge vortices of slender wings and the wind tunnel sidewalls. The theoretical model, in which the walls are represented by the image method, predicts an increase in vortex strength and its upward and inboard movement, due to the walls presence. The uncorrected experimental results show that by moving the walls closer to the model, the lift, drag and pitching moment coefficients are increased. The lift increase is due to the induced upwash effect that results in a higher linear lift and a stronger contribution of the vortices to the non-linear lift. Also, the changes in vortex position and the increase in its strength, resulting from the interaction with the side walls, are equivalent to the changes to the incidence increment induced by the lift effect.

Walton et al [112] experimented a half span 70° sweep with root chord c = 35.56 cm and thickness t = 12.7 mm and determined that the size of the gap between the wing root chord and splitter plate was very important when using a half-span model. It has been shown that there exists a range of gap widths where the surface flow patterns and vortex core location do not significantly change. Cunningham[107] experimented several half delta wing models ranging from 55° to 80° sweep having 30cm root chord and 1.6mm thickness, where he varied the size of the gap from zero to 1.6mm which was the estimated thickness of the splitter plate boundary layer. Over this range of gaps, he observed no discernible effects on the angle of attack at which vortex breakdown crossed the trailing edge.

Kegelman et al [105] did not vary the gap size but validated the use of the half-span models by running flow visualisation tests on similar small full-span models with and without the centre-line splitter plate. They concluded that the presence of the splitter plate did not alter the vortex trajectory nor influence the burst point. It should also be pointed out that Kegelman attached a piece of weather stripping to the wing root chord to prevent airflow through the gap.

Subrahmanyam et al [111] experimented on an aerofoil that has a root chord c = 12.5 cm and thickness t =16.8 mm and concluded that there is a loss of lift due to the presence of a gap, as a result of enhanced separation on the leeward side, which produces a shift in the zero lift angle of attack. Flow visualisation suggests that at the plate-wing intersection, the flow through the gap changes the separation pattern on the aerofoil near the plate.

Ericsson[48] has also looked at support interference, noting that its effect was more important during dynamic tests than static tests since it cannot be calibrated out. He also showed that the presence of a fuselage on a wing, which can be looked at as a source of interference and blockage, could affect the vortex breakdown dynamics of slender wings, thus affecting their aerodynamic properties.

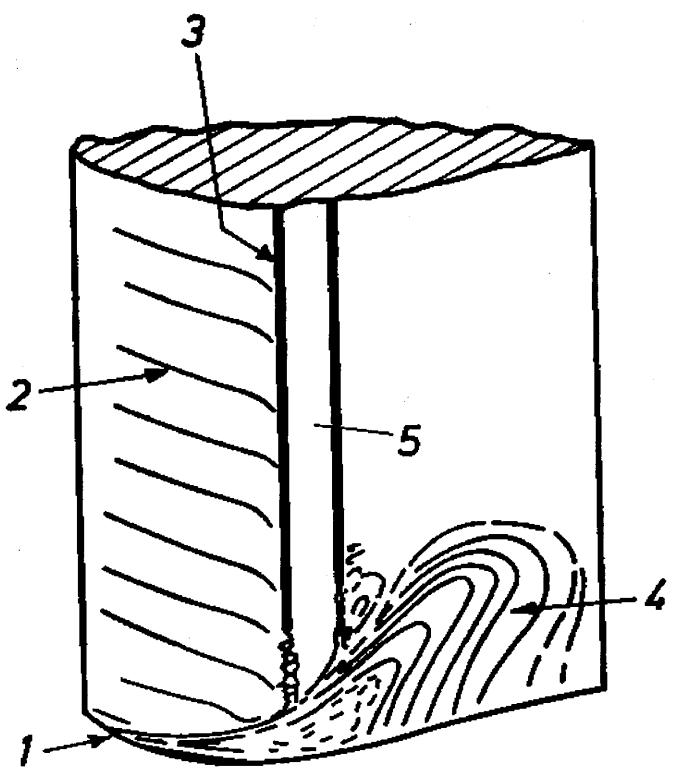

(Fig. 2.11) Typical flow pattern at wall juncture Re = 610,000.
1. Laminar separation; 2. Typical streaks; 3. Oil fall due to gravity; 4. Vortex; 5. 2-D separation bubble, reproduced from Galbraith[135]

2.8 Effect of Wall Boundary Layer on Leading Edge Vortex

When the boundary layer at the wall test section separates, it leads to the formation of vortical structures (vortices) formed by the rolling up of the viscous flow sheet , previously confined in a thin layer attached to the wall, which suddenly springs into the outer non-dissipative flow. Such vortices appear in a large number of circumstances and they often play a dominant role in the overall flow properties. The vortex is developed from the formation of vorticity within the fluid flow. The vorticity is simply defined as one of the two motion types available to a fluid particle, which allows it to rotate about its three axes (x, y, z).

The boundary layer on the end plate can effect the flow over the model near the juncture of the model and the plate, Galbraith[135] has observed that the corner boundary layer separates before the main aerofoil separation, at which point the corner flow is enhanced and results in a strong horseshoe vortex. The effect of this is to decrease the lift on the model close to the plate. Furthermore, trailing vortices resulting from such a change in lift would have an effect on the lift distribution on the model (Figure 2.11).

Verhaagen et al[110] investigated in a low speed wind tunnel on a large semi-span 76° swept delta wing model mounted to a reflection plate, the influence of the thickness and turbulence of the reflection plate boundary layer on the development of the flow over the delta wing. Results indicate that, near the apex of the delta wing, the vortex flow is strongly affected by the boundary layer on the reflection plate. Where at 10% chord an increase in the reflection plate boundary layer thickness results in a strong increase of turbulence and a reduction of the pressure gradient in the free shear layer from the leading edge. However they did not investigate the vortex trajectory and vortex breakdown.

Mendelson et al[23], carried out two-dimensional span-loading tests on an aerofoil model in a wind tunnel to determine working section wall boundary-layer effects and found that the load at the tunnel-wall may be as much as 10% lower than that at the centre of the tunnel working section. Changes in boundary layer thickness produce small changes in load, and at high angle of attack, average pitching moment for the wing may differ from that at the centre of the working section because of the non uniform stall.

Lan[42] studied a 70° sweep delta wing, using CFD, the effect of changes in free stream turbulence levels on wind tunnel data and noted that with increasing the turbulence intensity (Tu) the velocity profile indicates a much thicker boundary layer on the upper surface , and increasing the boundary layer thickness tends to push the secondary separation line outward .

Pedišius et al[43] showed that the free stream turbulence penetrated into most of the wall boundary layer to increase the turbulence level in and outside the boundary layer. Washburn[41] investigated, 76° sweep delta wing, two free stream turbulence levels, (Tu = 0.1% and 7.5%), in a wind tunnel, although the effect of the free stream turbulence on the location of the vortex breakdown was difficult to analyse due to the highly unsteady flow and the low density of the smoke, the more turbulent flow caused the breakdown location to fluctuate approximately 10 to 20 percent of chord, and an increase in free stream turbulence dramatically influenced the aerodynamic loads on the delta wing. It was also noted that the more turbulent free stream reduced vortex induced lift. It was unclear whether the reduction in vortex strength in the turbulence flow was due to the entrainment of the freestream turbulence, or instabilities in the shear layer from the leading edge.

2.9 Summary of the Literature Overview

It is clear that there is a requirement to continue using half span models when investigating vortex flows over highly swept wings. However, relatively little is known about the adverse effects of such a test configuration, particularly in relation to the influence of the end plate boundary layer on the development, trajectory and eventual breakdown of leading edge vortices. Previous work by Verhaagen et al[110] was limited to one configuration at a fixed angle of attack mounted on a simple splitter plate.

As a result an experimental programme is proposed to investigate the influence of changes in end plate boundary layer characteristics on the vortex behaviour for highly swept wings under both static and dynamic test conditions in a two different type of facilities: water tunnel and wind tunnel, for flow visualisation and surface static pressure measurements. A correlation between the water tunnel and the wind tunnel needed to be investigated including the effect of Reynolds Number. Also a method to predict the vortex breakdown from surface static pressure measurements will be investigated.

2.10 Proposed Program of Investigation

In order to investigate the effect of an end plate boundary layer on the leading edge vortex characteristics of a half-delta wing model, two facilities have been used, a vertical axes water tunnel and open return closed working section wind tunnel, dye filament visualisation, smoke visualisation and pressure measurement, as primary measuring tools in this investigation.

In the water tunnel investigation, the parameters were as follows:

(i) Four models were used 55° and 70° sweep delta wing models, with two different thickness/chord ratios (t/c=0.018, 0.036).
(ii) In static case motion, the models were tested at 5° to 35° in 5° increment.
(iii) In dynamic case motion, three reduced pitch rate were used: k=0.05, 0.1 and 0.15 for pitch-up and pitch-down.

In the wind tunnel investigation, the parameters were as follows:

(i) Three wall boundary layer configurations were generated and measured by flattened tube using a traverse gear.
(ii) One half-delta wing model 55° sweep, t/c=0.018 was tested at 10°, 20° and 30° AoA (static case).
(iii) Two reduced pitch rate were used, k=0.00111, 0.00628, for pitch-up and pitch-down.
(iv) Smoke visualisation technique has been applied to study the structure of the leading edge vortex and to correlate the vortex breakdown with the pressure measurement.

From the experimental data it will be possible to analyse and explain the influence of the end plate boundary layer on the vortical flow behaviour over the delta wing model.

3.1 Water Tunnel

The Cranfield College of Aeronautics water tunnel is a gravity fed type facility for studying a wide range of aerodynamic and fluid dynamic phenomenon. Its key design features are high flow quality, vertical orientation and continuous operation. (Figure 3.1)

Figure 3.1 Water Tunnel Test section, with Turntable, Servo Motor and Model

The test section is 22 cm x 22 cm x 108 cm long. The maximum usable test section flow velocity is approximately 0.2 m/sec. with a turbulence intensity of < 0.1 % on the centre line. The water tunnel is a gravity - fed arrangement which consists of three levels. The first level is the main tank reservoir, which contains ≈ 450 Imperial Gallons, fresh water can be filled and drained from it when it has been contaminated with dye after a long period of operation. The third level consists of the overhead tank (approximately 350 Imperial Gallons), which is the reservoir to the second level; the working section. (see Appendix A)

The flow is recirculated by a 1.5 kW, 2820 rev/min. pump, which is capable of pumping water from the main reservoir (first level) to the overhead tank (third level) in order to achieve the maximum flow speed of 0.2 m/sec. An outlet valve controls the flow rate through the test section. To maintain a laminar flow stream through out the test section a honeycomb material and a screen mesh is positioned upstream and downstream of test section. The three side walls of the test section are constructed of glass plate (16 mm thickness), whilst access is through a full-length door, which comprises the forth side. The white aluminium alloy door is fitted with three rotatable 14.5 cm diameter turntables, fitted with degree calibrated retaining rings. The centre ring was used to mount the model, where the distance from the centre ring to the top of the test section is 60 cm.

3.1.1 Flow Visualisation Technique

The technique of dye injection into the flow stream to act as a flow visualisation medium was chosen as being a relatively easily operated and effective method. Alternative ways, employed by other researchers experimenting in water tunnels, include hydrogen bubble generation and the use of polystyrene particles. Each method has its own particular area of usefulness. Dye injection visualisation is, however, considered to be a useful general technique for gaining a qualitative appreciation of flow field properties. Flow structure, vortex flow trajectory and vortex burst location are clear and both easy to recognise and record using either video film or still photographs. Unlike other flow visualisation techniques, the dye technique was free from any air bubbles or any other particles which may introduce interference in the flow.

The type of dye used in all the experiments reported here in is a fluorescent Malachite Green colour, made by Woburn Chemicals Limited. This type of dye is effective when illuminated with a simple spotlight. The concentration of the dye was approximately a ratio of 2 grams for 1 litre of water, (with this concentration after 2 hours of running the experiment continuously, the water in the test section must be drained and changed with fresh water).

To aid vortical flow visualisation, the dye was released from the apex of the half delta wing model. Holes were drilled on the leading edge of the model near the apex, the positioning of these holes were critical in order to prevent any effect of aerodynamic interference of the flow of the leading edge, that was achieved through a hypodermic tube connected to the 0.5 mm hole drilled along the leading edge of the model, see Appendix A. The method of dye supply was by placing a small reservoir above the over head tank (third level), from which the dye flowed due to the pressure difference.

A dye was allowed to flow slowly out of the small hole in the model surface. Sufficient output pressure could be maintained and controlled by the use of a brass tap mounted on the water tunnel door. A high supply pressure was neither required nor desirable since this would mean a high output jet velocity. This, in turn, could mean that the dye would be ejected through the boundary layer into the freestream or would significantly affect the flow field being studied. Flow rate is controlled by the tap and the pressure controlled by the reservoir height.

3.1.2 Water Tunnel Calibration

The speed of the flow in the working section had to be kept very low for two reasons, first, to ensure a laminar freestream, secondly to ensure a successful clear visualisation by the dye line from the apex of the wing model (steady and uniform). At high speeds the dye line would have been broken up and the general level of visualisation will be poor to visualise the vortical flow behaviour on the upper surface of the delta-wing model.

An ultrasonic flow meter (A500) was used to monitor flow velocity. (See Appendix B), this flow meter has no moving parts and it is less susceptible to corrosion damage, it is installed in the pipe below the second contraction. The flow meter uncertainty, as specified from the manufacturer (Sparling Meter Flow, Sussex, England), was ± 2 % of the actual reading. In order to check the accuracy of the ultrasonic flow meter, a simple test was performed.

By timing the descent of dye filament over the length of the test section for different ammeter reading, where a dye filament was released from the top of the working section for a length of 1 meter and the time was recorded over this length, this procedure was repeated 10 times for assurance. Using the linear regression analysis the following speed equation was found :

$\mathbf{Y = 3.054x - 12.264}$; y = flow speed ; x = amp. Readout
$\mathbf{R^2 = 0.9992}$

The percentage of error in calibrating the water tunnel flow by using this procedure was approximately 5% compared it to 2% of the manufacturer percentage of error. Therefore the manufacturer ultrasonic flow meter (A500) was accurate enough for the velocity measurement.

The water tunnel flow velocity was maintained throughout at a nominal value of 0.077 m/sec. corresponding to Re = 17000 based on the model centre line root chord. The turbulence intensity was measured by the Fibre-Film Probe Anemometer and it was ≤ 0.1 %. The turbulence intensity was measured as: $Tu = ((u^2)^{0.5} / \bar{U})$, where u is the instantaneous velocity and $\bar{U}$ is the mean flow velocity.

3.1.3 Generation of Working Section Wall Boundary Layers Profiles

Four different working section wall boundary layers were tested during the experimental program. Figure 3.2 shows the half-delta wing model attached to an end plate. The four boundary layers configurations artificially generated by:

1. Tunnel Wall (stand alone, clean, without any interference on upper surface of the tunnel wall).
2. End plate (a sharp edge plate, displaced 2.5cm from the working section wall to create the boundary layer thickness on the model).
3. Trip Wire 2.5 mm (a brass wire of 2.5mm diameter placed at the onset of the parallel flow section, 50cm from the model apex).
4. Trip Wire 6.5 mm.(a brass wire of 6.5mm diameter placed at the onset of the parallel flow section, 50cm from the model apex).

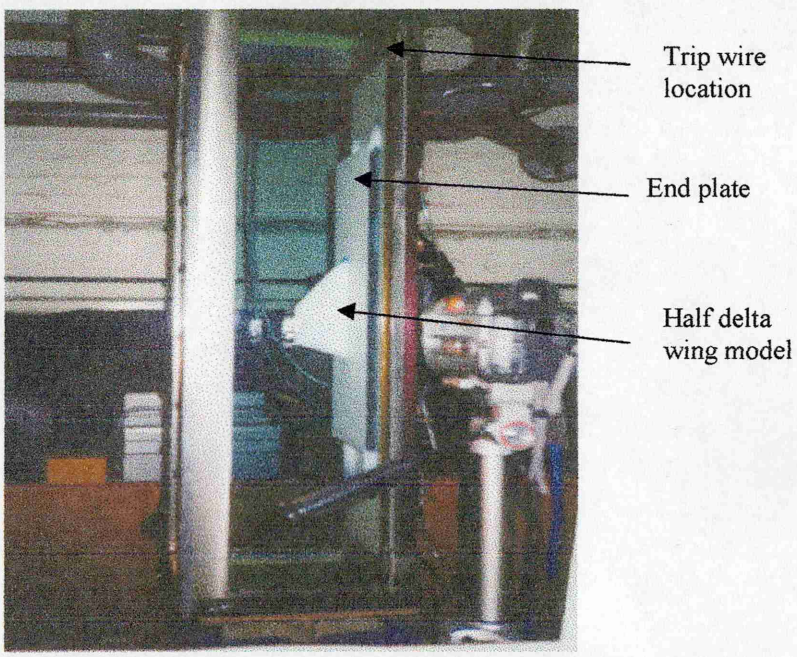

Figure 3.2 Half Delta wing model attached to the end plate

3.2 Models

Cropped half-delta wing planform models were used throughout the experimental programme. A cropped planform was used to reduce the working section blockage in terms of model projected frontal area. To study the sweep effect, 55° and 70° sweep leading edge were used, the 55° sweep was chosen where most of the latest fighter aircraft have a low sweep leading edge and 70° sweep was chosen since most of the researchers used this high sweep delta for comparison. There were four model configurations, two sweep leading edge models and two thickness/chord ratio models, as listed in Table 3.1 :

No.	Swept Leading edge	Trailing edge angle	Thickness	Span	AR
1	55°	20°	4 mm	8 cm	1.066
2	55°	20°	8 mm	8 cm	1.066
3	70°	10°	4 mm	6 cm	0.9
4	70°	10°	8 mm	6 cm	0.9

Table 3.1 Half Delta Wing Models

The models were manufactured from aluminium with a bevelled 45° leading edge (bevel side to leeward) and a flat bottom surface, (Figure 3.3), the root chord was kept constant for the four models, at 22 cm. The location of the rod connection to the model (rotation centre) was chosen to be 50 % chord length, in order to reduce any influence of the pitch -axis location on vortex breakdown, see Visbal et al [47]. The gap between the model and the wall is kept to be less than 1mm to prevent any gap interference effect.

3.3 Pitch Control Mechanism

The model is mounted on the centre ring of the three rings in the working section access panel and was connected to a turntable (Figure 3.5). The turntable rotation is controlled by a DC Servo Motor to enable the model to (pitch-up and pitch-down), for static and dynamic experiments. A PC is used with a Motion Architect card and software to control the input (model position) and the output (velocity feed back and actual movement) of the DC Servo Motor.

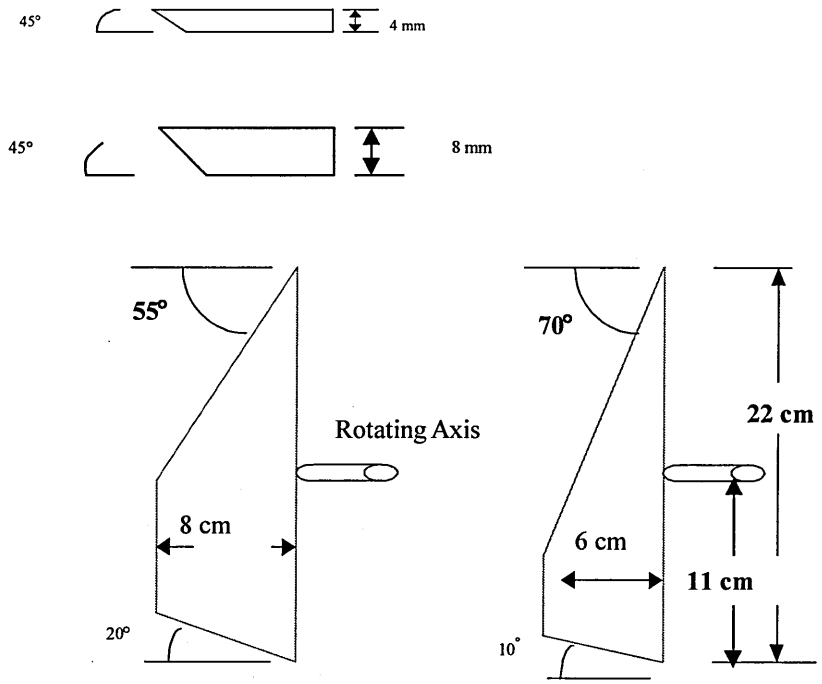

Figure 3.3 Half-Delta Wing Models

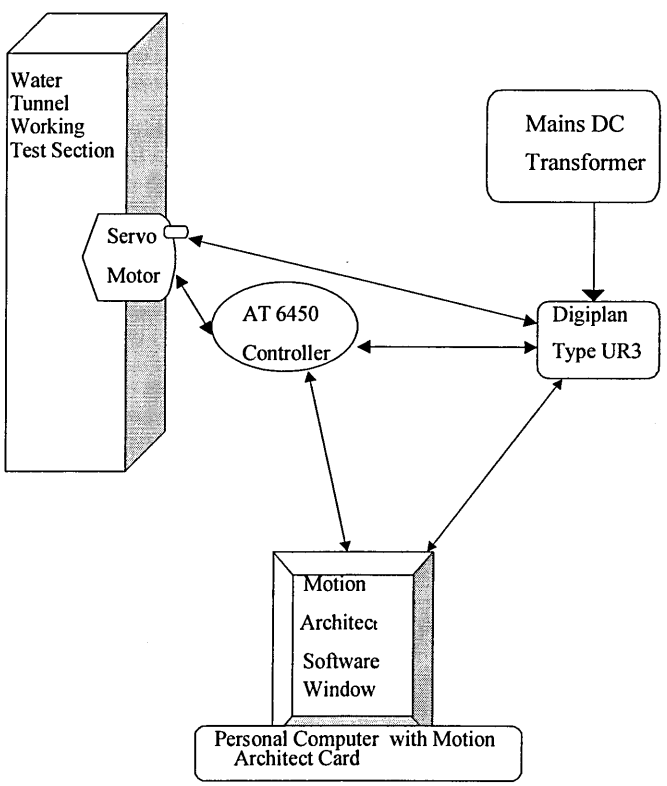

Figure 3.4 Schematic diagram of Servo Motor System Procedure

The position accuracy of the model movement is 36 second of arc (0.01°), the rate limit is 2°/sec, which correspond to the maximum pitch-up and pitch-down speed. Variable pitch rate (speed of the Servo Motor) is possible and it also has the capability of oscillation, given the amplitude and frequency of motion, (see Appendix C). Compumotor Motion Architect is a Windows based programming tool supplied with the AT6450 Motor Controller and it is designed to simplify the programming tasks associated with the motion generation. The signal from the DC Servo Motor was adjusted and controlled through the DC Servo Drive (DIGIPLAN) and the Motor Controller AT6450. (Figure 3.4). Appendix C shows the two types of Servo Motor applications, the static case and the dynamic case along with the program input written in C-language for the dynamic case.

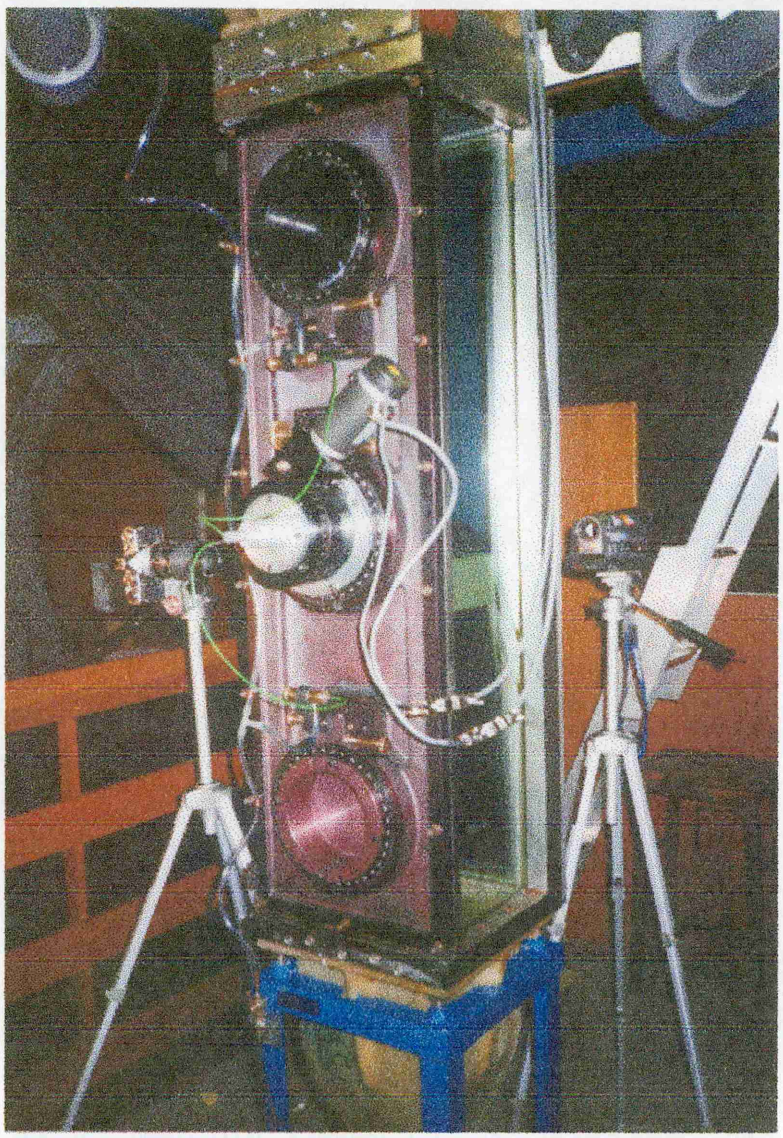

Figure 3.5 The encoder, motor and the turntable attached to the centre ring of the door working section

3.4 Velocity Measurement Technique

A Fibre-Film Probe Anemometer (FFPA) is used for the quantitative measurements of the four configurations of the boundary layers at the wall working section, see Appendix D. The film-probe (DANTEC 55R15) has cylindrical thin film sensors, which are 70 μm diameter quartz fibre, 3 mm long, covered by a nickel thin film approximately 2 μm in thickness. The Fiber - Film has lacquer – coated solder joints which enables it to be measured to the probes prongs whilst being insulated electrically from the surroundings.

The Fibre-Film Probe is mounted by a probe mounting tube (55H136), facing upstream, it is moved manually by a precision micrometer (0.01 mm accuracy) away from the wall test section, the initial distance from the wall is 1 mm, which is the thickness of the safety collar preventing the FFPA from touching the wall.

3.4.1 Calibration of Fibre-Film Probe Anemometer

A simple power law (King's law) is used for the initial FFPA calibration :

$E^2 = a + bU$, Where:

a and b are empirical constants determined by calibration, E: voltage, and U: free stream velocity.

The calibration is computed after the set-up and running the system which consists of : An analogue-to-digital (ADC) converter, a signal conditioning unit(DANTEC StreamLine), which is controlled by a PC and Stream Ware application software running under Windows, (Figure 3.6). The water tunnel working section velocity was the reference for the calibration.

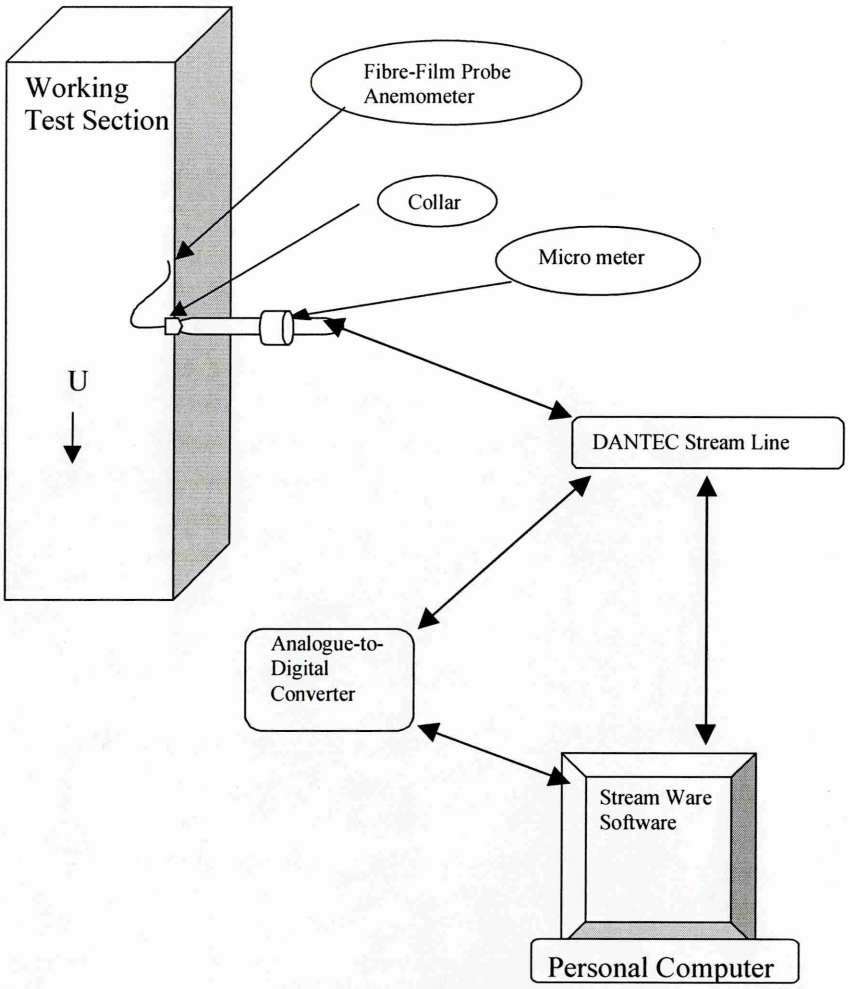

Figure 3.6 Schematic diagram of Fibre-Film Probe Anemometer Procedure

3.4.2 Data Acquisition and Reduction

The Streamware software sets up the anemometer modules, performs velocity and directional calibrations and provides an experimental platform, where automatic sequences of hardware set-up, traverses (manually – micrometer),data acquisition and data reduction can be carried out. A built in project manager provides full documentation of all measurement procedures and results. Voltage signal is fed directly to the A/D converter by using a signal-conditioning unit and a well chosen number of sample and sample time. Because of Hard Disk space availability, the sampling rate was chosen to be 10,000 in 20 sec for best results and the best compromised between accuracy and time. (see Appendix D).

After each run data was stored on the PC hard-drive in a format usable only with the 'Streamware' software. These files could then either be exported as an ASCII file or used as an input to a various functions within the 'Streamware' software.

3.4.3 Measurement of Errors

Two simple test were performed to check the effect of instrument sensitivity and the possibility that the FFPA probe holder assembly may cause intrusion effects.

In order to check that the probe holder assembly did not affect the flow at the Film-Fibre position, (note that the distance between the Film-Fibre and the collar assembly was 10 cm) two different size probe holders were used. In both cases the measurements were carried out at several working section speeds and the results in each case was identical. It was therefore concluded that the probe holder assembly had a negligible effect on the flow at the probe location (see Figure 3.6).

The FFPA was known to be very sensitive to temperature drift, (zero drift). It was noticed that the initial running temperature was 20°C and after a long continuous run (approximately 4 hours) the temperature of the flow rose to approximately 24°C. This resulted in a zero drift of approximately 7.0 % from the original measurement. In order to reduce this zero drift run times were limited to 2 hours.

3.5 Flow Visualisation Measurement

A Sony CCD-TRV94E HI 8 video camera is used for the qualitative photographic measurements in this experiment. This camera features a twin rotary head, helical scanning FM system, the video signal is PAL colour, CCIR standard, CCD image device, a focal distance of 4.1 – 61.5 mm (47 – 705 mm when converted to a 35 mm still camera) and the illumination range is 0.7 lux to 100,000 lux. In addition an Olympus OMI still photographic camera was used, which has a 35 mm lens with a focal distance of 2.8-16 mm and ASA 200 colour film. Figure3.7 shows the location of the Camcorder and the still camera.

Throughout the static experiment, the model upper surface was chosen for the measurement of the boundary layers influence on vortex breakdown. The wing was set to a specific angle of attack, using the Servo Motor, and after allowing the vortical flow to settle, the breakdown location was recorded. The procedure was repeated for a range of angle of attack : (0, 5, 10, 15, 17.5, 20, 22.5, 25, 27.5, 30, 35, 40 degrees).

In the dynamic test case the incidence range was from 0° to 40° for pitch-up and from 40° to 0° for pitch-down. A flash light was used such that 10° AoA intervals were recorded. A SVHS (Video cassette recorder) Hitachi 598EM, played back the flow visualisation record at a, variable, slow motion free of blurring. The vortex breakdown location in x-axis was observed and measured. After the pitch-up motion started and reached 40° AoA, the model stayed for 10 second in order to recover the lag (delayed by pitch-up), then start to pitch down. The pitch rate were used: α = 1°/sec, 2°/sec and 3°/sec, (see section 6.8.1), which correspond to a reduced pitch rate of k = 0.05, 0.1 and 0.15, where :

$k = \alpha^{\bullet} c / u$; $\alpha^{\bullet} = (\pi/180^{0})\alpha$

,where $\alpha^{\bullet}$ is in (rad /sec.) and α is in (degree/sec)

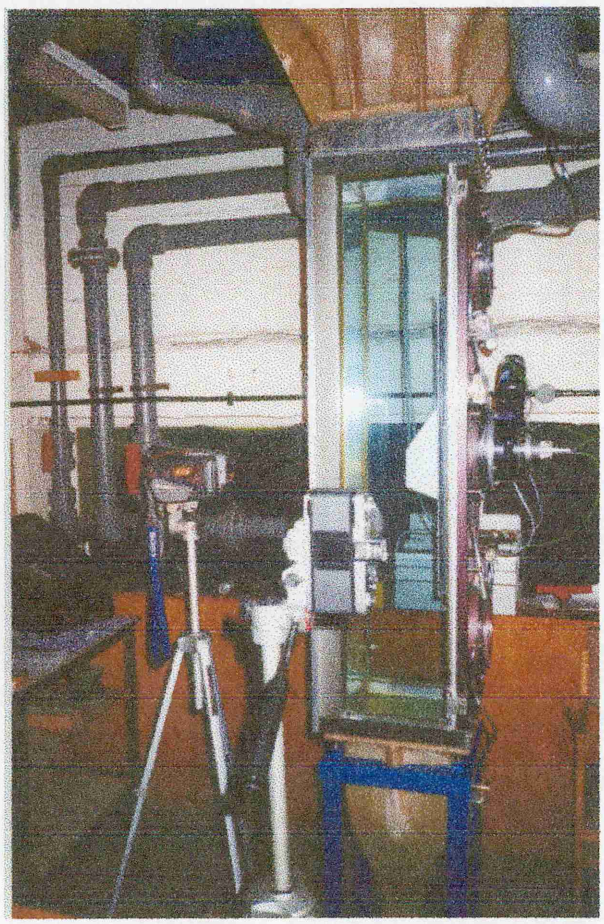

Figure 3.7 The location of the Camcorder and the still photograph camera

Chapter 4 Wind Tunnel Experimental Apparatus and Technique

4.1 Wind Tunnel

The ''Donnington'' wind tunnel in the College of Aeronautics at Cranfield University is a 3 ft x 3 ft (0.91 m x 0.91 m) closed working section, open return wind tunnel. Powered by an internally mounted motor driving a fixed pitch, variable speed fan, where the maximum speed in the working section is 32 m/sec. (for detail see Appendix E). It has a contraction ratio of 4:1 and a diffuser angle of approximately 2°. The working section is square with corner fillets varying from 15 cm to zero over its 2.46 m length.

A ground board (or 'end plate') is mounted 0.175 m above the floor of the working section. It has a length of 2.0 m and is 1.8 cm thick. The main purpose of this ground board is to displace the model from the working section floor boundary layer (see section 4.3.1 for details of techniques used to increase the end-plate boundary layer). The ground board consists of three sections, an elliptical leading edge section (15.1 cm in length), a middle section which is 60 cm in length where the 360° turntable is mounted and a trailing edge section. The turntable is controlled by a servomotor using motion architect software, as used in the water tunnel (see Appendix D). The model was mounted on the turntable where the distance from the end-plate leading edge to the model leading edge was 47 cm at zero incidence.

4.2 Calibration of the Wind Tunnel

The Donnington wind tunnel is equipped with two static pressure rings in the nozzle and in the settling chamber. The working section dynamic pressure is calibrated against the difference in pressure between the static rings. The calibration factor (K) has been calculated from the calibration of the static rings against the dynamic pressure and it was found to be K = 0.997 (see Appendix F). In order to have closer velocity between the water tunnel and the wind tunnel for a correlating study, the working section velocity was chosen to be 20 m/sec, correspond to a Reynolds Number of 479,000 based on the model root chord. Although the Reynolds Number was not the same, nor the reduced pitch rate (dynamic case) the same, between the water tunnel and the wind tunnel, this was the best low speed for surface static pressure measurements to investigate the vortical flow behaviour on the upper surface of the half-delta wing model with variable ground board boundary layers and variable reduced pitch rates.

4.3 Boundary Layer Test Procedure

4.3.1 Generation of the Ground Board Wall Boundary Layers

Three different working section wall boundary layers were used during The wind tunnel experiment, the three configurations were:

1. Ground board clean (without any modification to the elliptical leading edge of the ground board).

2. Sandpaper grit-40 placed at the leading edge of the ground board with a width of 5 cm and spanning the test section.

3. 3 mm diameter rod added to the end width of the sand paper (5 cm from the leading edge of ground board) spanning the test section. (see Figure 4.2).

Table 7.1 lists the result of all wind tunnel working section wall boundary layers configurations and values.

4.3.2 Traversing Probe Measurements

To measure the working section wall boundary layers, a y – z (cross stream) traverse mechanism and flattened pitot probe was used. The traverse consists of two vertically mounted screw-thread linear slides, with a horizontally mounted linear slide attached to the carriages of the vertical slides. The y – z motion is controlled by stepper motors which were driven by a PC based control system, in this experiment only the z – direction was used, where x (distance from the ground board leading edge) and y (location of wing model leading edge) were kept constant through all wall boundary layers measurements.

Since the blockage due to the traverse mechanism would be relatively high, checks were made to verify the effects of the traverse on the wind tunnel characteristics. The stream wise static pressure gradient was used as a benchmark for the empty test section characteristics. It was found that by mounting the probe on a rigid arm which placed the probe tip 45 cm ahead of the traverse feet, the static pressure at the probe tip was unaffected by the traverse presence. Therefore it was assumed that the effect of the traverse was minimal at the probe tip. The boundary layer profile was also checked, and no difference was seen due to the traverse position.

The measurement points were spaced so that they were closer together near the wall; in order to insure that a sufficient number of measurements were made in the logarithmic region. The first point was measured with the Pitot tube 1.5 mm from the surface of the ground board to ensure that the Pitot tube was not bending against the surface, making the initial value of z_0,the vertical distance, inaccurate. A typical value for the initial z step was 0.2 mm. After the fourth point this value was doubled. The traverse continued until consecutive values of free stream velocity, U, converged to within 0.2 % of each other (i.e. the pitot probe was in the free stream).

4.3.3 Data Acquisition

A personal computer and custom written software running under Microsoft Windows was used for data acquisition. The data acquisition controlled both the movement of the traverse and the reading of data to a text file. A schematic diagram of the system is given below (Figure 4.1):

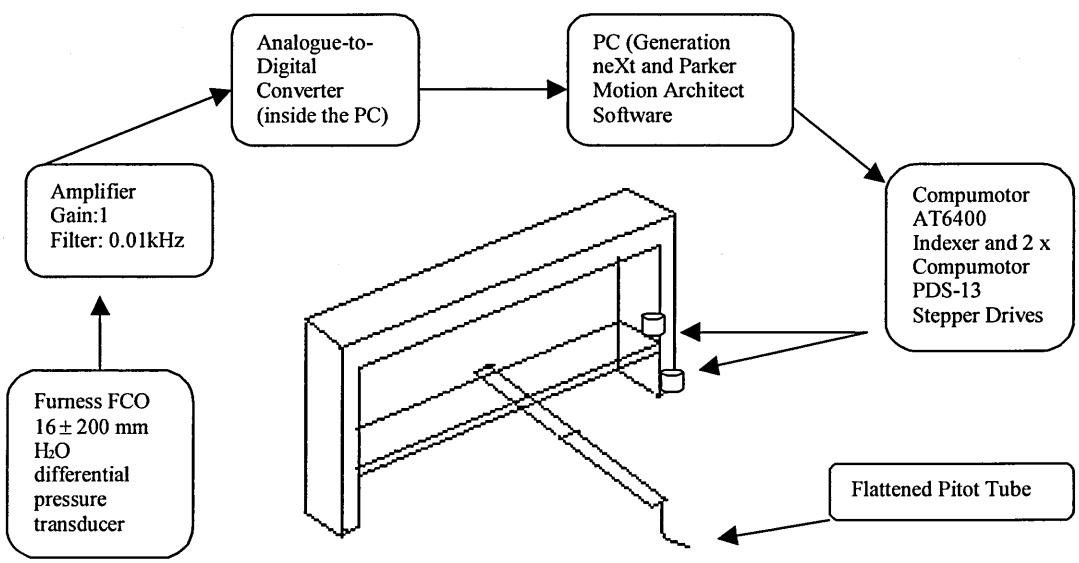

Figure 4.1 Schematic diagram of Traverse Gear Data Acquisition

Dynamic pressure was read using a single Furness FCO 16 ±200 mm H_2O differential micro-manometer (Serial Number 9601308) connected to both ports of a Pitot-static probe, located in the freestream. The electrical output of the pressure transducer was single-ended in nature, and was therefore susceptible to electrical noise. Examination with an oscilloscope revealed a sinusoidal oscillation superimposed over the output signal, and this was filtered using a 0.01 kHz filter. The pressure transducer was calibrated using a Druck DP 601 pressure calibrator.

Controlling software (Generation neXt), written in Microsoft Visual Basic was used, which would address an internally mounted Analogue-to-Digital Converter (ADC), and which would control the traverse via a second piece of software, Motion Architect. Thus the points at z-direction could be measured, and then data was taken at each point, with the motion being carried out automatically. Data was sampled at 200 Hz, over a five-second period, and the values averaged. Data was converted from the raw voltages read from the ADC board to corresponding pressures in the data acquisition, the program allowing for the effect of wind of zero offsets, and the transducer gains. Pressure value from the transducer was then stored in a text data file, along with the traverse co-ordinates for each set of pressure readings.

4.3.4 Data Reduction

Data reduction and data presentation was carried out using Microsoft Excel. Data was read in from the text files supplied by the generation neXt software. The pressure data were then non-dimensionalised to coefficient form to represent the non-dimensional velocity as follows:

$$\frac{u}{U} = \sqrt{\frac{q_{local} - p_0}{q - p_0}} \qquad 4.1$$

Where from first calibration of the wind tunnel factor K (see section 4.2):

$$q - p_0 = K\,(p_1 - p_2) \qquad 4.2$$

; $(p_1 - p_2)$ measured from the static rings and K=0.997

$$q_{local} - p_0 = (q - p_2) + (p_2 - p_0) \qquad 4.3$$

; $(q - p_2)$ measured from the local dynamic pressure, see Appendix E

To find the value of $(p_2 - p_o)$, which represent the difference between $p_1 - p_2$ and $p_2 - p_o$; an experiment has been performed for the local working section calibration and resulted in : $p_2 - p_o = a(p_1 - p_2)^2 + b(p_1 - p_2)$ which is a polynomial expression, where a = -0.0001 and b = 0.0118 :

$$p_2 - p_0 = a(p_1 - p_2)^2 + b(p_1 - p_2) \qquad 4.4$$

4.4 Wind Tunnel Model

A cropped half-delta wing platform model was used in this wind tunnel experiment. It has the same thickness/chord ratio (t/c) of the water tunnel model which is t/c = 0.018, it has a leading edge of $\Lambda = 55°$ and a trailing edge of 20°, a root chord c = 0.35 m, thickness t = 6.36 mm and a bevelled 45° leading edge with a flat bottom surface (bevel to leeward, same as water tunnel model, see Figure 3.3). The model was manufactured from aluminium. The location of the pitch-axis was chosen to be 50 % chord length, in order to reduce any influence of the pitch axis location on pressure measurement. The gap between the model and the wall was eliminated, since the model was attached to a rotating disk with diameter of 41 cm, where the model was placed on the middle of the rotating disk.

There are 45 pressure tappings on the upper surface of the wing model, 0.75 mm in diameter and connected to 1.6 mm copper tubes, laid in grooves of 1.7 mm X 2.0 mm deep and covered in with resin to give a smooth step free surface. The location of the pressure tapping was an irregular grid for two reasons: (i) in view of the irregular planform and (ii) to concentrate the location of the pressure tappings near the apex and the leading edge of the wing where the pressure gradient is expected to be high and most likely to be affected from the change of the ground board wall boundary layers. (Appendix G, includes a schematic diagram of the model and the pressure tapping locations).

4.5 Pitch Mechanism

The control pitch mechanism used in this wind tunnel experiment is identical to the one used in the water tunnel (servo motor) as detailed earlier in Chapter 3, with a few minor difference in the model attachment to the motor. In the water tunnel experiment, the model was attached to a rod and only the model rotated, but here due to the complex nature of the model attachment to the motor configuration, the disk that the model is mounted to, is also rotated, and care has been taken to ensure that there was no space or misalignment between the disk and the surface of the ground board.

4.6 Static Pressure Measurement Testing

The surface static pressure distribution was measured using 45 pressure tappings on the upper surface of the wing model at 10°, 20° and 30° angle of attack for each of the different ground board boundary layers. The tappings were connected via a scanivalve to the total port of a ±0.5 psi pressure transducer that was previously calibrated using a Druck pressure calibrator. The tunnel static rings were connected to the static port of the transducer, thus providing a freestream static pressure, which was previously corrected to the freestream static pressure in the test section (see Appendix E). The transducer output was filtered through a low-pass bandwidth filter (to remove noise) using 0.01 kHz filter and then input to an ADC (Analogue to Digital Converter). The transducer is driven and scanned under computer control software program CHART (Cambridge Electronic Design Limited) with a manual option to allow visual inspection of the output through a window of chart.

The pressure transducer output was sampled at 200 Hz for 10 seconds and stored in a text data file prior to transfer to Microsoft Excel for processing using the wind tunnel calibrations measured earlier. The corresponding pressure coefficient for each pressure tapping is transferred in a matrix form to a Mathworks MATLAB program which uses triangular interpolation in the Delaunay subroutine to plot the surface static pressure coefficient contours for the upper surface of the wing model. A schematic diagram for the pressure measurement system is shown in Figure 4.2.

4.7 Dynamic Pressure Measurement Testing

The procedure for measuring the dynamic pressure is very similar to that used during the static experiment except that an extra window has been created in the CHART program to represent the instantaneous angle of attack location as the wing model pitch-up or pitch-down for a specific reduced pitch rate. A rotary potentiometer is attached to the rotating disk. Two pitch rates were used: $\alpha = 3.64°/sec$ and $20.56°/sec$, which correspond to a reduced pitch rate $k = 0.00111$ and 0.00628; where :

$$k = \alpha^{\bullet} c / u \; ; \quad \alpha^{\bullet} = (\pi/180^{0})\alpha$$

,where $\alpha^{\bullet}$ is in (rad /sec.) and α is in (degree/sec)

A common reduced pitch rate could not be established between the water tunnel and the wind tunnel because of the discrepancy in Reynolds Number (17,000 and 479,000 respectively), where a low Reynolds Number was the ultimate for better flow visualisation in water tunnel and in the wind tunnel a high Reynolds Number was favourable for surface static pressure measurement.

With the same static pressure measurement procedure, and from the CHART program the coefficient of pressure could be calculated for each angle of attack (10°, 20° and 30°). The pressure contour plot could be obtained for both pitch-up and pitch-down at each reduced pitch rate and boundary layer configuration. Also pressure profiles could be obtained along a line of constant span or, chord. The model was pitched from 0° to 40° angle of attack pitch-up and held for 20 sec then pitched down from 40° to 0° , where each movement of pitch-up or pitch-down was measured for each single pressure tapping by using the manual option from the solenoid that controlled the scanivalve. A minimum of five hours was required to take one set of data.

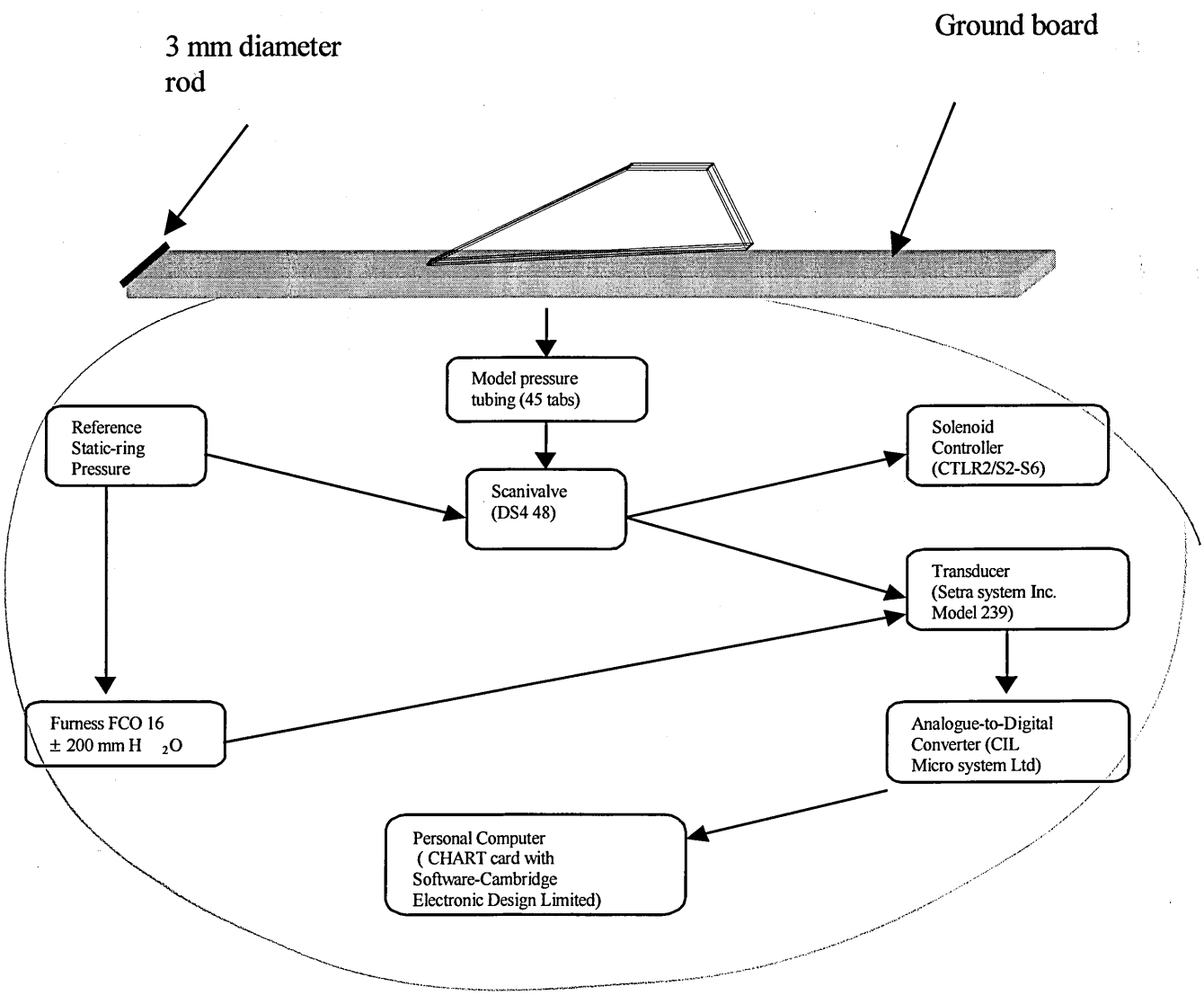

Figure 4.2 Schematic Diagram of Pressure Measurement System

4.8 Smoke Flow Visualisation Test Procedure

A wind tunnel smoke flow visualisation study is described herein. The half-delta wing model was tested at angle of attack 10°, 20° and 30°. The free stream velocity was 3 m/sec. which corresponds to a Reynolds Number (based on the root chord) of approximately 72,000. A low freestream velocity was chosen because details of the flow can be seen which are imperceptible at higher speeds. The smoke was generated by vaporising an oil (Propylene Glycol) in a heated probe. The smoke quantity was controlled by adjusting the smoke generator, using the oil reservoir, the probe temperature control and the oil pump control. As a result several trials were needed to establish the optimum configuration. The smoke generator was placed out side the wind tunnel working section, and the probe placed near the wing model leading edge. The position of the probe was very sensitive in order to reduce unnecessary effect on the model leading edge vortices and to create the optimum amount and quality of smoke to visualise the leading edge vortices. By this means, a uniform filament of smoke was introduced almost directly into the vortex sheet leaving the leading edge of the wing model.

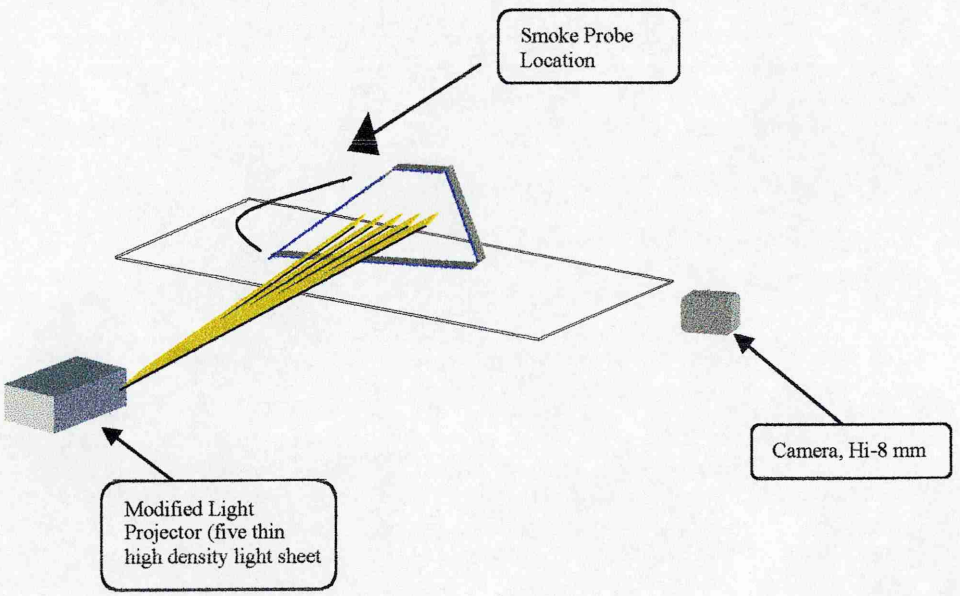

Figure 4.3 Schematic Diagram of Smoke Visualisation

To illuminate the smoke entrained into the leading edge vortex system, thin light sheets were used (Figure 4. 3). A modified light projector that could project five thin light sheets, (each displaced equally in distance from each other), was arrange such that, the light sheets could be moved along the chord of the wing model. The model was marked with an x, y grid in order to identify the location of the vortex core. A HI – 8 mm camera was placed in different positions for filming, the experiment was repeated for each position of the camera for repeatability and examination of the vortex behaviour. SNAP box tool with its software were used to capture the picture from the video film and visualise the vortex structure.

4.9 Data Accuracy, Repeatability and Error Analysis

4.9.1 Wind Tunnel Blockage

The presence of the wind tunnel walls modifies the flow field around the wing model, both in terms of effective angle of attack and velocity. These effects are known as interference upwash and blockage, respectively. The development of empirical wind tunnel correction techniques and a full set of formulae and graphs are included in Pope [178] and Garner et al [182].

In this experiment the wall induced upwash effect was not considered since it was very small. The angle of attack range of 10° to 40°, resulted in working section blockage, as a ratio of projected frontal area to working section cross sectional area, ranging from 0.6 to 2.1 % . Table 4.1 represents the blockage of the model frontal area to the wind tunnel frontal area.

AOA	Model frontal area	% frontal model/test section
10	0.005 cm^2	0.6 %
20	0.01 cm^2	1.1 %
30	0.015 cm^2	1.6 %
40	0.021 cm^2	2.1 %

Table 4.1 Working section blockage, as a ratio of projected frontal area to working section cross sectional area

4.9.2 Error in Transducer and Traverse Positioning

An estimation of measurement error has been carried out, and a statement of the magnitude of these errors will be made.

Transducer : The pressure transducer calibration was found to be consistent and repeatable to within 0.25 %. Using a 12-bit analogue-to-digital converter, which could read to an precision of 1 mV.

Traverse Positioning : The positioning error of the traverse was linked to the resolution of the positioning system. The traverse mechanism used a 0.5 mm pitch lead screw to drive the traverse carriage, thus one rotation of the stepper motor would yield 0.5 mm of travel. The motor was 200 step/rev , thus giving the motion system a nominal precision of 0.0025 mm.

4.9.3 Flattened Pitot Probe Position Correction

The location of the flattened pitot probe is established using feedback from the precision traverse system, once a datum position has been fixed, probe location is monitored according to rotation of the stepper motor. In order to allow for deflection of the probe mounting system under aerodynamic load, the datum position is taken to be the point of contact of the probe lower surface with the ground plane – wind on. This is established by a simple electrical continuity circuit through the probe and ground plane.

The effective point of measurement is taken to be the centre of the open end of the probe, unless the probe is considered to be in a shear layer. Measurement in a shear layer results in stream line displacement around the probe which move the effective measurement point away from the surface. A correction to allow for this is given by MacMillan[179,180] :

$$Z_0 = (0.5 + 0.15)d$$

Where: Z_0 is the minimum displacement of the measuring point from the ground plane.
d is the flattened probe height.

The height of the probe used in the current series of measurements is 0.45 mm. This results in a minimum measurement height of 0.293 mm. The correction to the probe position, applied through the boundary layer and assumed to be independent of Reynolds Number was 0.0675 mm.

4.9.4 Pressure Tubing

A possible source of error in the pressure measurement is the pressure tubing. The characteristics of a series of tube/transducer connections may be described by their frequency response function (FRF), defined as the Fourier transform of the system unit impulse response function.

Increasing the length of the tube reduces the magnitude of the resonance peak and shifts its position to lower frequencies. The phase lag is observed to increase with increasing tube length, Bergh[181]. In this experiment the tube correction method was not applied. The length of tubing used in this experiment was less than 1.0 m, based on Bergh data, the rough extrapolation of the time lag was approximately 0.03 seconds. The change in angle of attack for low reduced pitch rate is approximately 0.1° and 0.6° for the high reduced pitch rate.

4.9.5 Repeatability

Several data sets were taken in order to asses the repeatability of the technique using a clean tunnel boundary layer configuration at 30° angle of attack, two runs were reduced and the data is presented in (Figure 4. 4). While the change in pressure is very small, it may be seen that the interpolated lines of pressure correlate well, resulting in an excellent degree of repeatability in this case. The small differences in the interpolated pressure result are assumed to be due to the tendency of the wind tunnel to vary during a run.

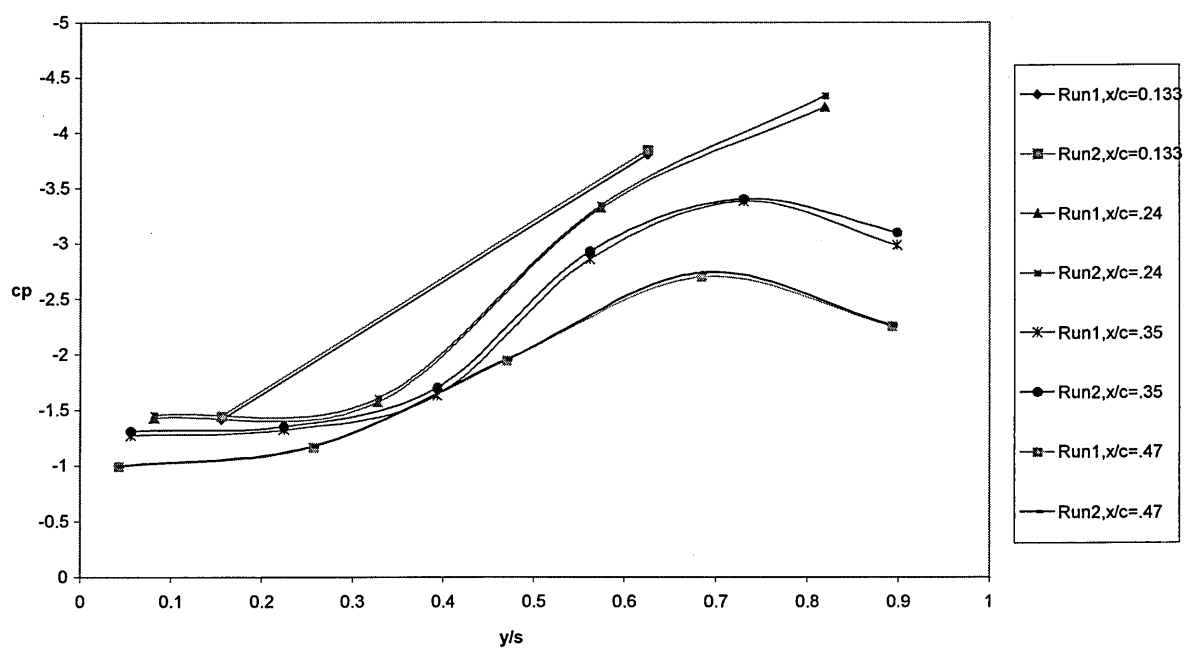

Figure 4.4 Cp distribution vs. local y/s, Delta55, AOA=30deg., R=1 for Run#1 & #2

Chapter 5 Wall Boundary Layers Measurements Results and Discussion

5.1 Theory of Wall Boundary Layer

For a viscous flow over a flat plate, Figure 5.1, the viscous effects are contained within a thin layer adjacent to the surface. At the surface, the flow velocity is zero, this is no slip condition, above the surface, the flow velocity increases in the y direction until it equals the free stream velocity, which will occur at a height above the wall equal to δ. More precisely, δ is defined as that distance above the wall where u = 0.99U, where U is the free stream velocity at the outer edge of the boundary layer and u is the local free stream velocity.

At any given x station, the variation of u between y = 0 and y = δ, u = u(y), is defined as the velocity profile. Within the boundary layer, this profile is different for different x stations. Another boundary layer property is the displacement thickness δ^*, which is physically the distance through which the external inviscid flow is displaced by the presence of the boundary layer.

$$\delta^* = \int_0^y (1 - \frac{u}{U}) dy \qquad 5.1$$

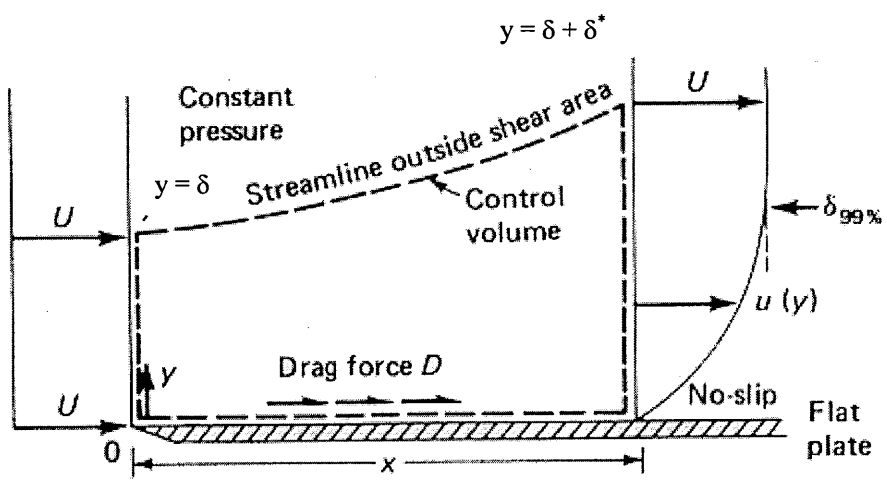

Fig. 5.1 Control Volume for Analysis of Flow past a Flat Plate. Reproduced from White[45]

5.2 Blasius solution

For an incompressible, two dimensional flow over a flat plate at 0° angle of attack such as that shown in Figure 5.1, ρ = constant, μ = constant and dp/dx = 0. The boundary layer equations derived from the Navier – Stokes equations could be reduced and simplified to:

$$2f''' + ff'' = 0 \qquad 5.2$$

Equation 5.2 is called the Blasius equation for an incompressible laminar flow over a flat plate. A numerical solution of Blasius equation shows that $f' = 0.99$ at approximately $\eta = 5.0$, where $\eta = y\sqrt{\frac{U}{vx}}$ and $f'(\eta) = \frac{u}{U}$, see White[45] . The boundary layer thickness, which was defined earlier as that distance above the surface where u = 0.99U is :

$$\eta = y\sqrt{\frac{U}{\nu\, x}} = \delta\sqrt{\frac{U}{\nu\, x}} = 5.0 \quad , \text{ or } \quad \delta = \frac{5.0x}{\sqrt{\mathrm{Re}}} \qquad 5.3$$

$$\delta^* = 1.72\sqrt{\frac{\nu\, x}{U}} \quad or \quad \delta^* = \frac{1.72x}{\sqrt{\mathrm{Re}}} \qquad 5.4$$

comparing equation 5.3 and 5.4, it shows that $\delta^* = 0.34\,\delta$.

For incompressible turbulent flow over a flat plate, the boundary layer thickness is given approximately by White[45] :

$$\delta = \frac{0.37\,x}{\mathrm{Re}^{1/5}} \qquad 5.5$$

Comparing equation 5.3 and 5.5 it show that the turbulent boundary layer thickness varies approximately as $\mathrm{Re}^{-1/5}$ in contrast to $\mathrm{Re}^{-1/2}$ for laminar boundary layer. Also, the turbulent value of δ grows more rapidly with distance along the surface, $\delta \propto x^{4/5}$ for a turbulent flow in contrast to $\delta \propto x^{1/2}$ for a laminar flow, Figure 5.3.

In the case when the local static pressure decreases with distance downstream in the flow direction, the velocity at the edge of the boundary layer increases and the conditions are referred to as a favourable pressure gradient. The flow is not decelerated so markedly at the wall, leading to a fuller velocity profile, Figure 5.2, and the boundary layer grows more slowly along the surface than for a flat plate. The converse case is when the pressure increases and mainstream velocity decreases along the surface. The external pressure gradient is said to be unfavourable or adverse. This is because the pressure forces now reinforce the effects of the shearing action and shear stress at the wall. Consequently the flow decelerates more markedly near the wall and the boundary layer grows more rapidly than in the case of the flat plate.

Throughout the current series of tests, the boundary layer on the wall test section is assumed to have developed as if it were on a smooth flat plate in a low pressure gradient. A comparison between this simple theoretical model and the actual measurements taken in the water tunnel and wind tunnel is made in section 5.2 and section 7.2 respectively.

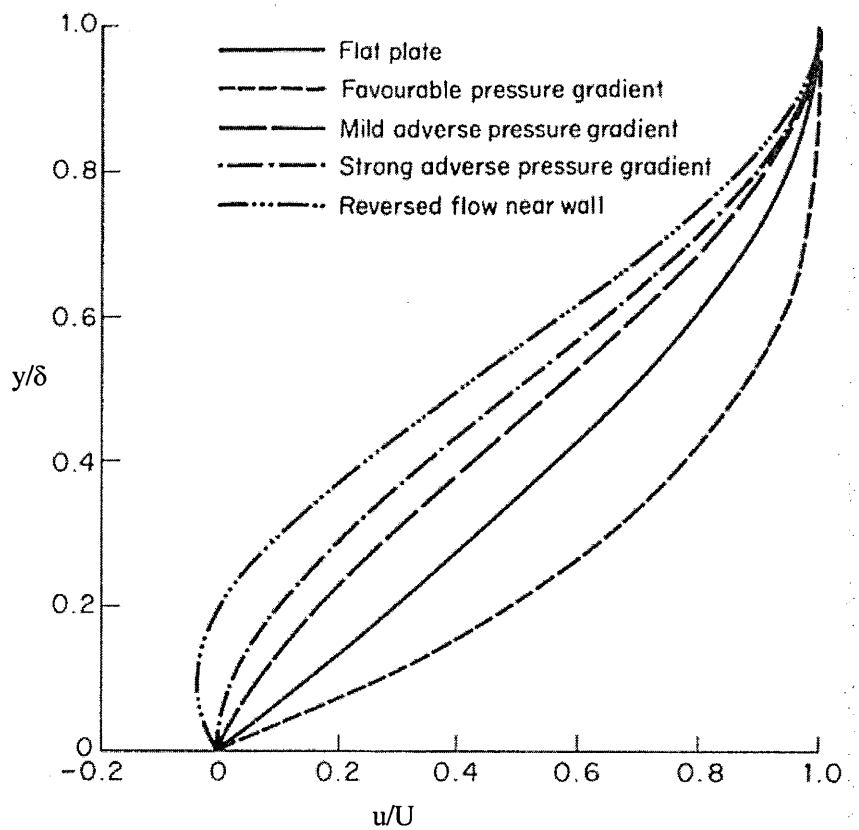

Figure 5.2 Effect of external pressure gradient on the velocity profile in the boundary layer. Reproduced from Schetz[100]

5.3 Hot Film Probe Anemometer Measurement

A series of measurements, using a single hot film anemometer probe, were made of the wall boundary layer velocity profile. In view of the local Reynolds Number it was assumed that the wall boundary layer would be laminar and consequently be compared to the ideal Blasius profile detailed in the previous section.

The origin of the zero pressure gradient was taken to be at the working section inlet which is 0.5m upstream of the probe mounting position and where the trip wires are placed. For the end plate boundary layer configuration, the origin was taken to be the leading edge, 0.21 m upstream of the probe mounting position.

The end plate configuration, which has the lowest wall boundary layer thickness, is a rectangular board (20cm x 62cm) that is displaced 2.5cm from the tunnel wall and has a sharp leading edge, the thickness is 1mm. It is coated in white laminated paint, which has a very smooth surface. The same paint was applied to the working section wall surface. The end plate was attached to the access panel of the water tunnel (see 3.1, Figure 3.2), where a space of 1cm was allowed along each side of the end plate to the tunnel side walls. The boundary layer thickness of the end plate configuration was reduced compared to the clean tunnel and other wall boundary layer configurations. Table 5.1 lists the results and Figures 5.4 to 5.7 show the value in terms of δ and δ^* for all wall boundary layer configurations. As explained earlier, the boundary layer thickness, δ, was obtained from the velocity profile data, corresponding to u/U=0.99, where U is the free stream velocity and u is the local free stream velocity. The uncertainty of this calculation is approximately 3%. δ^* is obtained by integration of the curve as shown from Figures 5.4 to 5.7, according to equation 5.1.

5.3.1 Characteristics of the Various Water Tunnel Wall Boundary Layers

The wall boundary layer thickness at the model location was artificially thickened by introducing progressively larger diameter trip wires traversing the working section wall at x = 0.5 m, (which is the length from the trip wire to the film probe position or the apex of the wing model). The procedure of measuring the thickness of the boundary layer on the wall test section is detailed in section 3.4., the velocity profiles are given in Figures 5.8 and 5.9.

No.	Configuration	δ (mm)	δ* (mm)
1	End plate	6.73	2.42
2	Tunnel Wall	8.4	2.896
3	Trip Wire 2.5 mm	10.0	3.7
4	Trip Wire 6.5 mm	14.0	3.827

Table – 5.1 Wall Boundary Layer Test section

It can be seen from Figure 5.8 that the wall boundary layer thickness increases due to the addition of progressively larger diameter trip wires as expected. However the boundary layer velocity profile remains laminar, see Figure 5.10. Although a relatively large 6.5mm trip wire, (thickest trip wire), was introduced upstream of the end plate, the velocity profile remained laminar and did not trip to a turbulent velocity profile Figure A8. This is assumed to be due to the low tunnel speed (0.077 m/sec. R_e = 32,000), at which the flow separates at the obstacle (6.5 mm trip wire) and the resulting shear layer reattaches downstream, the resulting boundary layer remaining laminar.

5.3.2 A Comparison between Measured Boundary Layer Profiles and Established Theory

In Figure 5.10, non-dimensional boundary layer velocity profiles for each of the five wall configurations considered , are plotted together with the established Blasius profile and $1/7^{th}$ power law profile for laminar and turbulent zero pressure gradient boundary layers respectively. It is clear that all the five configurations executed laminar profiles.

All the tests were carried out at a mean flow velocity of 0.077 m/sec. which corresponds to a local Reynolds Number, of 16,800 for the end plate configuration and 32,000 for the rest of the wall boundary layer configurations, where the Reynolds Number is based on the distance between the trip wire and the probe location as mentioned earlier.

The Blasius solution (equation 5.9) for the end plate configuration, predicts a local boundary layer thickness of $\delta = 8.1$ mm at this location. Thus compares to a value of 6.73 mm measured using the hot film probe anemometer, see Figure 5.4.

For the clean tunnel wall boundary layer configuration the Blasius solution predicts a local boundary layer thickness of $\delta = 11.2$ mm and the measured value is $\delta = 8.4$ mm. Thus suggests that the virtual origin of the assumed zero pressure gradient boundary layer is actually further downstream than the start of the parallel flow section. Or that the small favourable pressure gradient in the working section (attributed to wall boundary layer growth) has suppressed the boundary layer development.

This concludes the quantitative boundary layer theoretical and experimental measurement of the water tunnel, where the next chapter will consider the influence of the end plate boundary layer thickness on the vortical flow of the delta wing model.

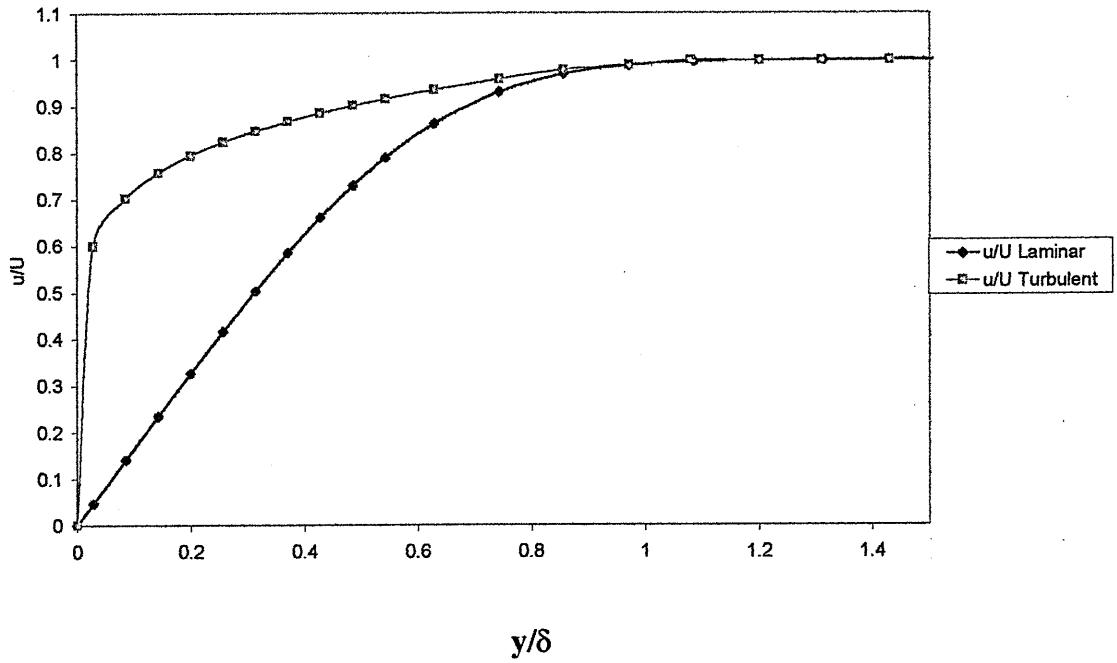

Figure 5.3 Comparison of the shapes of laminar and turbulent boundary layer velocity profiles

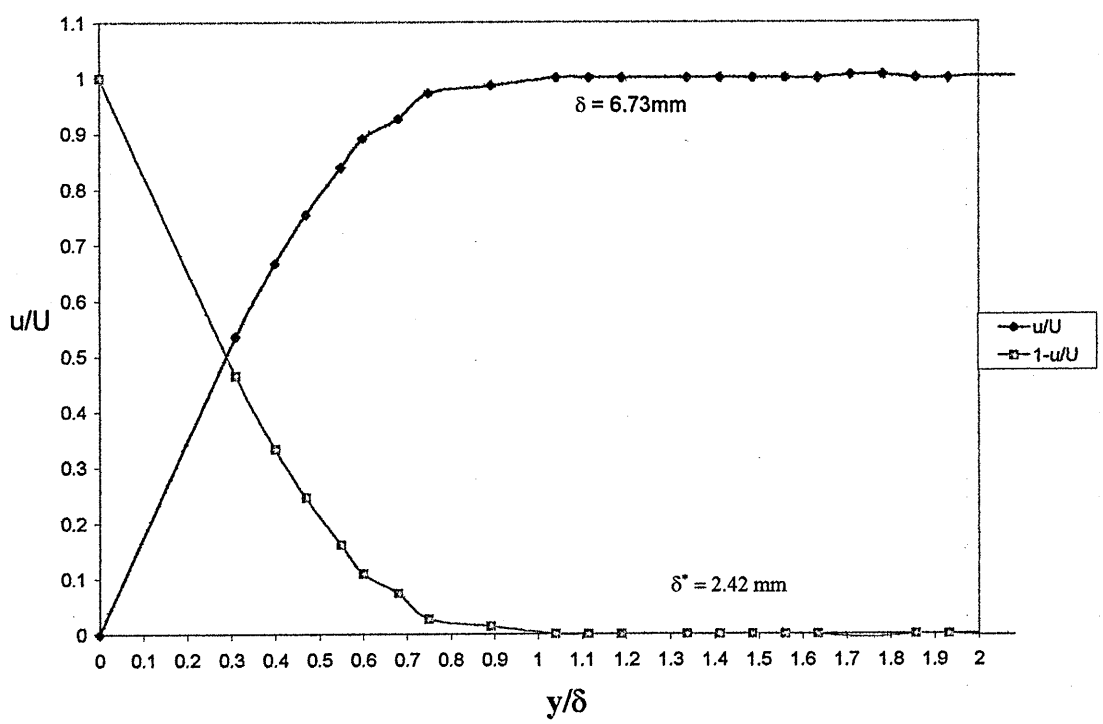

Figure 5.4 Water tunnel end plate velocity profile (U = 0.077m/sec.)

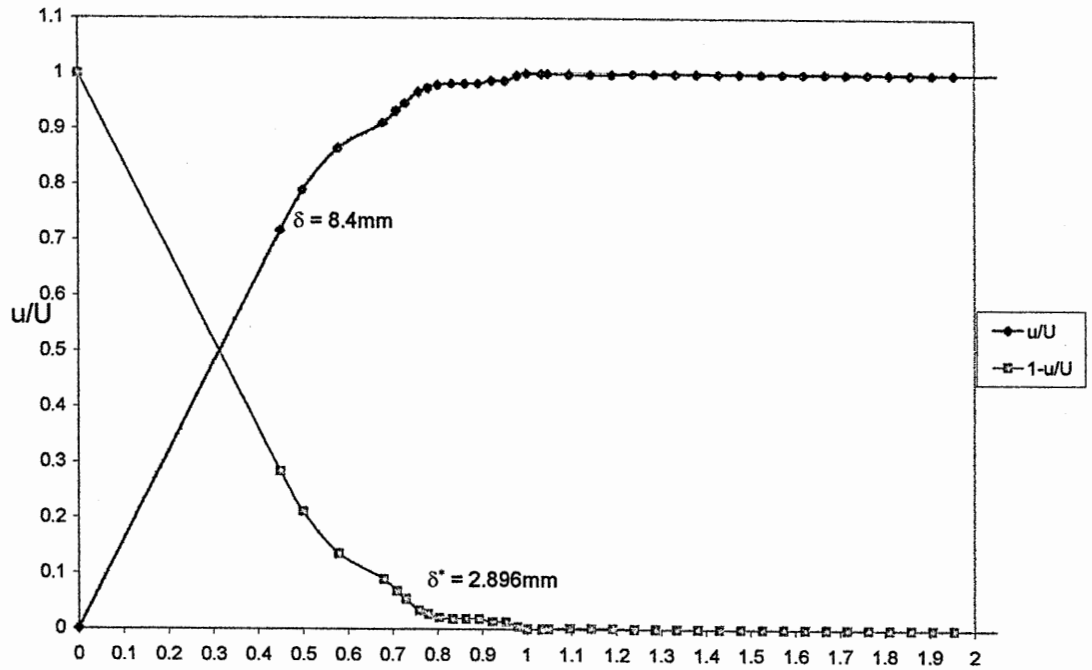

Figure 5.5 Water tunnel clean wall velocity profile (U = 0.077 m/sec.)

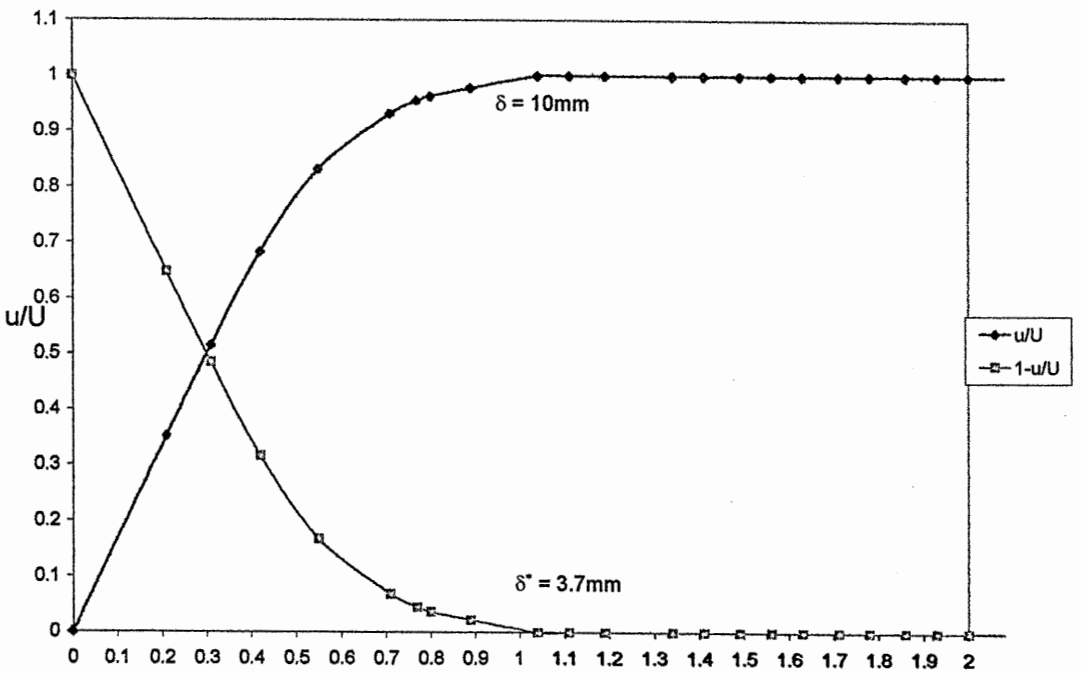

Figure 5.6 Water tunnel wall velocity profile with 2.5mm trip wire (U = 0.077m/sec.)

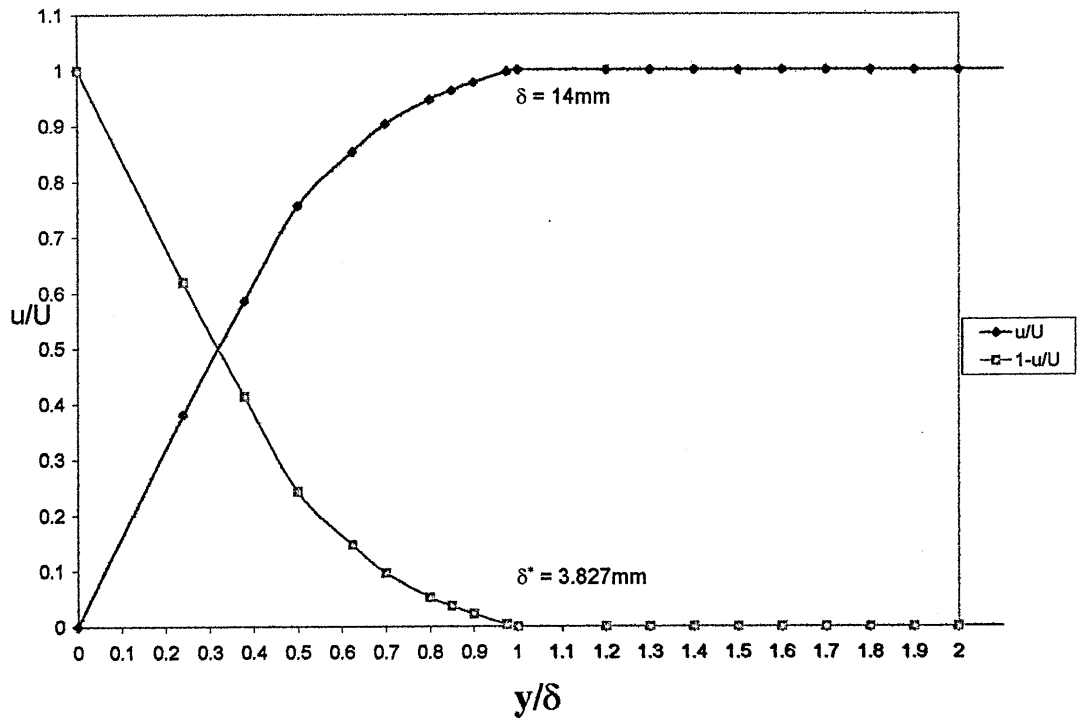

Figure 5.7 Water tunnel wall velocity profile with 6.5mm trip wire (U = 0.077m/sec.)

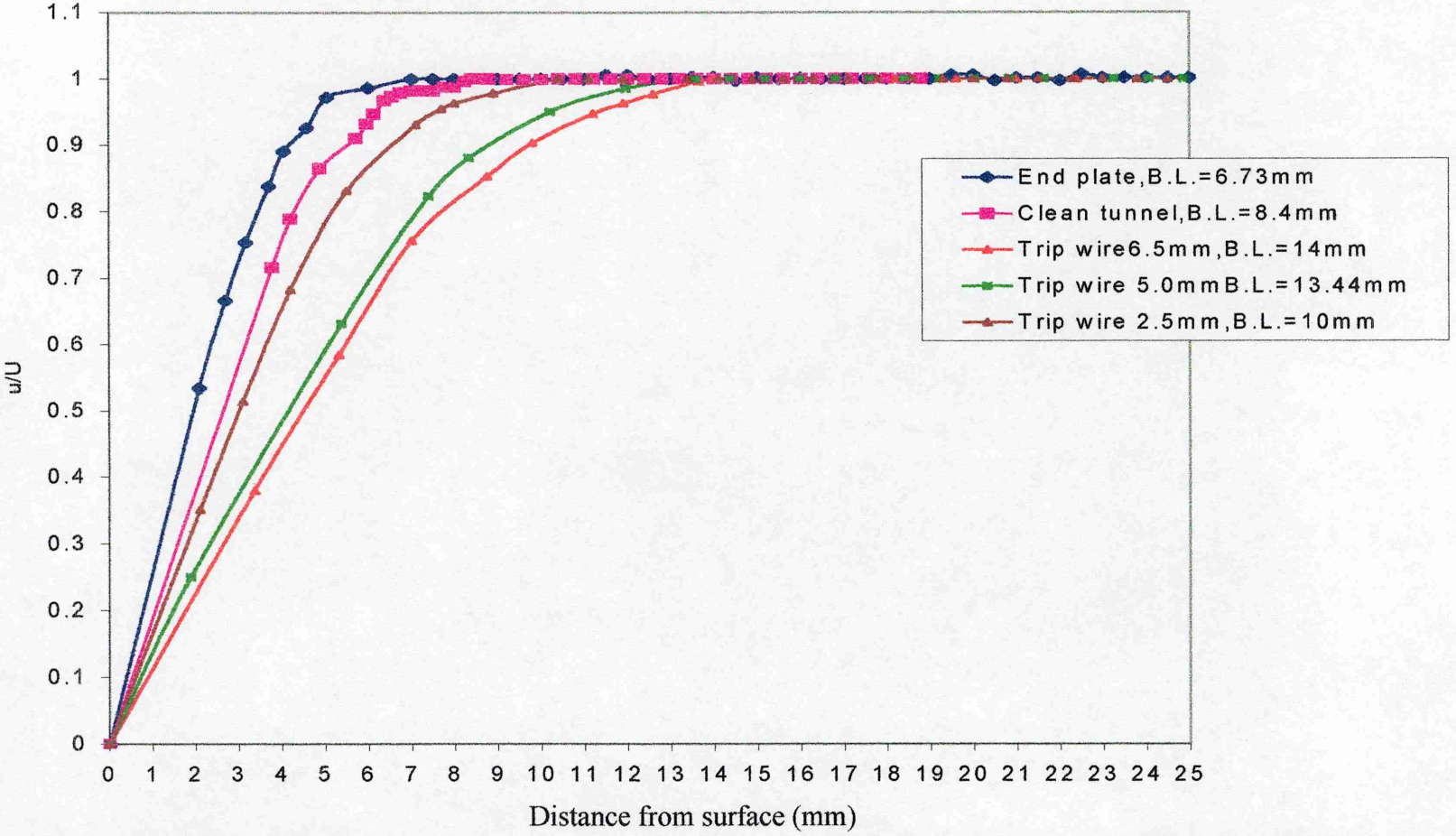

Figure 5.8 Comparison of water tunnel end plate and wall boundary layer velocity profiles (U = 0.077m/sec.)

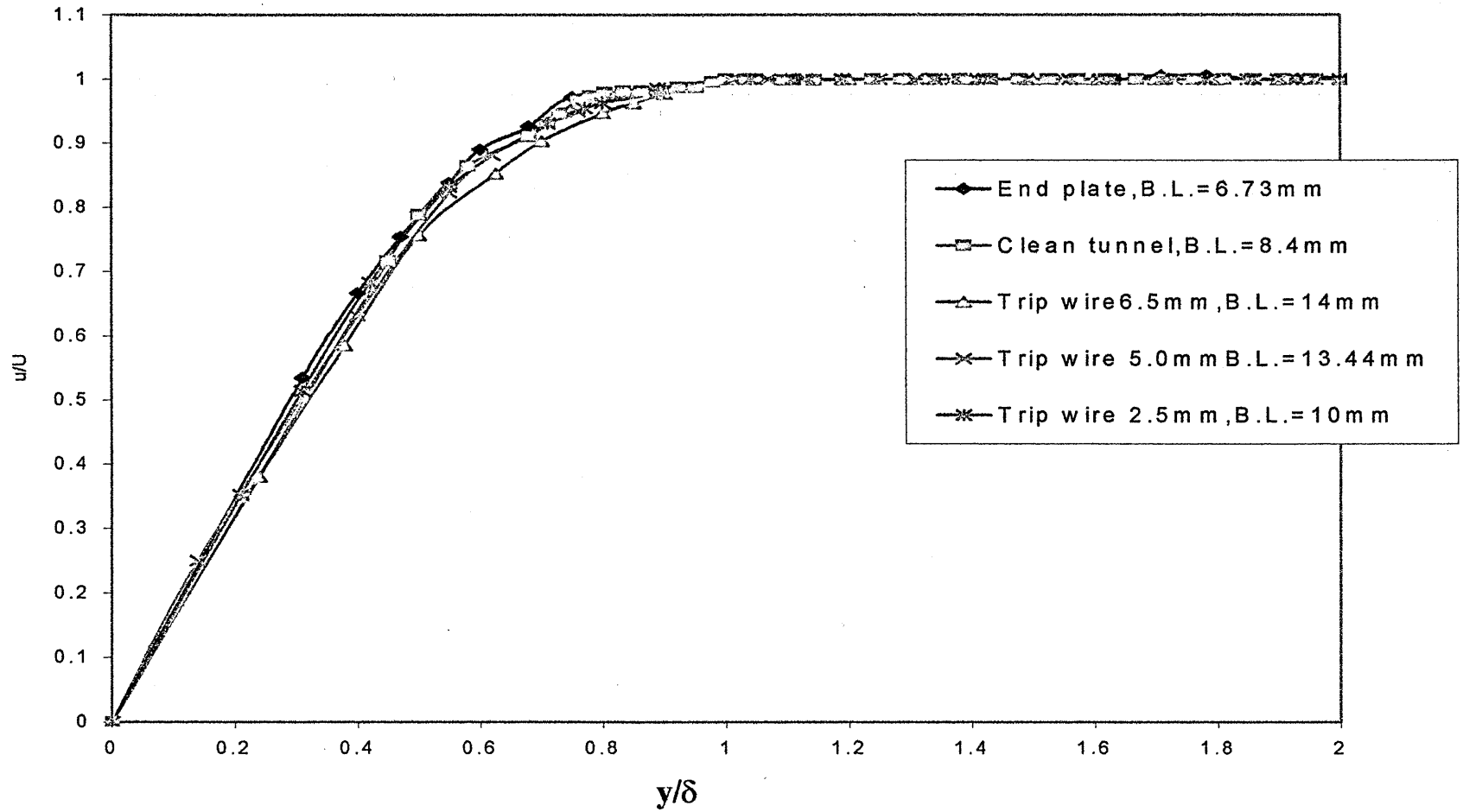

Figure 5.9 Comparison of water tunnel end plate and wall boundary layer velocity profiles (U = 0.077 m/sec.)

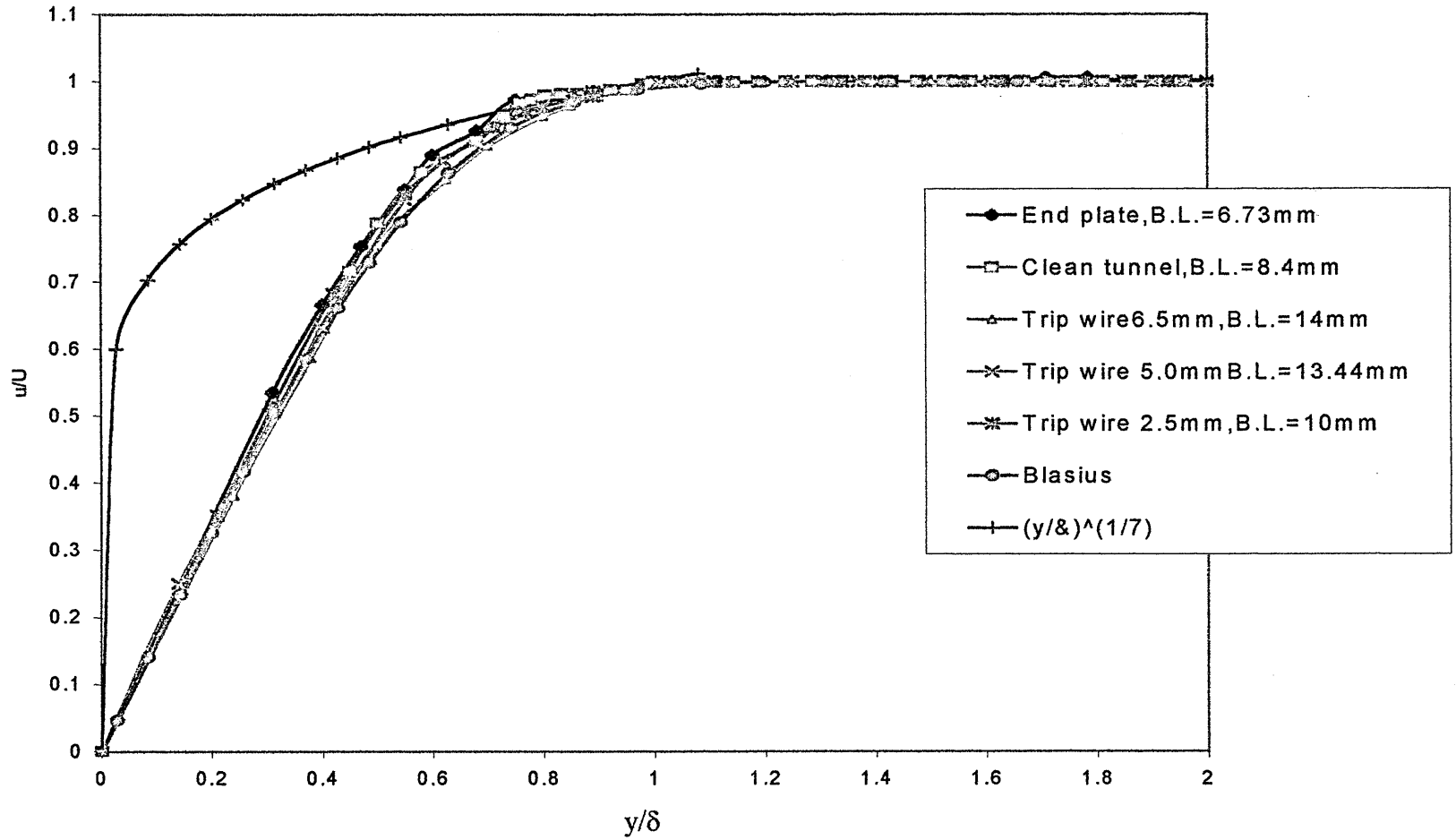

Figure 5.10 Comparison between idealised, zero pressure gradient, turbulent and laminar velocity profiles and those measured on the water tunnel end plate and wall velocity profiles (U = 0.077m/sec.)

Chapter 6 Flow Visualisation Results and Discussion

Flow visualisation is not only an aid to understanding a flow but can also be a measurement tool in itself. It can provide information about the whole flow, rather than just the part where a probe is located, and is thus a potentially valuable technique.

Throughout the experiments reported here, flow visualisation of the vortical flow over the upper surface of the wing model and its breakdown point, were made using a coloured dye fluid injected from the apex of the wing. The vortex breakdown points were visually determined from video/photographs, and expressed in terms of a non-dimensional distances using the root chord length (c) relative to the wing apex. (see section 3.1.1 for flow visualisation technique). The use of a half delta wing model means that the effects of asymmetric flow fields cannot be considered. (In particular asymmetric vortex bursting over the wing).

6.1 Definition of 3D Co-ordinate Axis of Vortex Trajectories

Data reduction involved locating the vortex breakdown position in x, y and z co-ordinates, with the aid of a grid in the x-y plane drawn on the wing surface, see figure 6.1. the origin of the co-ordinate system is the wing apex and all distances are non-dimensionalised by the root chord (c). In the y – direction the grid is expressed in terms of a fraction of the chord length, from the root chord to the tip of the wing model. Each grid element was chosen to be 1 cm (for x and y location), (Figure 6.1), where the maximum value of (y/c) = 0.364 and 0.273 for the 55° and 70° swept wing respectively.

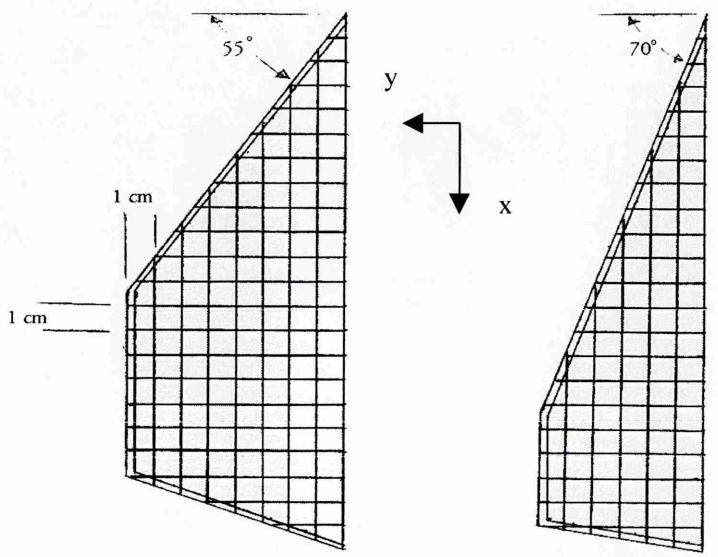

Figure 6.1 Wing Model, 55° and 70° sweep, with 1 cm surface grid

It was straight forward to aid interpretation of the video film with a grid in the z – direction. Vortex breakdown position is expressed, as the distance away from the model surface normalised by the wing root chord (c). The data is presented in terms of (z/c) vortex breakdown vs. AoA.

An important consideration when attempting to make a qualitative analysis of flow visualisation data is the quality of the original video material and the characteristic and repeatability of the observer. To address the later part each experiment for each configuration was repeated at least 3 times. In general this procedure produced estimates of vortex breakdown position which were within 5% for the x and y positions and within 10% for the z position.

During the steady state measurements the actual location of vortex breakdown was seen to oscillate in the x direction. The vortex breakdown position at any angle of attack was taken to be the mid point of the forward and rearward locations. Typically, within the angle of attack range considered (especially at high angle of attack, 25° to 35°), vortex breakdown measurements repeated to within ± 1.5 cm corresponding to ± 6.8 % chord.

Primary and secondary vortices were observed in the vortical flow, but for the purpose of this study, only the vortex breakdown position of the primary vortex was considered.

6.2 Influence of Wall Boundary Layer Characteristics on Vortex Burst Position

Figure 6.4 shows a comparison between data from this experiment for the 70° half-delta wing model and that of other researchers. Similarly Figure 6.5 compares data for the 55° half-delta wing model from this experiment with other researchers. The Figures confirm a consistent trend and also, as the wall boundary layer thickness increases, the relative effect on vortex burst position of changes in wall boundary layer thickness. (No data is available from other researchers on wall boundary layer thickness for comparison).

Dye was released from the apex of the model and the vortical flow behaviour was studied in terms of the breakdown point and the leading edge flow behaviour. The test sequence in each case was to progressively increase angle of attack in 5 degree increments starting at zero and ending at 40 degrees.

At each angle of attack, the flow is allowed to settle before the video sequence is taken for the primary vortex position measurement. Figures 6.6 to 6.11 show still photographs taken of the vortex breakdown position over the upper surface of the wing model.

When analysing the effect of changes in wall boundary layer thickness on vortex burst position, the gap between the model and the end-plate must be considered. Regardless of how small this gap is, there is a possibility that flow will pass through and influence the flow in the region of the end plates. When the model is at incidence, fluid moves from the windward to the leeward surface through the gap and can cause early separation on the leeward surface near the model root. For a small span model the area of separation could be a considerable fraction of the total area and thus cause a big discrepancy in the measured data.

Several researchers have studied this phenomenon, see Kegelman et at[105] and Walton et al[112]. Subrahmanyam et al [111] experimented on an aerofoil that has a root chord c = 12.5 cm and thickness t =16.8 mm and concluded that there is a loss of lift due to the presence of a gap, as a result of enhanced separation on the leeward side of the wing model. This also results in a displacement of the zero lift angle of attack.

The wing span of the four models was 8 cm and 6 cm for the 55° and 70° sweep respectively and each model had two thickness t = 4 mm and t = 8 mm. An experiment was carried out to study the effect of the gap size, where it was found that for a $\leq$ 2 mm gap size the flow characteristics were not affected for all models. Throughout this experiment the actual gap between the model and the end plate was less than 1.0mm. Walton et al [112] experimented a half span 70° sweep with root chord c = 35.56 cm and thickness t = 12.7 mm and determined that a half-delta wing appears to be a suitable substitute for a full-span delta wing when investigating vortex breakdown location, provided the gap is less than 1mm.

Appendix H list detailed Figures illustrate the variation of vortex burst location with angle of attack, and its dependence on each of the parameters considered, namely thickness/chord ratio (t/c), wing sweep (Δ) and wall boundary layer thickness (δ). In general, as the AoA increases the vortex breakdown position moves upstream. Numerous investigators have noted this behaviour, notably Earnshow et al[94], Payne et al[15], Gad – el. – Hak[23] and Visbal et al[47]. The flow downstream of the vortex breakdown is unsteady and results in a sudden stall of the wing, ie. a considerable loss in lift and a significant change in pitching moment, see Lamar[53] and Rao et al[55].

Figure 6.12, shows the variation of vortex breakdown position (x/c) on the upper surface of the wing vs. AoA for each of the wall boundary layers considered of 55° swept delta and t/c = 0.018. The data shows a clear general trend with vortex breakdown position moving upstream as the wall boundary layer thickness increases.

From the video sequences, it is clear that at low AoA (10° to 20°), the vortex breakdown position for each of the four boundary layer configurations tested is seen to vary quite consistently. However at high AoA (25° to 30°), the vortex breakdown position for the four boundary layer configurations is fairly close to each other. This suggests that changes in wall boundary layer thickness have little influence on vortex burst position when vortex burst has reached the wing apex.

The vortex breakdown position data suggests that the thickest end plate boundary layer configuration has a more significant impact on vortex burst location than the other boundary layer configurations.

6.3 Influence of Model Thickness/Chord ratio on Vortex Breakdown Position

Figure 6.13 shows the effect of the model thickness/chord ratio on the location of vortex breakdown vs. AoA. It is clear that the effect of changes in wall boundary layer thickness on the vortex breakdown location depends on the model thickness. The thickness to chord ratios used in this experiment were 0.018 and 0.036, increasing the wing thickness/chord ratio delayed vortex breakdown. This result is in agreement with the previous researchers, Huang et al[101]. In particular Earnshaw et al[95] concluded that the influence of cross-section shape on burst location could not be neglected, even for thin delta wings. Earnshaw's data shows that when thickness /chord ratio was increased vortex breakdown position was delayed. However it is not possible to differentiate between an increase in t/c and an increase in the induced angle of the section at the leading edge.

It is recognised that as the model thickness/chord ratio is increased, the radius of the leading edge is also increased. This increased radius tends to have a retarding effect on the development of the leading edge vortex by modifying the leading edge pressure gradient, where in this case it maintains attached leading edge flow and delays vortex formation. Stollery et al[184] showed that having a rounded leading edge on a 60° delta wing increased the lift to drag ratio (L/D) over almost the entire lift coefficient range tested. In this experiment, the shape of the leading edge was kept constant (bevelled at 45°), where only the width or radius is increased by increasing the thickness of the model.

The leading edge bevel was positioned on the leeward side of the wing for all the experiments reported here, (unlike most other researchers who used the windward side). Kegelman[105] showed that inverting the bevel side from windward to leeward side (positive cambered) retarded vortex breakdown, hence the effective angle of attack of the upper surface is reduced. Also there is a possibility of a secondary separation from the inner edge of the bevel.

The influence of changes in wall boundary layer thickness on vortex breakdown position for the 55° swept wing are summarised in Figure 6.14. The data are presented in terms of non-dimensional breakdown location (x/c), normalised by the vortex breakdown location $(x/c)_{max}$ of the thinnest boundary layer, $\delta = 6.73$ mm. This was done for each angle of attack and wing thickness to chord ratio (t/c). It can be seen that the variation of vortex breakdown position is similar for each wing configuration.

Similarly, Figure 6.15 compares $(x/c)/(x/c)_{max}$ for the same thickness/chord ratio ($t/c = 0.018$) but with different wing sweep. It is clear from these data that the influence of the wall boundary layer thickness on vortex burst position is much more dependant on sweep than thickness/chord ratio.

6.4 Influence of Sweep Angle on Vortex Breakdown Position

Figure 6.16 shows the influence of model leading edge sweep angle on the location of vortex breakdown vs. AoA for the two half-delta wing models tested. Generally, as the sweep angle of the wing model is increased, the location of the vortex breakdown moves downstream. The data also show that the influence of the wall boundary layer is independent of sweep of the delta wing, the vortex burst is seen to occur earlier for the thicker wall boundary layer for both the 55° and 70° swept wings.

Figures 6.17 to 6.20 illustrate the effect of changes in thickness/chord ratio and sweep angle respectively. As the thickness/chord ratio increases the vortex breakdown position (y/c) tends to move away from the root. Figure 6.19 shows that as the sweep angle increases from 55° to 70°, the vortex breakdown location (y/c) moves outboard (away from the root). It should be noted that from Figure 6.19, the primary effect of sweep is to move the vortex burst downstream, and the outboard movement then just follows from the sweep of the vortex core.

Kegelman et al[127] show that at a given angle of attack, the leading-edge vortex on a simple delta wing is stronger for the 60° sweep than for the 70°. Ekaterinaris et al [126] used a 3D Navier-Stokes numerical simulation and predicted that a decrease of the sweep angle resulted in increased suction peaks on the leeward side. Washburn et al[35] showed that the reduction in sweep resulted in a stronger primary vortex and caused the shear layer to separate more normally to the wing upper surface. As sweep decreases, the curvature of the shear layer in the cross-plane increases near the leading edge and the structures form closer to the leading edge. Therefore for any wall boundary layer configuration, as the sweep angle increases, the local velocity on the upper surface of the wing is decreased.

Another effect of sweep angle is found in Figures 6.21 to 6.24 which depict the vortex origin, found simply by extrapolating the first three point from the line of the vortex core trajectory on the graph to the apex. It is seen that the position of the vortex origin from the root was not affected by the boundary layer displacement, however it was different for each delta wing model sweep, the displacement from the wall being 5.83mm and 11.67mm for delta sweep 55° & 70° respectively.

6.5 Effect of Wall boundary Layer on Vortex Trajectory

As discussed in section 6.1, the lateral location of vortex breakdown was studied. Figures 6.17 to 6.20 show the variation of lateral vortex breakdown position (y/c) vs. AoA for each model configuration tested.

Also Figures 6.21 to 6.24 show the influence of changes in wall boundary layer thickness on the vortex core trajectory in terms of x/c vs. y/c; As the AoA is increased the vortex core trajectory tends to move toward the root of the wing model, other researchers have observed the same trend, Rediniotis el at [22]. Also, as the boundary layer thickness is increased the same trend is observed , the vortex core trajectory moved toward the root of the wing model.

The general trend is for vortex breakdown position to move upstream (toward the wing apex), with an inboard shift (towards the wing root) as AoA is increased. This has been seen by other researchers, Hebbar et al [61] and Verhaagen et al [110].

Figures 6.17 to 6.20 illustrate the influence of wall boundary layer thickness on lateral vortex breakdown position which appears to displace the vortex breakdown position forward, (hence inboard) as the boundary layer thickness increases irrespective of sweep angle.

Data summarising the non-dimensional vertical location of vortex burst vs. AoA for each model configuration and wall boundary layer tested is given in Figures 6.25 to 6.28.

Figure 6.29 shows the influence of the wall boundary layer on vertical vortex breakdown position (z/c) vs. AoA for 55° swept delta and t/c = 0.018. As the wall boundary layer thickness increases the vortex breakdown position tends to move away from the model surface and then moves back towards it, note that this trend is different at each AoA.

The influence of changes in wall boundary layer thickness on vortex breakdown position (z/c) for the 55° swept wing are summarised in Figure 6.30. The data are presented in terms of non-dimensional breakdown location (z/c), normalised by the vortex breakdown location $(z/c)_{max}$ of the thinnest boundary layer, $\delta = 6.73$ mm. This was done for each angle of attack.

The influence of wall boundary layer thickness is very clear in terms of its effect on the height of the vortex burst. At a given angle of attack, as the thickness of the wall boundary layer is increased, the vortex burst location will move away from the surface.

Figures 6.31 to 6.33 represent the cross section in y – z plane for different x/c location, (x/c=0.14, 0.18 and 0.27), of the delta 55°, t/c=0.018, which supports not only the previous explanation but also shows that as the angle of attack is increased the vortex burst location will also move away from the surface.

Figures 6.25 and 6.26 illustrate the influence of changes in thickness/chord ratio on the vortex breakdown position in the z-direction. As the thickness of the leading-edge of the wing model increased, the vortex breakdown position is moved toward the model surface. The same trend is observed at low angle of attack, but it moved away from the model surface at high angle of attack, see section 6.3.

Figure 6.27 and 6.28 show the effect of the wing model sweep angle on the vortex breakdown position in the z-direction, where as the sweep angle increased from 55° to 70° the vortex breakdown position in z-direction moved toward the surface of the wing model. It seems that the difference between the effect of sweep on vortex breakdown location in terms of (z/c) vs. AoA is much more pronounced with the thicker wall boundary layer where the vortex origin, as explained before (section 6.4), is much further away from the root for the 70° sweep than 55° sweep delta. Also figures 6.34 to 6.36 show the vortex core trajectory in the z-direction x/c vs. z/c for all boundary layers and for a different angles of attack (10°, 20° and 30°) where, as the angle of attack increased, the vortical vortex core moved away from the wing model surface and then toward the surface at high AoA.

6.6 Analysis of Wall Boundary Layer Influence on Vortical Flow Trajectory and Burst position

The flow around a half delta wing – end plate junction is a very complex, highly three-dimensional flow. Figure 6.2 show a simplified wing-end plate junction flow typical of that considered by many previous researchers in this field. The dominating flow characteristic is the mean secondary flow structure known as the horseshoe vortex. This vortical flow structure is created by a combination of two effects, the skewing and stretching of the transverse vorticity present in the incoming boundary layer as it passes the wing, and the rolling up of the incoming fluid along the centreline due to the large adverse pressure gradient created by the wing geometry.

The horseshoe vortex has a number of characteristics that, in most practical situations, are undesirable. The horseshoe vortex acts to bring high momentum, freestream fluid into the corner between the wing and surrounding surface. This energises the flow and it also greatly increases the surface shear stress, Devenport et al[196].

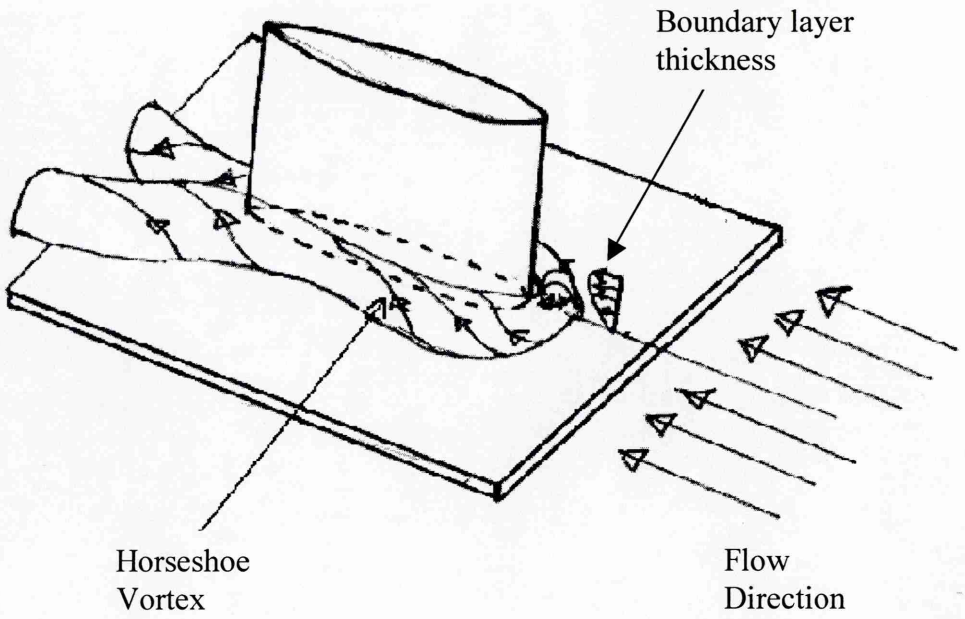

Figure 6.2 Wing – end plate junction flow with horseshoe vortex

To study the influence of an end plate boundary layer on a half delta wing flow, an understanding of both the end plate boundary layer and the horseshoe vortex is needed. Barber[192] examined a number of NACA 65 series symmetric strut-wall intersections and concluded that the path of the horseshoe vortex is determined by the interaction of the onset boundary layer flow with the strut pressure field. The vortex strength is dependent on the edge velocity and the local boundary layer thickness. Increasing the end plate boundary layer thickness resulted in a large horseshoe vortex, while, in contrast, a thin end plate boundary layer resulted in a very small horseshoe vortex.

In the current series of experiments, it is assumed that a horseshoe vortex forms at the wing/end-plate junction and that its size increases with increasing end plate boundary layer thickness. This horseshoe vortex will be likely to interact with the wing vortex. Briley et al[197] studied, using CFD, the horseshoe vortex flow past strut/end wall configurations having both unswept and 45° swept leading edges, they concluded that the strength of the horseshoe vortex at the leading edge is significantly reduced by the swept leading edge and outside the horseshoe vortex region, a cross flow parallel to the swept leading edge and directed outward away from the end wall occurs due to the swept geometry.

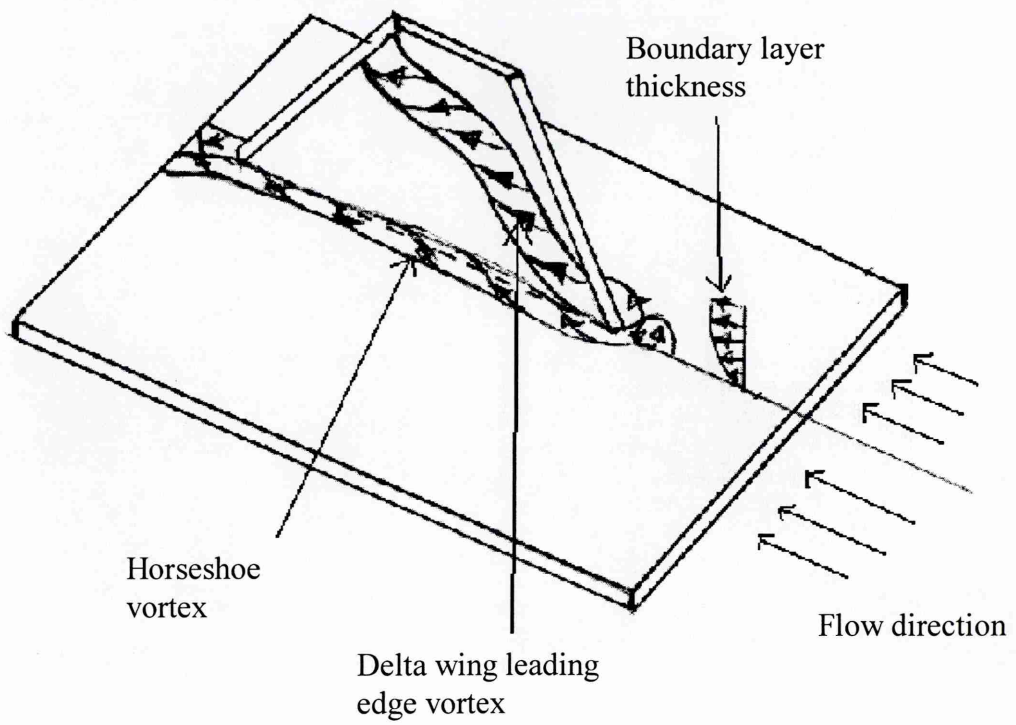

Figure 6.3 Half delta wing – end plate with horseshoe and delta wing leading edge vortices

The sense of rotation of the horseshoe vortex that forms around a half delta wing is illustrated in Figure 6.3, where it shows that the horseshoe vortex is rotating in the opposite direction to that of the delta wing leading edge vortex. The direction of rotation of the horseshoe vortex was noted by most of the researchers previously mentioned.

Since there is no mechanism for the destruction of vorticity, vorticity levels in the vortex core decay only by cross diffusion and annihilation of vorticity of opposite signs, Morton[39]. As the horseshoe vortex interacts with the leading edge of the half delta wing primary vortex, it causes some loss to the primary vortex, since they are of opposite sign.

Shizawa et al[195] examined the structure of a horseshoe vortex of a flat wing attached to flat wall at different angle of attack, and concluded that the horseshoe vortex acts as if it would shorten the span of the wing, and causes the loss of the flow, where the loss was large at the suction side of the wing and as the angle of attack increased, at the suction side, the horseshoe vortex shifted away from the wing to the free stream direction and remained in the same distance from the wall. At the pressure side, the horseshoe vortex shifted away from the wall, but remained in the same distance from the wing.

As the end plate boundary layer thickness is increased, it is assumed that the size of the horseshoe vortex is also increased. Interaction between the horseshoe vortex and the half delta leading edge vortex may result in a reduction in strength of the wing vortex since they are counterrotating. This loss of strength appears from the flow visualisation data as early vortex breakdown.

Vortex breakdown is influenced by two factors: (1) the swirl angle of the vortex, the ratio of the rotary to axial velocity components, see Gursul et al[29], and (2) the imposed adverse pressure gradient. This adverse pressure gradient may be considered to consist of two components. The first is due to the growth of the vortex core resulting from vorticity diffusion, and second, the pressure gradient associated with enforcement of the Kutta condition at the wing trailing edge and its associated pressure recovery. As the vortex breakdown moves upstream, by increasing the angle of attack, the leading edge vortex circulation is reduced, Traub[151].

In this experiment, the interaction between the horseshoe vortex and the half delta wing leading edge vortex may result in a reduction of the swirl angle of the wing leading edge vortex due to the opposite sense of rotation. This reduction of circulation tends to move the vortex breakdown upstream.

6.7 Effect of Blockage

In order to investigate the effect of model projected frontal area blockage on the flow field a series of tests were made using a smaller model, (20% less in area but with the same thickness/chord ratio), and compared with that of the original 55° sweep configuration.

AoA	55° sweep t/c=0.018, A=118.65cm^2	55°swept (20%less area) t/c=0.018 A=94.92cm^2
5	2.1 %	1.4 %
10	4.2 %	2.8 %
15	6 %	4 %
20	8.3 %	5.5 %
25	10 %	6.8 %
30	12 %	8 %
35	13.9 %	9 %
40	15 %	10 %

Table – 6.1 Working section blockage expressed as a ratio of projected frontal area to working section cross sectional area

Table 6.1 details the projected frontal area to working section cross sectional area blockage ratios for both model configurations in the AoA range 5° to 40° Figures 6.37 and 6.38. These blockage values compare favourable with other tests e.g, Gad-el-Hak[23] and Hebbar et al[61].

The data suggest that blockage (a wall induced upwash effect) causes the effective angle of attack to increase by 2° and the vortex breakdown location is seen to move up stream with increasing wing size for a given angle of attack by 5 to 10% c due to the effective angle of attack being larger. Other researchers have observed the similar effect, see Pelletier et al[128] and Ericsson et al[184]. No attempt was made to correct the data for the effect of blockage, since this upwash effect is very small for the highest angle of attack considered here, 35°.

6.8 Influence of Dynamic Behaviour

In previous sections the steady state or static condition was studied using flow visualisation in the water tunnel. It is important now to consider the dynamic case in which the flow conditions are seen to be dependant on whether the model is pitching-up or pitching-down.

This dynamic phenomena plays an important role in determining the aerodynamic properties of a wing, Rediniotis el at [22]. An understanding of dynamic separation needs a detailed survey of surface static pressure on the wing, such a survey along with smoke flow visualisation in a wind tunnel is presented in the following chapter. In this chapter flow visualisation studies were carried out for static and dynamic cases in the water tunnel , where the location of the vortex breakdown is identified in terms of dispersion of the coloured dye filament.

6.8.1 Effect of Reduced Pitch Rate

When the wing model is subjected to a dynamic motion (pitch-up or pitch-down) , the structure of the vortex core, its development and eventual breakdown can be expected to be a strong function of the reduced pitch rate (k) where ;

$$k = \alpha^{\bullet} c / u \; ; \qquad \alpha^{\bullet} = (\pi/180^{0})\alpha$$

,where $\alpha^{\bullet}$ is in (rad /sec.) and α is in (degree/sec)

This dimensionless pitch rate represents the ratio of the wing chord (c) to the wave length ($u / \alpha^{\bullet}$) of the forced motion. Reduced pitch rates of $k =$ 0.05, 0.1 and 0.15 were used in this experiment, which correspond to 1°/sec, 2°/sec and 3°/sec respectively, other researchers used similar reduced pitch rates(chapter 3)[23,24,49]. This reduced pitch rate range was the optimum range for slow and fast pitch-up and pitch-down, which also gives the most readable and best visualised vortex breakdown on the upper surface of the wing model. The range of angle of attack in dynamic motion was from 0° to 40° both pitch-up and pitch-down, within this range vortex breakdown was attainable. For angles greater than 40° the flow is generally separated with no recognisable vortex formation. In the static case these flow conditions were seen at AoA greater than 35°.

At each reduced pitch rate (both for pitch-up and pitch-down), measurements of vortex breakdown location were made based on the analysis of video film records of the flow field for each model configuration and wall boundary layer condition. Figures 6.39 and 6.40 present the dynamic vortex breakdown location (x/c) vs. AoA for each configuration and pictures 6.6 to 6.11 are still frames taken from the video film to illustrate this effect.

During the dynamic pitch up motion, separation started as the angle of attack increased from 0° , where the vortical flow developed at the leading-edge , and a vortex sheet peeled off from the leading-edge before rolling up into the separation vortex. The separation region is seen to propagate forward from the trailing edge to the apex of the wing as the angle of attack increased. At high angle of attack the separation reached the apex where it is clear that the vortex is fully developed.

From pictures 6.6 to 6.11 , it can be seen that, at any particular angle of attack , the flow patterns were very different during a pitch-up and a pitch-down motion. The separation region during a pitch-down is visually clearer than that in a pitch-up case, indicating the existence of a hysteresis effect. Other researchers noticed the same phenomena Telionis et al[22] , Gad-el-hak[23] and Atta et al[24] .

This hysteresis effect appears more pronounced as the reduced pitch rate is increased from $k = 0.05$ to 0.15 . Figures 6.39 and 6.40 show the effect of reduced pitch rate in this experiment . At a low value of reduced pitch rate ($k = 0.05$) , vortex burst is characterised by a gradual appearance and stabilisation of the vortex core during the pitch-up motion. After the core is established, vortex breakdown occurs in the normal way, but is significantly displaced with respect to the stationary wing model (static case). For a low reduced pitch rate the vortex core breakdown occurs in the classical spiral mode, as shown from the pictures. The difference between static and dynamic vortex burst position is seen to be greater at high reduced pitch rates, where it also changed to a bubble type.

6.8.2 Influence of wall boundary layer on dynamic behaviour

The influence of the wall boundary layer on vortex breakdown position was discussed in section 6.2 for the static case, however the same influence of the end-plate boundary layer configurations were applied in dynamic motion. Figure 6.39 and 6.40 illustrate its influence at the reduced pitch rate $k = 0.05$ and $t/c = 0.018$ for 55° and 70°swept delta wing respectively.

Figure 6.39 shows an asymmetry in the effect of boundary layer thickness, where there is seen to be more effect on dynamic pitch-up than on pitch-down for the 55° sweep case and only an offset for the 70° sweep. In this case the differences were attributed to the development of vortex breakdown between the pitch-up and pitch-down cases. Flow visualisation studies showed that during a pitch-up motion the vortex breakdown does not have sufficient time to achieve the corresponding static condition.

In general, as the wall boundary layer thickness is reduced, vortex breakdown position occurs further downstream during both pitch-up and pitch-down, compared to the thickest wall boundary layer case.

Figure 6.41 gives a comparison between static and dynamic cases of vortex breakdown position for 55° swept delta model, t/c = 0.018 for k = 0.05 and 0.1. The static vortex breakdown position, for all angles of attack, is located between that for the pitch-up and pitch-down vortex breakdown positions. Table 6.2 summarises the configurations discussed in this chapter.

The effect of both wing thickness/chord ratio, (t/c=0.018 & 0.036) and wing sweep (55° & 70°), on vortex dynamic breakdown was studied, Figures 6.42 to 6.47 illustrate the axial location of vortex breakdown with angle of attack and suggest that the effects of hysteresis dominate the behaviour. During pitch-up or pitch-down, the vortex breakdown was delayed for the thickest model as discussed from section 6.3 (static case) and as the sweep increased from 55° to 70° the vortex breakdown was delayed during pitch-up or pitch-down as discussed from section 6.4 (static case). As the reduced pitch rate decreased from k=0.15 to k=0.05 the vortex breakdown position is moved down stream for both cases of increasing the thickness/chord ratio or sweep angle as discussed in the static case, section 6.7.1.

Figures 6.48 to 6.51 represent a comparison of the different vortex breakdown positions between pitch-up and pitch-down (the hysteresis effect). This can be seen by comparing the change in $(x/c)_{\text{vortex breakdown}}$ against angle of attack(where the change in $(x/c)_{\text{vortex breakdown}}$ is the difference between the vortex breakdown location pitch-up and pitch-down). This data is used to clarify the effect of changes in wall boundary layer thickness on vortex breakdown position for both thickness/chord ratio effect and sweep effect during pitch-up and pitch-down. The data in Figure 6.48 for the 55° sweep wing shows significantly more hysteresis than for the 70° sweep wing case Figure 6.49, clearly the influence of the wall boundary layer on hysteresis is much greater for the 55° sweep wing. It is possible that the wall boundary layer does not influence hysteresis for the 70° sweep wing.

WALL BOUNDARY LAYER THICKNESS (MM)	DELTA SWEPT 55° T/C=0.018	DELTA SWEPT 55° T/C=0.036	DELTA SWEPT 70° T/C=0.018	DELTA SWEPT 70° T/C=0.036	STATIC CASE AOA= 0°→40°	DYNAMIC UP 0°→40° DOWN 40°→0° K=0.05	DYNAMIC UP 0°→40° DOWN 40°→0° K=0.1	DYNAMIC UP 0°→40° DOWN 40°→0° K=0.15
6.73 mm	All	-	-	-	-	-	-	-
8.4 mm	-	-	-	-	-	-	-	-
10 mm	-	-	-	-	-	-	-	-
14 mm	-	-	-	-	-	-	-	-

Table 6.2 summary of configurations considered in this chapter

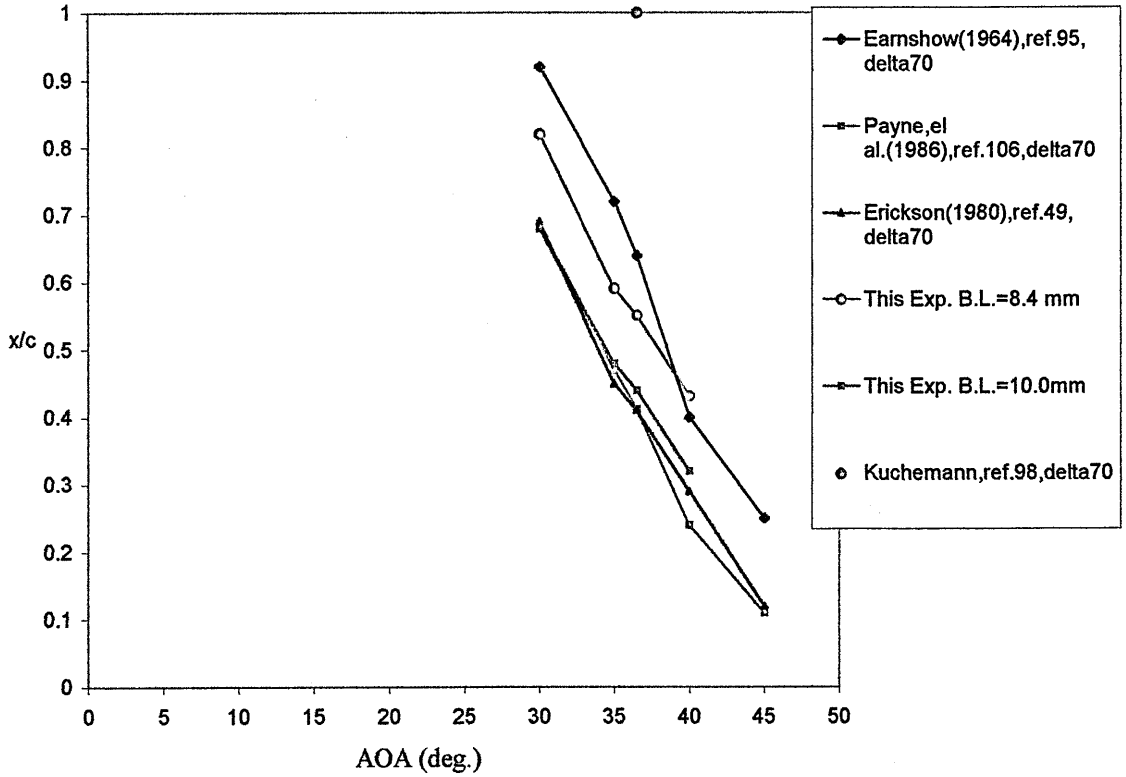

Figure 6.4 A comparison of vortex breakdown position vs. AoA between the current experiment(delta 70 deg. Swept, t/c=0.018, of 8.4mm and 10.0mm wall boundary layers) and previously published data

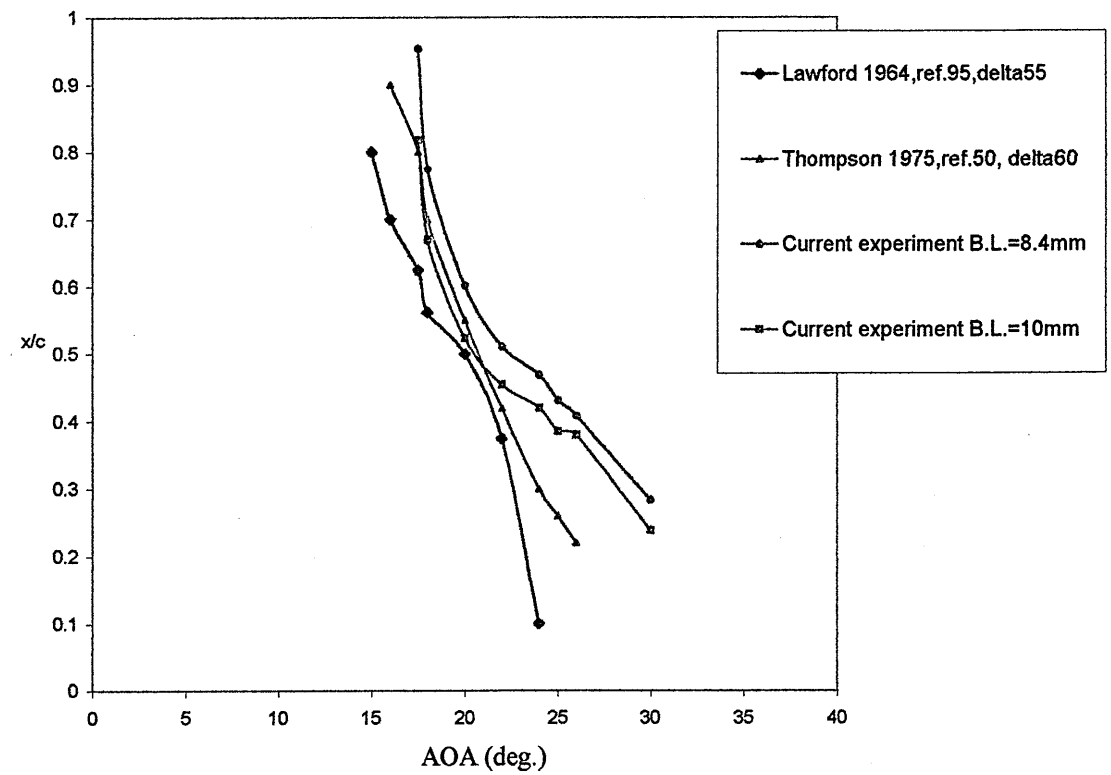

Figure 6.5 A comparison of vortex breakdown position vs. AoA between this experiment(delta 55 deg. Swept, t/c=0.018, wall boundary layer 8.4mm and 10.0mm.) and previously published data

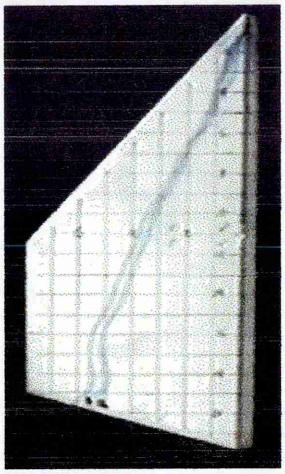

Delta55, B.L.=6.73mm, Static
AOA=10deg.

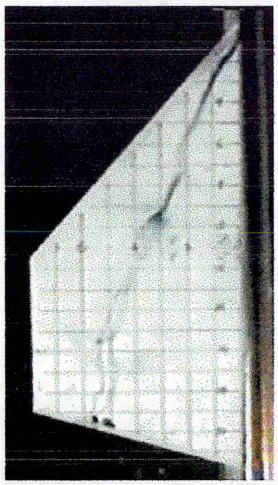

Delta55, B.L.=14mm, Static
AOA=10 deg.

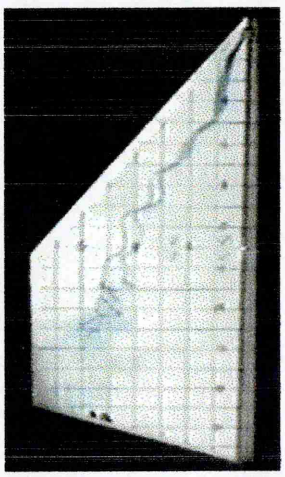

Delta55, B.L.=6.73mm, Static
AOA=20 deg.

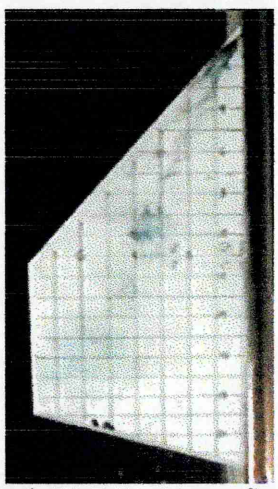

Detla55, B.L.=14mm, Static
AOA=20 deg.

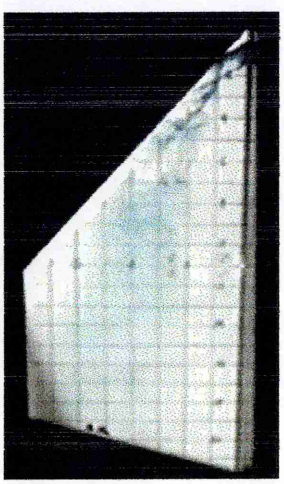

Delta55, B.L.=6.73mm, Staic
AOA=30 deg.

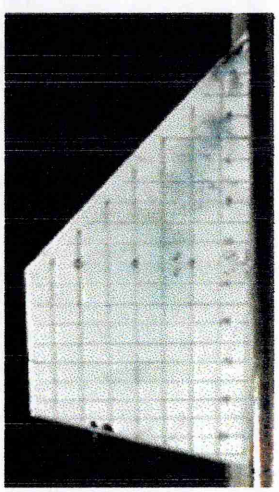

Delta55, B.L.=14mm, Static
AOA=30 deg.

Figure 6.6 Picture, Static, Vortex breakdown position, Delta 55° Sweep, t/c=0.018, B.L.=6.73mm, 14.0mm, AoA= 10°, 20° and 30°

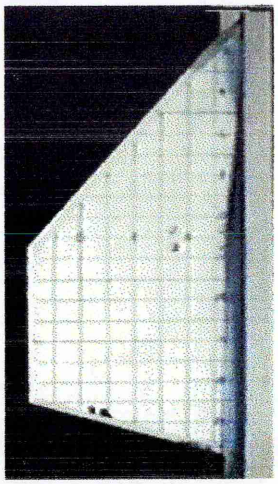

Delta55, B.L.=6.73mm, k=0.05
10deg. Pitch-up

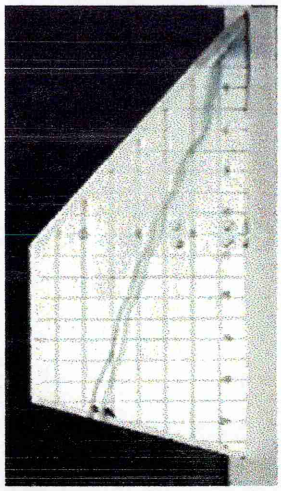

Delta55, B.L.=6.73mm,k=0.05
10 deg., pitch-down

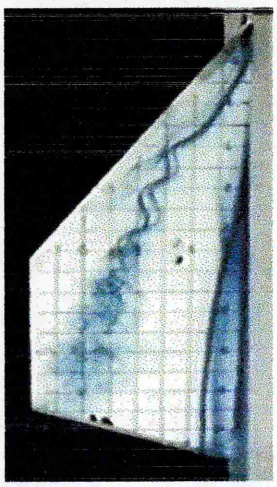

Delta55, B.L.=6.73mm, k=0.05
20deg., pitch-up

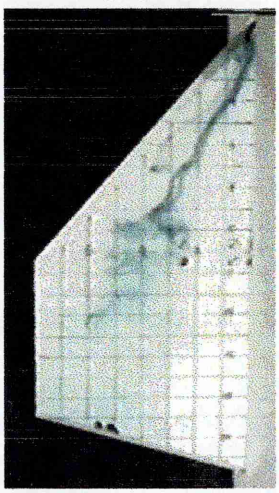

Delta55, B.L.=6.73mm, k=0.05
20 deg., pitch-down

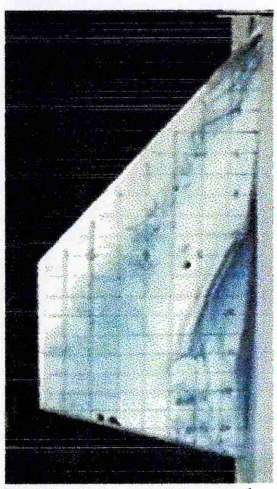

Delta55, B.L.=6.73mm, k=0.05
30 deg., pitch-up

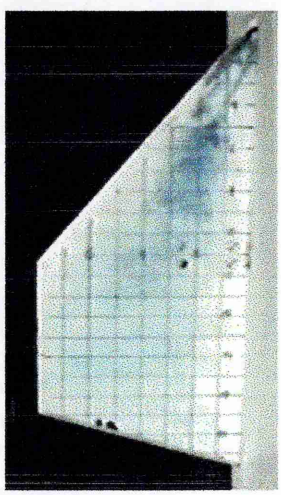

Delta55, B.L.=6.73mm, k=0.05
30 deg., pitch-down

Figure 6.7 Picture, Dynamic Pitch-up and Pitch-down, Delta 55° sweep, t/c=0.018,B.L.=6.73mm, Reduced pitch rate, k=0.05, AoA=10°, 20° and 30°

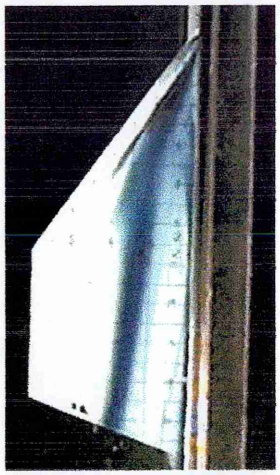

Delta55, B.L.=14mm, k=0.05
10deg. Up

Delt55, B.L.=14mm, k=0.05
10deg. Down

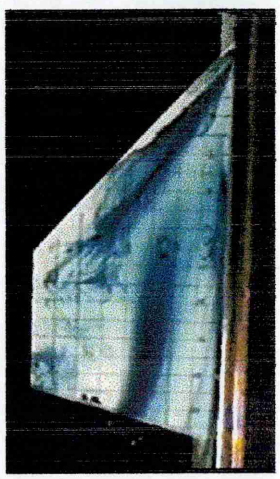

Delta 55, B.L.=14mm, k=0.05
20deg. Up

Delta55, B.L.=14mm, k=0.05
20deg. Down

Delta55, B.L.=14mm, k=0.05
30deg. Up

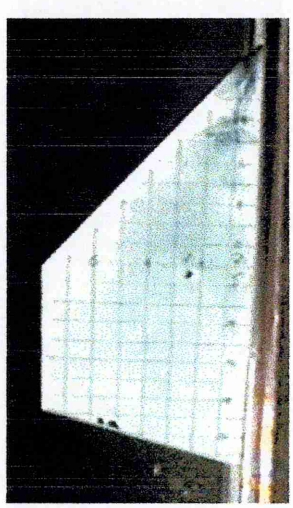

Delt55, B.L.=14mm, k=0.05
30deg., Down

Figure 6.8 Picture, Dynamic Pitch-up and Pitch-down, Delta 55° sweep, t/c=0.018,B.L.=14.0mm, Reduced pitch rate, k=0.05, AoA=10°, 20° and 30°

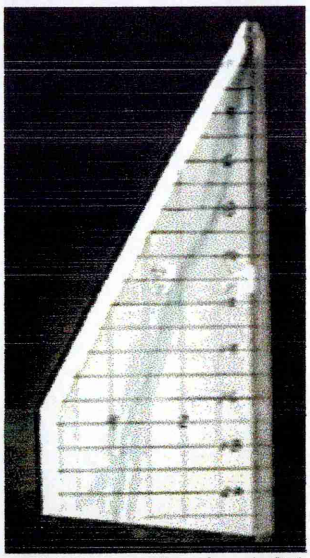

Delta70, B.L.=6.73mm, Static, AOA=10deg.

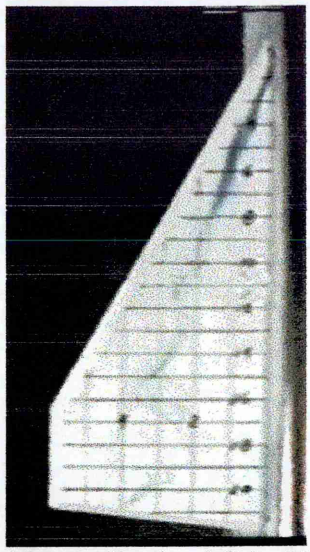

Delta 70, B.L. = 14 mm, Static; AOA=10deg.

Delta 70, B.L.=6.73mm, Static, AOA=20deg.

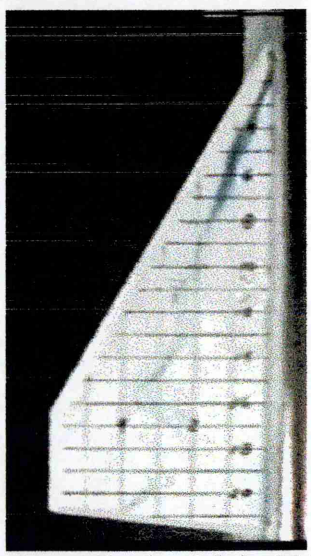

Delta 70, B.L.=14mm, Static, AOA=20deg.

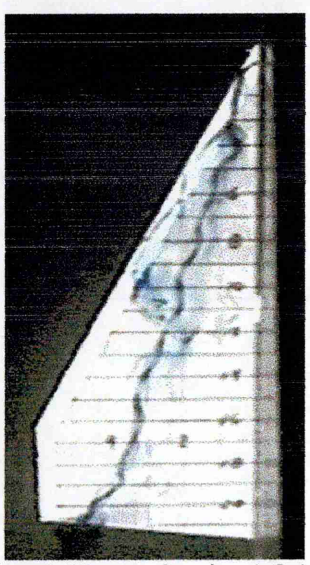

Delta 70, B.L.=6.73mm, Static, AOA=30deg.

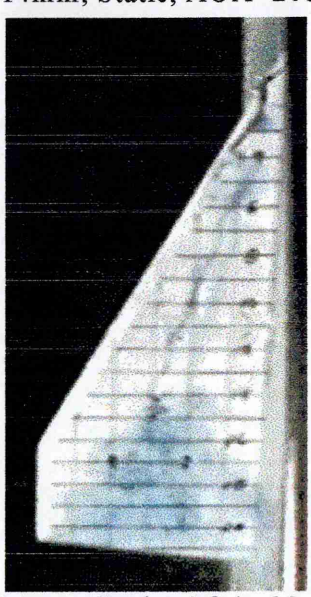

Delta 70, B.L.=14mm, Static, AOA=30 deg.

Figure 6.9 Picture, Static, Vortex breakdown position, Delta 70° sweep, t/c=0.018, B.L.=6.73mm, 14.0mm, AoA=10°,20° and 30°.

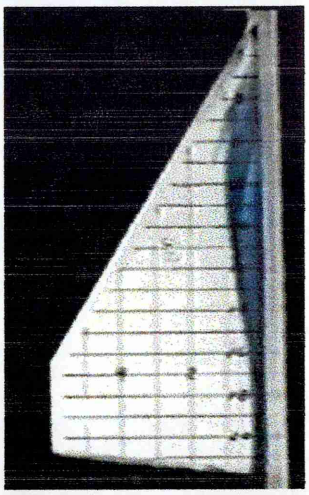

Delta 70, B.L.=6.73mm,
k=0.05, AOA=10deg., Up

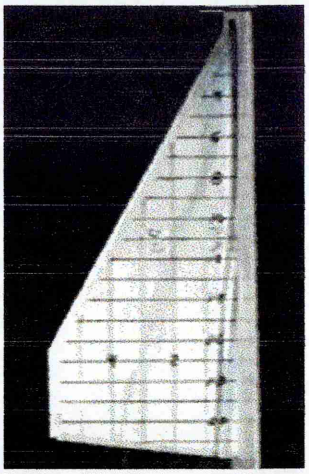

Delta 70, B.L.=6.73mm,
k=0.05,AOA=10 deg., Down

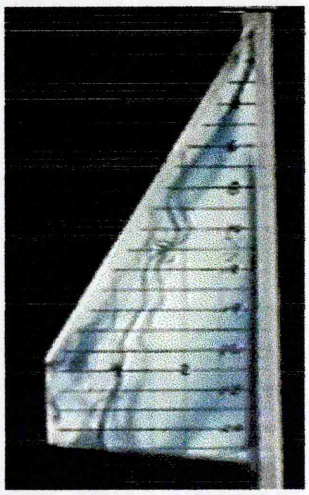

Delta 70, B.L.=6.73mm,
k=0.05, AOA=20deg., Up

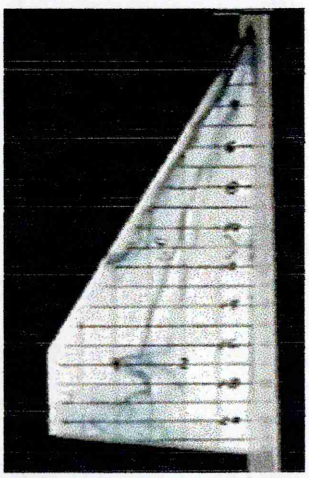

Delta 70, B.L.=6.73mm,
k=0.05, AOA=20deg., Down

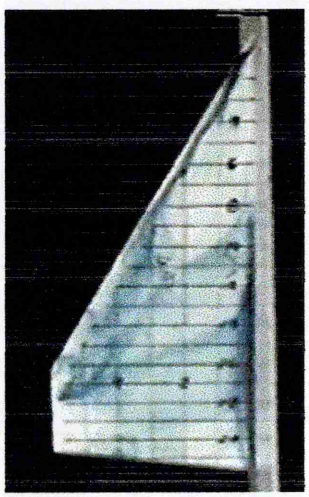

Delta 70, B.L.=6.73mm,
k=0.05, AOA=30deg., Up

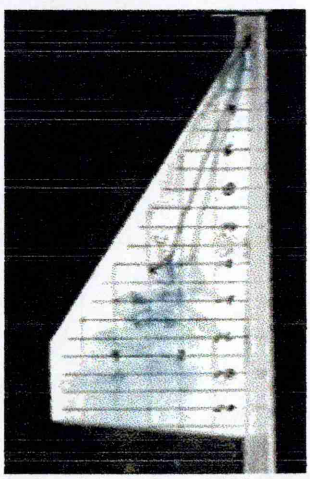

Delta 70, B.L.=6.73mm,
k=0.05, AOA=30deg., Down

Figure 6.10 Picture, Dynamic Pitch-up and Pitch-down, Delta 70° sweep, t/c=0.018, B.L.=6.73mm, Reduced pitch rate, k=0.05, AoA=10°, 20° and 30°

Delta70, B.L.=14mm,
k=0.05, AOA=10deg. UP

Delta70, B.L.=14mm,
k=0.05, AOA=10deg. Down

Delta 70, B.L.=14mm,
k=0.05, AOA=20deg. UP

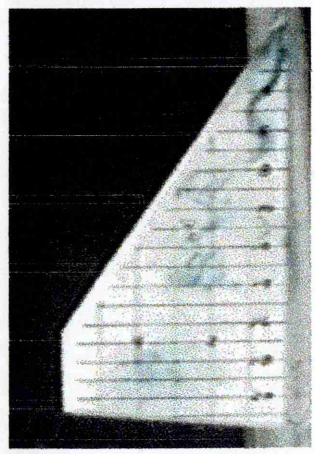

Delta 70, B.L.=14mm,
k=0.05, AOA=20deg., Down

Delta 70, B.L.=14mm,
k=0.05, AOA=30deg. UP

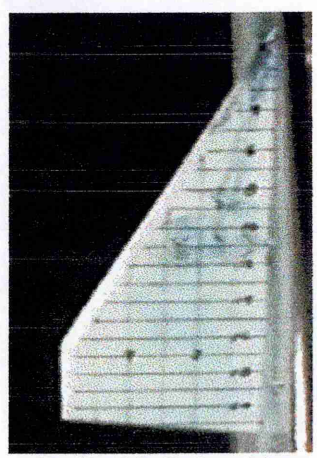

Delta 70, B.L.=14mm,
k=0.05, AOA=30deg., Down

Figure 6.11 Picture, Dynamic Pitch-up and Pitch-down, Delta 70° sweep, t/c=0.018, B.L.=14mm, Reduced pitch rate, k=0.05, AoA=10°, 20° and 30°

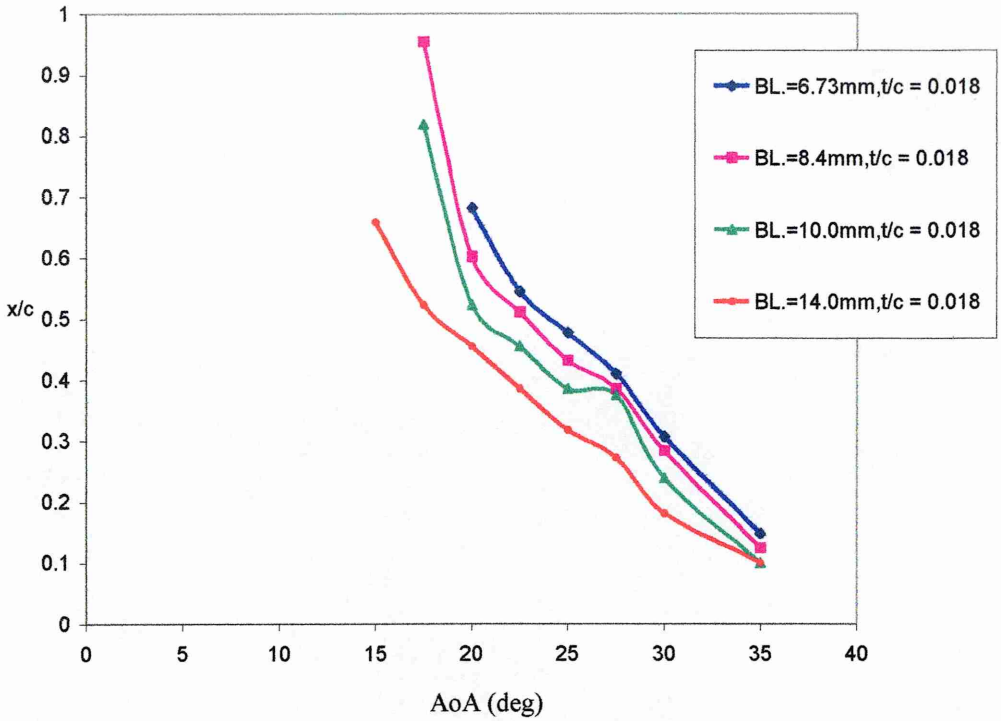

Figure 6.12 Influence of wall boundary layer thickness on vortex breakdown position for 55 deg. Swept delta wing. (t/c)=0.018

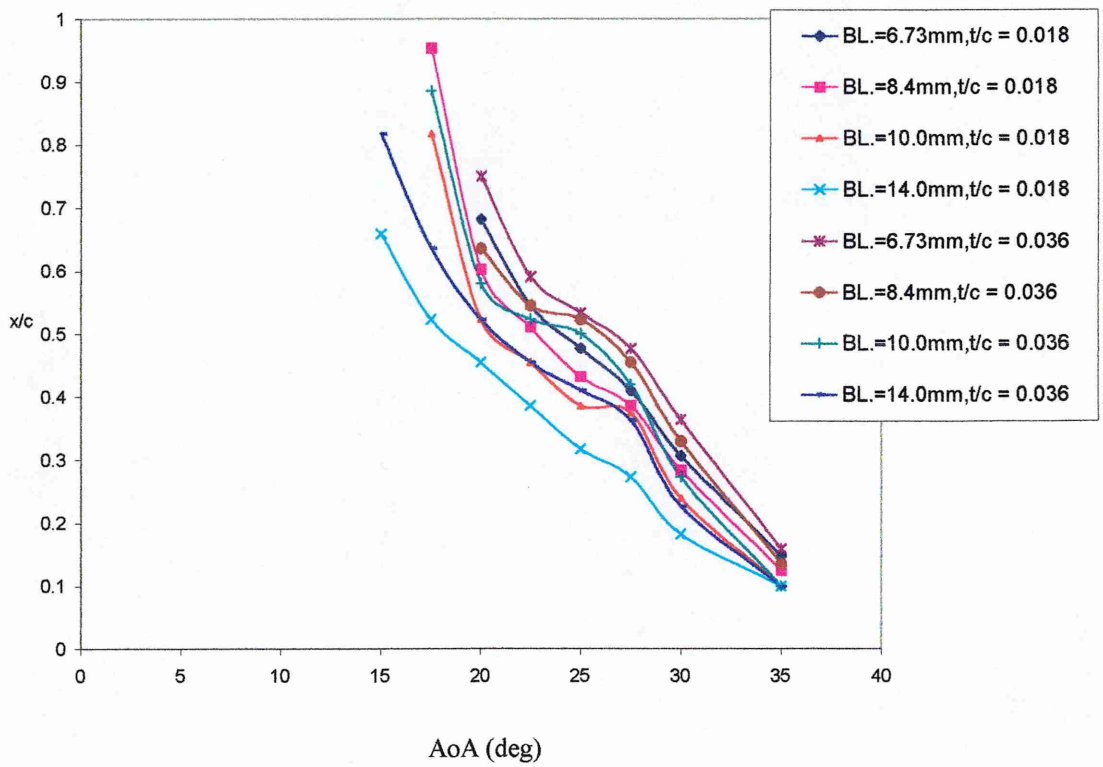

Figure 6.13 Effect of thickness/chord ratio on vortex breakdown position for 55 deg. swept delta, for all wall boundary layer thickness

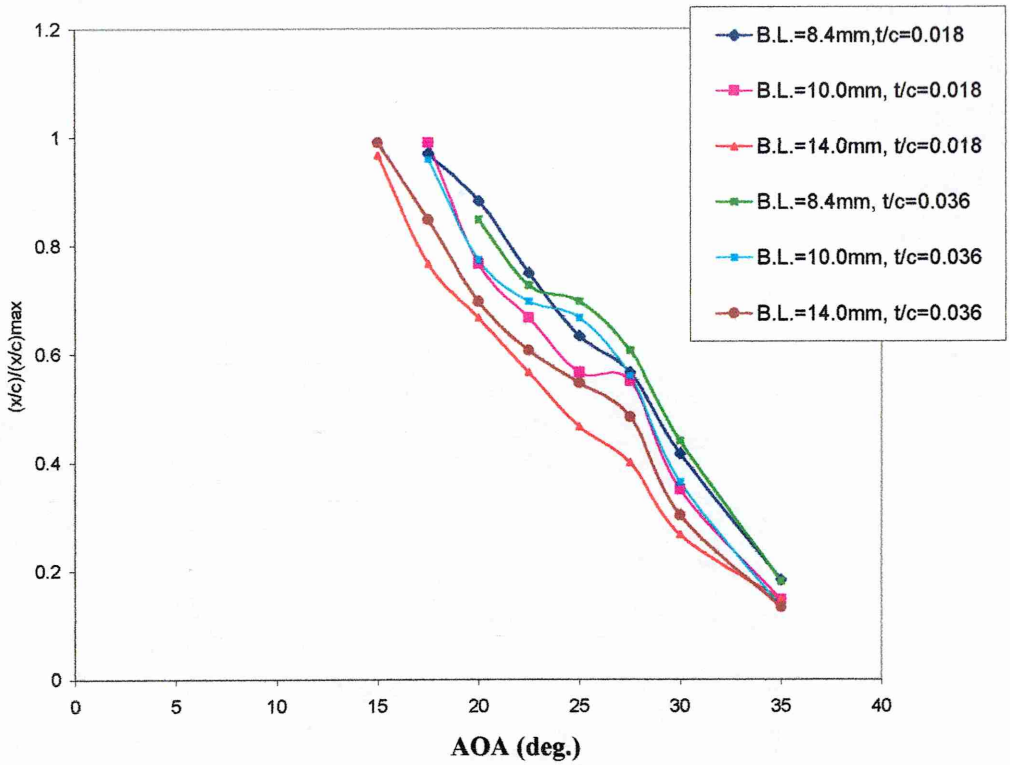

Figure 14 Normalised (x/c)/(x/c)max vs. AOA for 55 deg. swept delta, t/c = 0.018 and 0.036 for all boundary layers

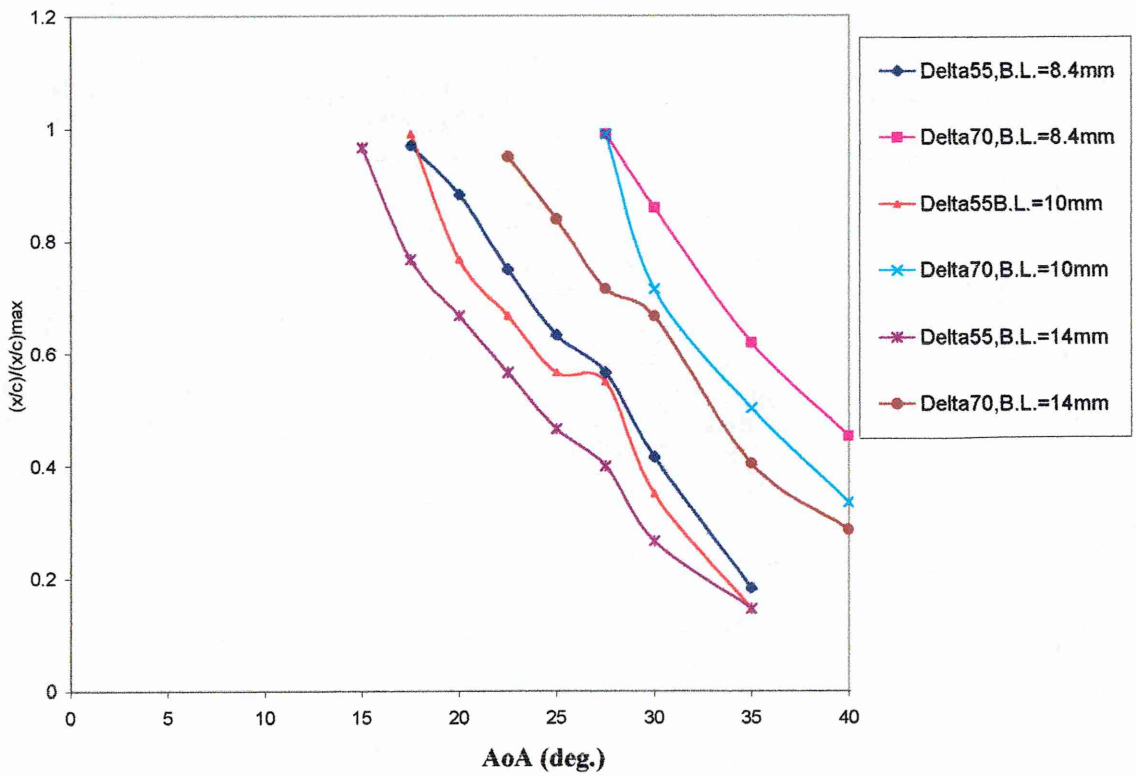

Figure 6.15 Normalised (x/c)/(x/c)max for delta 55 swept wing vs. AOA for 55 and 70 deg. swept delta, t/c = 0.018 for all boundary layers

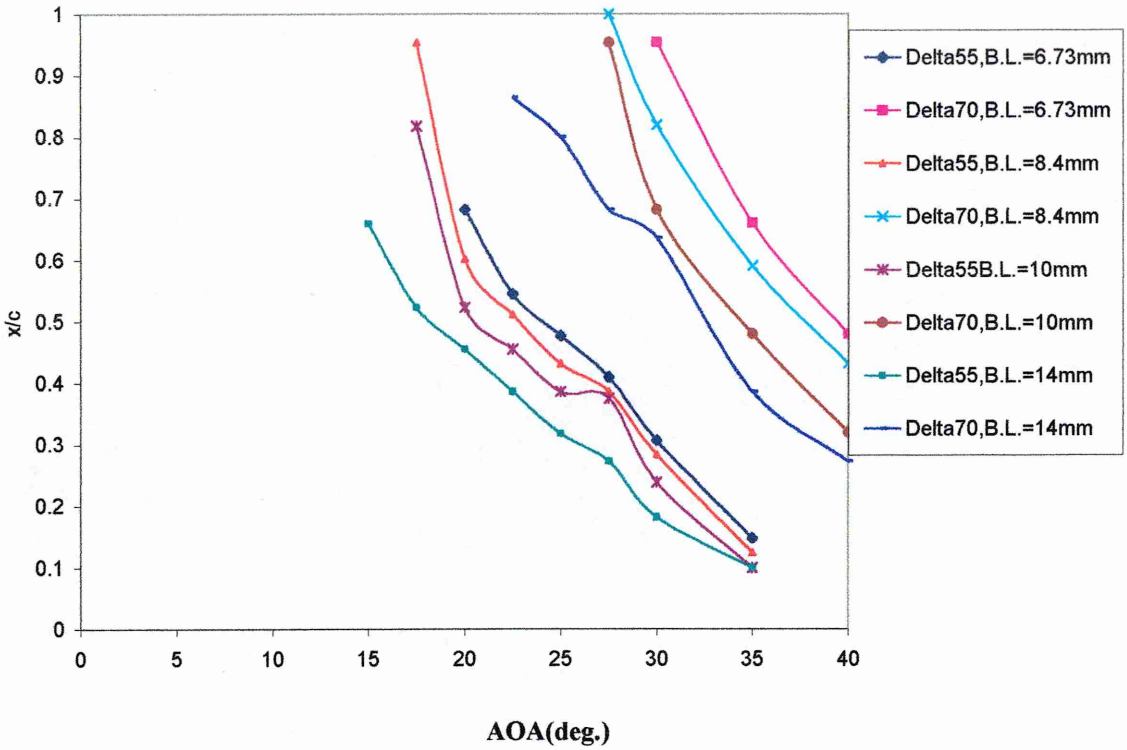

Figure 6.16 Effect of sweep on vortex breakdown position for all boundary layers, t/c = 0.018 for 55 deg. and 70 deg. swept delta

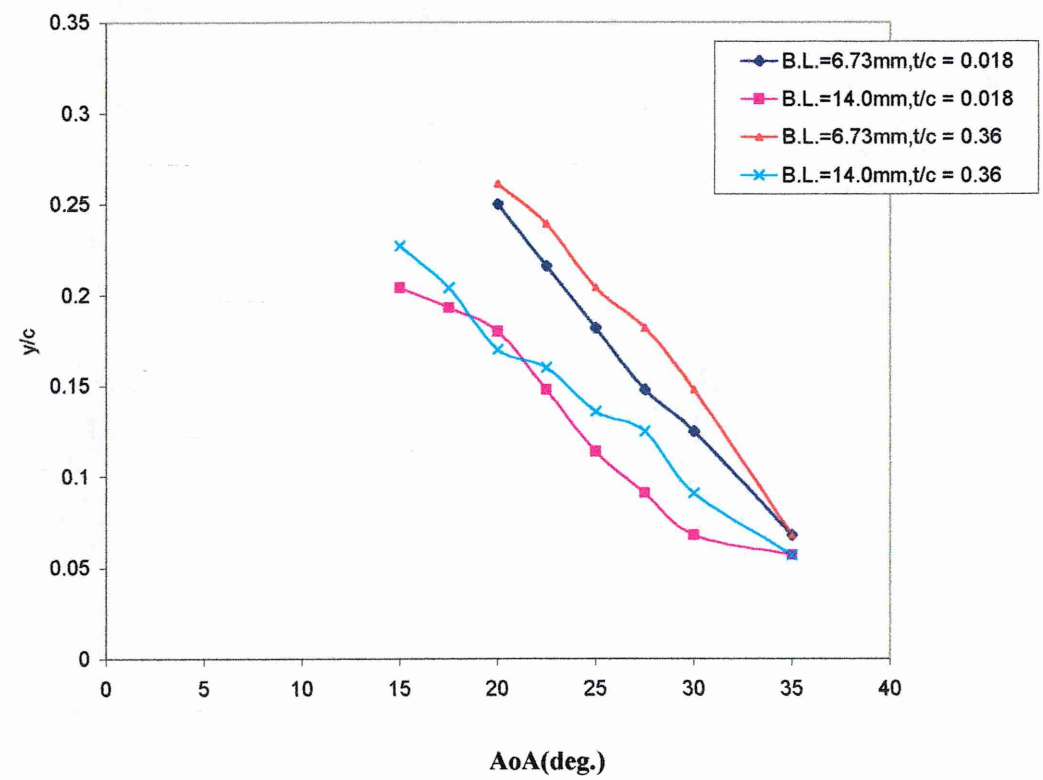

Figure 6.17 Effect of thickness/chord ratio on lateral vortex breakdown position vs. AoA for 55 deg.swept delta.

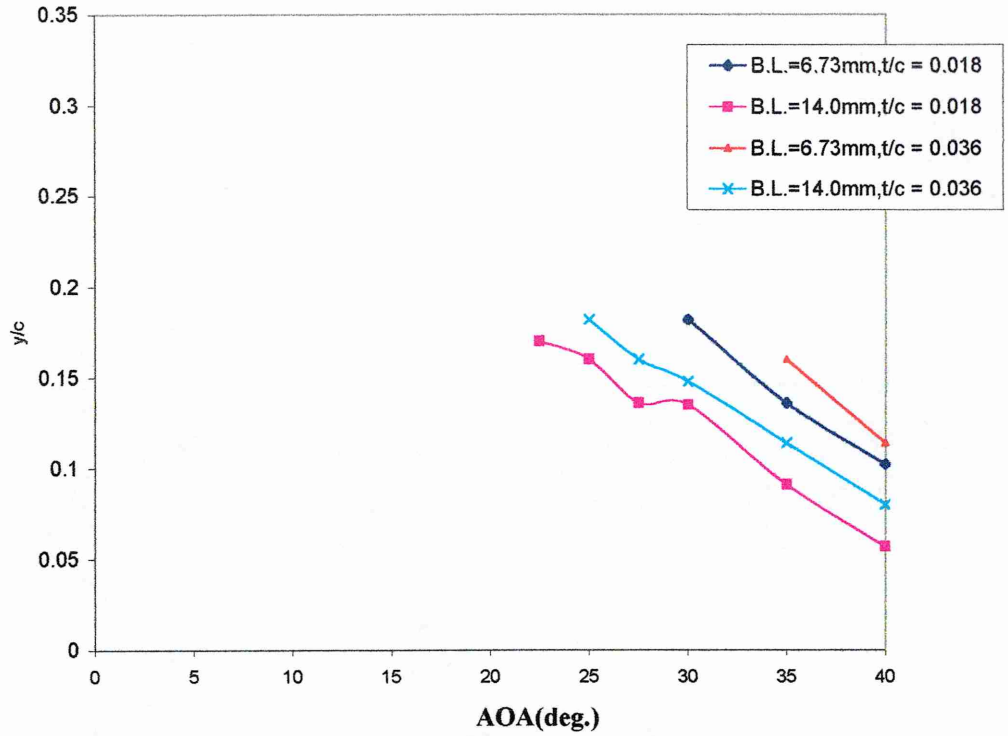

Figure 6.18 Effect of thickness/chord ratio on lateral vortex breakdown position vs. AoA for 70 deg.swept delta.

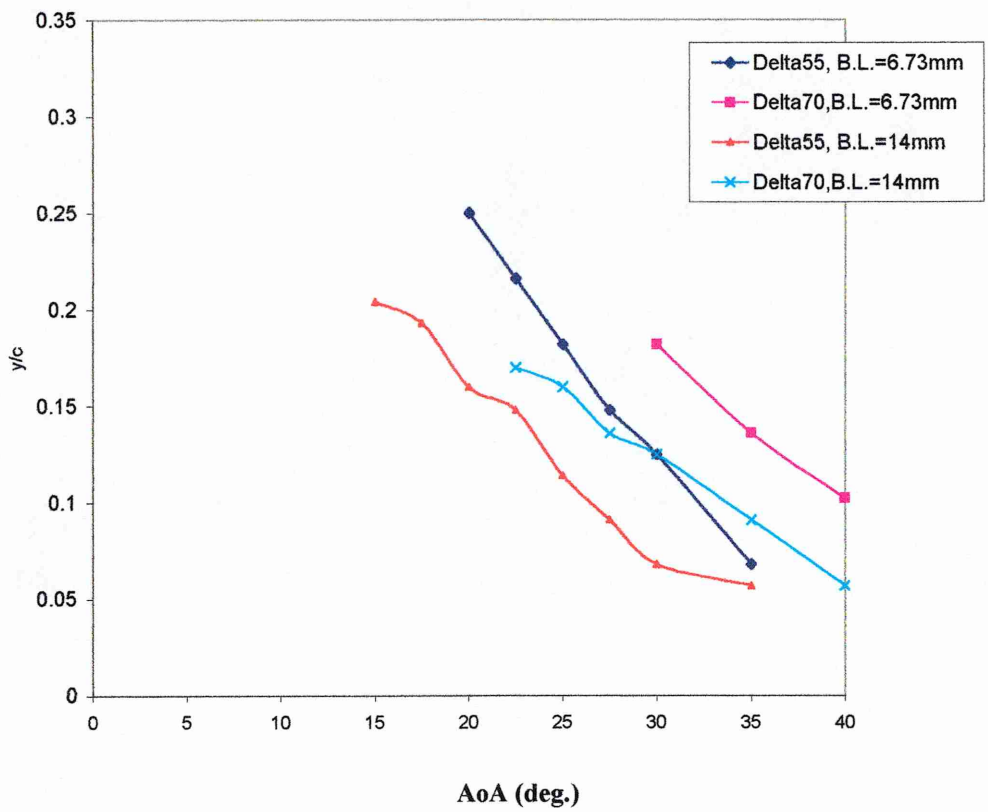

Figure 6.19 Effect of wing sweep on lateral vortex breakdown position vs. AoA, t/c=0.018

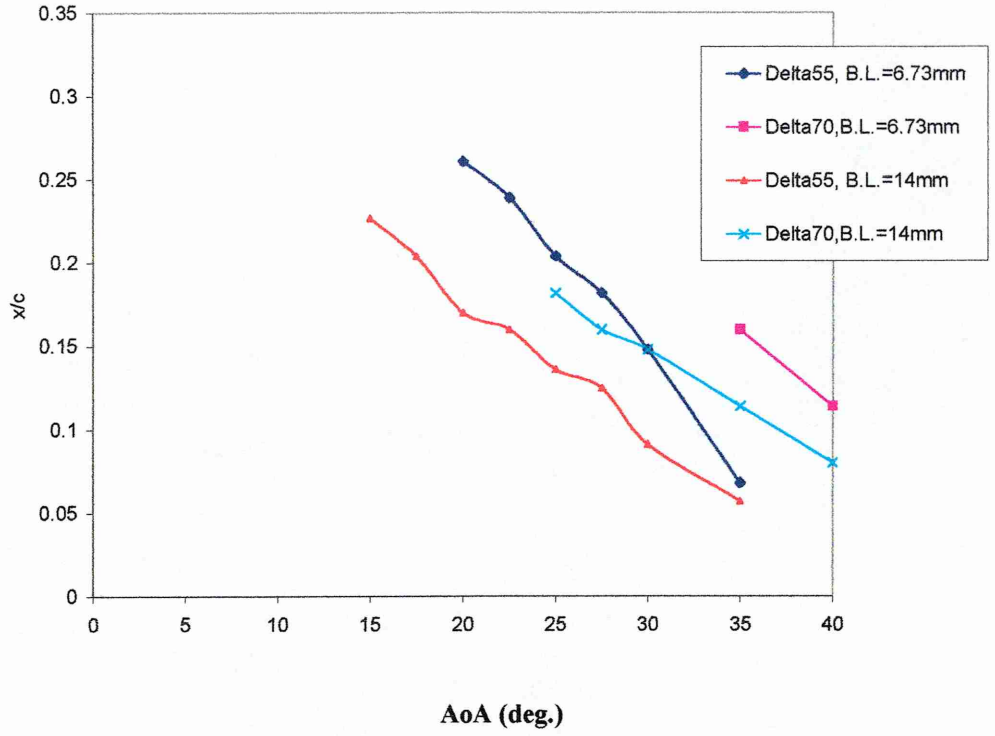

Figure 6.20 Effect of wing sweep on lateral vortex breakdown position vs. AoA, t/c=0.036

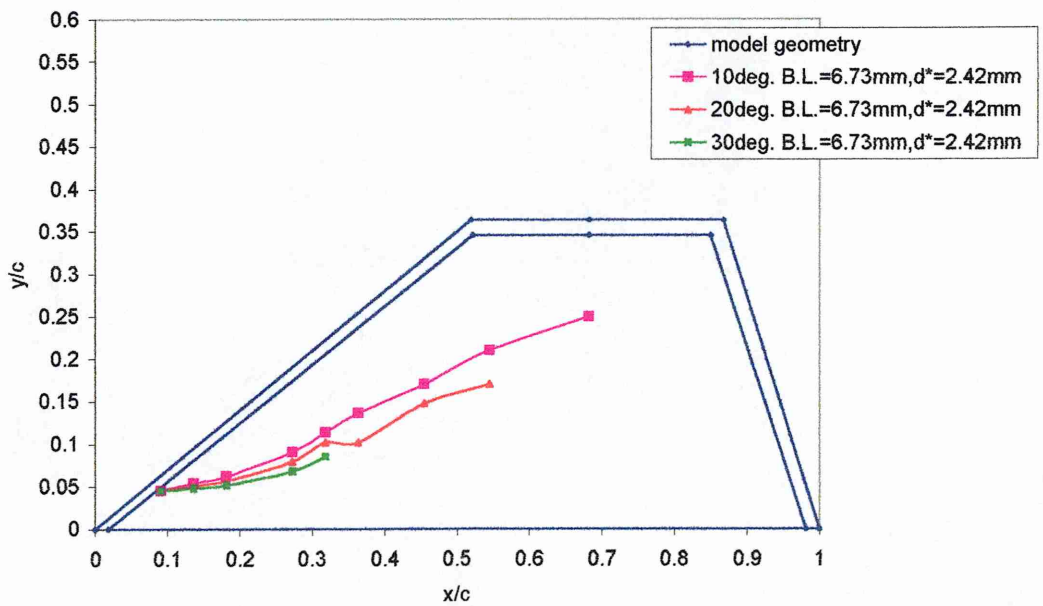

Figure 6.21 Position of vortex origin from vortex core trajectory, x/c vs. y/c ; Delta 55, t/c=0.018, for (B.L.=6.73mm), vortex origin from wall=5.83mm

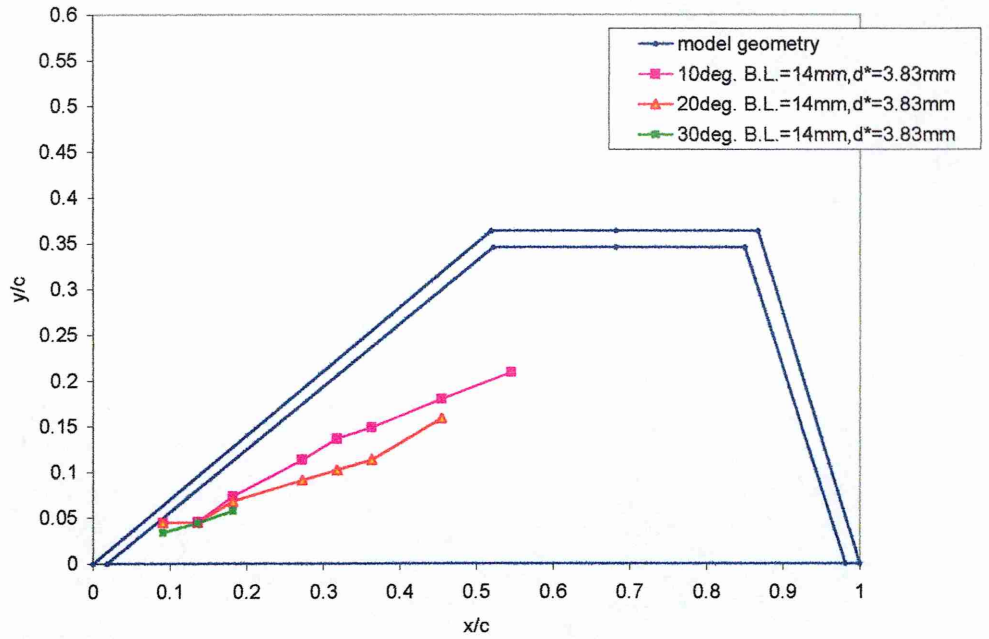

Figure 6.22 Position of vortex origin from vortex core trajectory, x/c vs. y/c ; Delta 55, t/c=0.018, for (B.L.= 14mm), vortex origin from wall=5.83mm

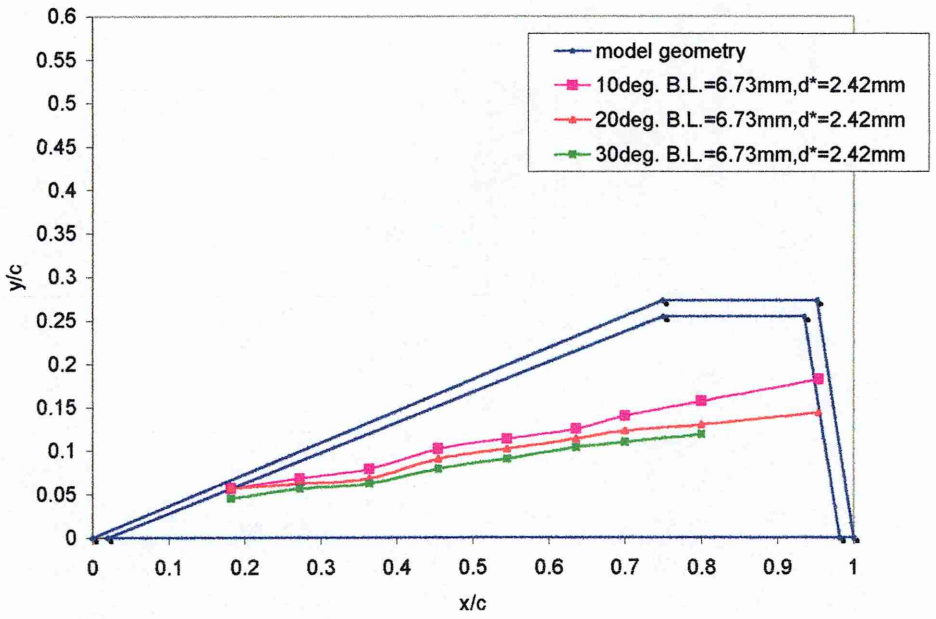

Figure 6.23 Position of vortex origin from vortex core trajectory, x/c vs. y/c ; Delta 70, t/c=0.018, for (B.L.=6.73mm), vortex origin from wall=11.67mm

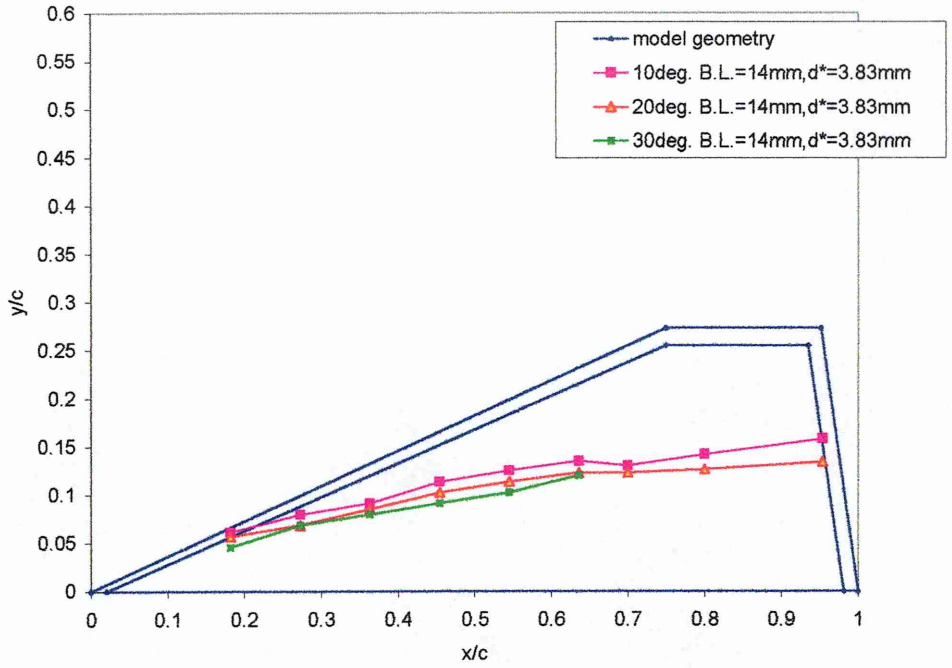

Figure 6.24 Position of vortex origin from vortex core trajectory, x/c vs. y/c ; Delta 70, t/c=0.018, for (B.L.= 14mm), vortex origin from wall=11.67mm

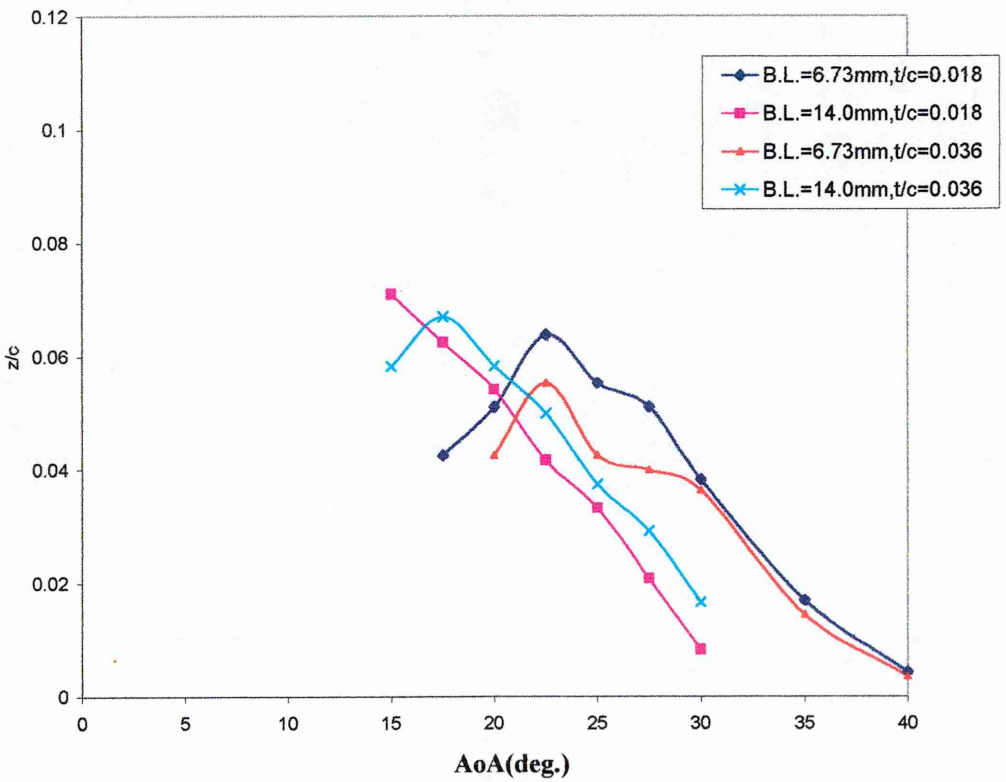

Figure 6.25 Effect of thickness/chord ratio on the variation of vertical location of vortex breakdown position vs. AoA for 55 deg.swept delta

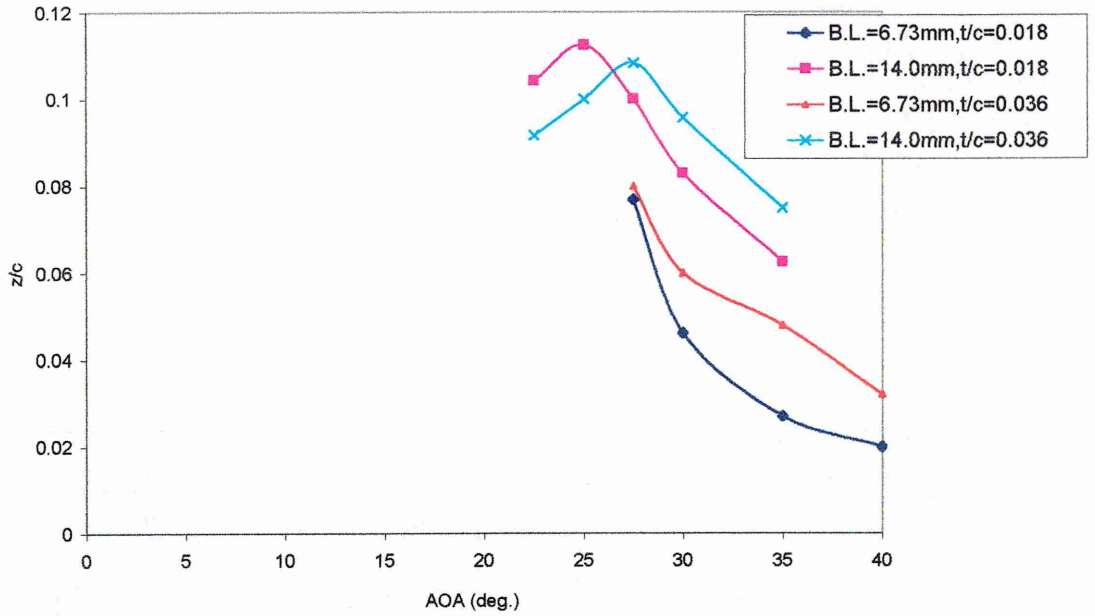

Figure 6. 26 Effect of thickness/chord ratio on the variation of vertical location of vortex breakdown position vs. AoA for 70 deg.swept delta

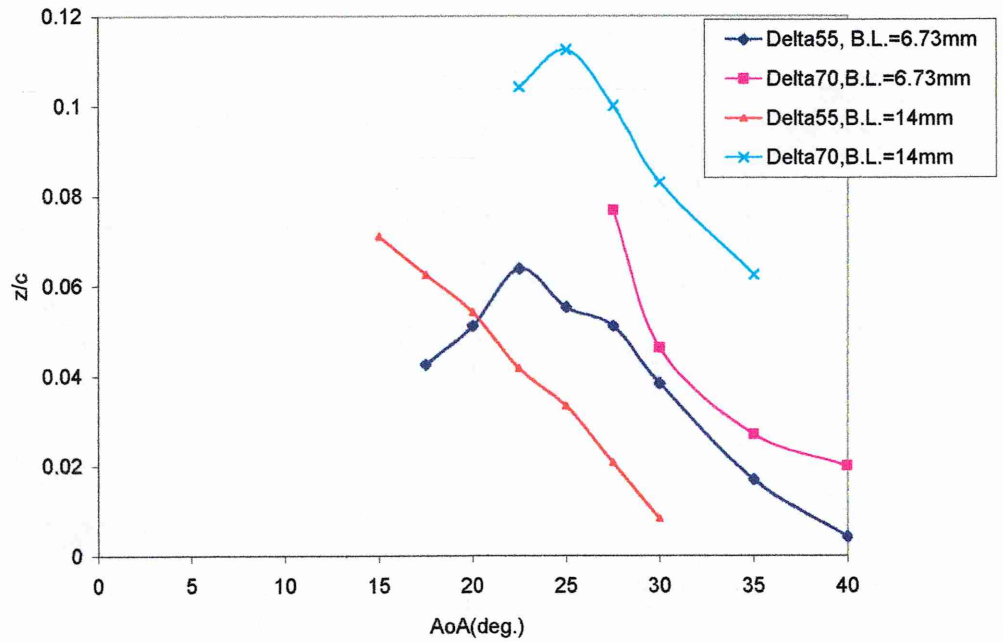

Figure 6.27 Effect of wing sweep on the variation of vertical location of vortex breakdown position vs. AoA for 55 and 70 deg.swept delta, t/c=0.018

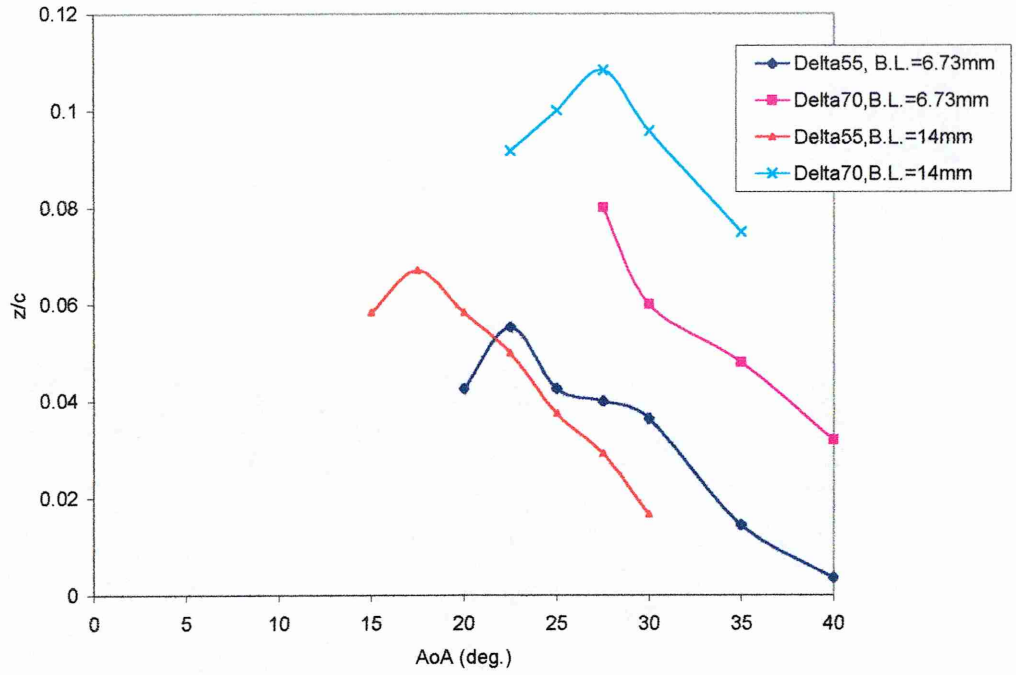

Figure 6.28 Effect of wing sweep on the variation of vertical location of vortex breakdown position vs. AoA for 55 and 70 deg.swept delta, t/c=0.036

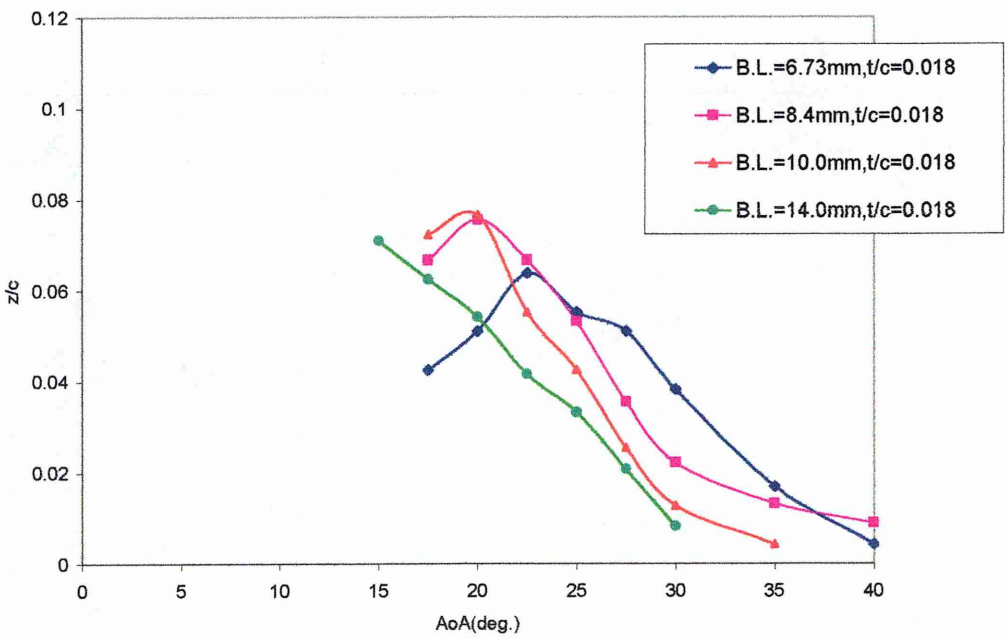

Figure 6.29 Influence of wall boundary layer thickness on the variation of vertical location of vortex breakdown vs. AoA for 55 deg. Swept delta, t/c = 0.018.

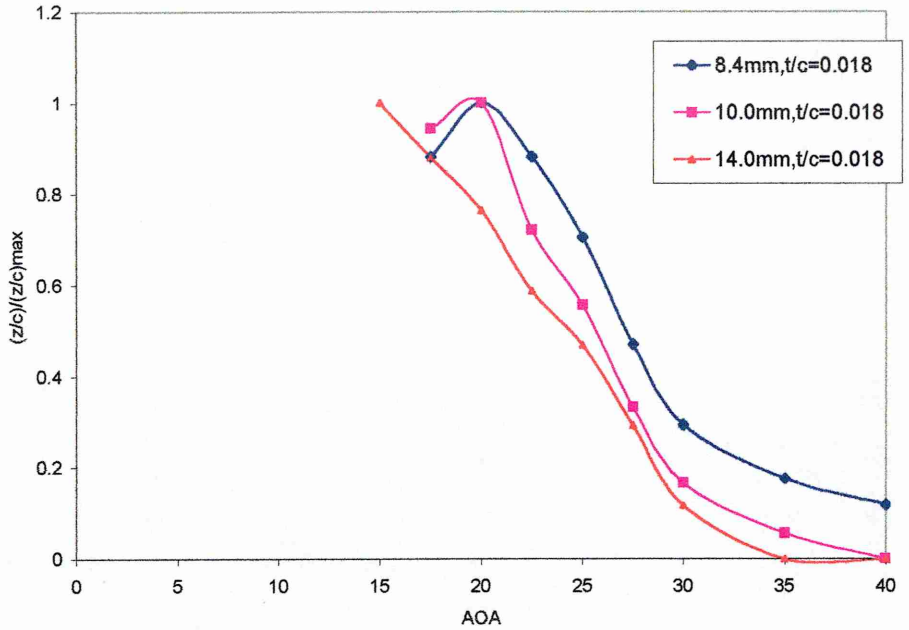

Figure 6.30 Normalised (z/c)/(z/c)max vs. AOA for 55 deg. swept delta for all wall boundary layers

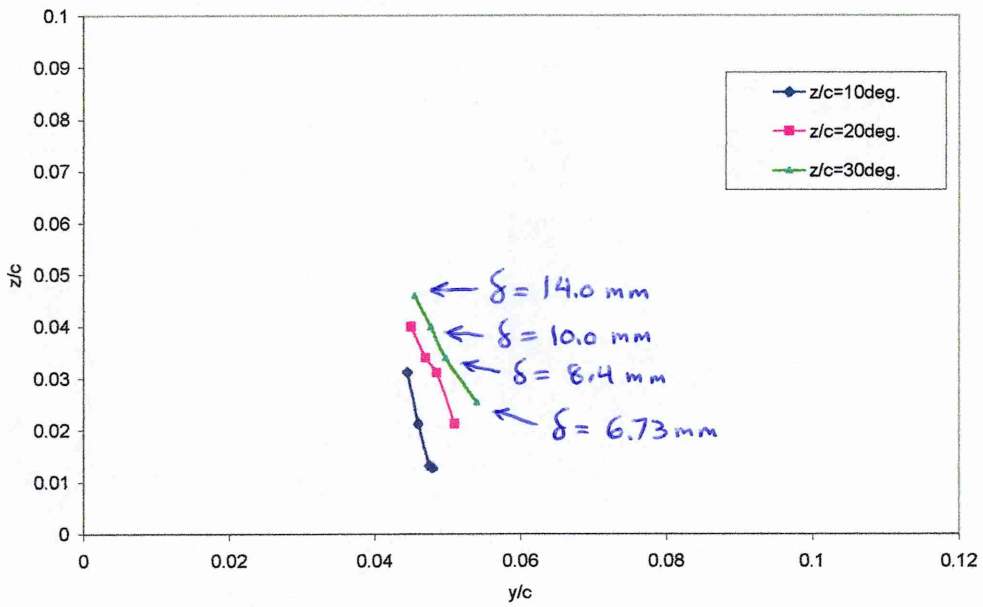

Figure 6.31 Cross section of y/c vs. z/c @ x/c = 0.14 for all boundary layer @ AOA=10,20 and 30 deg.

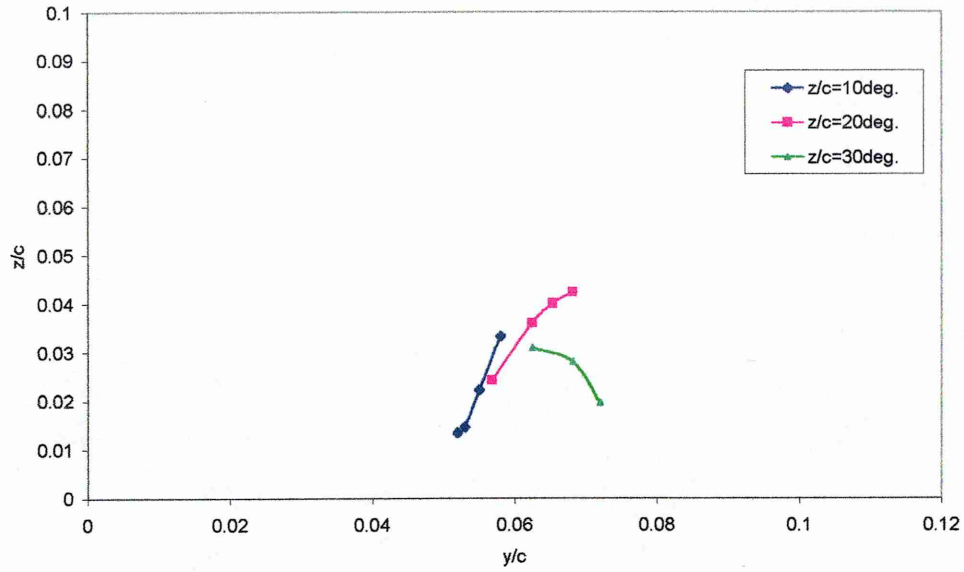

Figure 6.32 Cross section of y/c vs. z/c @ x/c = 0.18 for all boundary layer @ AOA=10,20 and 30 deg.

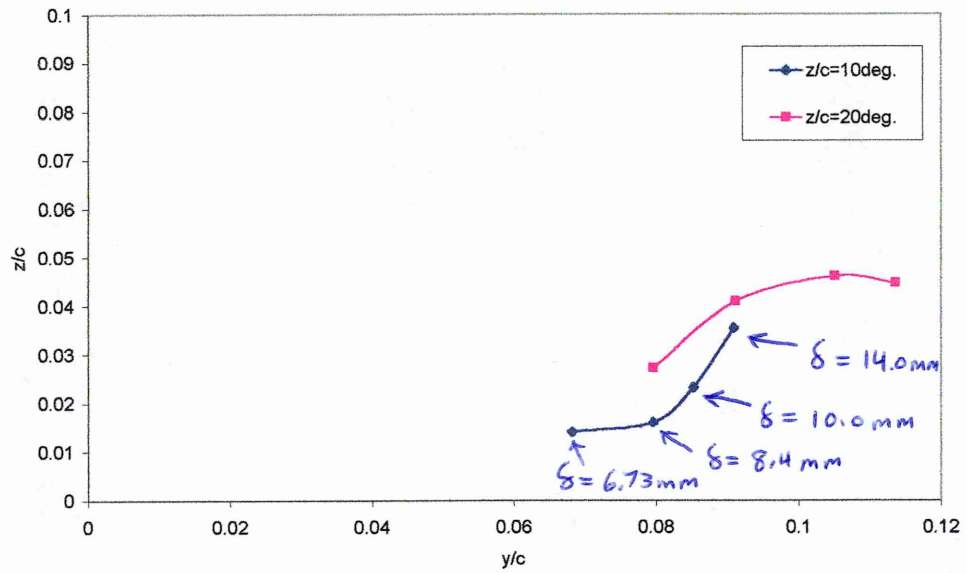

Figure 6.33 Cross section of y/c vs. z/c @ x/c = 0.27 for all boundary layer @ AOA=10,20 and 30 deg.

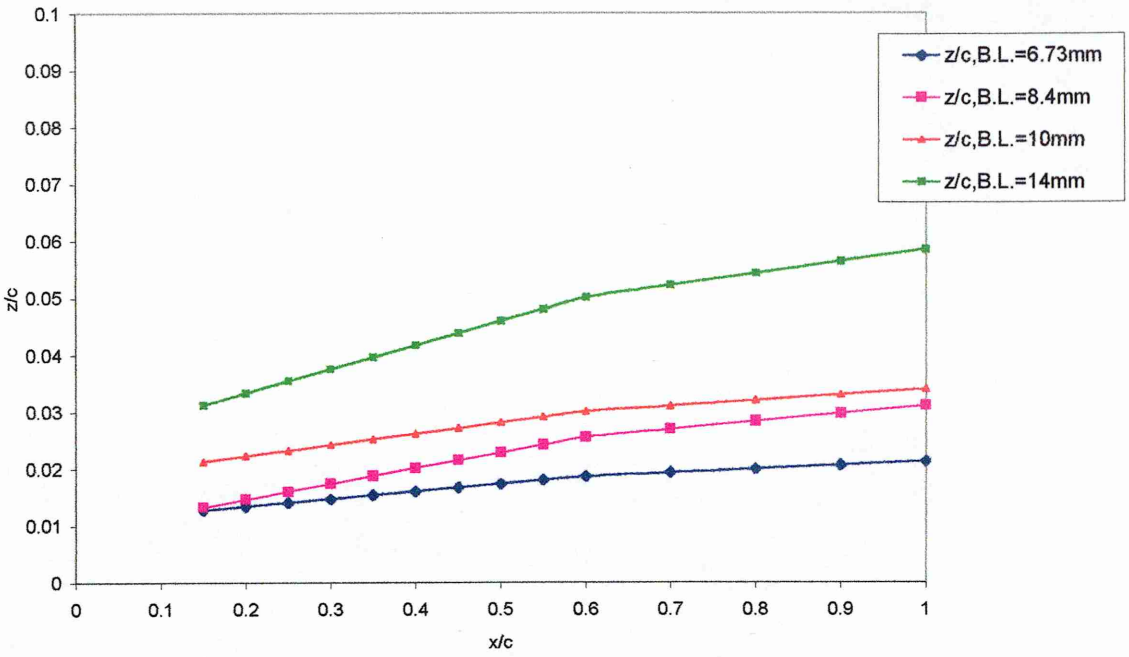

Figure 6.34 Vortex core location of x/c vs. z/c; Delta 55, t/c=0.018, AOA=10deg., for all Boundary layers

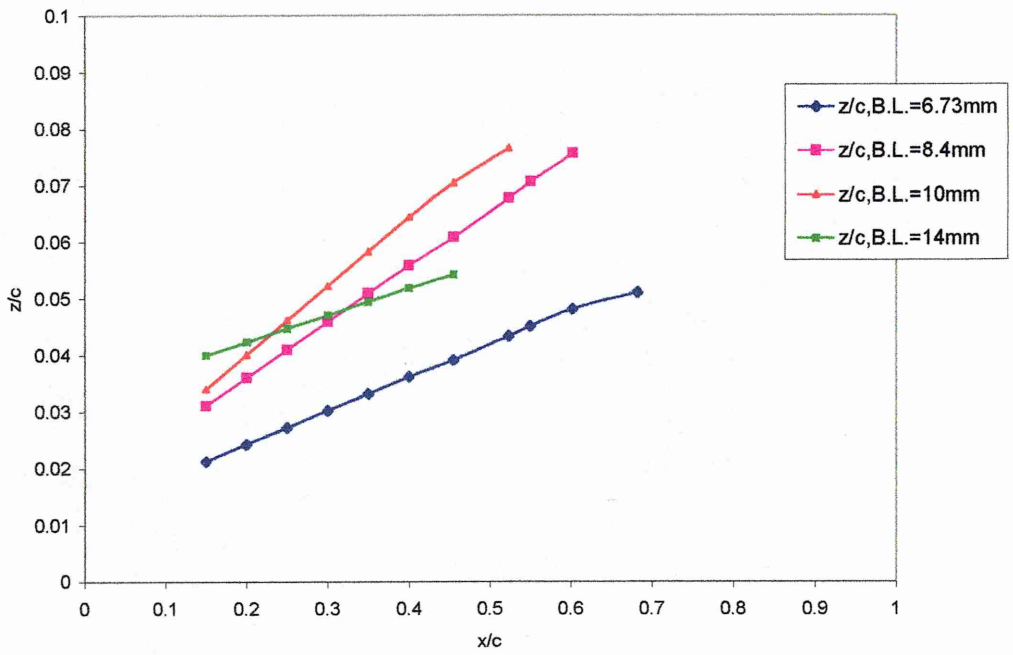

Figure 6. 35 Vortex core location of x/c vs. z/c; Delta 55, t/c=0.018, AOA=20deg., for all Boundary layers

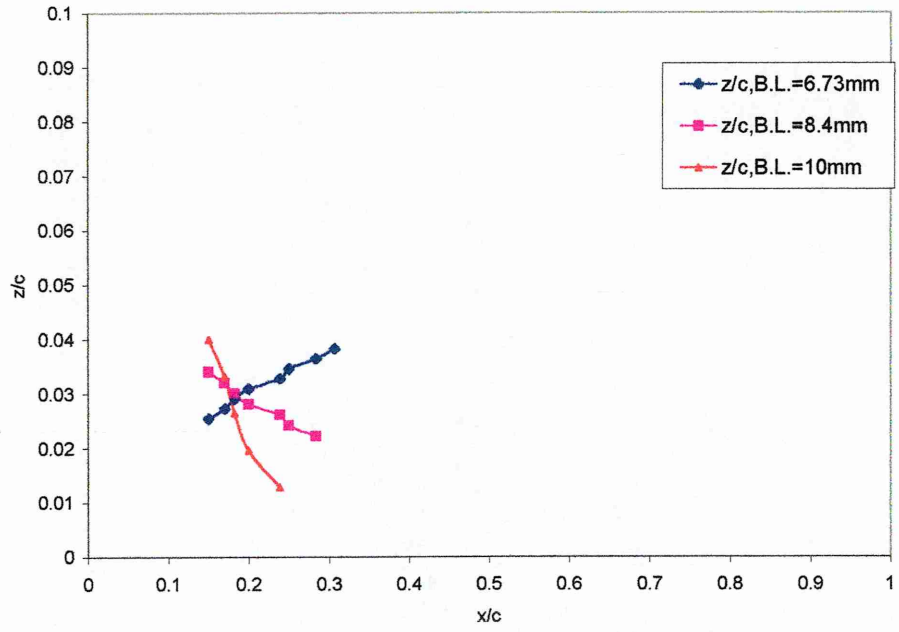

Figure 6.36 Vortex core location of x/c vs. z/c; Delta 55, t/c=0.018, AOA=30deg., for all Boundary layers

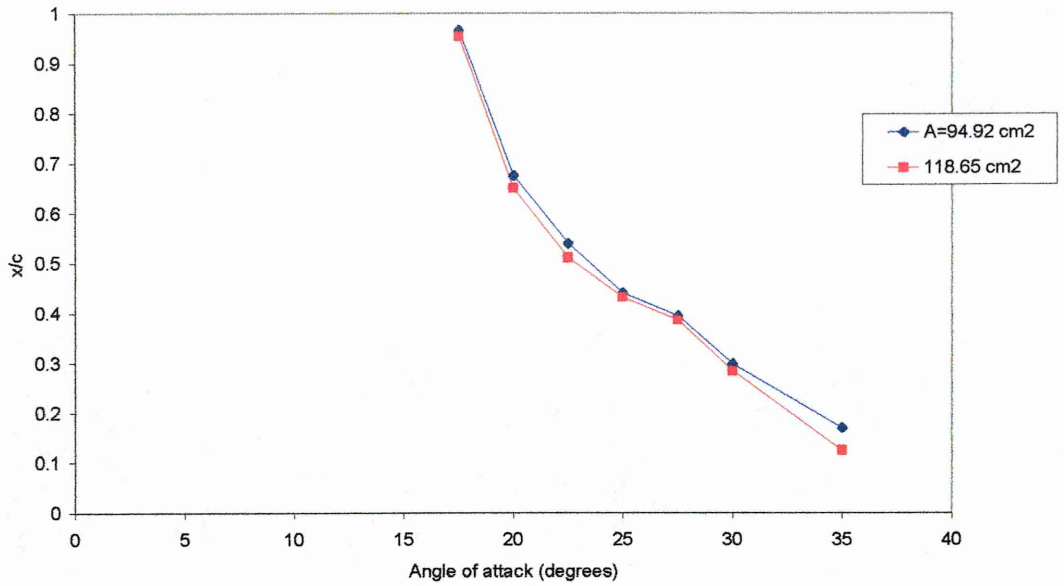

Figure 6.37 Vortex breakdown position x/c vs. AOA for 55° swept delta wing models (original and 20% less area), t/c=0.018, for Tunnel Wall boundary layer configuration

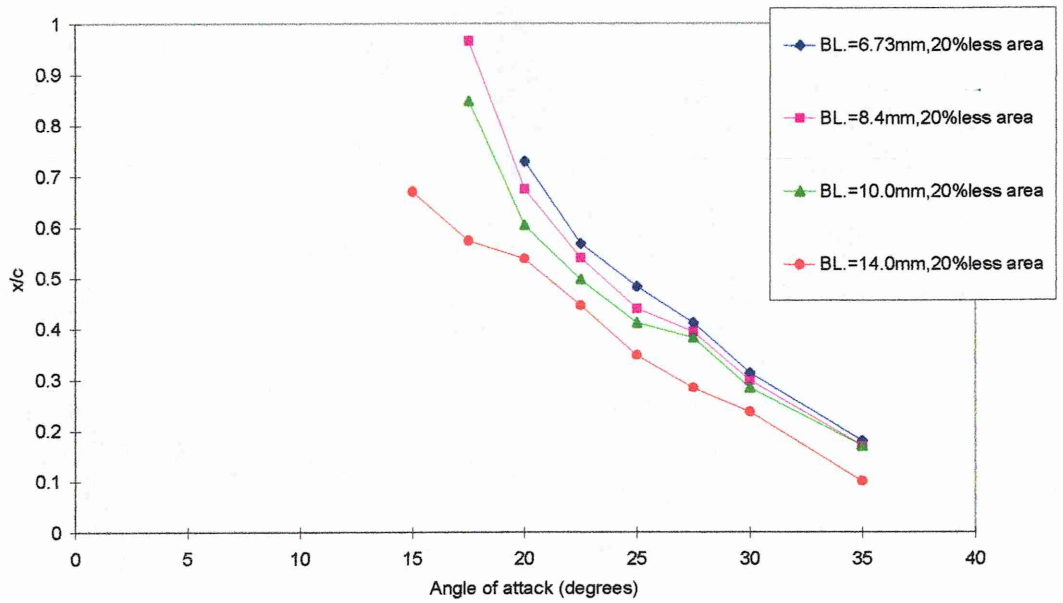

Figure 6.38 Vortex breakdown position x/c vs. AOA for 55° swept delta wing model(20% less area), t/c=0.018, for all boundary layer configurations

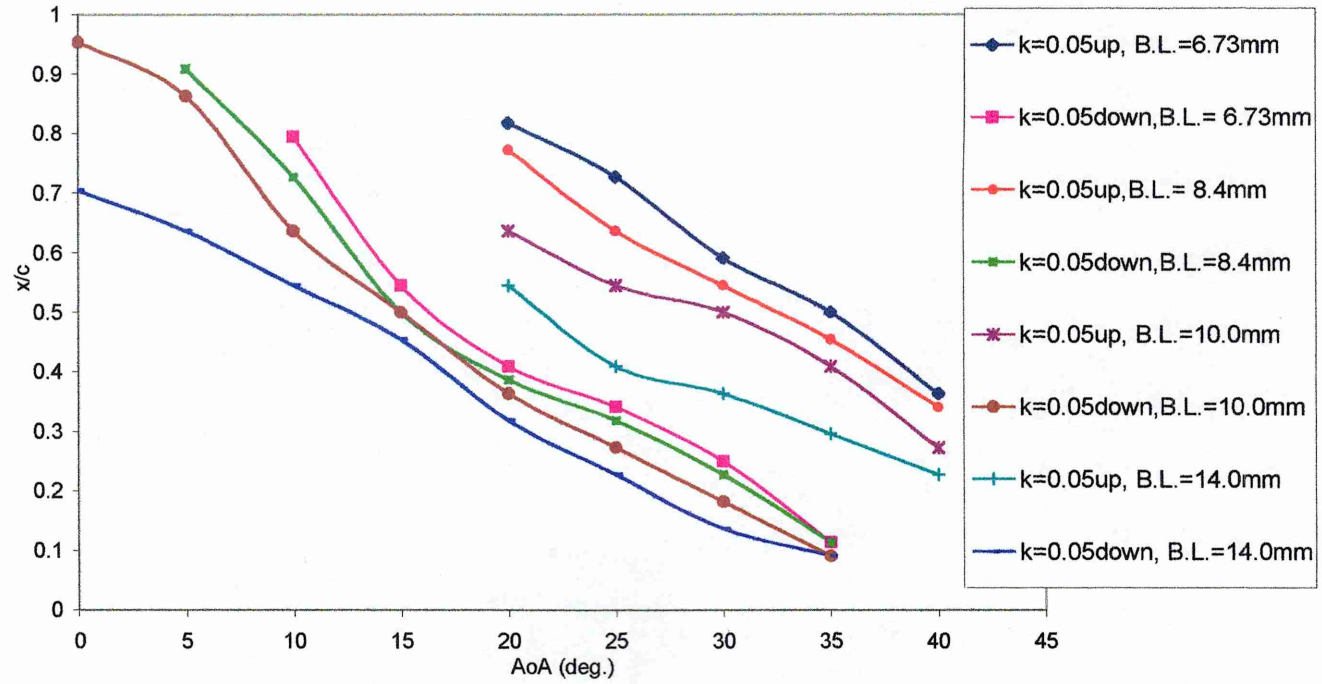

Figure 6.39 Influence of wall boundary layer thickness on vortex breakdown position x/c vs. AoA, 55 deg. Swept delta, for all wall boundary layers thickness, t/c = 0.018, k = 0.05

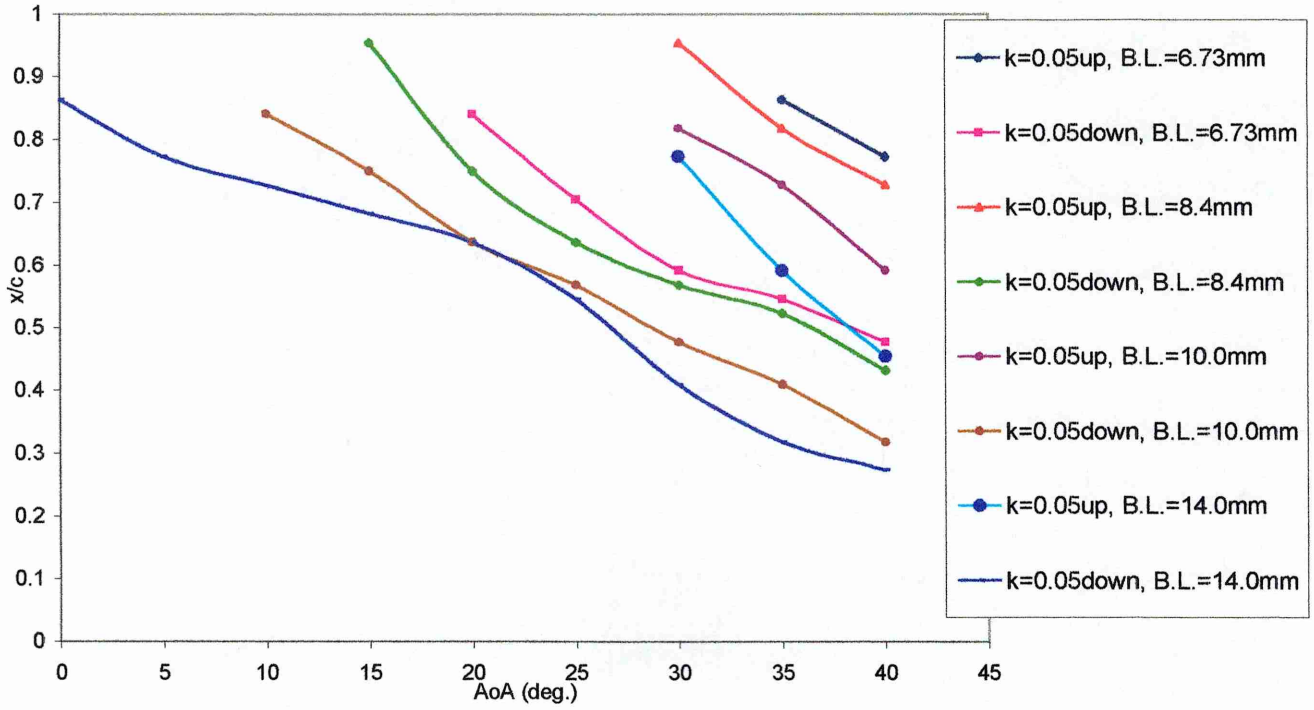

Figure 6.40 Influence of wall boundary layer thickness on vortex breakdown position x/c vs. AoA 70 deg. Swept delta, for all boundary layers thickness, t/c = 0.018, k = 0.05

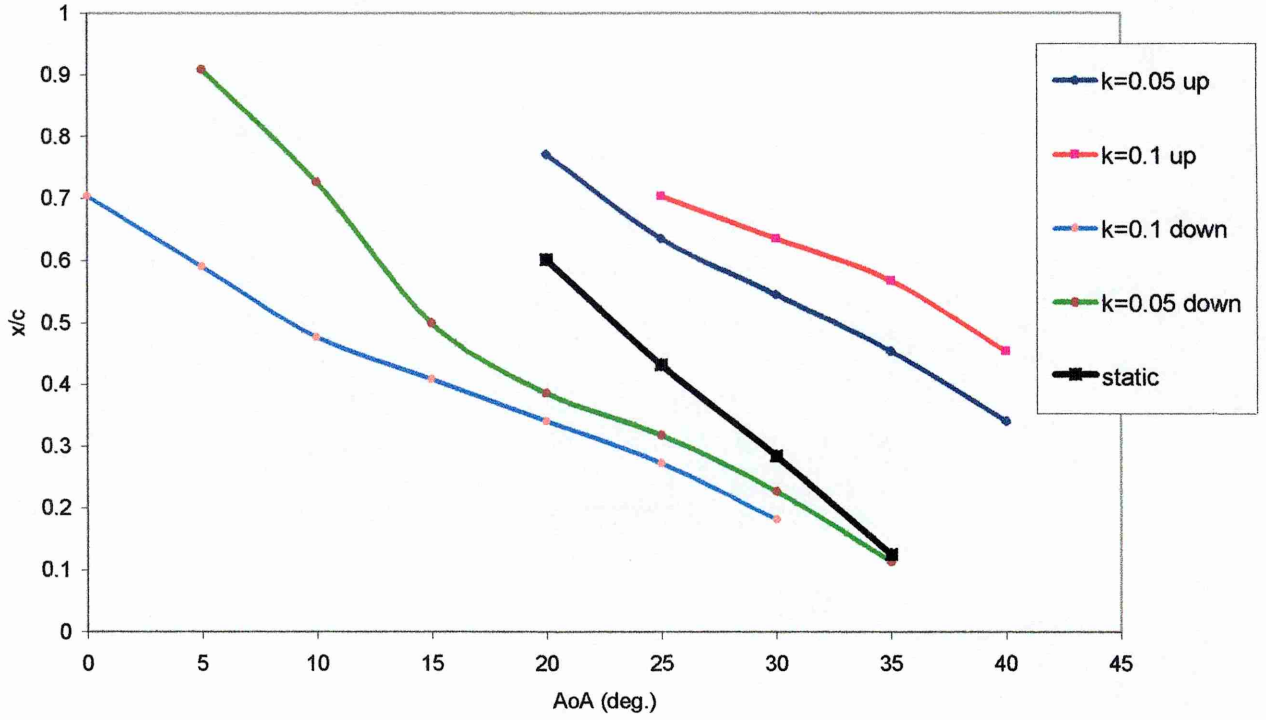

Figure 6.41 Comparison of Static and Dynamic effect, 55 deg. Swept delta, t/c = 0.018, boundary layer = 8.4mm, k = 0.05 and 0.1

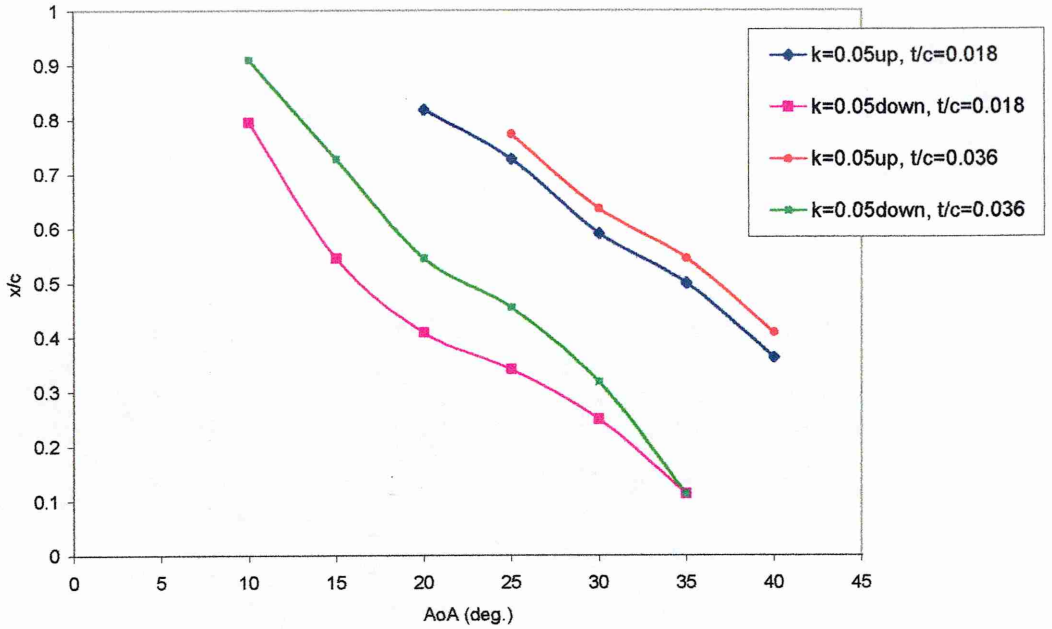

Figure 6.42 Effect of thickness on vortex breakdown position x/c vs. AoA, 55 deg. Swept delta, boundary layer = 6.73 mm

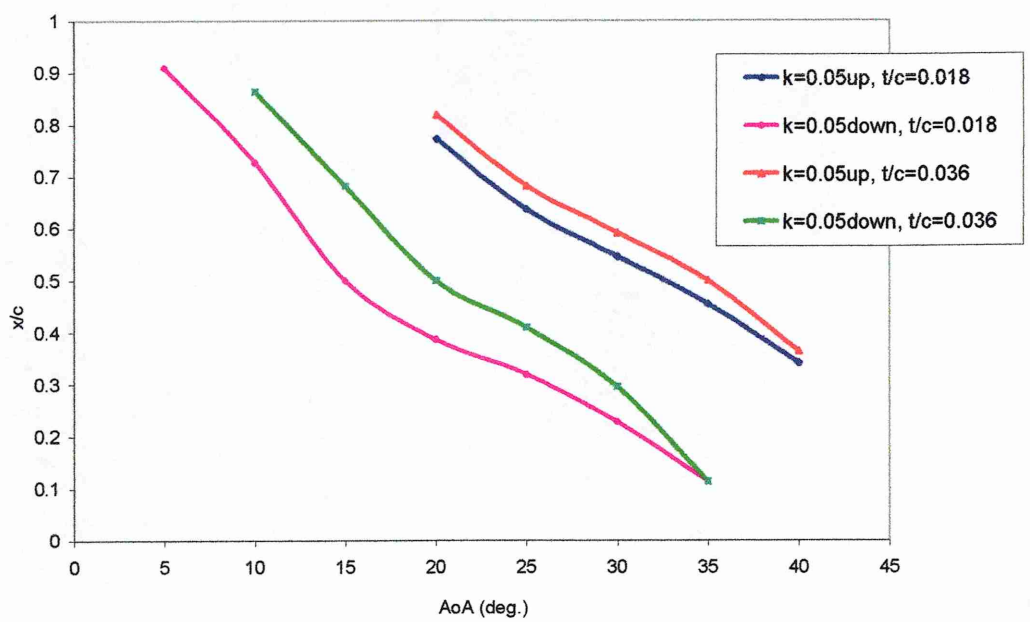

Figure 6.43 Effect of thickness on vortex breakdown position x/c vs. AoA, 55 deg. Swept delta, boundary layer = 8.4 mm

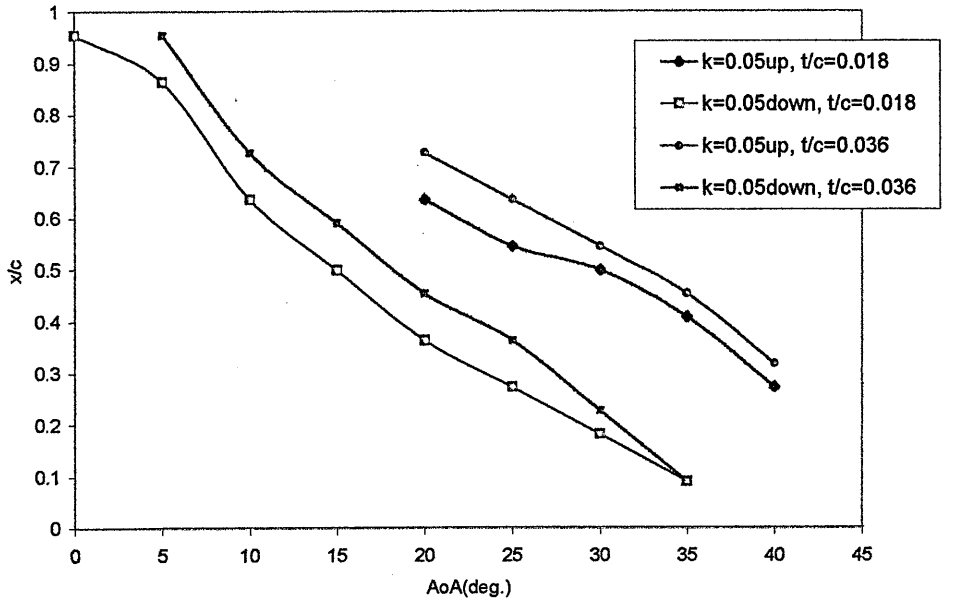

Figure 6. 44 Effect of thickness on vortex breakdown position x/c vs. AoA, 55 deg. Swept delta, boundary layer = 10mm

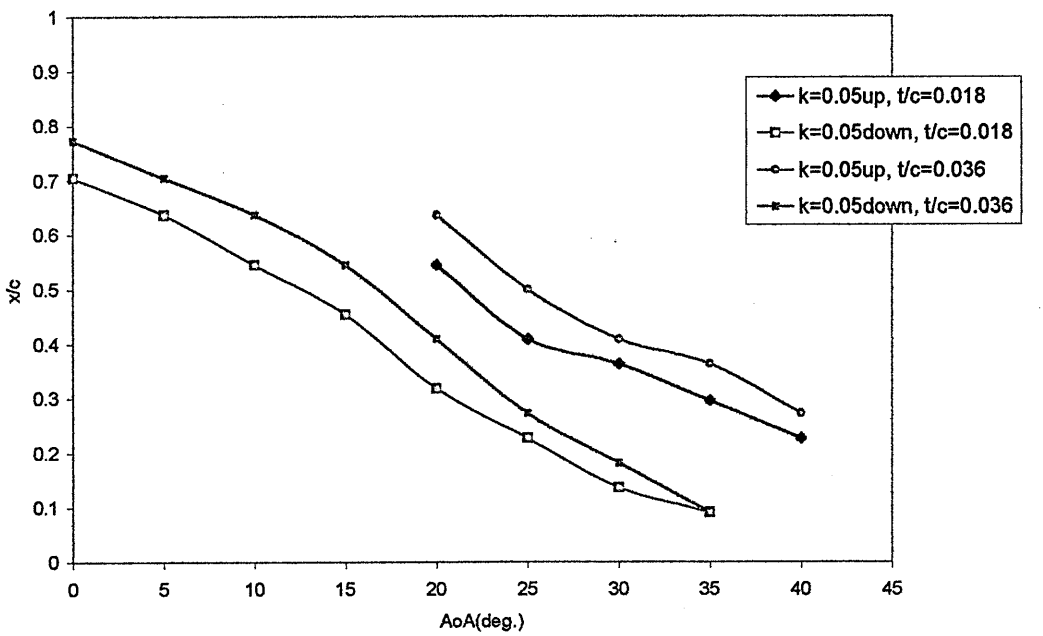

Figure 6.45 Effect of thickness on vortex breakdown position x/c vs. AoA, 55 deg. Swept delta, boundary layer = 14mm

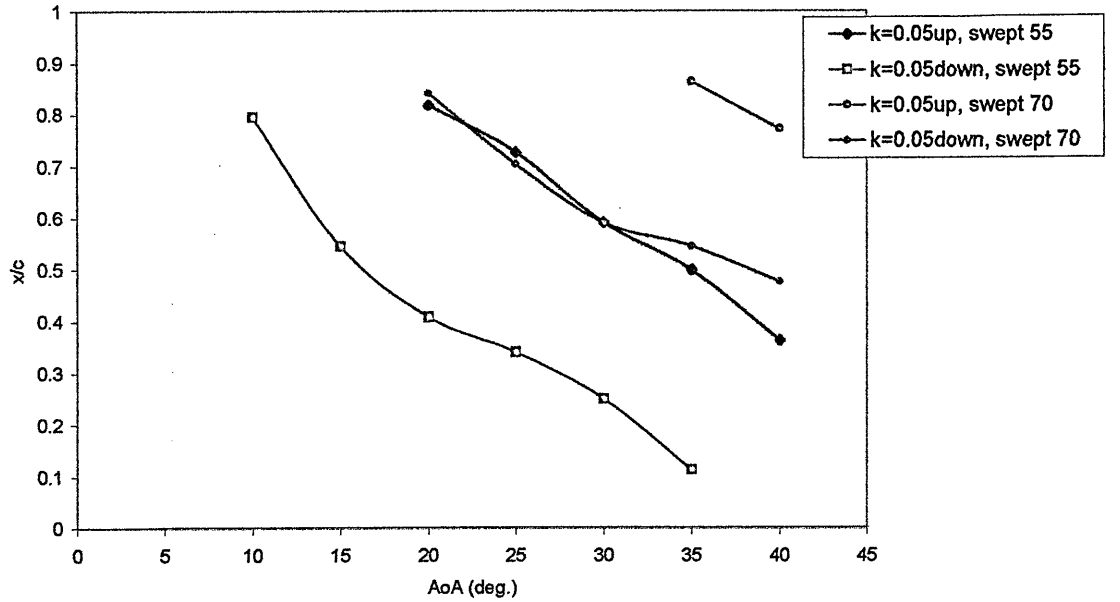

Figure 6. 46 Effect of wing sweep on the vortex breakdown position, 55 deg. And 70 deg. Swept delta, t/c = 0.018, boundary layer = 6.73 mm

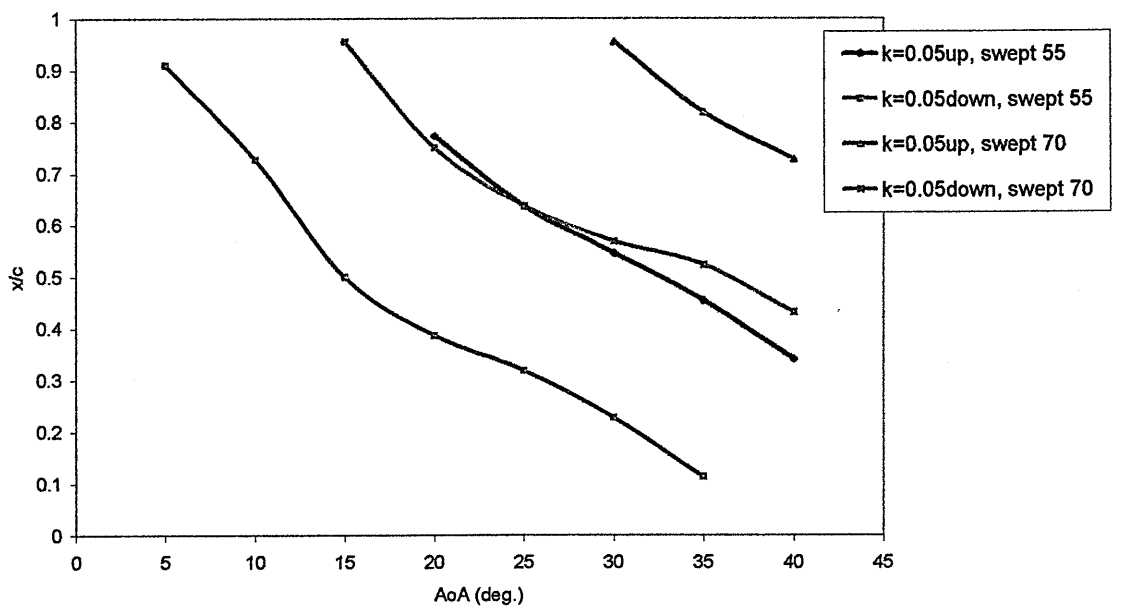

Figure 6.47 Effect of wing sweep on the vortex breakdown position, 55 deg. And 70 deg. Swept delta, t/c = 0.018, boundary layer = 8.4 mm

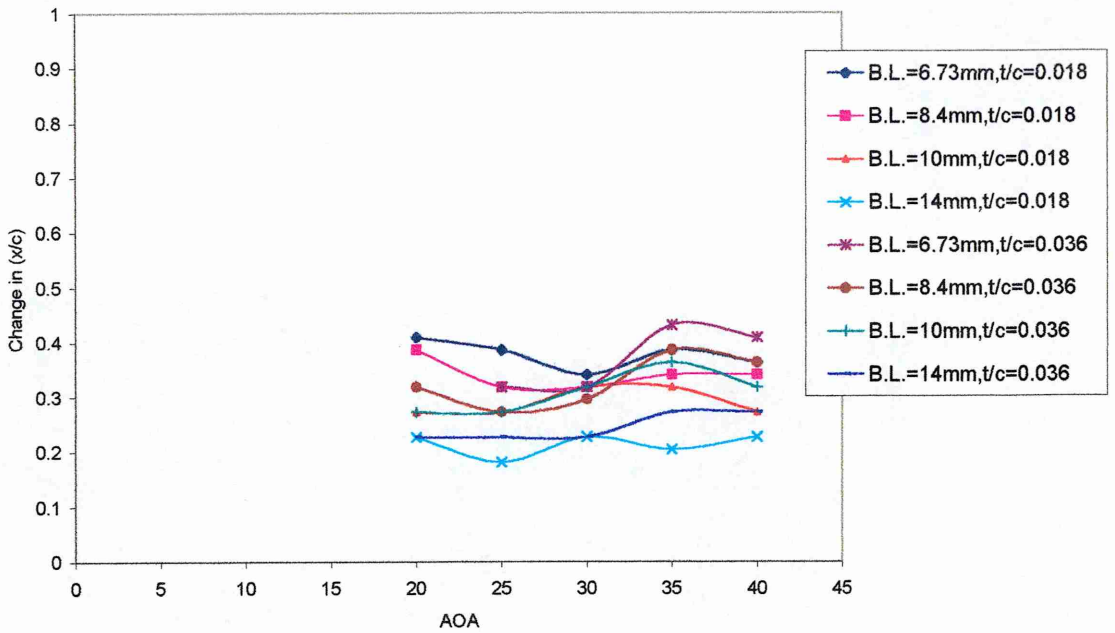

Figure 6.48 Change in (x/c) of pitch-up & down , swept delta 55 deg., for t/c=0.018 & 0.036, for all boundary layers

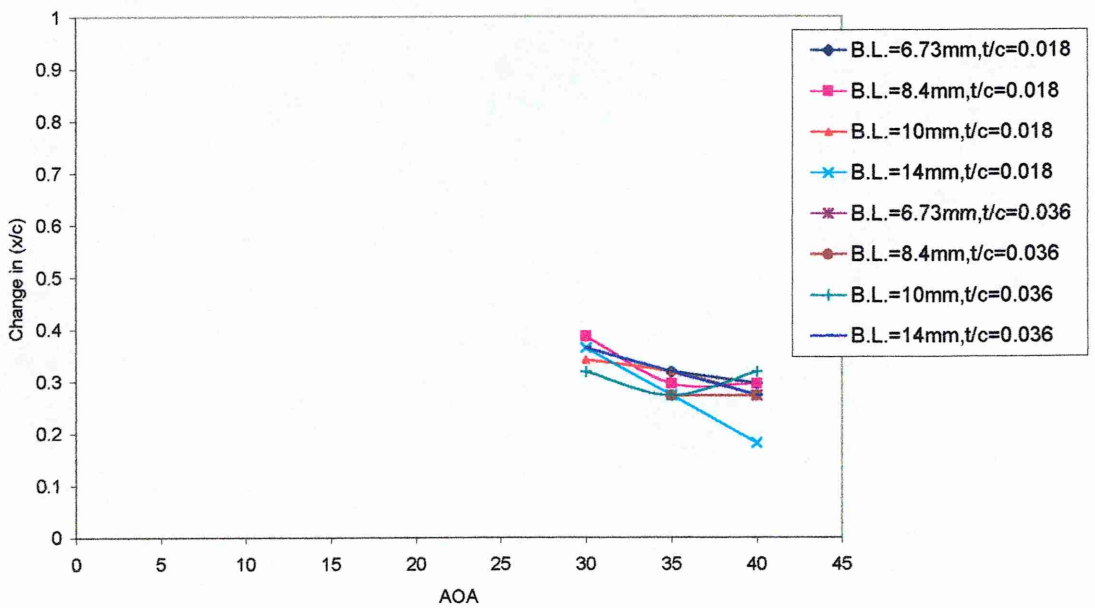

Figure 6.49 Change in (x/c) of pitch-up & down , swept delta 70 deg., for t/c=0.018 & 0.036, for all boundary layers

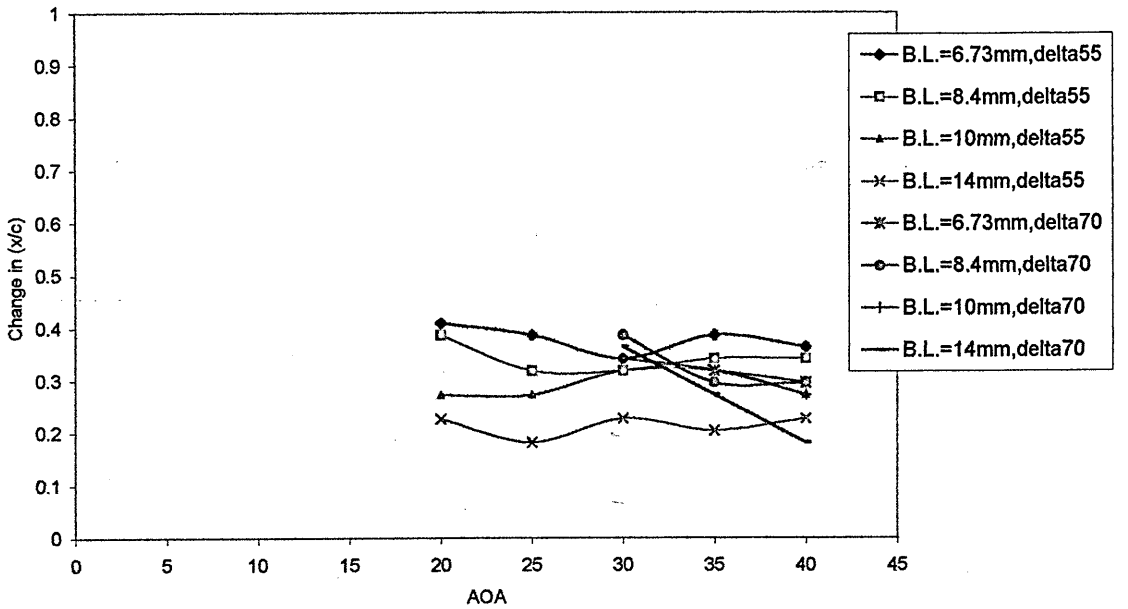

Figure 6.50 Change in (x/c) of pitch-up & down, t/c=0.018, for swept delta 55 & 70 deg., for all boundary layers

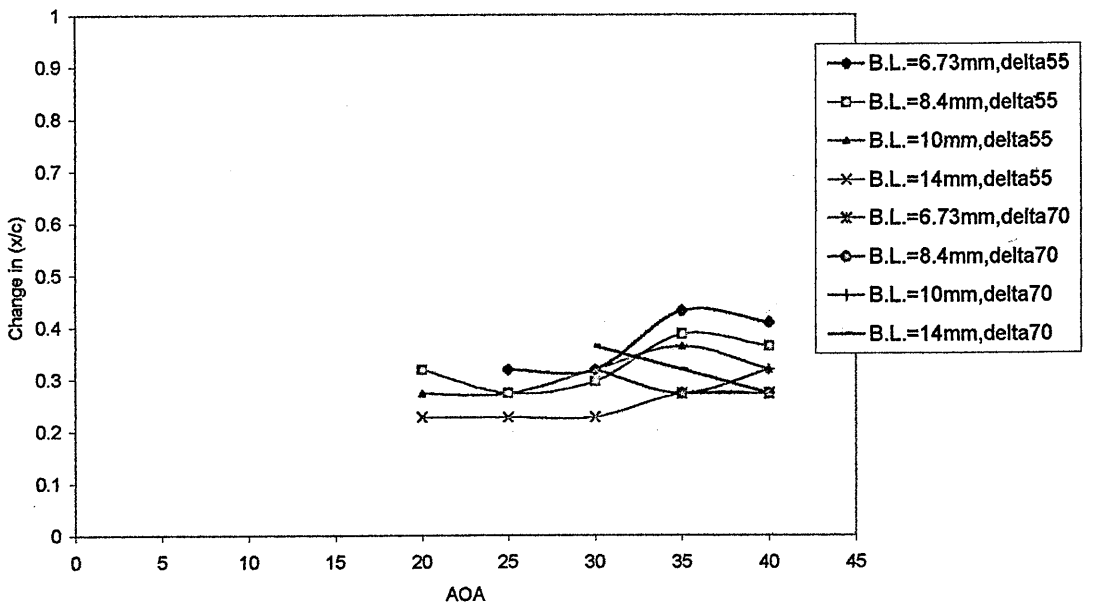

Figure 6.51 Change in (x/c) of pitch-up & down, t/c=0.036, for swept delta 55 & 70 deg., for all boundary layers

Chapter 7 The Influence of Changes in the Wind Tunnel Wall Boundary Layer on Upper Surface Static Pressure Measurements, Results and Discussion

The primary objective of the wind tunnel phase of the test programme was to obtain quantitative surface static pressure data for the upper surface of the half delta wing platform model, under the influence of a range of wall boundary layer conditions. In addition smoke flow visualisation studies were carried out to correlate vortex trajectory and vortex breakdown data with that obtained in the water tunnel.

7.1 Pitot-Tube Measurement of Wind Tunnel Wall Boundary Layer

Velocity profiles for each of the wind tunnel wall boundary layer conditions were measured 0.47m downstream from the leading-edge of the ground board, (the apex location of the half-delta wing model), using a traversing flattened pitot-probe. The various end-plate boundary layer configurations are detailed in Chapter 4.

7.2 Characteristics of the Wind Tunnel Wall Boundary Layers

The procedure used to measure the ground board boundary layer thickness is detailed in Chapter 4. Table 7.1 lists the results of all wind tunnel boundary layer configurations at the specific axial location in the working section. The boundary layer thickness (δ) was taken to be the point where $u = 0.99\ U$:

No.	Configuration	δ (mm)	δ^* (mm)
1	Baseline ground board (clean)	14	3.65
2	Grit sand 40 (at leading edge of ground board)	24	5.12
3	Grit sand 40 + 3mm rod (at leading edge of ground board)	33	6.89

Table 7.1 Wind tunnel wall boundary layer

Velocity profiles for each of the three wall boundary layer configurations are given in Figures 7.1 to 7.3. The clean ground board wall boundary layer configuration gives the thinnest boundary layer (δ = 14.0 mm). This increased to δ = 33 mm with the addition of a grit 40 sand paper and 3 mm wire.

7.3 Correlation with Established Profile

Figure 7.4 and 7.5 represent non-dimensional boundary layer velocity profiles for all three wind tunnel ground board boundary layer configurations. It is clear that all boundary layers velocity profiles suggest a turbulent ($1/7^{th}$ power law) profile in contrast to the laminar profiles seen in the water tunnel.

A theoretical estimate of the ground board boundary layer thickness can be made by assuming the expression derived by Prandtl[45] :

$$\delta = \frac{0.37\,x}{(\mathrm{Re}_x)^{1/5}} \qquad 7.1$$

Where in this case x = 0.47 m, freestream velocity = 20m/sec giving a local Reynolds number R_e = 643512 and a boundary layer thickness of δ = 12 mm. This theoretical value comes very close to the experimental result for the wind tunnel clean configuration, where δ = 14.0 mm. Boundary layer theory and measurement are detailed in Chapter 5.

7.4 Influence of the Wall Boundary Layer on the Wing Surface Static Pressure Distribution (Static case)

The variation of surface static pressure coefficient with angle of attack for each configuration tested is presented in three formats. Figures I1 to I12 show the span wise pressure distribution at various axial stations. (See Appendix I detailed all Figures of span wise and axial wise pressure distribution). Figures I13 to I24 show the corresponding chord wise distributions at different stations on the wing span. Surface static pressure contours are given in Figures 7.6 and 7.7. In each case the measurements were limited to the two extreme wall boundary layer cases, R1 representing the thinnest wall boundary layer (δ = 14 mm) and R5 representing the thickest wall boundary layer (δ = 33mm) and at angles of attack of 10°, 20° and 30°.

Surface static pressure in the form of axial or spanwise distributions at various stations is presented in order to highlight specific features of the flow influenced by the changes in the wall boundary layer thickness. Presentation of the data is in terms of a non-dimensional axial location, (x/c) and spanwise location, (y/s), (y/s represent the spanwise location with respect to local semi-span and y/c represent spanwise location with respect to local chord wise). Note that surface pressure tappings were not distributed uniformly over the area of the model of interest.

7.4.1 Spanwise Pressure Distribution

General characteristics of the spanwise pressure distribution are studied by comparing Figures I1 and I2 at 10° AoA, Figures I3 and I4 at 20° AoA and Figures I5 and I6 at 30° AoA. At 10° AoA, the data show very little difference in spanwise pressure distribution when the wall boundary layer thickness is increased. (It is important to note that the location of the pressure tapping on the upper surface of the wing model are not uniformly spaced. As a result the actual minimum pressure may not be measured and through out the minimum measured pressure is referred to as the suction peak).

Above 10° angle of attack, (Figure I3 and I4), a minimum pressure is evident in the pressure profile, due to the presence of the leading-edge vortex over the surface of the wing. Although the vortex core is located some distance above the wing, its position can be detected at the surface by this minimum pressure peak. The vortex moves inboard with increasing angle of attack, see Lowson[12] and Roos et al[105], from Figures I3 and I4 it can be seen that at 20° angle of attack the suction peak is located at 85 % (y/s) and by 30°, Figure I5 and I6, it has moved to approximately 69 % (y/s).

Comparing Figures I3 and I4, which depict the spanwise Cp distribution at 20° angle of attack for the smallest and largest wall boundary layers respectively, the minimum surface static pressure coefficient at x/c = 0.3 is –3.7 for the thin boundary layer and this increases to –3.0 as the boundary layer thickness is increased. At 30° AoA ,(Figure I5 and I6), this increase in the minimum Cp is more apparent; -4.0 for the thin wall boundary layer and –2.8 for the thickest case.

It can be seen that the magnitude of peak suction pressure is influenced by wall boundary layer thickness at 20° and 30° angle of attack. The main effect in this angle of attack range appears to be a decrease in inboard pressure as a result of decreasing boundary layer thickness this is particularly evident at 30° angle of attack.

Traub and Rediniotis[139] showed from the spanwise pressure distribution over a 60° delta wing model, (with spanwise tappings located at 60% of the root chord, as a fraction of the local semispan (y/s)), that at 30° angle of attack, the effect of vortex breakdown is seen to be one of increasing the width of the suction peak.

In order to analyse the influence of changes in wall boundary layer thickness the difference in pressure coefficient between the thickest boundary layer (R5) and the thinnest (R1) is presented in terms of spanwise location on the wing for angles of attack of 10°, 20° and 30°, see Figures 7.8 to 7.10. It can be seen that the change in pressure between the thinnest boundary layer configuration (R1) and the thickest (R5) is clear even at the very low angle of attack .

A general impression from Figure 7.8 to 7.10 is that the influence of the wall boundary layer is predominantly outboard of (y/s) = 0.40, and greatest at the higher AoA. This is to be expected inview of the location of the vortex core.

7.4.2 Axial Pressure Distribution

General characteristics of the axial pressure distribution are studied by comparing Figures I13 and I14 at 10° AoA, Figures I15 and I16 at 20° AoA and Figures I17 and I18 at 30° AoA. At low AoA, the data show very little difference in axial pressure distribution when the wall boundary layer thickness is increased. As the angle of attack increased from 20° to 30°, Figures I15 to I18, an increase in boundary layer thickness resulted in the minimum pressure coefficient (Cp_{min}) reaching -2.8 for the minimum wall boundary layer thickness (R1) compared with –2.5 for the maximum wall boundary layer thickness (R5) at y/c = 0.0571.

When the data is plotted in a different way to see the change in the axial pressure distribution between the minimum and the maximum wall boundary layer thickness, Figures 7.11 to 7.13, it can be seen that increasing the wall boundary layer thickness has very little influence on the axial Cp distribution at 10° angle of attack. As the angle of attack increases, there is a general tendency for an increase in wall boundary layer thickness to increase the static pressure particularly near the suction peak and at locations up to mid semi-span.

Figure 7.6, wall boundary layer thickness of R1 (δ = 14mm) and R5 (δ = 33mm) and Figure 7.7, the third wall boundary layer thickness of R3 (δ = 24mm), represent surface static pressure contour plot (x/c vs. y/c). The contours are generated from the surface pressure tapping map by triangular interpolation between three adjacent data points. This is achieved with the Delaunay software suit within MATLAB[201], found to be the most accurate method for producing contours from a non-rectangular grid of measurements.

The contours clearly show that, as the angle of attack is increased, the peak suction pressure increases, this confirms the previously discussed data but in this case the movement of the peak suction pressure in particular is clearly seen in moving upstream to the wing apex.

The reduction in peak suction pressure is clearly seen in the 20° and 30° angle of attack data, as the boundary layer thickness is increased. The influence of a change in boundary layer thickness is seen to be progressive as depicted in the contour data for the three boundary layer cases tested (R1, R3 and R5), which represent wall boundary layers of δ = 14mm, 24mm and 33mm respectively. Figure 7.14 represents the change in pressure coefficient between the thinnest and the thickest wall boundary layers, normalised and presented as a colour contour map. It confirms what can be seen from Figures 7.11 to 7.13 where, as the angle of attack increases, an increase in wall boundary layer thickness tends to increase the static pressure particularly near the suction peak and at locations up to mid semi-span.

The surface static pressure coefficient contours, (Figure 7.6 and 7.7) and the change in axial pressure distribution Figures 7.11 to 7.13, show that an increase in wall boundary layer thickness results in an increase of the pressure gradients on the upper surface of the wing model. At approximately 45 % chord location, the effect of the boundary layer thickness becomes much smaller. Where for the thickest boundary layer (R5), the region of minimum pressure, or suction, is narrower or has a reduced value of minimum pressure compared to the thinnest boundary layer (R1) for various angles of attack. Downstream of the 45 % chord wise location, no effect is notable on the axial pressure distribution. The following section 7.5 analysis the influence of wall boundary layer thickness on surface static pressure.

7.5 Analysis of Wall Boundary Layer Influence on Surface Static Pressure

An increase in wall boundary layer thickness is assumed to influence the size and strength of the horseshoe vortex, as explained earlier in section 6.6. This increase in horseshoe vortex size is assumed to influence the position of vortex breakdown on the upper surface of the half delta wing model. As the horseshoe vortex increases in size and interacts with the leading edge vortex of the half delta wing, the surface static pressure of the wing model is affected. The surface static pressure, Figures I1 to I6 and Figures I12 to I18 for both the axial and spanwise distribution respectively all show an increase in surface static pressure as the wall boundary layer thickness increased. Also Figures 7.6 and 7.7 which represent the surface static pressure contour plots show an increase in surface static pressure as the wall boundary layer thickness increased.

This increase in surface static pressure is assumed to be due to an increase in the size of the horseshoe vortex as the wall boundary layer thickness is increased, see Barber[192]. Because of the interaction between the horseshoe vortex and the half delta wing leading edge vortex, this may result in a reduction in strength of the wing vortex since they are counterrotating. This loss of strength appears in the surface static pressure data as a decrease in the pressure suction peak. Therefore, the thickness of the wall boundary layer will determine the nature of the downstream flow field.

7.6 Influence of Wall Boundary Layer on Dynamic Behaviour

During a dynamic pitch change, high angle of attack delta wing aerodynamics involves hysteric behaviour both in the leading-edge vortex position and in the force and moment coefficients. Hysteric behaviour in the position of vortex breakdown and the vortex core, has been noted by a wide range of researchers, including Gad-el-Hak et.al.[23] and Rockwell[148]. Gad-el-Hak found that for a 45° delta wing oscillating from 10° to 20° angle of attack, there was a hysteresis in the vortex core position between pitch-up and the pitch-down. As a result, in the current series of experiments, the surface static pressure on a pitching delta wing is studied and analysed in order to understand the effect of the splitter plate wall boundary layer on dynamic and hysteresis behaviour.

7.6.1 Effect of Reduced Pitch Rate

The reduced pitch rates used in this test were k = 0.00111 (slow motion) and k = 0.00628 (fast motion), as has already been discussed (see section 4.7). Telionis[22] experimented with a fast reduced pitch rate of k = 0.0089 for a 70° sweep delta wing model and confirmed an evidence of hysteresis in the development of the flow and the pressure distributions beneath the core of the vortex show that vortex burst moves forward as incidence increases.

Figures 7.15 to 7.20 represent the surface static pressure contours in the dynamic case, both for pitch-up (0° to 40°) and pitch-down (40° to 0°). The angles of attack selected for presentation are 10°, 20° and 30° each at three wall boundary layer thicknesses (R1, R2 and R5). As explained in section (7.4), only the surface area covered by static pressure tapings, a non-uniform (x/c) vs. (y/c), grid is presented.

Figure 7.15 gives data for the 'slow' reduced pitch rate (k = 0.00111) case ranging from pitch-up angle of attack of 10°, 20° and 30° to a pitch-down of 30°, 20° and 10°. It can be seen that, at the low angle of attack, (10°), the pressure is approximately constant over the model surface. As the angle of attack increases the pressure near the leading edge begins decreasing, and at an angle of attack 30°, indicates a high suction peak pressure. Notice that the pressures follow the model motion; the maximum and minimum Cp. values occur very near the minimum and maximum angles of attack, respectively.

The location of the suction peak as the angle of attack is increased, varies from approximately 30 % (x/c) moving toward the model apex. During pitch-down it starts from the apex and moves rearward to the 30 % (x/c) chord location. Over this angle of attack range the surface static pressure contour plots exhibit a clear difference between pitch-up and pitch-down.

Figures 7.18 gives data for pitch-up and pitch-down over the same angle of attack range but for a 'fast' reduced pitch rate (k = 0.00628). As the angle of attack is increased, the pressure decreases, with lower pressures occurring forward on the wing. Unlike the reduced pitch rate data from Figure 7.15, the minimum pressures do not correspond to the maximum angle of attack. In Figure 7.18 at 30° angle of attack, pitch-down, the suction peak is well developed at the leading-edge, but it shows that it has a smaller suction peak than the pitch-up case at the same angle of attack. Compare this with Figure 7.15 of a slow pitch rate and the difference is assumed to be due to the vortex burst lag which arises as a result of flow reattachment during pitch-down.

The reason for this suction peak is a result of the reformation of leading-edge vortices over the surface of the wing. The highest suction peak occurs near 30° angle of attack during the pitch-up. After this angle, the pressure collapses as the flow over the wing becomes fully separated at 40° angle of attack. At approximately 30°, pitch-down, the pressure begins decreasing and the suction peak is formed. This indicates that the flow is no longer separated, and the leading-edge vortices have reformed over the wing. As the wing continues pitching down to approximately 20°, the breakdown moves toward the trailing-edge and eventually off the wing.

7.6.2 Influence of the Wall Boundary layer during Dynamic Pitch Changes

The pressure contour plots, Figures 7.15 to 7.20, depict the effect of the ground board wall boundary layer thickness during dynamic pitch changes. Three wall boundary layers configurations were tested (R1, R3 and R5), corresponding to a thickness of: 14mm, 24mm and 33mm respectively. In the case of the dynamic test, (pitch-up and pitch-down), each boundary layer been tested for two different reduced pitch rates. The effect of changes in the wall boundary layer thickness is evident in the dynamic case, as discussed in section 7.4. At higher angle of attack, the effect of wall boundary layer thickness in the dynamic case is very obvious, (see Figure 7.22). At 30° angle of attack, from Figure 7.15 to 7.20, during pitch-down, the data show an influence of the wall boundary layer on the model upper surface pressure, which are higher than both the pitch-up and the static case.

Figure 7.21 shows the location of the peak suction pressure plot during static testing for all wall boundary layer thicknesses at 20° and 30° AoA taken from pressure contour plots. In this static case, the location of the suction peak is a function of angle of attack.

This is also true for the dynamic case, see Figure 7.22. However , hysteric behaviour was seen in the suction peak location. Figures 7.15 to 7.20 show both the pitch-up and the pitch-down pressure contours for both reduced pitch rates k = 0.00111 and 0.00628. The location of the suction peak pressure, during pitch-up at 30° AoA, Figure 7.15, appears to be near x/c=0.45 , y/c=0.225. however, the location of the suction peak during, pitch-down, from the same figure, shows it to be approximately at x/c=0.35 , y/c=0.15. The suction peak surface pressure moves upstream toward the apex and inward as the model is pitched-up and downstream and outward as the model is pitched-down. The location of the suction peak from the static case , Figure 7.6, is approximately at x/c=0.4, y/c=0.2.

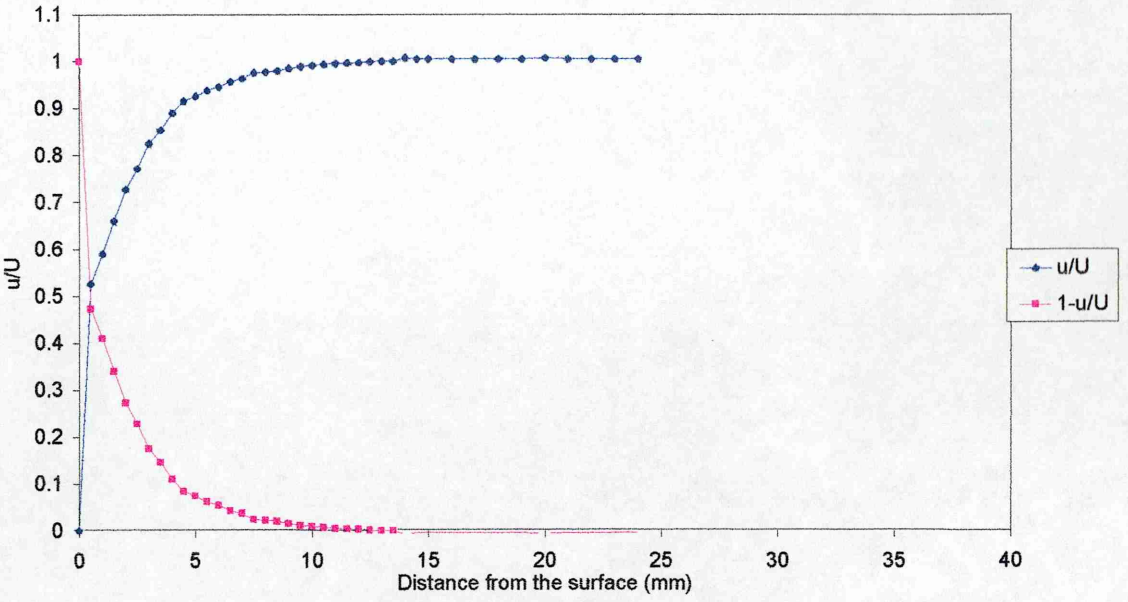

Figure 7.1 Ground board boundary layer velocity profile for clean configuration, (R1), δ.=14 mm, δ*=3.65mm

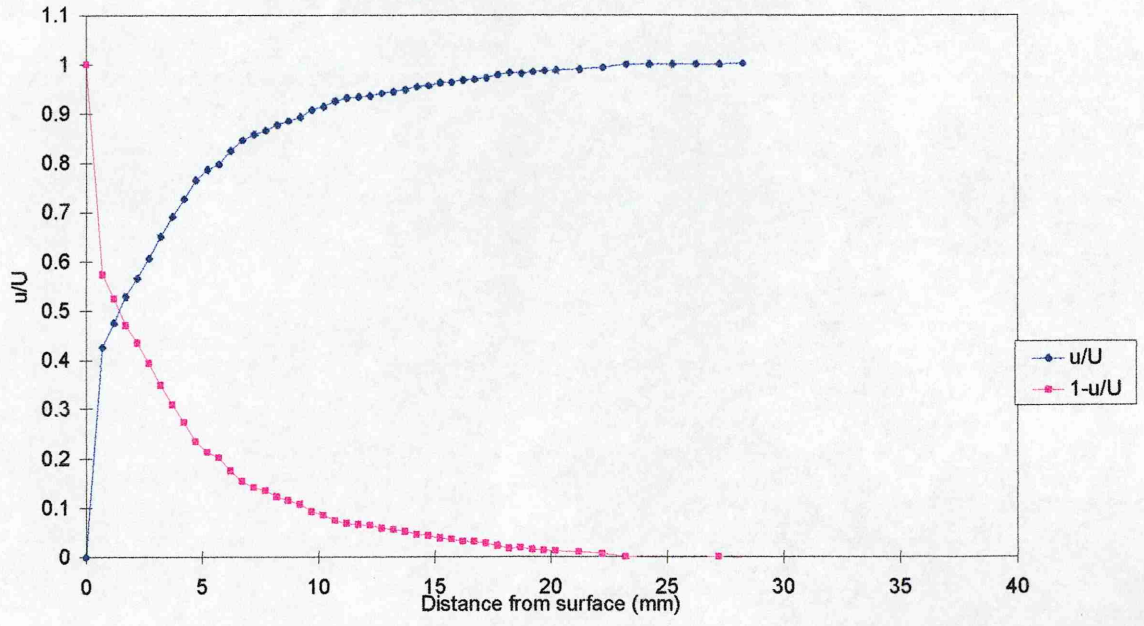

Figure 7.2 Ground board velocity profile with grit=40 ,(R3), δ.=24mm, δ*=5.12mm

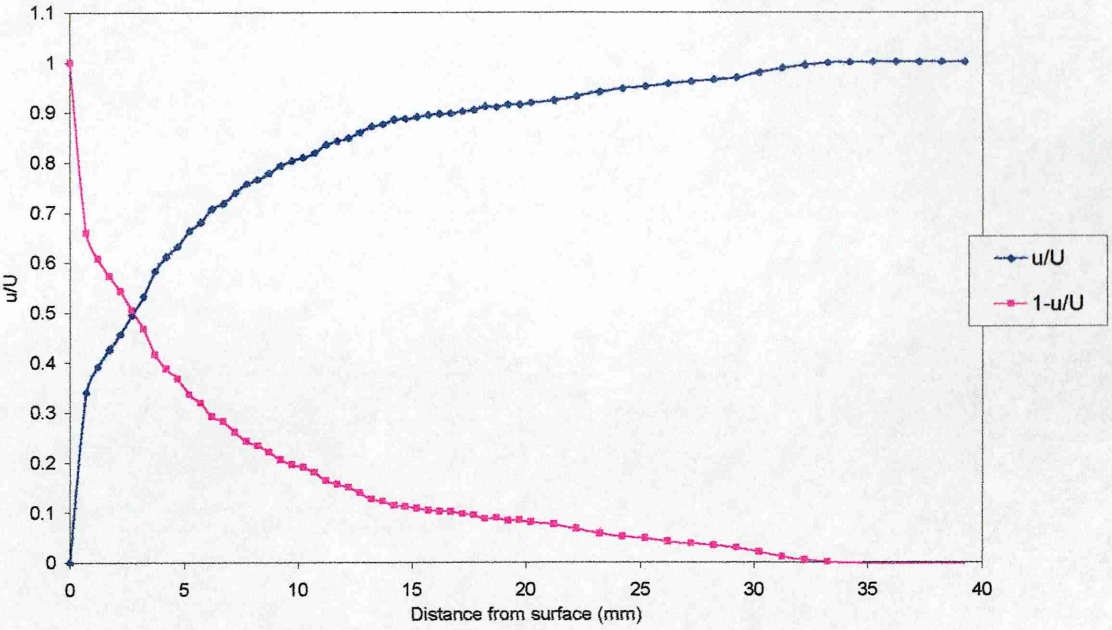

Figure 7.3 Ground board velocity profile with grit=40+3mm wire (R5) δ.=33mm, δ*=6.89mm

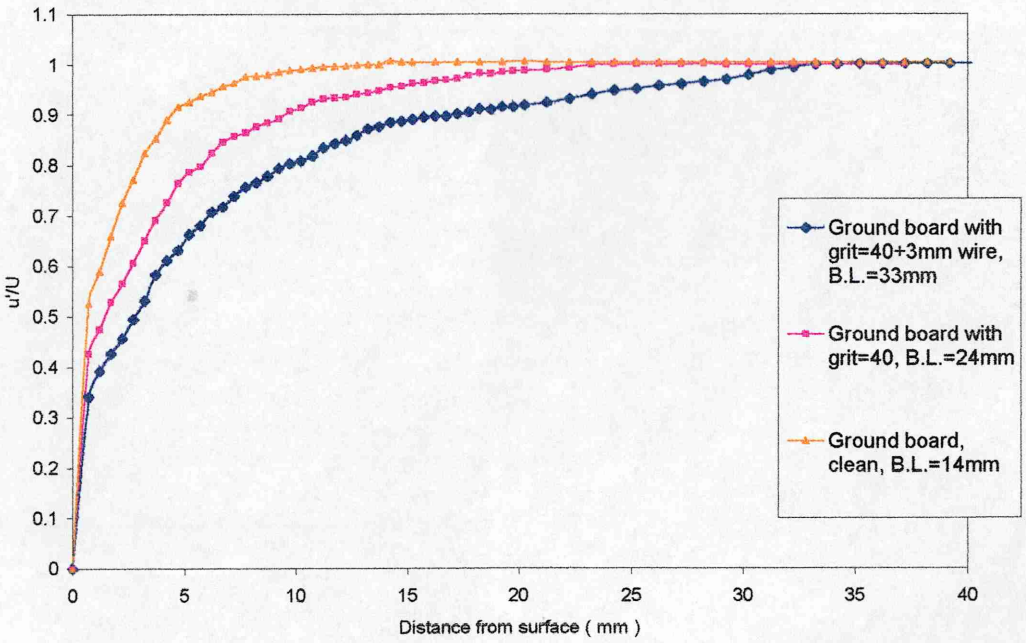

Figure 7.4 Comparison of wind tunnel ground board velocity profile of all boundary layers configurations

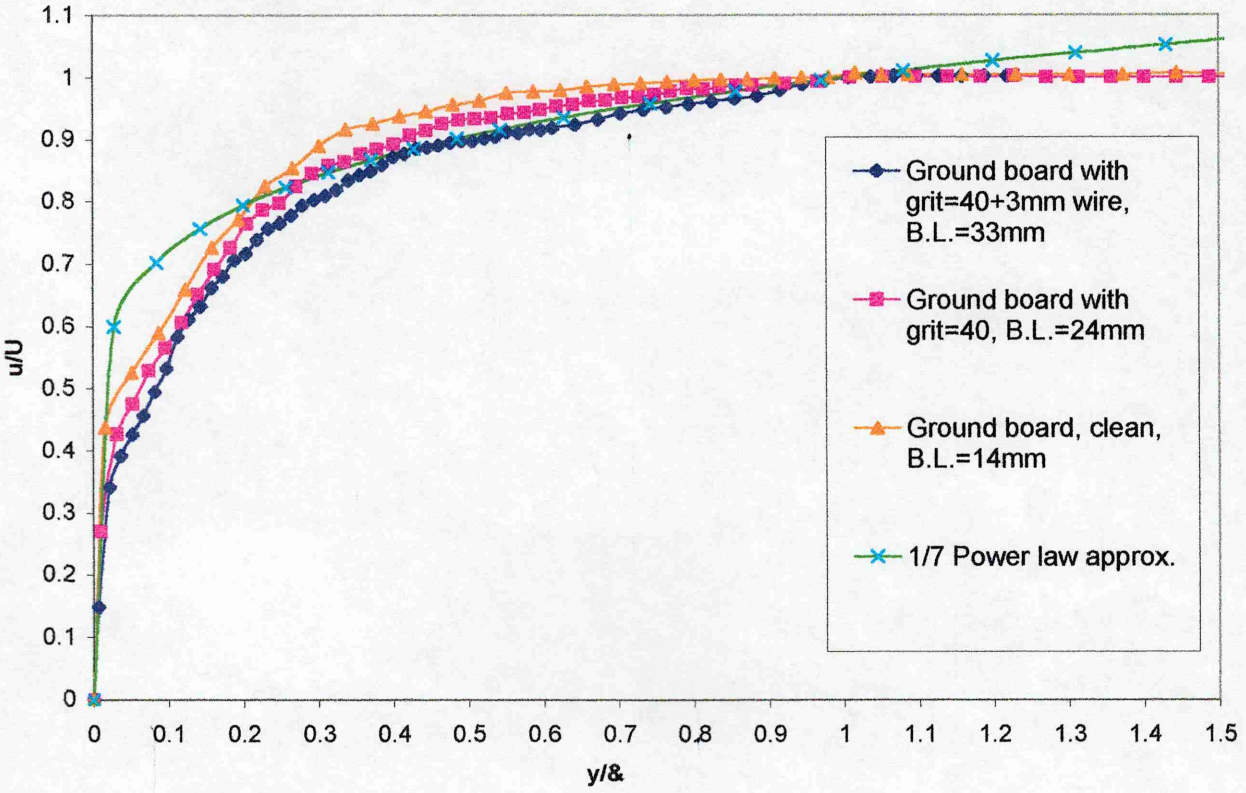

Figure 7.5 Comparison of wind tunnel ground board velocity profile of all boundary layers configurations with 1/7 power law approximation

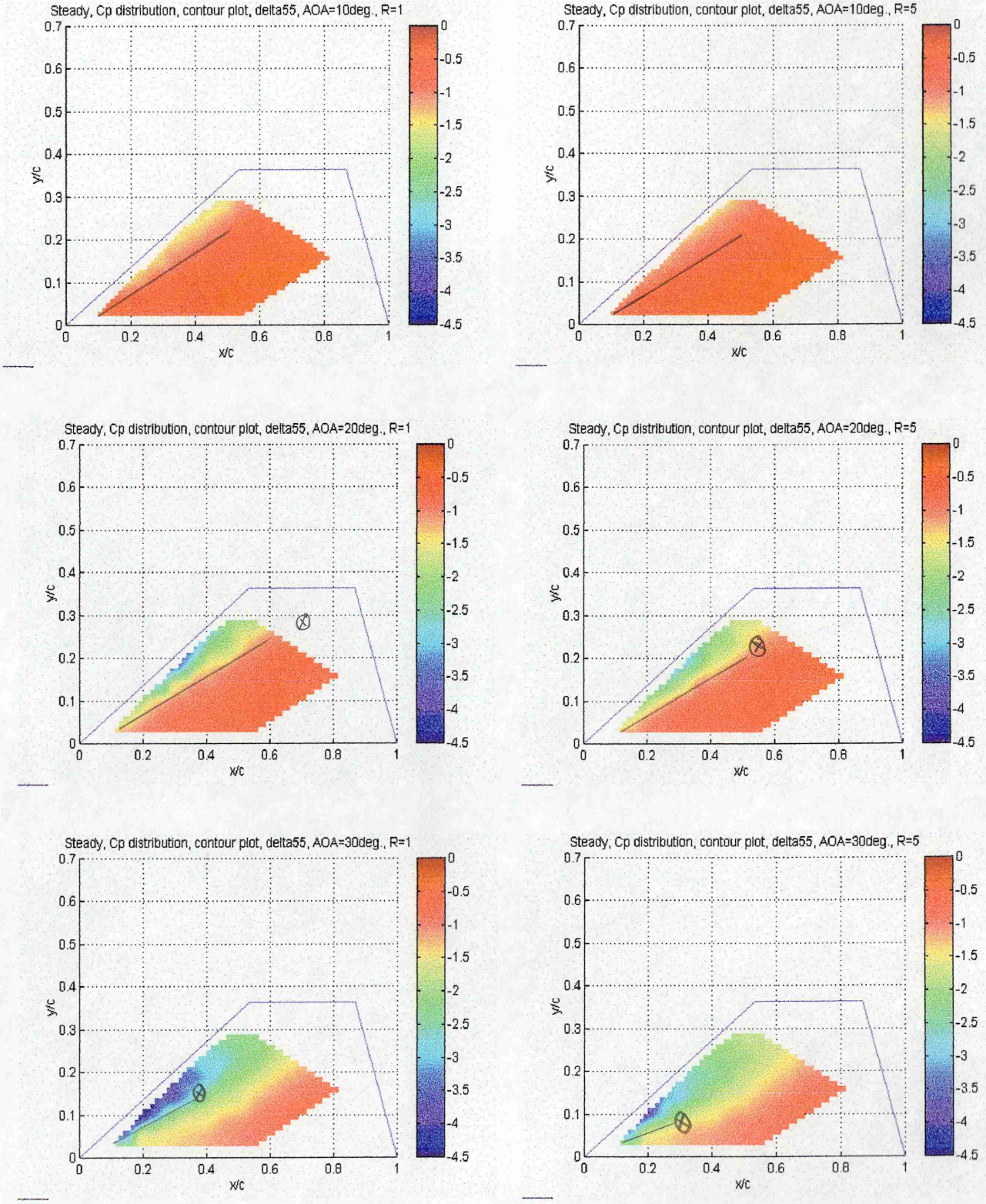

Figure 7.6 Surface static pressure coefficient (cp) distribution for 55° sweep delt with (t/c)=0.018. Wall boundary layer condition R1 ans R5 correspond to δ=14mm and 33mm respectively. The solid line corresponds to the vortex core trajectory taken from the corresponding water tunnel from visualisation studies at Re=17,000 , ⊗ signifies vortex burst

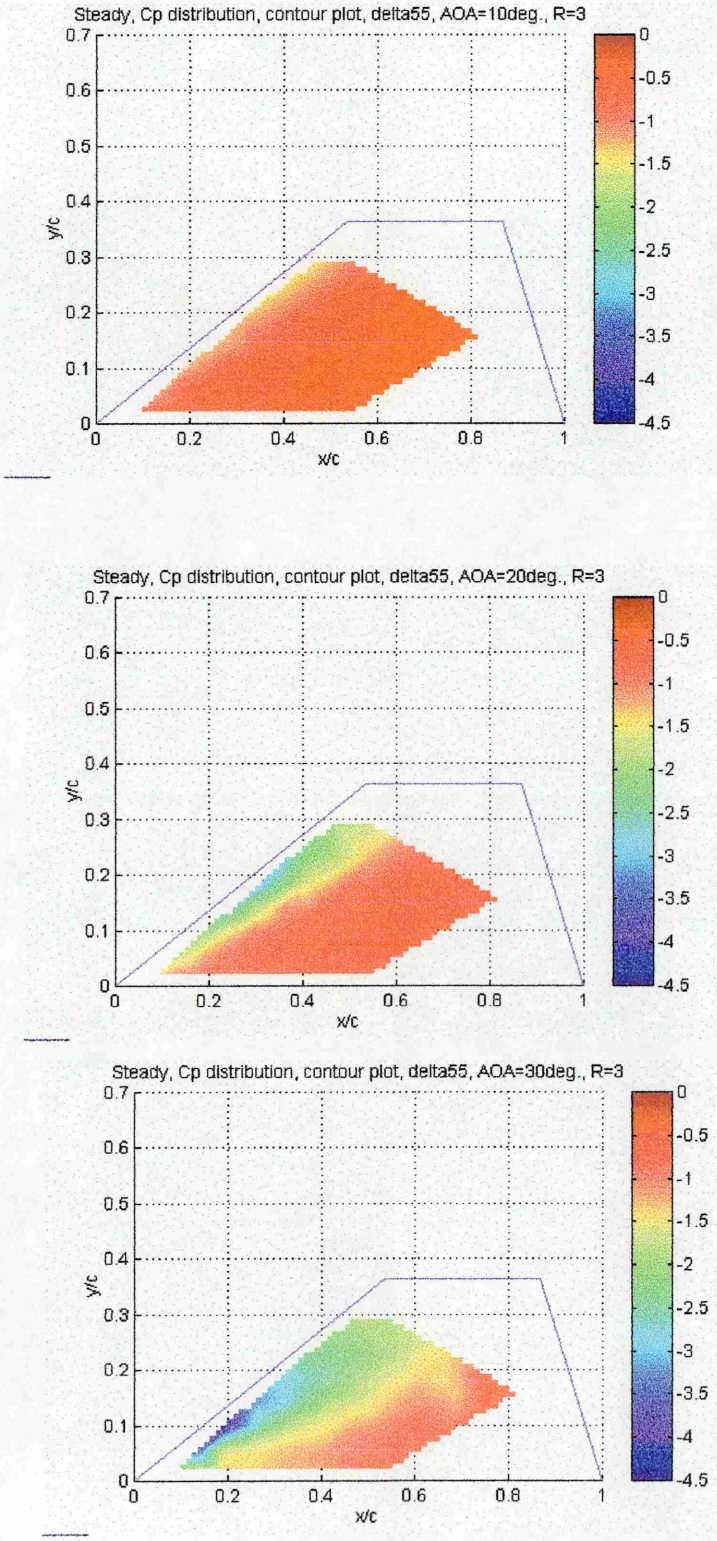

Figure 7.7 Cp distribution, Static, Delta 55° sweep, t/c=0.018, B.L.=24mm

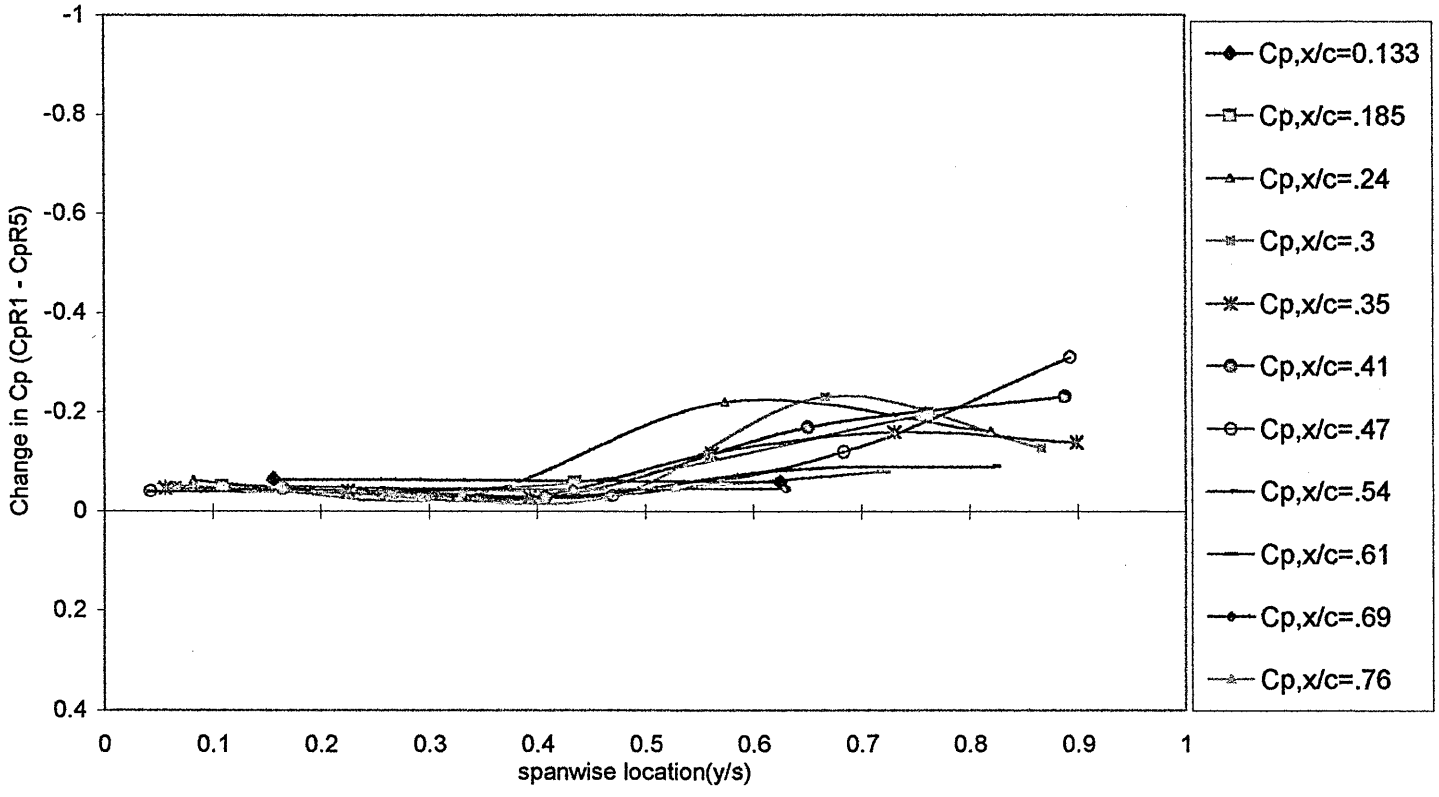

Figure 7.8 Change in spanwise Cp distribution vs. local y/s, Delta55, AOA=10deg., for boundary layers R1 &R5

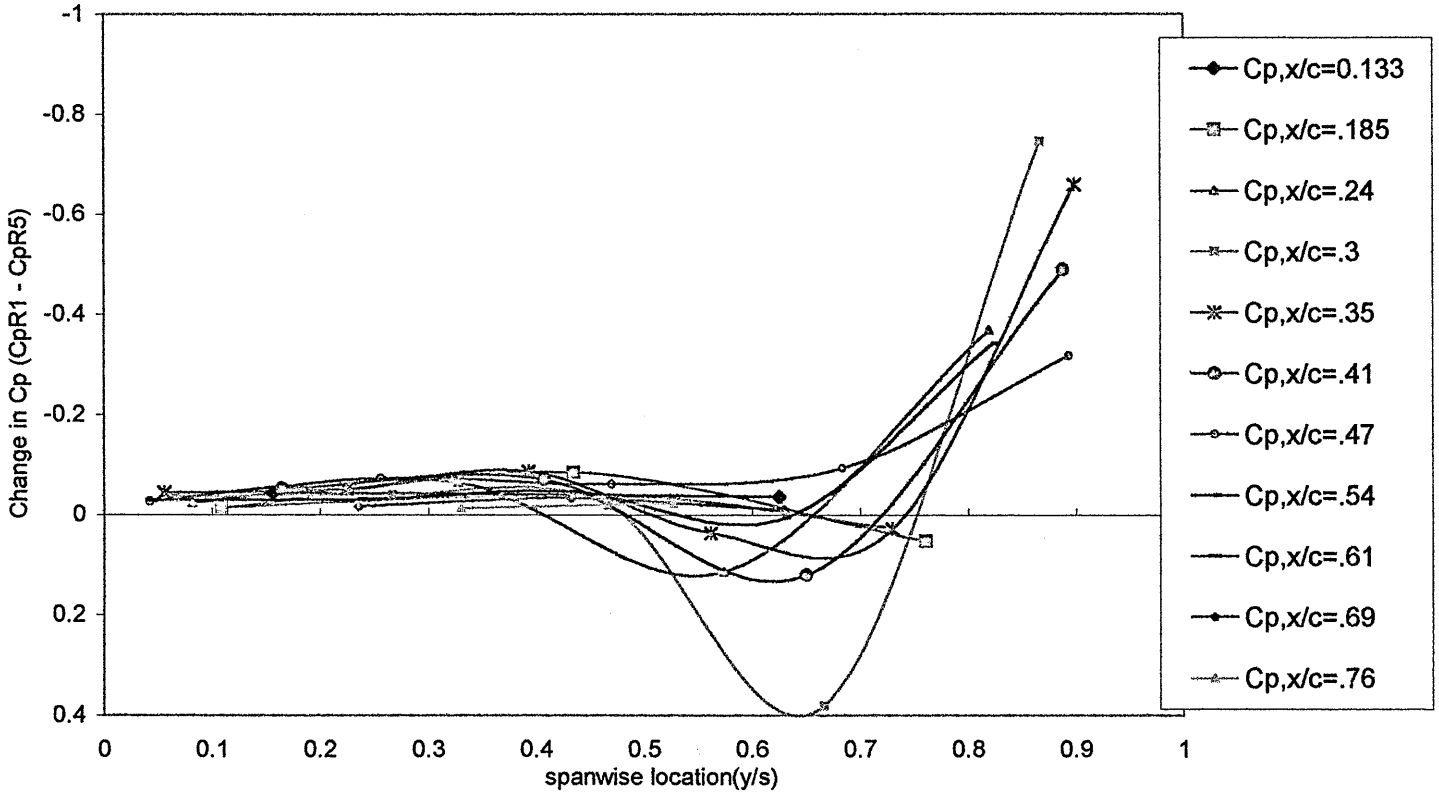

Figure 7.9 Change in spanwise Cp distribution vs. local y/s, Delta55, AOA=20deg., for boundary layers R1 &R5

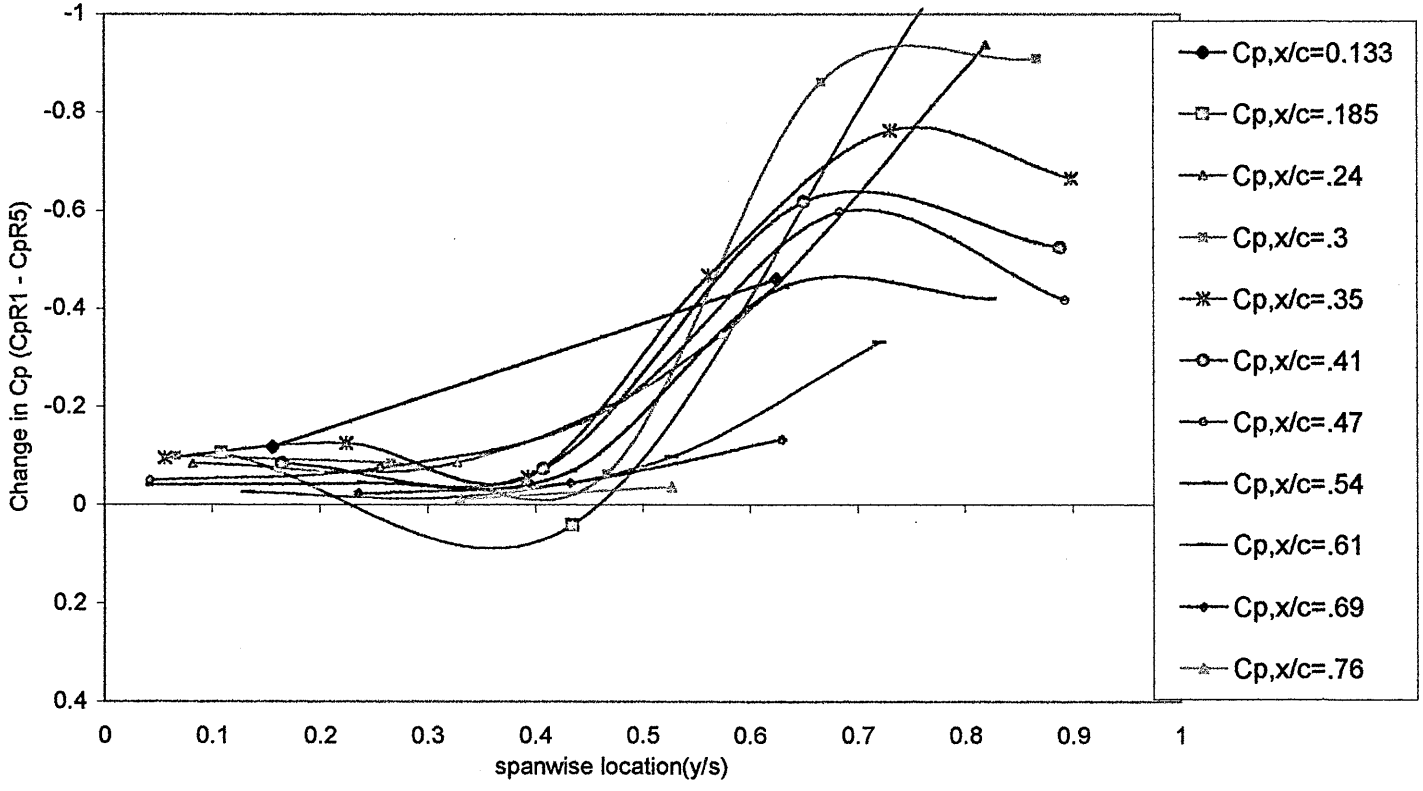

Figure 7.10 Change in spanwise Cp distribution vs. local y/s, Delta55, AOA=30deg., for boundary layers R1 &R5

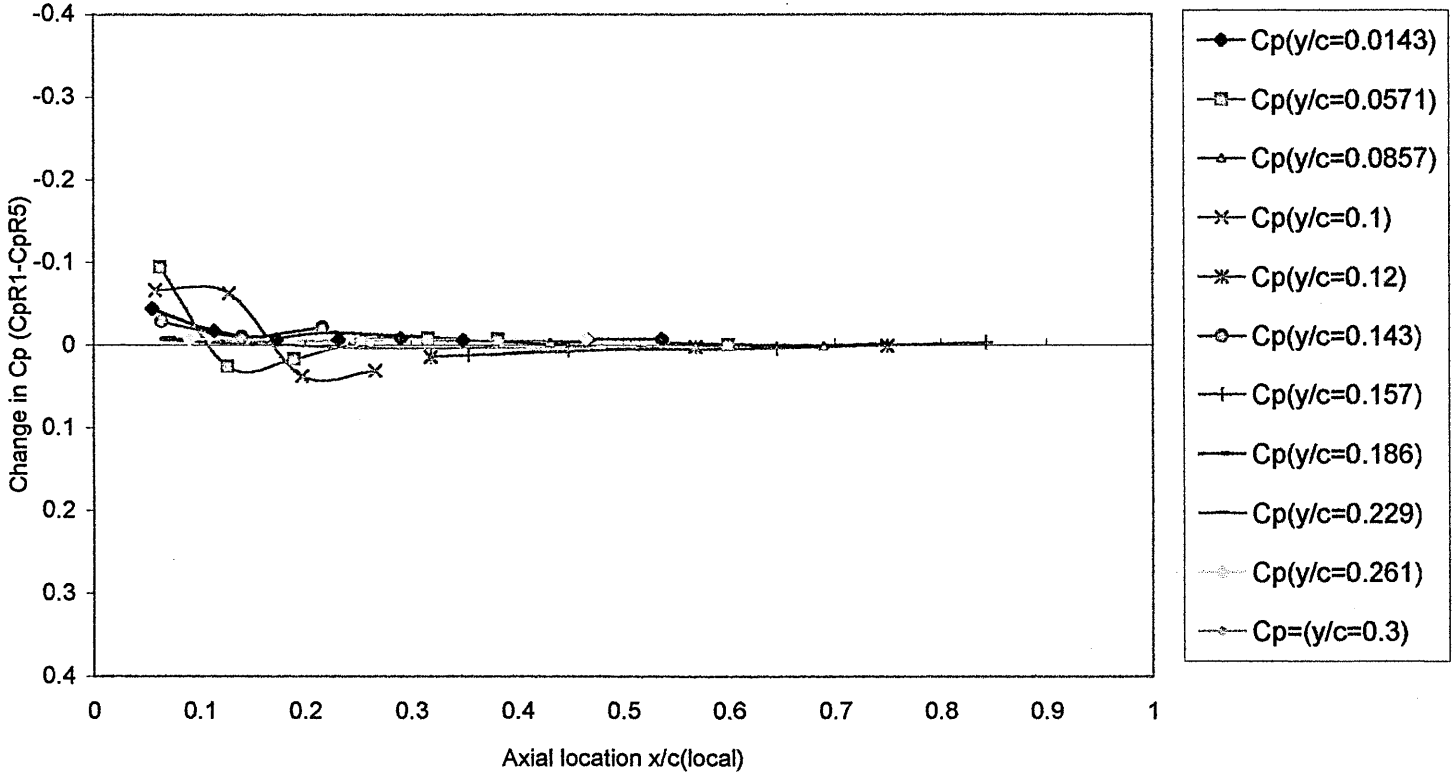

Figure 7.11 Change in axial Cp distribution vs. local y/s, Delta55, AOA=10deg., for boundary layers R1 &R5

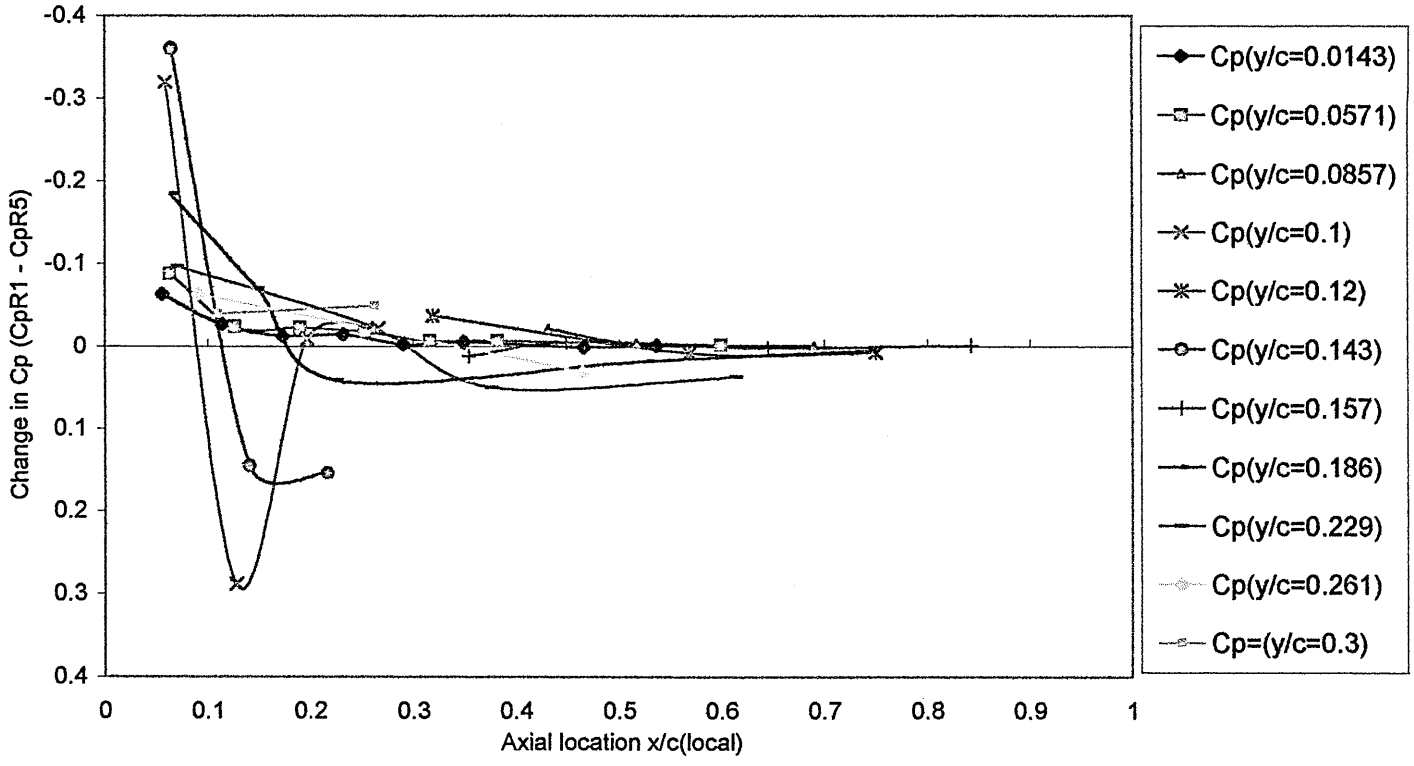

Figure 7.12 Change in axial Cp distribution vs. local y/s, Delta55, AOA=20deg., for boundary layers R1 &R5

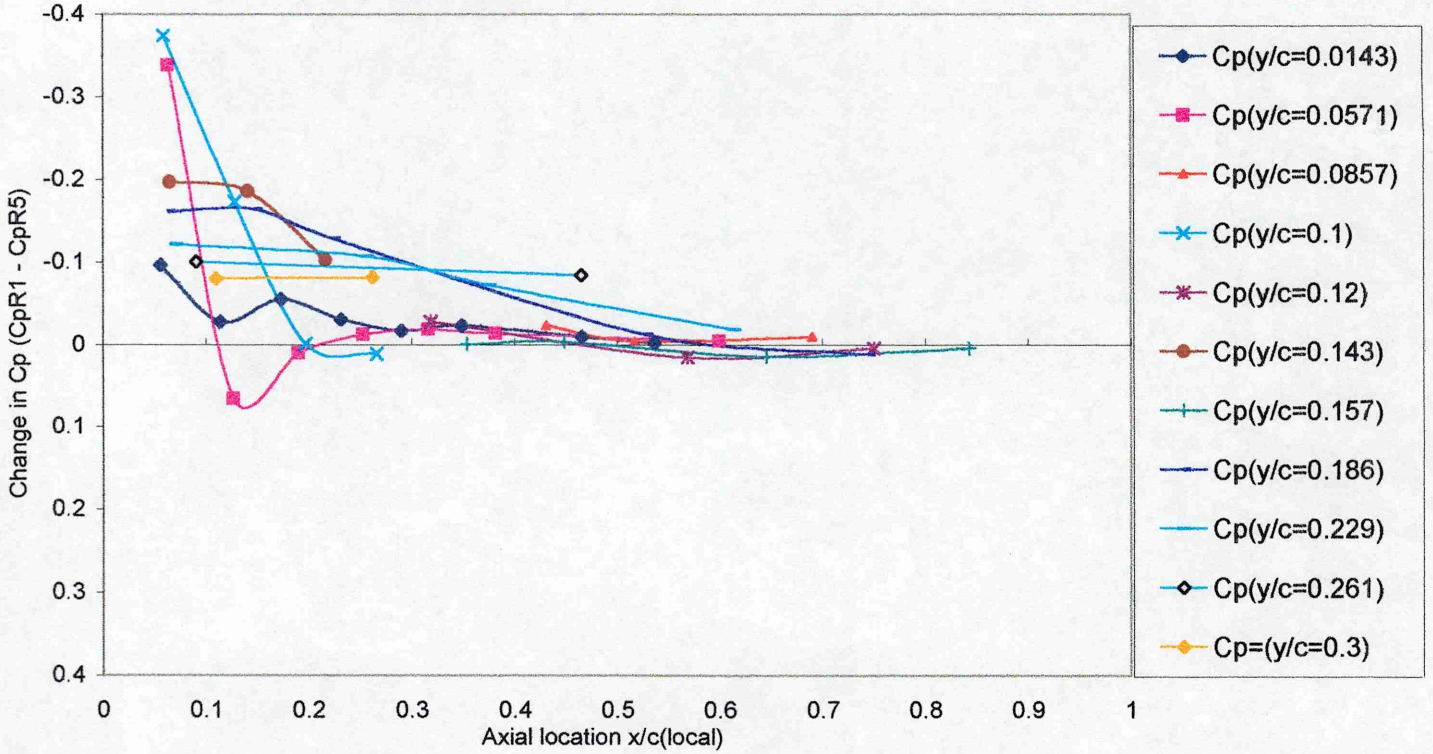

Figure 7.13 Change in axial Cp distribution vs. local y/s, Delta55, AOA=30deg., for boundary layers R1 &R5

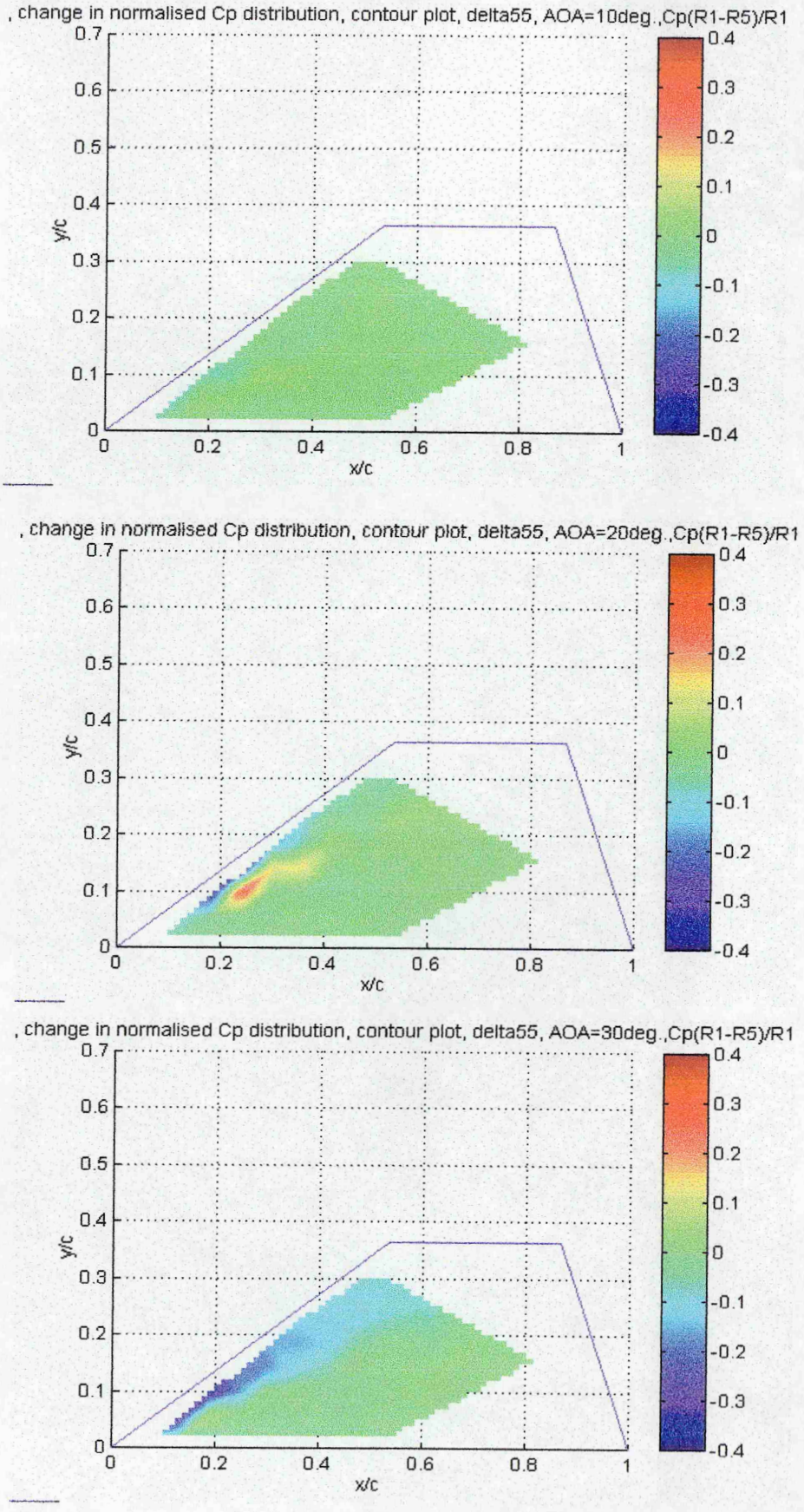

Figure 7.14 Change in normalised Cp distribution, Cp(R1-R5)/R1, Delta 55° sweep, t/c=0.018, AoA=10°, 20° and 30°

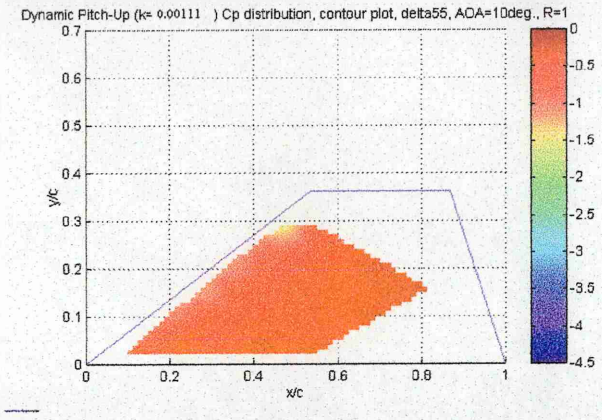

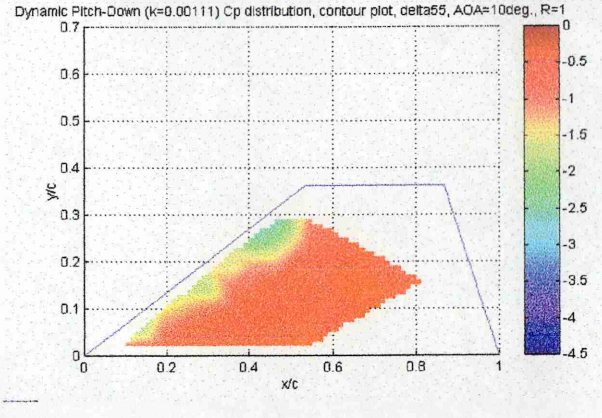

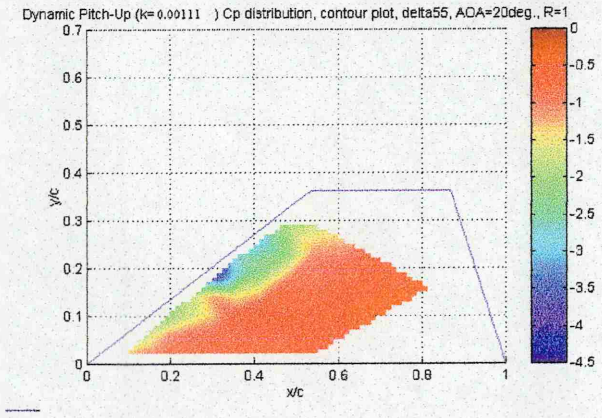

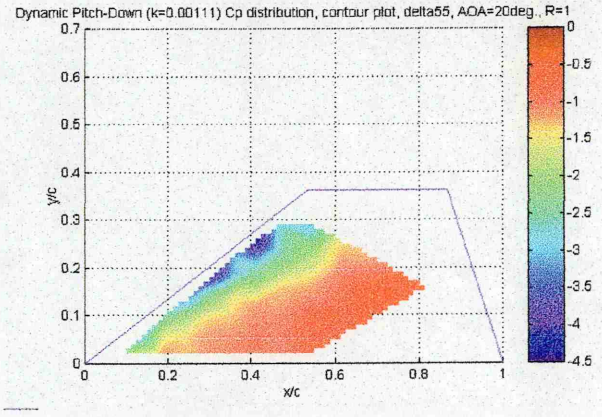

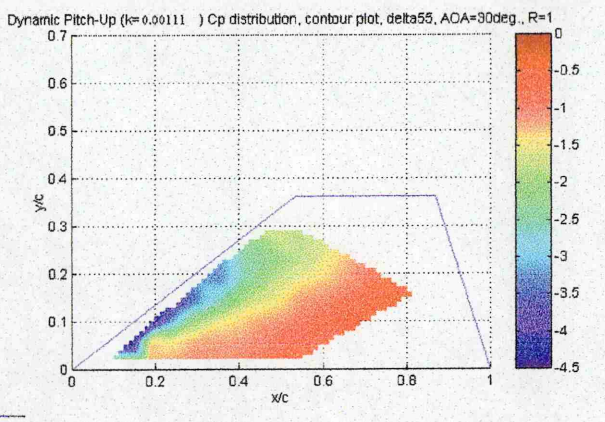

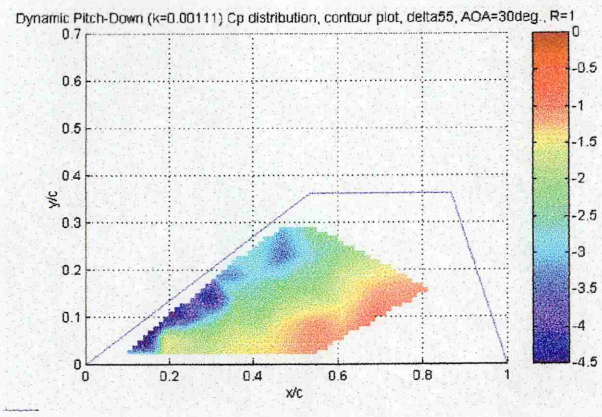

Figure 7.15 Cp distribution, Dynamic (pitch-up & down), k = 0.00111, Delta 55° sweep, t/c=0.018, B.L.=14mm

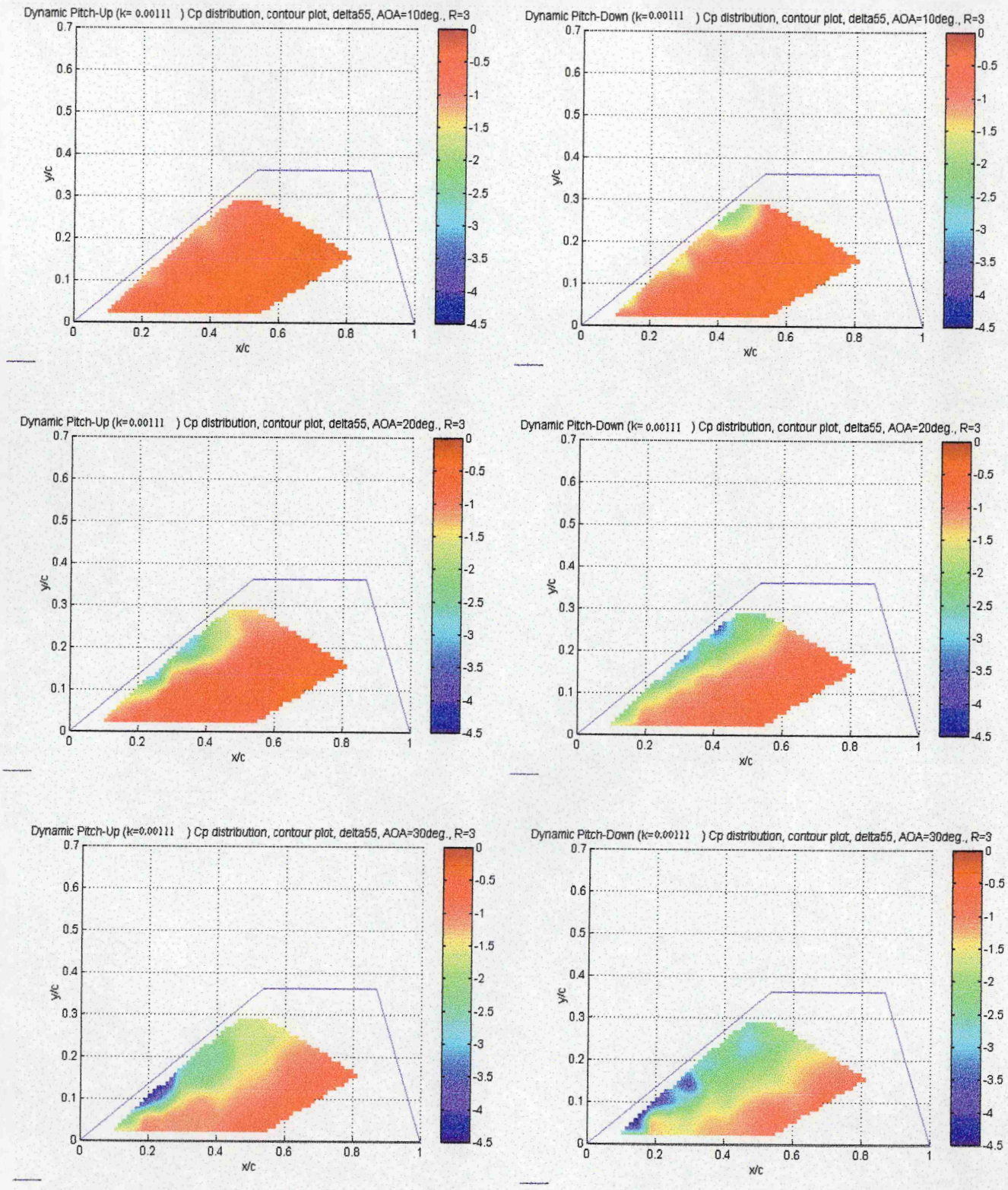

Figure 7.16 Cp distribution, Dynamic (pitch-up & down), k = 0.00111, Delta 55° sweep, t/c=0.018, B.L.=24mm

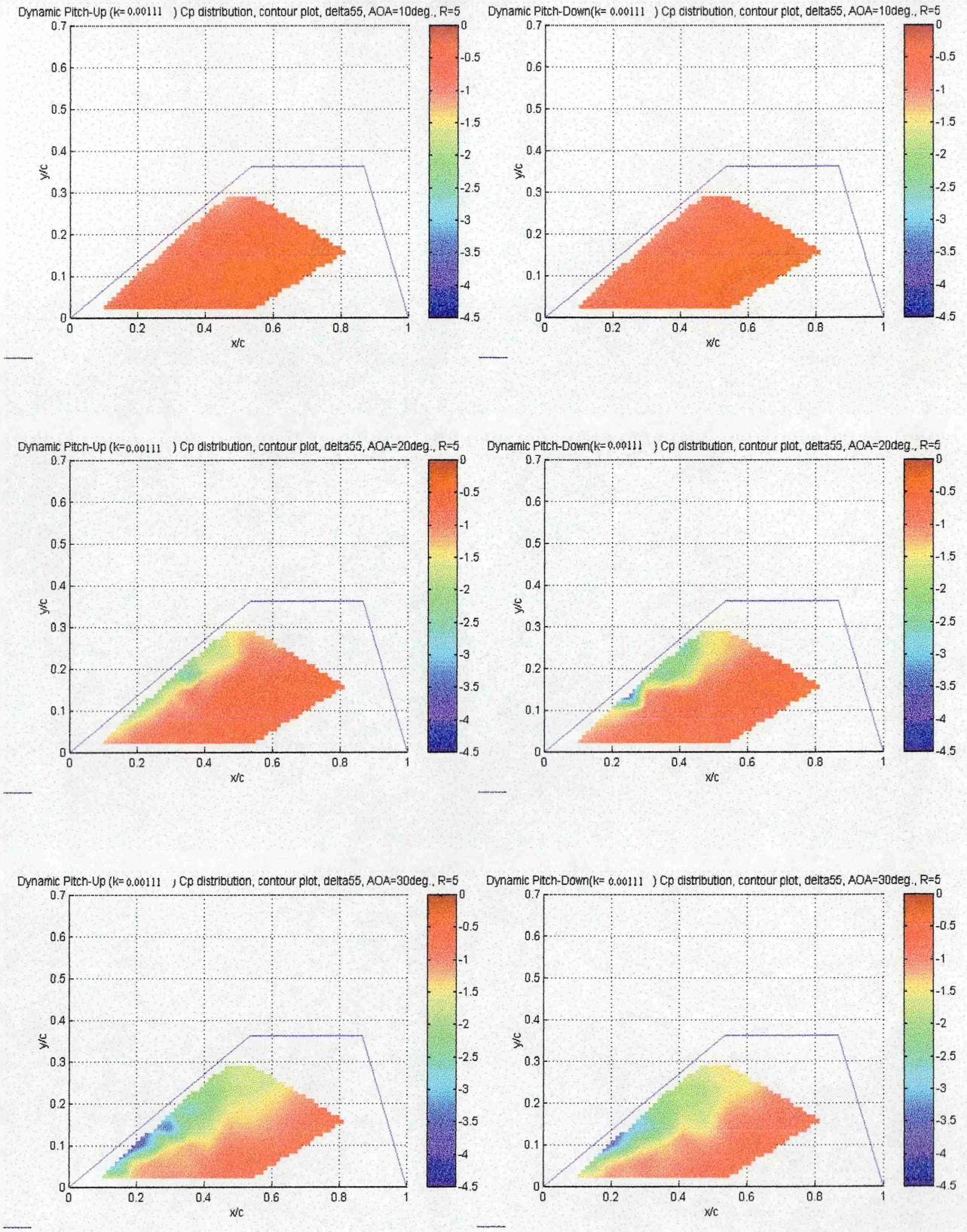

Figure 7.17 Cp distribution, Dynamic (pitch-up & down), k = 0.00111, Delta 55° sweep, t/c=0.018, B.L.=33mm

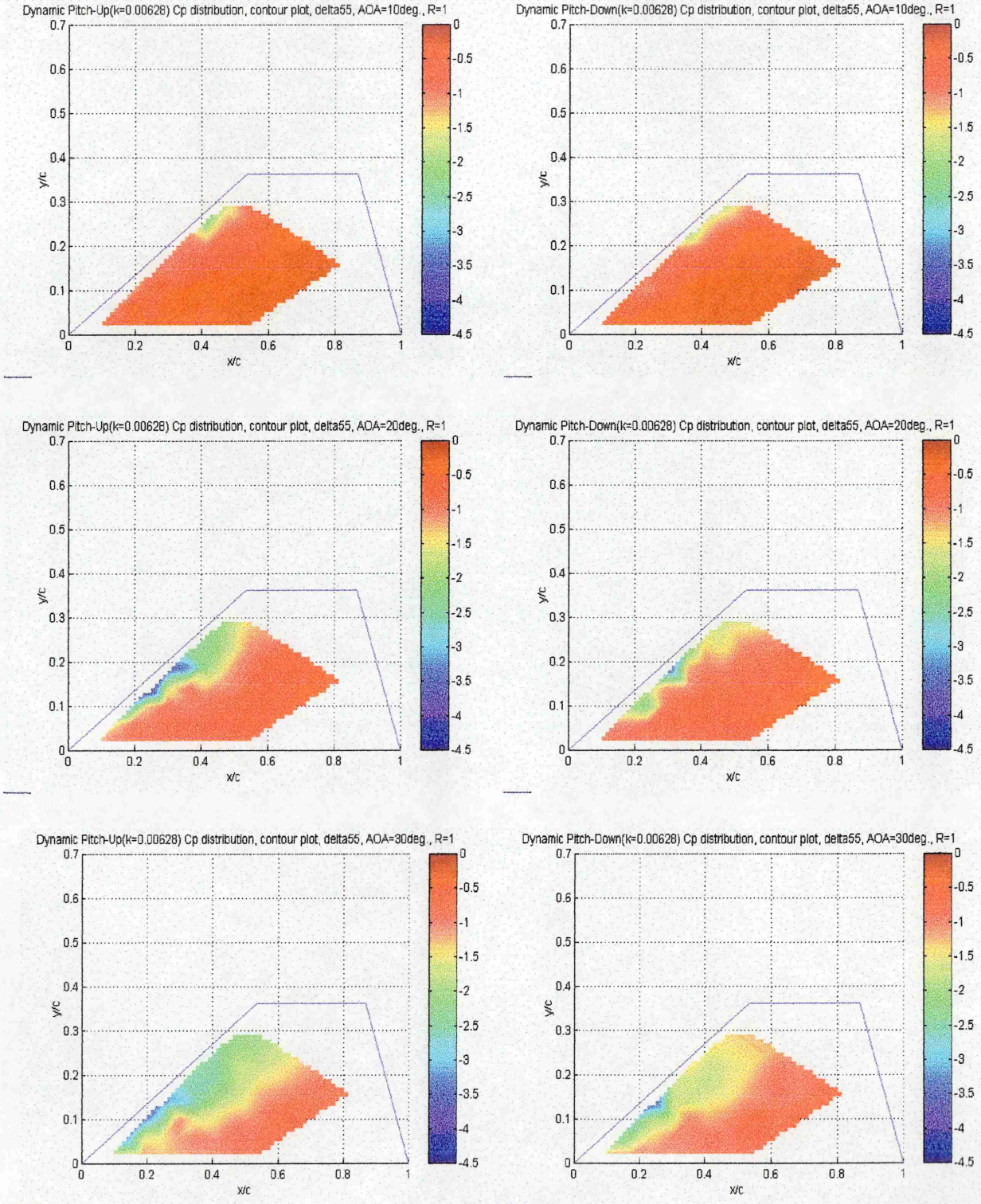

Figure 7.18 Cp distribution, Dynamic (pitch-up & down), k = 0.00628,
Delta 55° sweep, t/c=0.018, B.L.=14mm

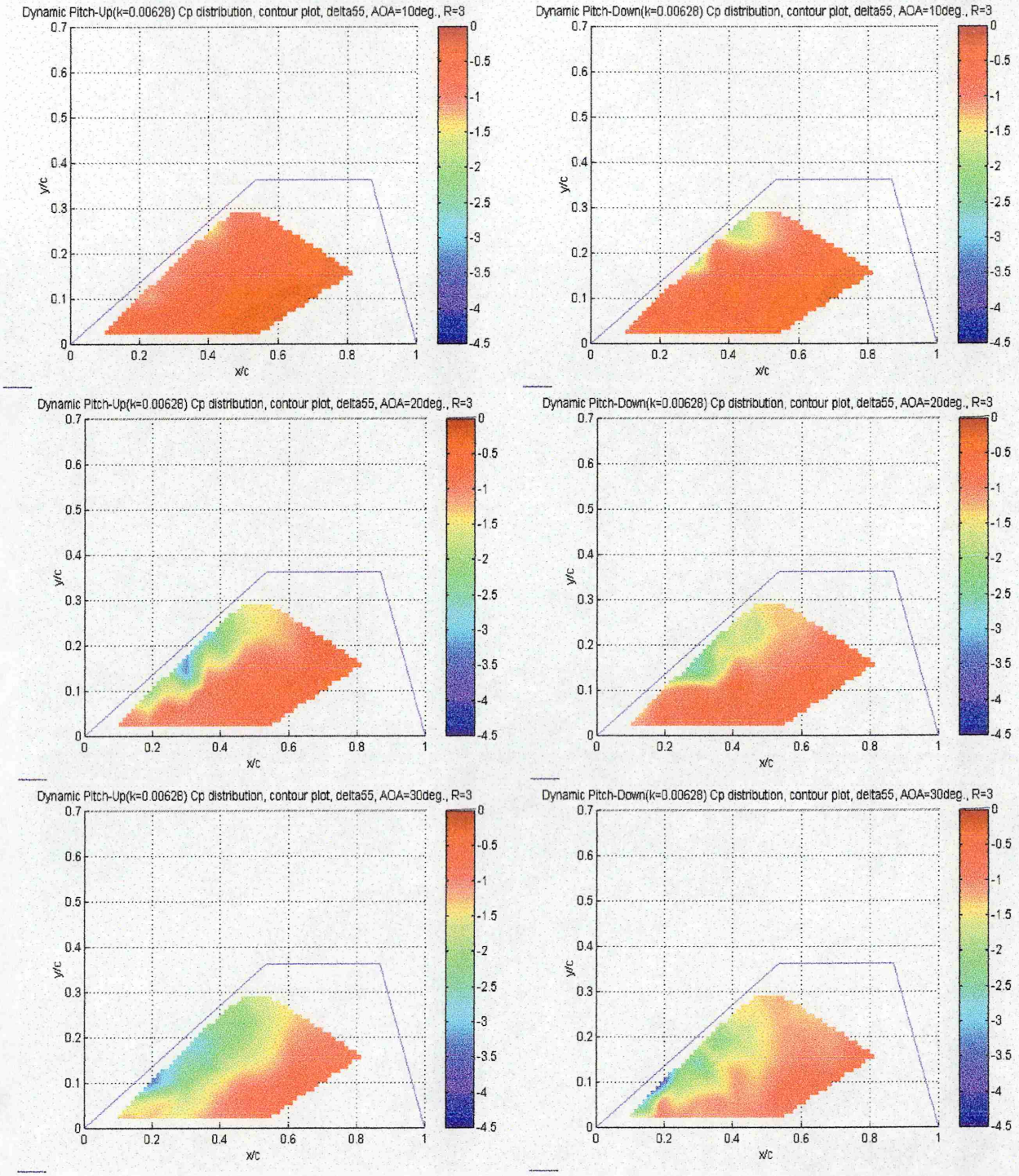

Figure 7.19 Cp distribution, Dynamic (pitch-up & down), k = 0.00628,
Delta 55° sweep, t/c=0.018, B.L.=24mm

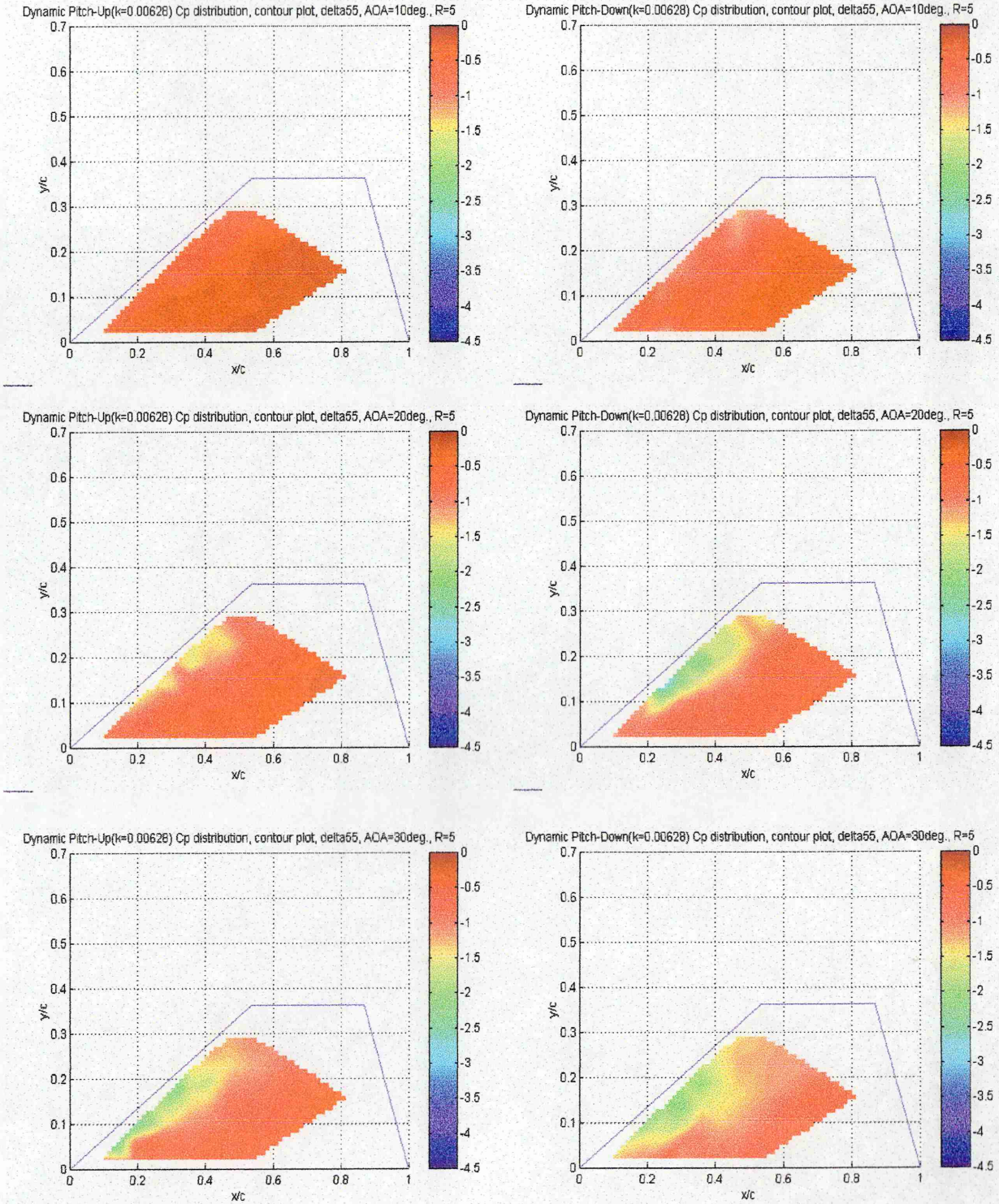

Figure 7.20 Cp distribution, Dynamic (pitch-up & down), k = 0.00628, Delta 55° sweep, t/c=0.018, B.L.=33mm

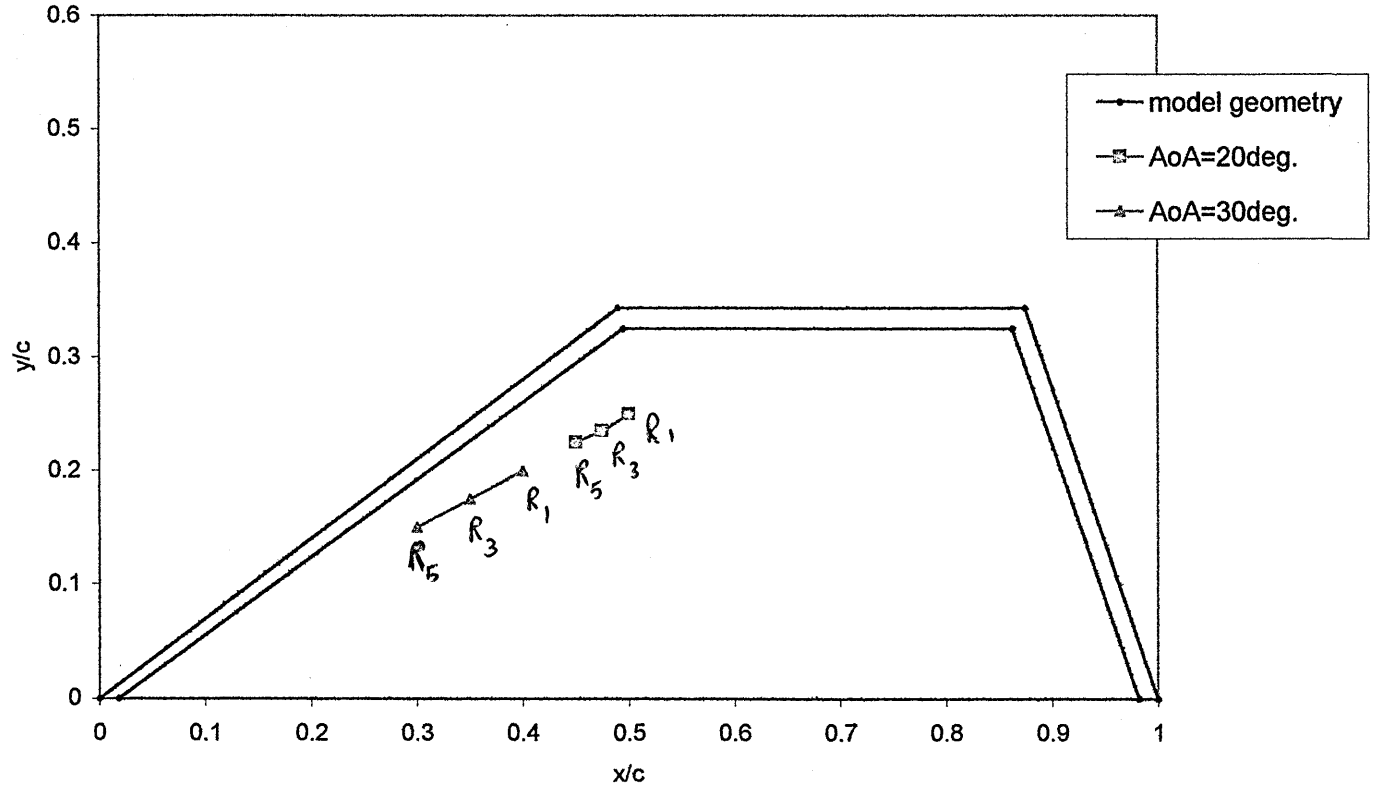

Figure 7.21 Static-location of Centre pressure Cp from contour plots for delta 55, All boundary layers, @ 20 and 30 deg AoA

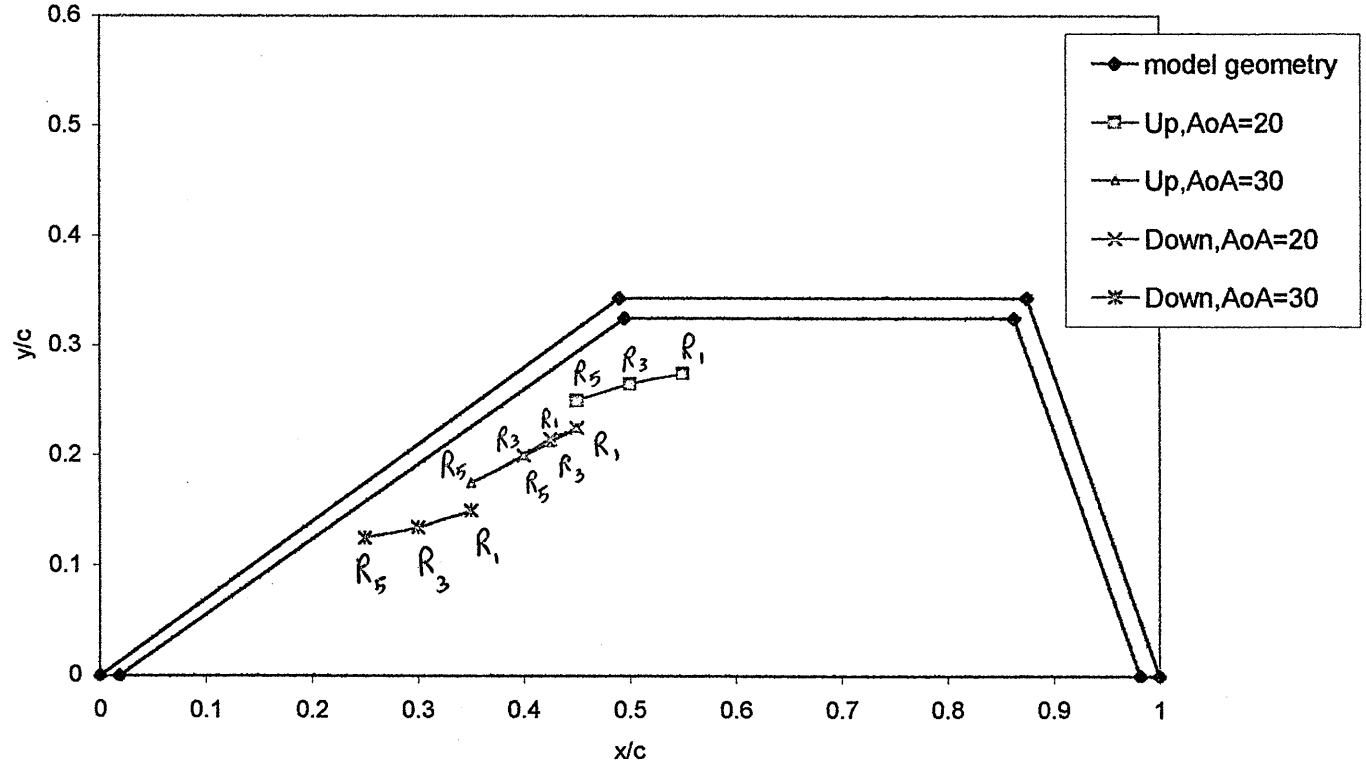

Figure 7.22 Dynamic(k=0.00111)-location of Centre pressure Cp from contour plots for delta 55, All boundary layers, @ 20 and 30

Chapter 8 Wind Tunnel Flow Visualisation Results and Discussion

In order to correlate with earlier water tunnel studies, (Chapter 6), and to investigate the influence of Reynolds Number on the flow field, a series of tests were carried out using smoke to investigate vortex trajectory and breakdown position in the wind tunnel.

8.1 Smoke Visualisation

During this experiment, smoke was introduced along the leading edge on the upper surface of the wing model, such that it was entrained into the leading-edge vortex in order that breakdown could be studied. Smoke filaments were illuminated by a light sheet from a projector as explained in Chapter 4. A total of five separated light sheets, displaced equally, are moved across the flow field. Operating the wind tunnel at relatively low speed resulted in better resolution of flow features due to a higher density of smoke. This resulted in a Reynolds Number, based on a root chord, of approximately 72000. Figures 8.1 to 8.6 illustrate that there is a difference, (in flow visualisation quality), between a tunnel speed of 3 m/sec and 6 m/sec (R_e = 72000 and 144,000 respectively). As a result a free stream velocity of 3 m/sec was chosen for all flow visualisation tests.

The technique for defining vortex breakdown position is explained using Figures 8.5 and 8.7. The five light sheets through the leading-edge vortex are located, (i) upstream of the vortex breakdown, (ii) at the beginning of the breakdown, and (iii) well downstream of the breakdown point. Upstream of the breakdown, the core of the vortex appears as a dark spot in the centre of the smoke-filled region. The dark spot exists because particles of flow visualisation smoke, are centrifugally spun out of the highly rotational sub core. At the onset of vortex breakdown, the dark spot becomes a ring as the vortex core begins to expand around the stagnant fluid that fills the centre of the breakdown vortex. Roos et al[147] used the same method of flow visualisation, (smoke), in a wind tunnel to define vortex trajectory and breakdown on a 60° and 70° delta wing, Lowson[125] also used the same flow visualisation method to investigate the vortex core position of a 70° delta wing.

Breakdown refers to a sudden and often dramatic structural change which usually results in the turbulent dissipation of the vortex. It is characterised by a sudden deceleration of the axial flow in the vortex core, the formation of a small recirculatory flow region, a decrease in the circumferential velocity and an increase in the size of the vortex. Downsteam of the breakdown point, the dark spot no longer exists, as the highly rotational vortex centre has diffused over the entire smoke-filled core of the vortex as depicted in the most downstream vortex ring in figure 8.5.

8.1.1 Smoke Tunnel General Vortex Characteristics

Figures 8.8 and 8.9 represent the smoke tunnel data of vortex trajectory location in terms of x/c vs. y/s and x/c vs. z/s respectively, for an angle of attack of 10°, 20° and 30°. As the angle of attack is increased the vortex core moves upstream toward the apex and away from the surface of the wing, other researchers noted the same behaviour, Kegelman et al[105] on a 70° delta wing, also Payne et al[106] who investigated 70°, 75°, 80° and 85° sweep delta wing models.

8.2 Correlation Between Water Tunnel and Wind Tunnel

This section will discuss a correlation between the water tunnel and the wind tunnel data. The water tunnel provided a powerful flow visualisation technique for both quantitative and qualitative investigations of delta wing flow. However, in the wind tunnel, accompanying pressure measurements have typically been performed at significantly higher Reynolds Number because of sensitivity and accuracy limitations of typical pressure measurement instrumentation at low dynamic pressures. In order to analyse the differences and establish a correlation between the water and wind tunnel results, data of aerodynamic parameters, (such as model related non-dimensional, position, Reynolds Number and wall boundary layer thickness), must be considered.

8.2.1 Vortex Trajectory

The model thickness/chord ratio (t/c) was the same in both facilities, (t/c = 0.018). The water tunnel Reynolds Number is 17,000, and the wind tunnel Reynolds Number was 479,000. This disparity in Reynolds Number may lead to differences in the flow field, but there are other factors may also be significant, the main parameter of interest here being wall boundary layer thickness. The water tunnel and the wind tunnel wall boundary layer thickness were different, see section 5.2 and 7.2 respectively.

Figure 7.6 represents the surface static pressure contours for the 55° swept delta wing taken from the wind tunnel data. The solid line, superimposed on the contour plot, represents the vortex core trajectory taken from the water tunnel flow visualisation studies. It can be seen that, as the angle of attack is increased, the surface static pressure suction peak, (from wind tunnel), increases and moves upstream toward the apex of the wing. The vortex core trajectory, (from the water tunnel), has the same trend, the vortex core trajectory moves upstream toward the apex of the wing.

At 20° angle of attack the suction peak is already established and as the angle of attack is increased to 30° this increases in magnitude and moves to the apex. The same can be seen for the vortex trajectory line from the water tunnel data. On the same figure the influence of the wall boundary layer thickness can be seen from the pressure contour plots, (wind tunnel), and the vortex trajectory line, (water tunnel), in moving the vortex trajectory line toward the apex, note that the influence of the wall boundary layers from the wind tunnel and the water tunnel are comparable.

It should be noted that there are some differences between the surface static pressure contour plots from the wind tunnel data and the vortex trajectory from the water tunnel data, mainly at low angle of attack. The difference in Reynolds Number between the two facilities may be a significant parameter. Lowson[12] compared vortex core positions for a range of Reynolds Numbers for 70° sweep delta wings and noted a significant scatter existed in the data. He suggested that although the results appear to justify low Reynolds Number studies of high Reynolds Number delta wing flows, care should be applied in certain areas in extrapolating from low to high Reynolds Number. Traub et al[139] investigated the influence of Reynolds Number on delta wing aerodynamics and noted that for a 60° delta wing, the vortex breakdown at a given angle of attack was delayed as the Reynolds Number decreased and the form of the spanwise pressure distribution at $R_e = 2x10^4$ differs from that seen at a $R_e = 4x10^4$ and $6x10^6$ where the variation of surface pressure and vortex trajectory with R_e was gradual.

Although changes in wall boundary layer thickness do influence vortex breakdown location and development, (as explained earlier in section 6.5 – increases in wall boundary layer thickness move the vortex trajectory towards the wing apex), the dominant influence between the two facilities is Reynolds Number.

8.2.2 Vortex Breakdown

In addition to vortex trajectory it is important to correlate the vortex breakdown position between the water tunnel and the wind tunnel. The method is to analyse the behaviour of the peak suction pressure induced by the leading edge vortices, (minimum pressure coefficient Cp_{min}), which vary with angle of attack for a given chord wise location, with the vortex characteristic from smoke flow visualisation.

Figure 8.10 shows the difference in vortex breakdown between the wind tunnel-smoke, (Re=72,000) and the water tunnel (Re=17,000) for the same delta 55° sweep and t/c=0.018.

Greenwell and Wood [172] analysed the surface static pressure data, using a shape parameter derived from a simple potential flow model, to determine the position of the burst point with comparable accuracy to that of flow visualisation technique. They showed that the half-width of the suction peak is a function solely of the vortex height above the wing surface.

Surface static pressure data from the wind tunnel made it possible to collate the spanwise location of the suction peak, the spanwise and vertical location of the vortex core along with the smoke flow visualisation. Due to limitations in terms of the number of pressure tappings on the wing model, the 'peak' in the curve depicting the spanwise pressure distribution could not always be identified. At the lowest angle of attack considered, the 'peak' was taken to be the lowest Cp measured. At higher angle of attack this was not a problem and the peak was easily identified.

To illustrate the method outlined above, the spanwise location of the suction peak (y_{min}/s) from wind tunnel surface static pressure data is plotted against spanwise location of vortex core trajectory (y_v/s) from the smoke tunnel visualisation data in Figures 8.11 to 8.13, Figures 8.13 to 8.15 represent the measured vortex height, half width of the suction peak ($y_{0.5}/s$) from wind tunnel surface static pressure, plotted against vortex core height (z/s) from smoke tunnel visualisation data.

Figures 8.11 to 8.16 show a good correlation between vortex breakdown and the behaviour of the half-width parameter. Thus confirms the ability to determine vortex characteristics and burst location from surface static pressure measurements.

However, there are differences between the two sets of data, this is believed to be due to the differences in smoke visualisation velocity, as mentioned before, where the Reynolds Number was (72000) and the velocity of the surface static pressure measurement where the Reynolds Number was (479000).

A further comparison between smoke tunnel and water tunnel data can be made in terms of the vortex breakdown position. Figure 8.10 illustrates a consistent trend in vortex breakdown position with angle of attack between the two facilities, but there is typically a 30% difference in the actual position. Thus may be due to differences in the Reynolds Number and the wall boundary layer thicknesses discussed in section 8.2.1. Another factor introduced here is the effect of smoke probe interference that was seen to delay vortex burst (see section 4.8).

Figure 8.17 compares the vortex trajectory between the water tunnel (Re=17,000), smoke tunnel (Re=72,000) and the work of Earnshow et al[95] (Re=340,000), for a 55° sweep delta. The differences of the vortex trajectory in this Figure are caused by parameters such as:

(i) The model frontal area, which has an influence on vortex burst location and development. Pelletier et al[28] and Ericsson et al[184] showed that increasing the size of a 70° delta wing model caused the vortex breakdown to occur closer to the apex because of the wall-induced upwash effect that increased the effective angle of attack promoting early vortex breakdown.

(ii) Model geometry, such as, the bevelled location, as explained in section 6.3, where most of previous researchers had their bevel at the windward. In this experiment, the bevel was at the leeward side and the wing was cropped.

(iii) The wall boundary layer thickness, as mentioned in section 7.4.2 and how it influences on vortex flow behaviour over the delta wing model.

(iv) The Reynolds Number, which in the smoke wind tunnel was nominally 5 times that in the water tunnel (from Re=17,000 to Re=72,000). The data presented by Earnshaw et al[95] was collected at Re=340,000.

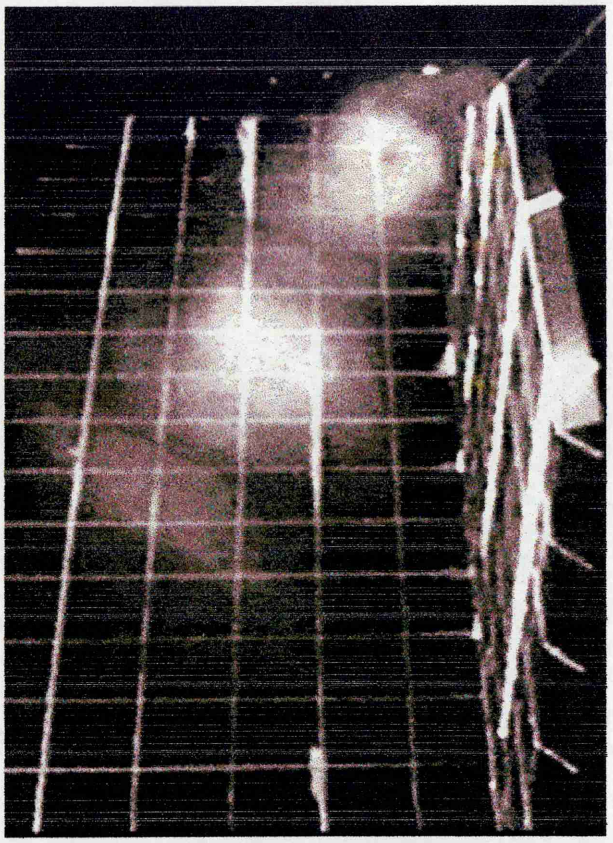

Figure 8.1 Smoke tunnel, Delta 55° sweep, AOA = 30°, velocity = 6 m/sec

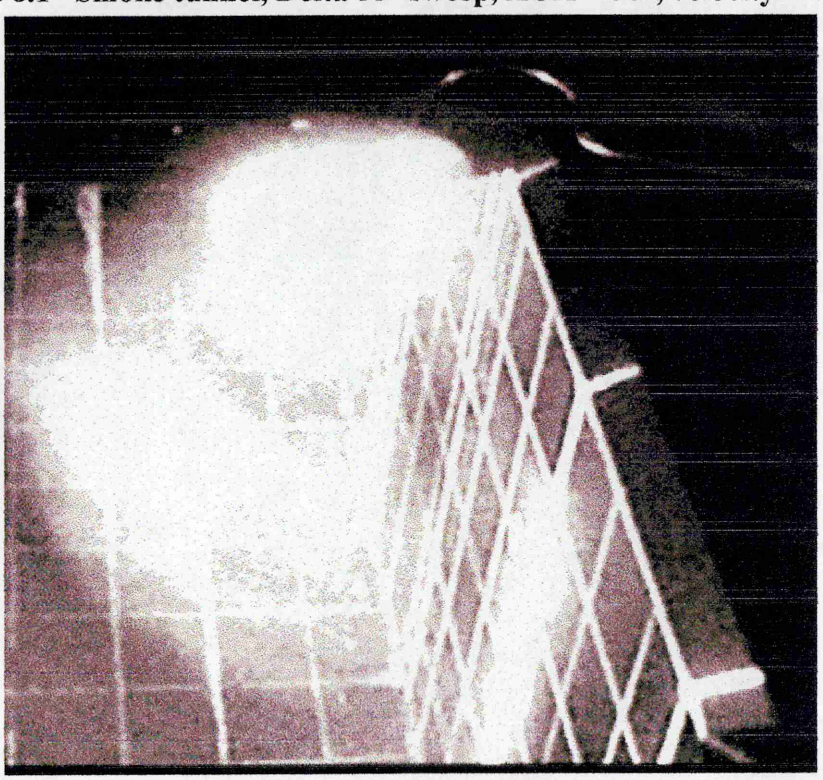

Figure 8.2 Smoke tunnel, Delta 55° sweep, AOA=40°, v = 6m/sec

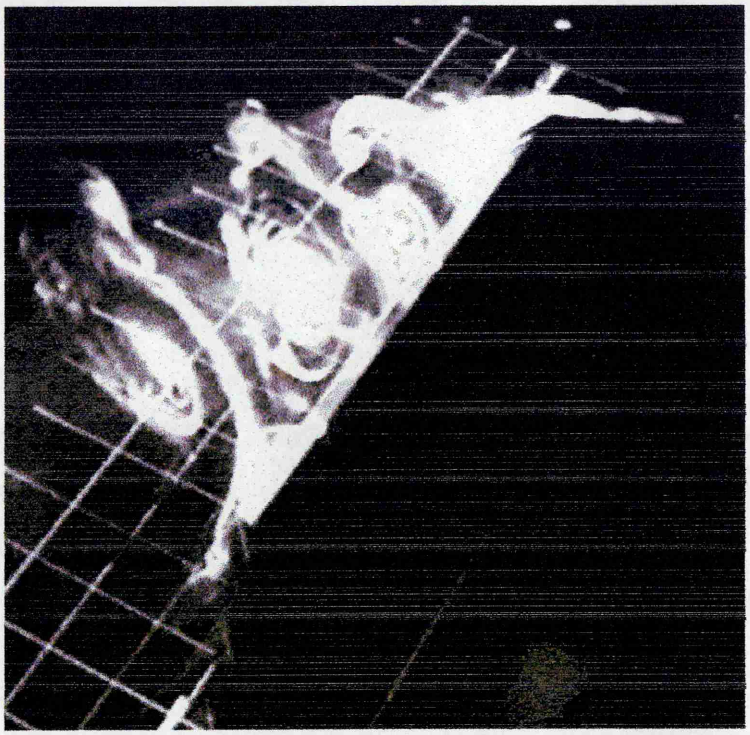

Figure 8.3 Smoke tunnel, Delta 55° sweep, AoA = 10°, v= 3m/sec

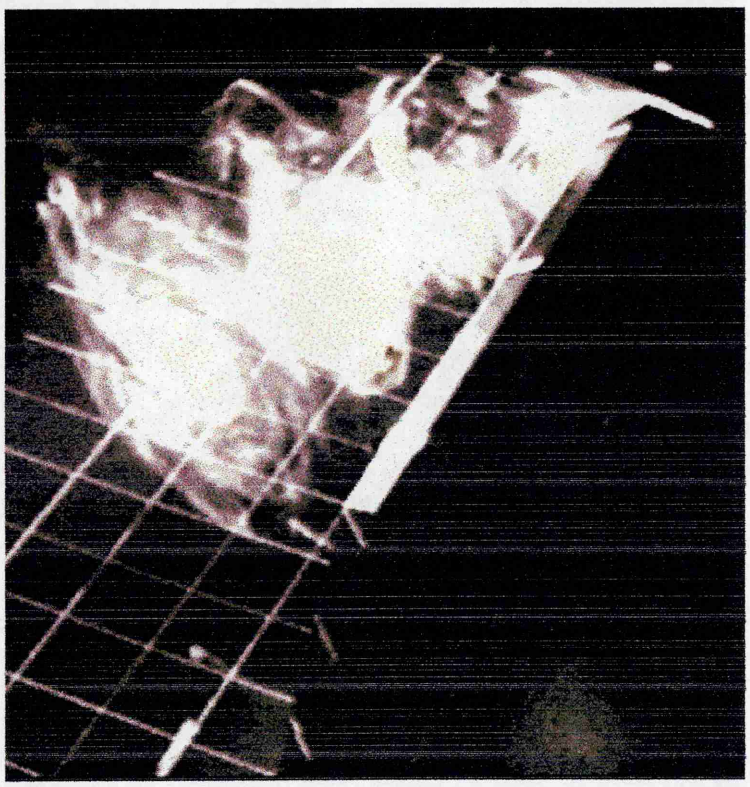

Figure 8.4 Smoke tunnel, Delta 55° sweep, AOA=20°, v = 3m/sec

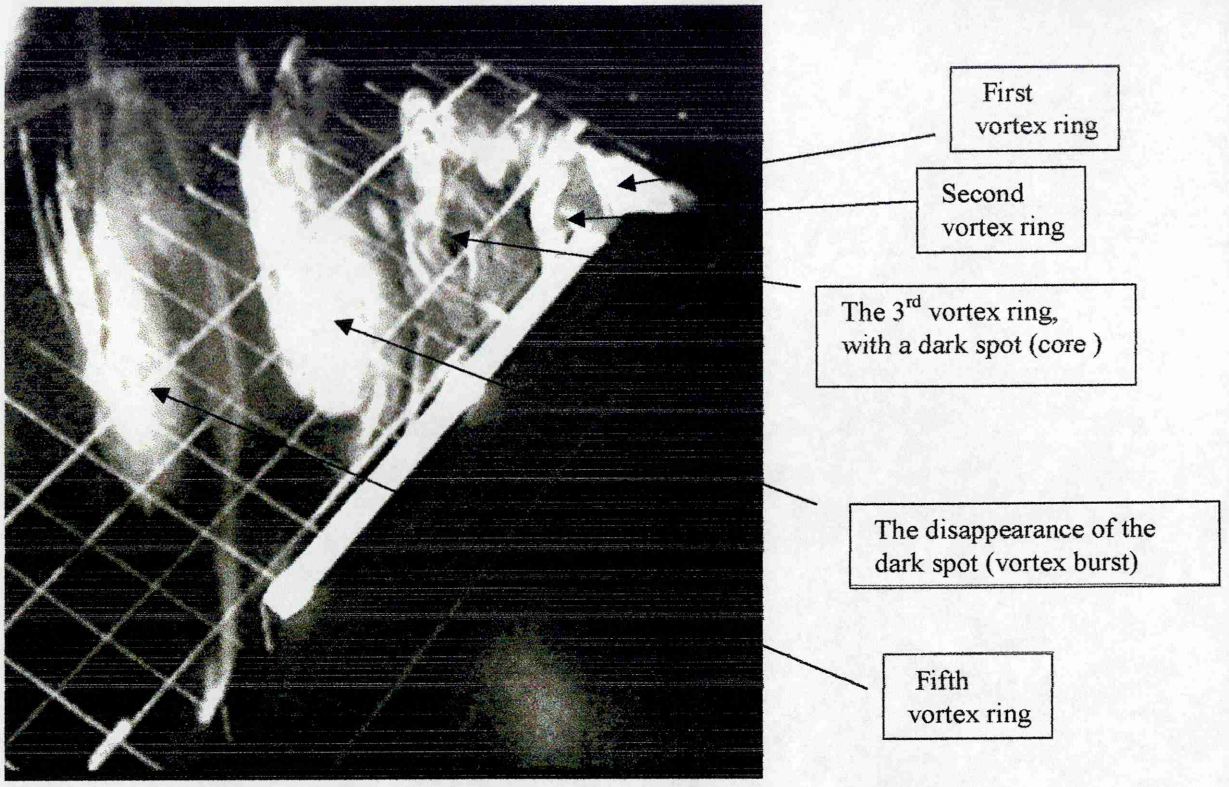

Figure 8.5 Smoke tunnel, Delta 55 sweep, AoA=30°, v = 3m/sec

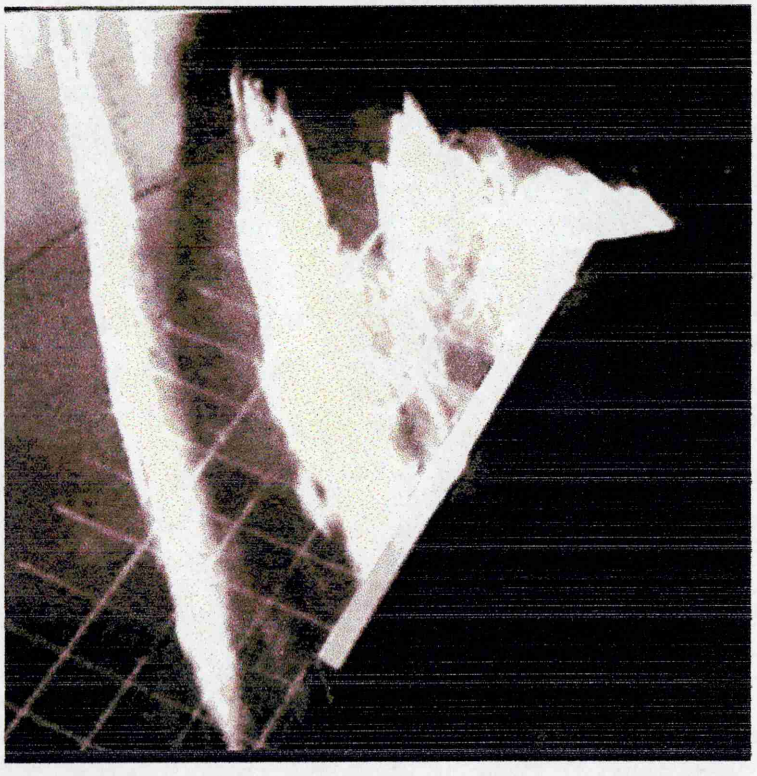

Figure 8.6 Smoke tunnel, Delta 55 sweep, AoA = 40°, v = 3m/sec

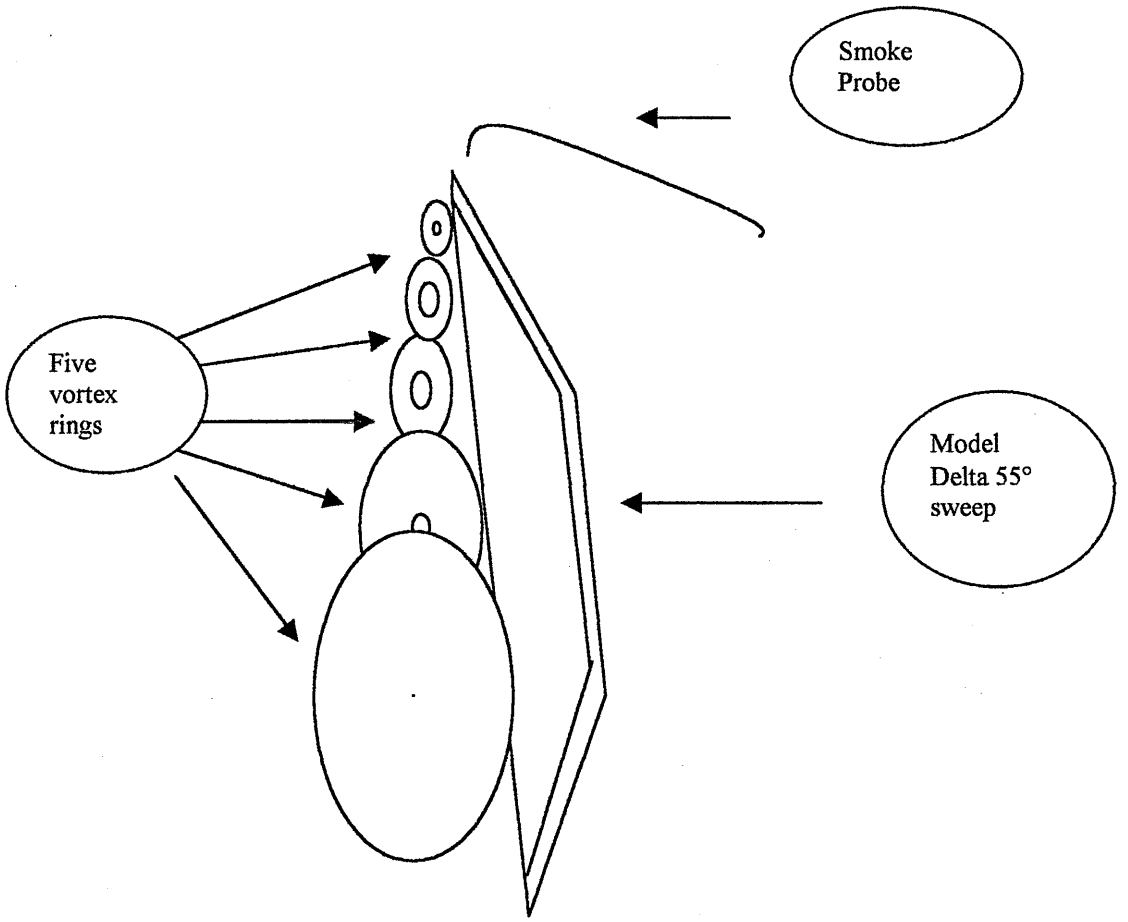

Figure 8.7 Sketch of smoke vortex ring showing the core trajectory, Delta 55 sweep, Re = 72,000.

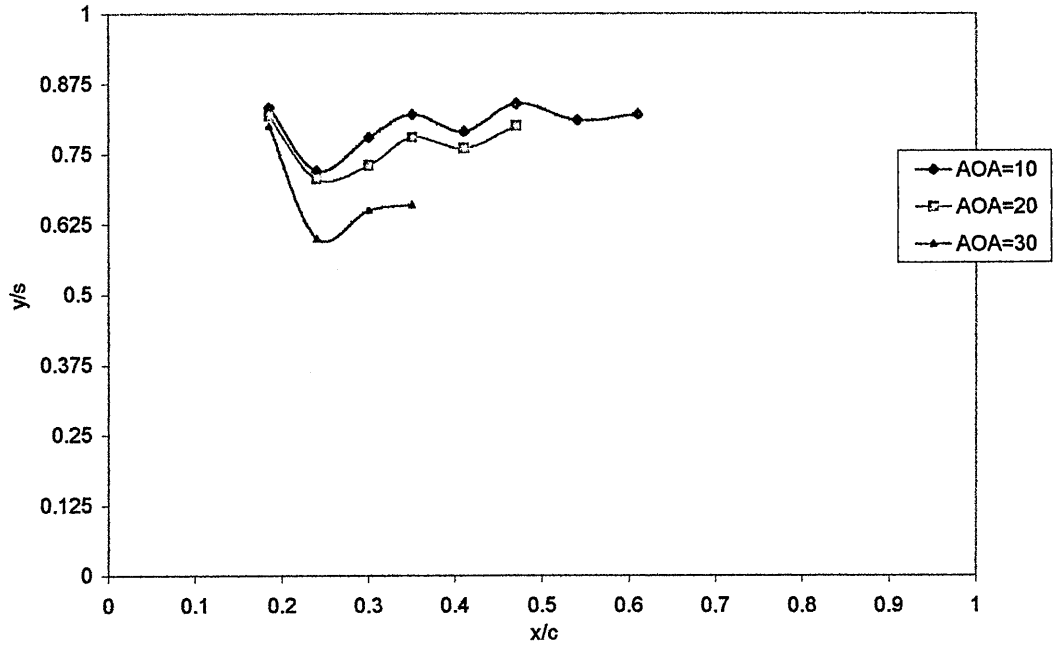

Figure 8.8 Wind-Tunnel, Smoke, Vortex flow trajectory x/c vs. y/s local, Delta 55 sweep, Re=72000

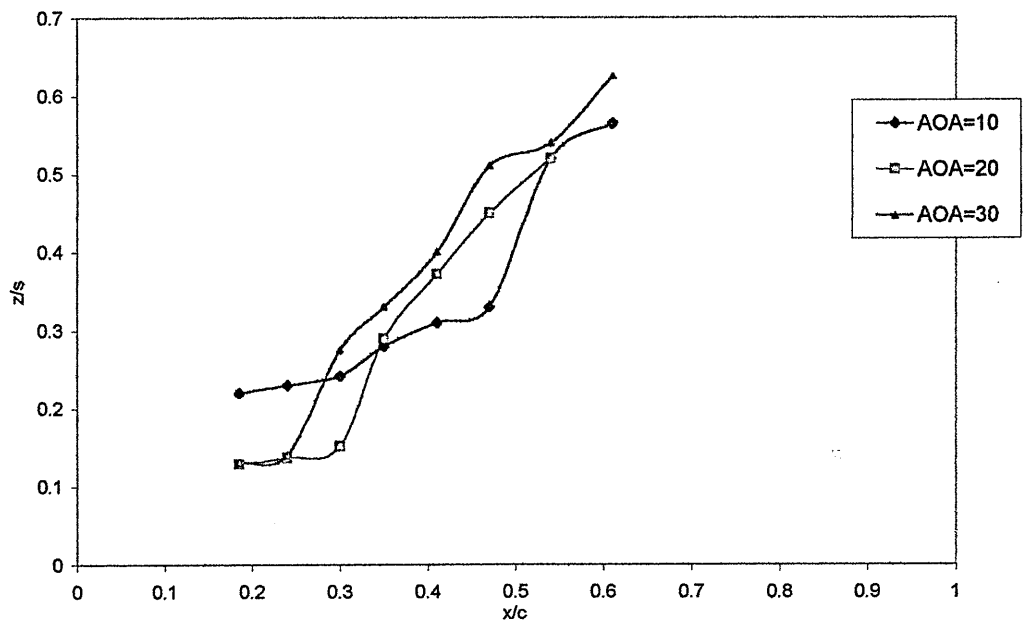

Figure 8.9 Wind tunnel, smoke, Vortex flow trajectory x/c vs. z/s local, delta 55 sweep, Re=72000

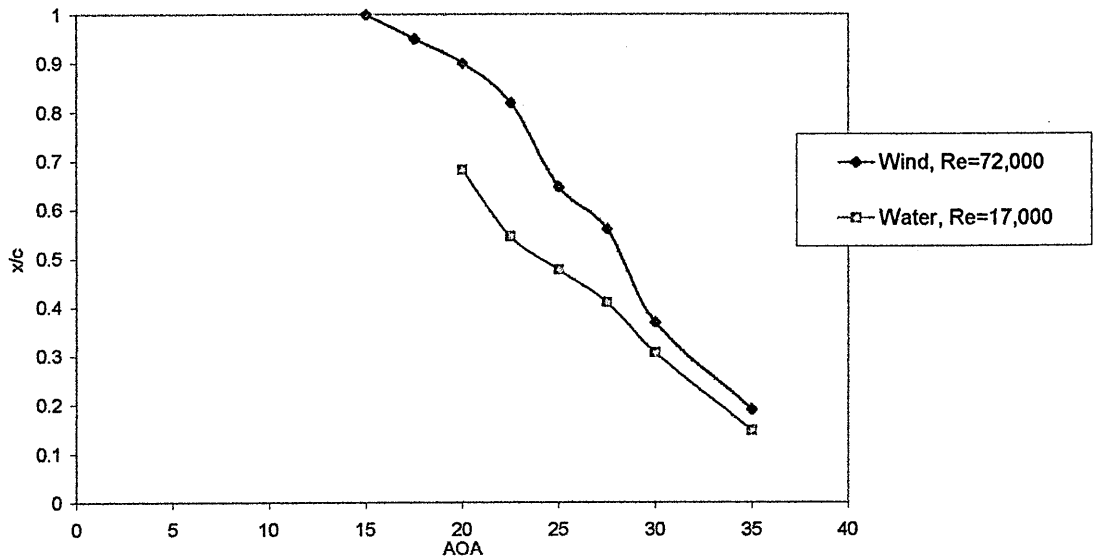

Figure 8.10 Wind tunnel (smoke),Re=72000 and Water tunnel,Re=17000, x/c breakdown position for 55 deg. sweept delta, t/c=0.018

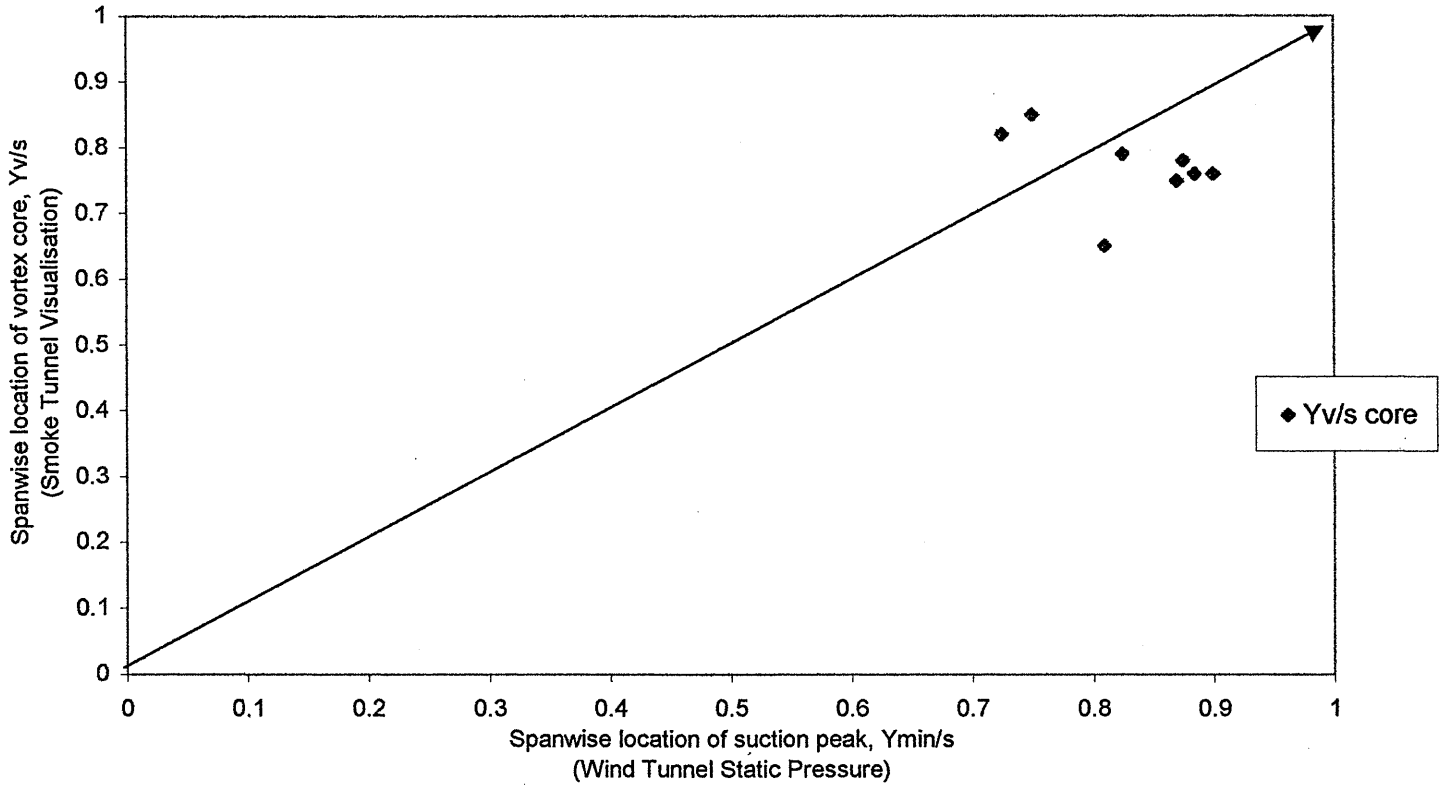

Figure 8.11 Spanwise location of vortex relative to suction peak; Delta55, AOA=10deg. Wind tunnel, Re=479,000 and smoke tunnel Re=72,000

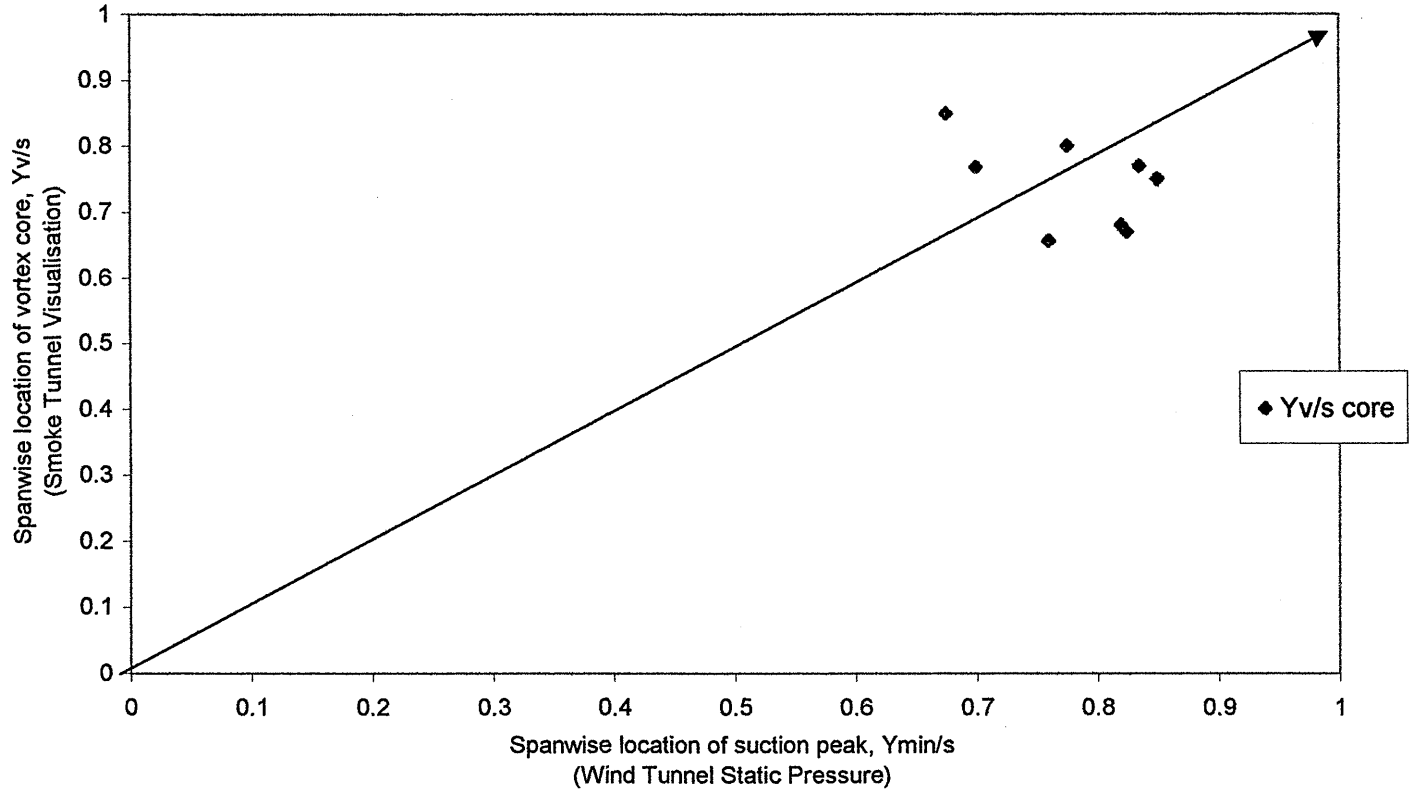

Figure 8.12 Spanwise location of vortex relative to suction peak; Delta55, AOA=20deg. Wind tunnel, Re=479,000 and smoke tunnel Re=72,000

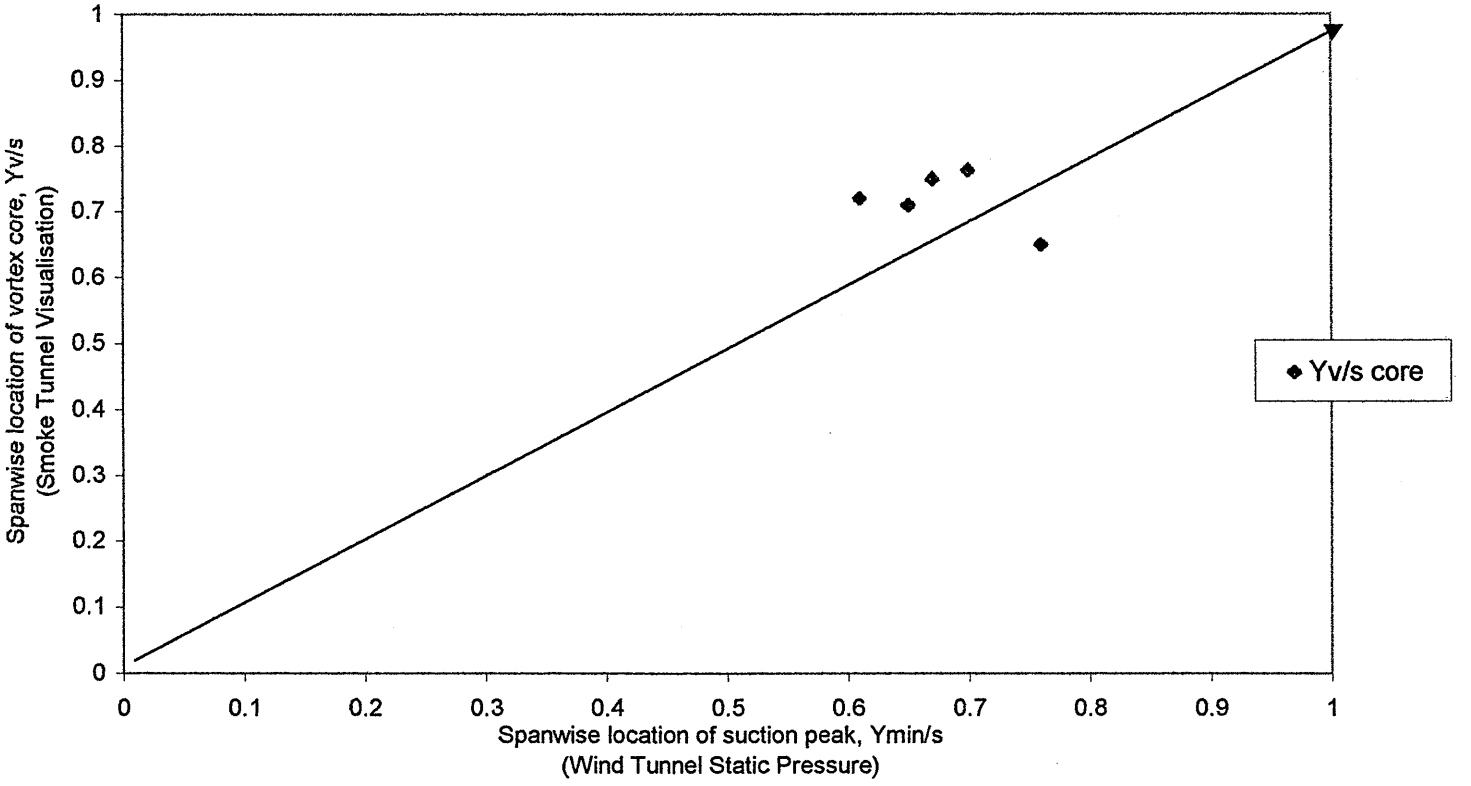

Figure 8.13 Spanwise location of vortex relative to suction peak; Delta55, AOA=30deg. Wind tunnel, Re=479,000 and smoke tunnel Re=72,000

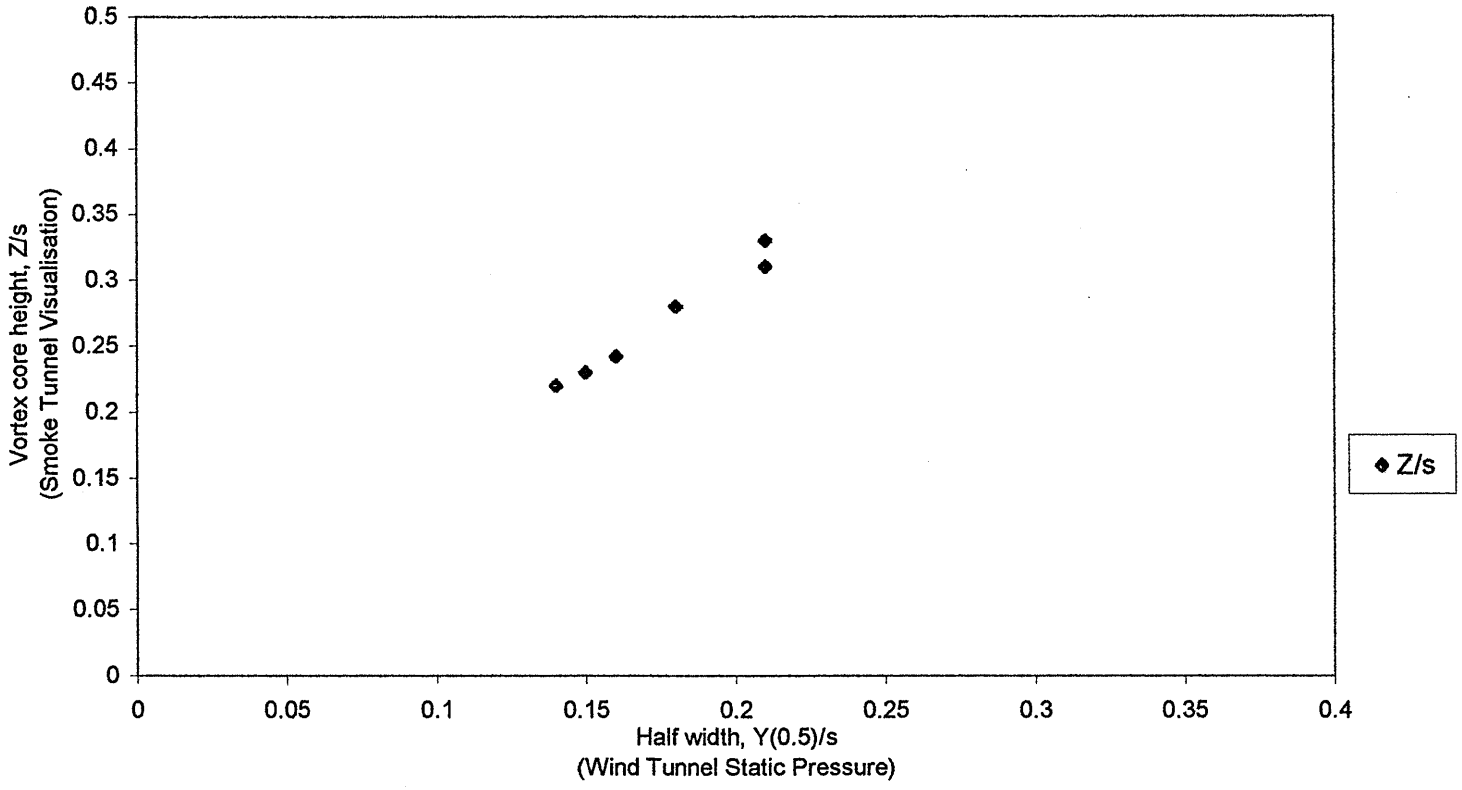

Figure 8.14 Measured vortex height compared with simple model; Delta55, AOA=10deg. Wind tunnel, Re=479,000 and smoke tunnel Re=72,000

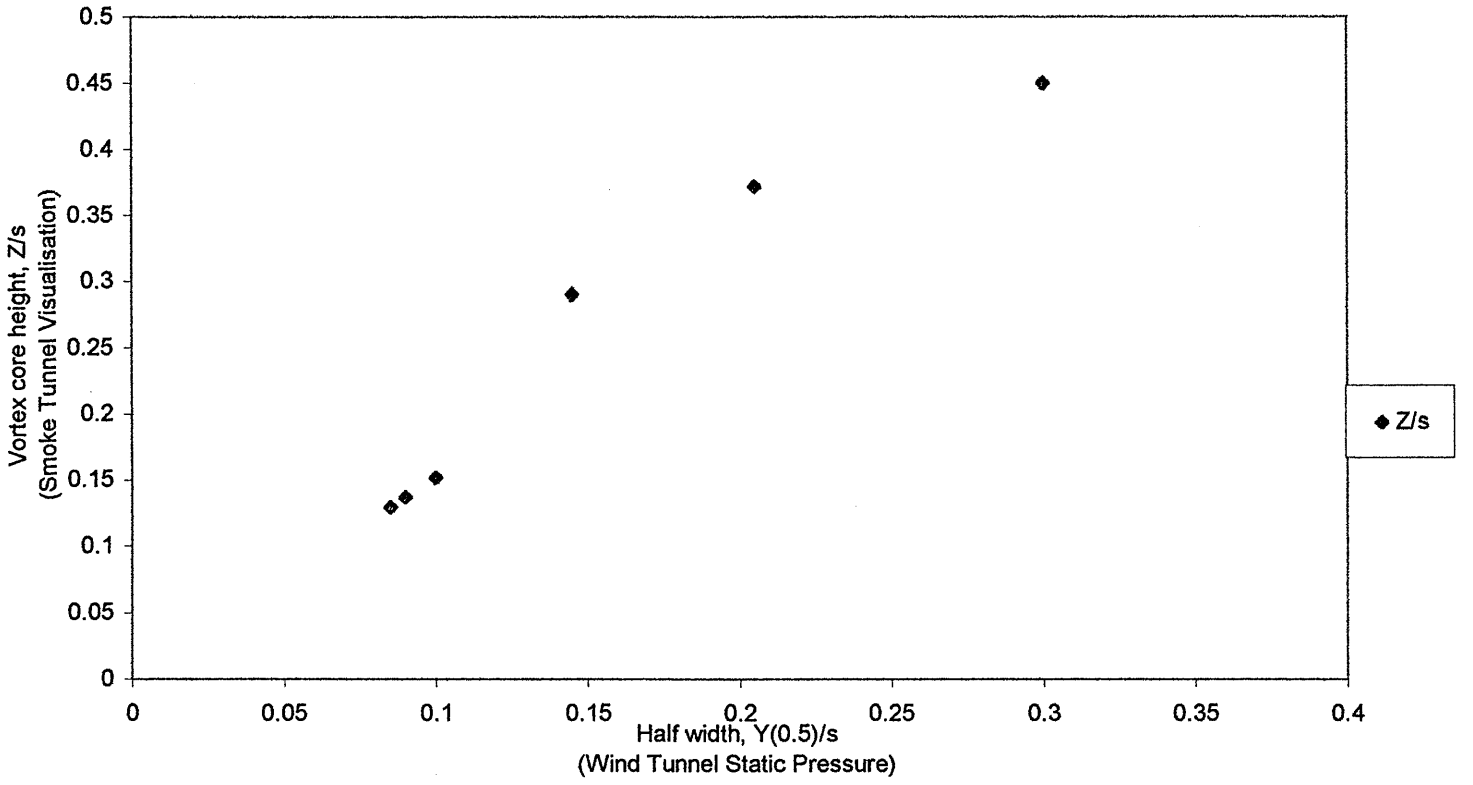

Figure 8.15 Measured vortex height compared with simple model; Delta55, AOA=20deg. Wind tunnel, Re=479,000 and smoke tunnel Re=72,000

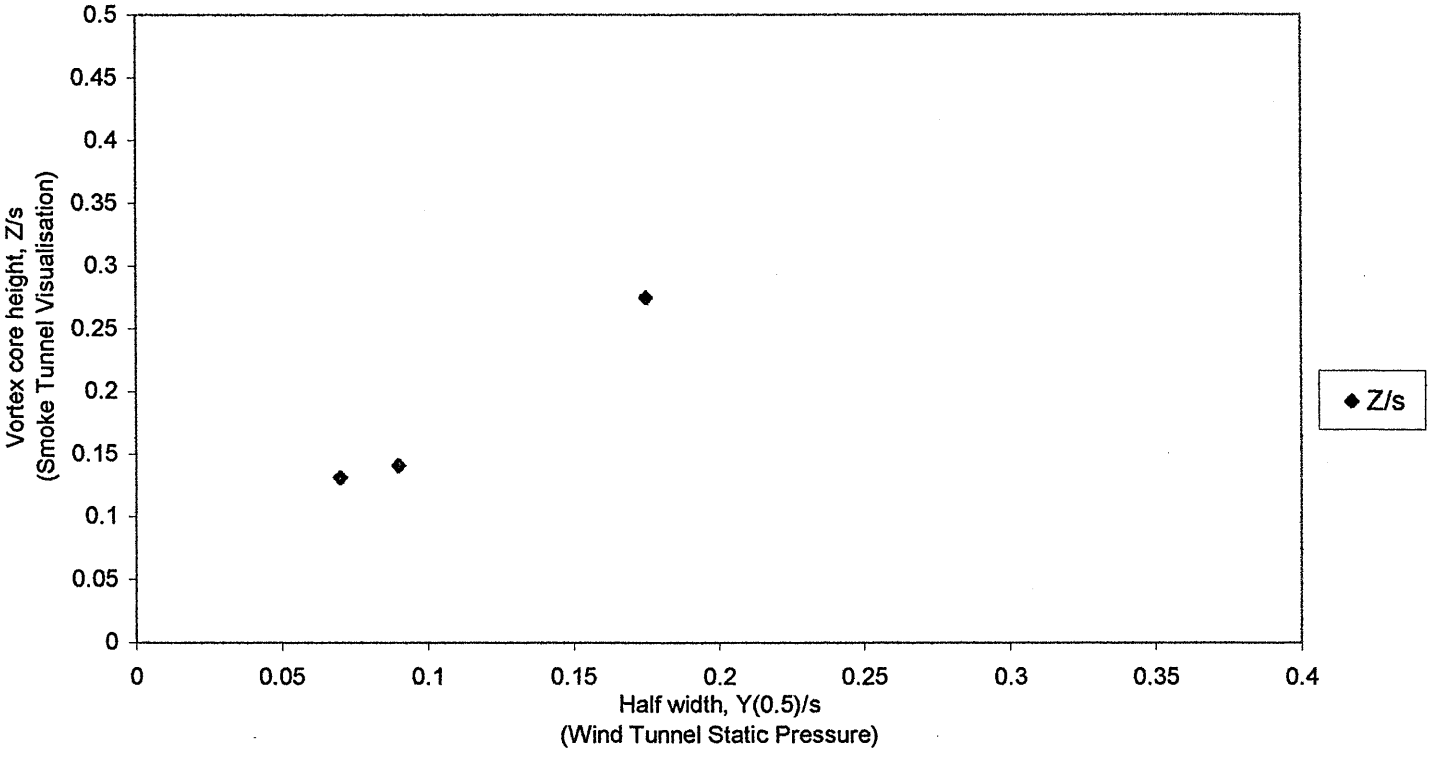

Figure 8.16 Measured vortex height compared with simple model; Delta55, AOA=30deg. Wind tunnel, Re=479,000 and smoke tunnel Re=72,000

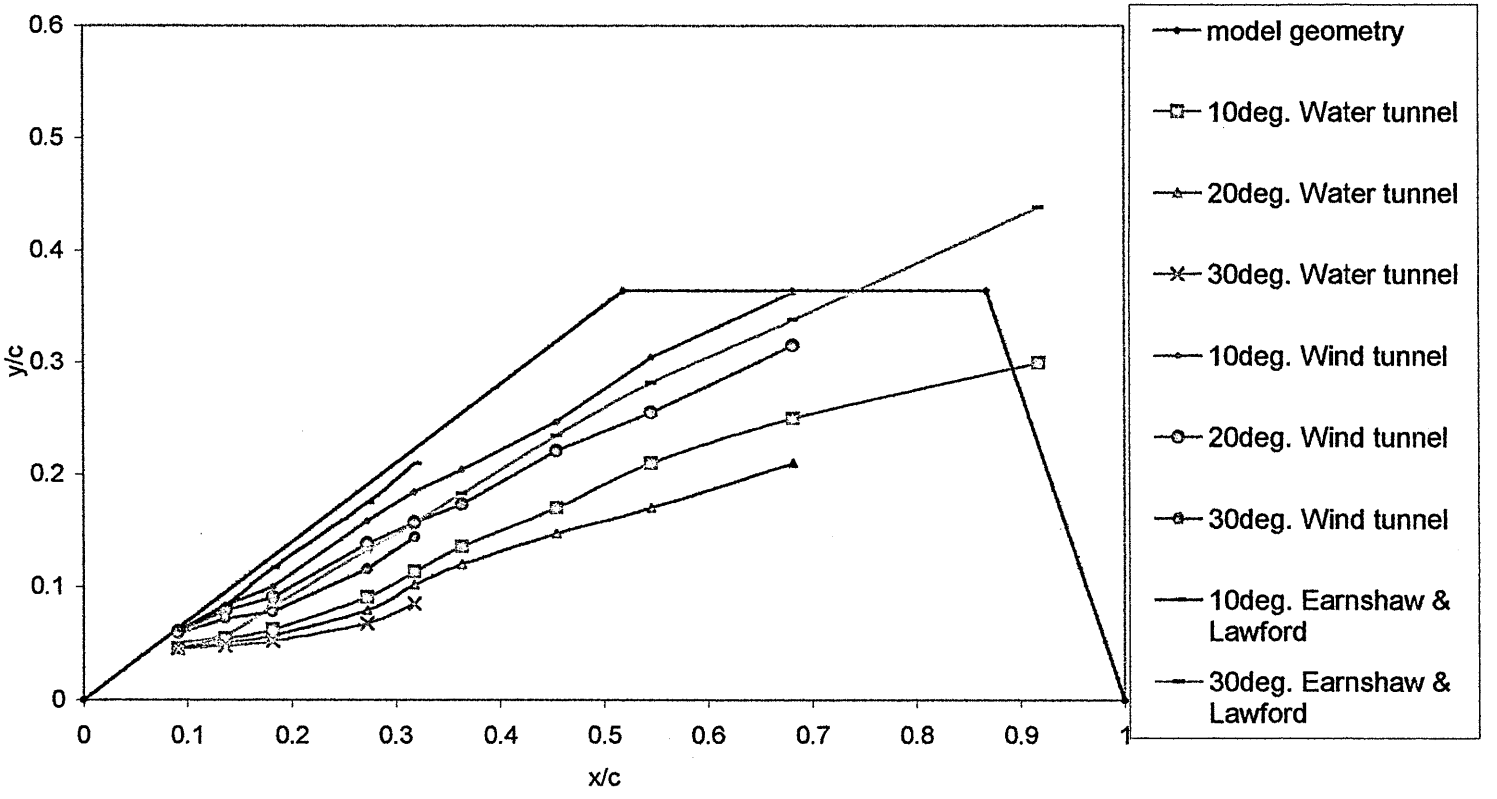

Figure 8.17 Comparison of Wind tunnel,Smoke,Re=72,000, B.L.=14mm and water tunnel Re=17,000, B.L.=6.73mm and Earnshaw & Lawford 1966, Re=340,000; Vortex flow trajectory x/c vs. y/c, Delta 55 sweep

Chapter 9 Conclusions

An experimental investigation has been carried out to study and understand the influence of an end plate boundary layer on half delta wing models at low Reynolds Number. The programme involved measurements in two facilities; a vertical water tunnel which was used for flow visualisation studies and a conventional closed working section wind tunnel for both flow visualisation and surface static pressure measurements. In both facilities dynamic and steady state or static measurements were made on half delta wing models with 55° and 70° sweep and varying thickness/chord ratio under the influence of a number of artificially generated end plate boundary layers.

1. Test conditions in the water tunnel (root chord = 22 cm, semi span = 8cm for the 55° and 6 cm for the 70° sweep), resulted in a Reynolds Number of 17,000 (based on model root chord) and 479,000 in the wind tunnel (for a root chord = 35 cm and semi span = 12 cm). The corresponding artificially generated end plate boundary layers had a displacement thickness in the range of 6.73mm to 14.0mm in the water tunnel with a laminar velocity profile and 14.0mm to 33mm in the wind tunnel with a turbulent velocity profile.

2. In both facilities, for all model configurations tested, vortex burst was seen to move upstream, inboard and away from the surface as the angle of attack is increased. This was apparent for both dynamic and static test conditions and is consistent with the findings of previous researchers.

3. Vortex core trajectory is seen to move inwards towards the wing root with increasing angle of attack for all model configurations tested in both dynamic and static test conditions.

4. Vortex breakdown position is seen to move upstream and hence inboard toward the wing root as the end plate boundary layer thickness is increased.

5. In terms of vortex core trajectory, increases in end plate boundary layer thickness are seen to displace the vortex core trajectory inward towards the wing root and away from the wing surface.

6. During dynamic tests an increase in wall boundary layer thickness is seen to suppress the hysteric behaviour of the vortex trajectory. The wall boundary layer thickness had a much greater effect on dynamic pitch-up than on dynamic pitch-down for the 55° sweep and a little effect for the 70° sweep wing.

7. Surface static pressure measurements at Reynolds Number of 479,000, during both static and dynamic tests, make it possible to see that the influence of changes in wall boundary layer thickness are small, often insignificant, at (x/c) locations greater than 0.45. This is consistent with an increase in wall boundary layer thickness promoting earlier vortex breakdown.

8. Changes in end plate boundary layer thickness are assumed to influence the magnitude of the horseshoe vortex which forms at the junction of the half delta wing and end plate. The interaction of this vortex with the wing leading edge vortex is thought to lead to changes in trajectory and breakdown location that are consistent with the sense of rotation of both flow features.

9. Correlation between smoke flow visualisation (of both vortex breakdown and trajectory) and surface static pressure measurements, using the half-width of the suction peak as a parameter, was good.

10. Differences between vortex characteristics in the water tunnel and wind tunnel were consistent with previous work which showed that an increase in Reynolds Number increased the vortex pressure suction peak and moved vortex breakdown upstream.

Chapter 10 Future Work

This research program has shown the effect of changes in the thickness of an end-plate boundary layer on the vortical flow behaviour of a half-delta wing model. Further insight would be gained from detailed measurements of the entire flow field over the surface of the wing model, using a five hole probe and an LDV (Laser Doppler Velocimetry) technique. This would give insight into the off-surface three-dimensional flow field and the end-plate boundary layer effects. An accurate measurement could be made of the fluctuating, unsteady part of the flow field that has been affected by the changes in boundary layer thickness, since these could not be ascertained from the water tunnel flow visualisation or from the measured surface static pressure distributions. Data from a five hole probe or LDV, would enable a validation of suitable CFD model.

The results may translate to wing-body configurations, primarily the influence of fuselage boundary layer flows on a wing. Further experimental data would be needed to confirms this.

Correlation between smoke flow visualisation and surface static pressure measurements in terms of vortex trajectory and breakdown was encouraging. However it was limited by the finite number of surface pressure tappings available on the model surface and in some cases, by difficulties in resolving vortex position from the smoke flow visualisation video film.
An improved experimental programme would:

(i) use a more extensive pressure tapped model to reduced the need for interpolation and
(ii) use an improved camera location to aid identification of the vortex.

Chapter 11 References

1 Whitford , R. Design for air combat. Janes publishing Co. Ltd. London , 1987.

2 Hebbar, S. and Platzer, M. Visualisation study of the vortical flow over a double- delta wing in dynamic motion . AIAA 93-3425.

3 Jones, J.P. A note on Professor Squire's analysis of the vortex break down phenomenon. ARC 22142 FM 2991.

4 Sarpkaya,T. Vortex break down in swirling conical flows. AIAA Journal Vol.9 , No.9.

5 Visbal, M. Computational and physical aspects of vortex break down on delta wing. AIAA 95-0585.

6 Visbal, M. and Gordnier, R. Origin of computed unsteadiness in the shear layer of delta wings . J. Aircraft Vol.32, No.5.

7 Leibovich, S. Vortex stability and break down : survey and extension AIAA J. Vol.22,No. 9 Sep.1984.

8 Lambourne, N. and Bryer, D. The bursting of leading – edge vortices some observation and discussion of the phenomenon. ARC 22775 FM3085 April 1961.

9 Wedemeyer, E. Stable and unstable vortex separation in high angle of attack aerodynamics. AGARD CP-247 Jan.1979.

10 Benjamin, T. Theory of the vortex break down phenomenon. Journal of Fluid Mechanic. Vol. 14, 1962 pp.593 – 629.

11 Hall, M. A theory for the core of a leading – edge vortex. Journal of Fluid Mechanic. Vol.11 , 1961 pp.209 – 228.

12 Lowson, M. Visualisation measurements of vortex flows. Journal of Aircraft Vol.28, No. 5.

13 Gordnier, R. Numerical simulation of a 65 deg. Sweep delta wing flow field for static roll angle. AIAA 95-0082.

14 Lowson, M., Riley, A. and Swales, C. Flow structure over delta wing. AIAA 95-0586.

15 Payne, F. and Nelson, R. Visualisation of leading edge vortices on a series of flat plate delta wings. NASA CR 4320 April 1991.

16 Verhaagen, N., Jenkins, L., Kern, S. and Washburn, A. A study of the vortex flow over a 76/40 deg. Double-delta wing . AIAA 95-0650.

17 Hebbar, S and Platzer, M. Pitch rate /side slip effects on leading edge extension vortices of an F/A-18 aircraft model. J. Aircraft Vol.29, No.4 Aug. 1992.

18 Rediniotis, O and Schaeffler, N. View of a breakdown: Scientific visual analysis of vortex breakdown over a delta wing. AIAA-95-0116.

19 Hang, X and Hanff, E. Prediction of leading edge vortex break down on delta wing oscillating on roll. AIAA 92-2677.

20 Visbal, M. Structure of vortex break down on a pitching delta wing . AIAA 93-0434.

21 Visbal, M. Onset of vortex break down above a pitching delta wing . AIAA J. Vol.32, No.8 Aug. 1994.

22 Rediniotis, O., Klute, S., Hoang, N. and Telionis, D. Dynamic pitch-up of a delta wing. AIAA J. Vol.32, No.4 April 1994.

23 Gad-el-Hak, M. and Ho, C. The Pitching delta wing. AIAA Journal Vol.23, No.11 November 1985.

24 Atta, R. and Rockwell, D. Leading – edge vortices due to low Reynolds number flow past a pitching delta wing. AIAA J. Vol.28, No. 6 June 1990.

25 Wendt, B., Greber, I. and Hingst, W. The Structure and Development of Streamwise Vortex Arrays Embedded in a Turbulent Boundary Layer. AIAA 92-0551.

26 Batchelor, G. Axial flow in Trailing Line Vortices. Journal of Fluid Mechanics, Vol.20, part4, pp645-658, 1964.

27 Reynolds, G. and Abtahi, A. Three dimensional vortex development , break down and control. AIAA 89-0998.

28 Lin, J. and Rockwell, D. Transient structure of vortex break down on a delta wing. AIAA J. Vol.33, No.1 Jan.1995.

29 Gursul, I. and Yang, H. Vortex break down over a pitching delta wing. AIAA 94-0536.

30 Ahmed, S. and Chandrasekhara, M. Reattachment studies of an oscillating airfoil dynamic stall flow field. AIAA 91-3225.

31 Ericsson, L. Pitch down dynamic stall characteristics. AIAA 94-0535.

32 Schreck, S., Faller, W. and Luttges, M. Dynamic reattachment on a down ward pitching finite wing. Journal of Aircraft Vol.33, No.2 April1996.

33 Chodhuri, P. and Knight, D. Two-dimensional unsteady leading edge separation on a pitching airfoil . AIAA Journal. Vol.32,No.4 April 1994.

34 Doligalski, T. and Walker, C. Vortex interactions with walls. Annual Review of Fluid Mechanics. 1994 pp.573-616.

35 Washburn, A. and Visser, K.. Evolution of vortical structures in the shear layer of delta wings . AIAA 94-2317.

36 Baker, C. The laminar horse shoe vortex. Journal of Fluid Mech. 1995 pp.347-367.

37 Tulapurkara, E., Ramjee, V. and Rajasekar, R. Interaction between boundary layer and wakes of different bodies . AIAA Journal. Vol.28 No.6 June 1990.

38 Cutler, A. and Bradshaw, P. Vortex boundary layer interaction. AIAA 89-0083.

39 Morton, B.R. The generation and decay of vorticity. Geophysics Fluid Dynamics, 1984 vol. 28 pp277 – 308.

40 Squire, H.B. The Growth of a vortex in turbulent flow. The Aeronautical Quarterly August 1965, PP. 302-306.

41 Washburn, A. Effect of external influences on subsonic delta wing vortices. AIAA 92-4033.

42 Lan, E. Calculated effect of free stream turbulence on aerodynamic characteristics of a delta wing . AIAA J. Vol.33,No.9 Sep.1995.

43 Pedisius, A., Janusas, V. and Zygmantas, G. Distortion of the structure of the turbulent boundary layer by high free stream turbulence . Fluid Mech.-Soviet Research Vol.20, No.5 Sep.1991.

44 Kim, B. and Chung, M. Experimental study of roughness effects on the separated flow over a backward facing step. AIAA J. Vol.33 No.1 1995.

45 White, F. Vicous fluid flow. McGRAW-HILL. Second edition 1991.

46 Atta, R. and Rockwell, D. Hysteresis of vortex development and break down on an oscillating delta wing. AIAA Journal. Vol.25,No.11 Sep.1987.

47 Visbal, M. and Gordnier, R. Pitch rate and pitch axis location effects on vortex break down onset. Journal of Aircraft Vol.32, No. 5 Oct.1995.

48 Ericsson, L. Pitch rate effects on delta wing vortex break down. Journal of Aircraft Vol.33, No.3.

49 Ericsson, L. Vortex break down dynamics on pitching delta wings.AIAA 95-1777-CP.

50 Thompson, D. A water tunnel study of vortex break down over wings with highly swept leading edges. Aerodynamic Note 356, ARL/A.356 May 1975.

51 Ekaterinaris, J. and Schiff, L. Numerical simulation of incidence and sweep effects on delta wing vortex break down. Journal of Aircraft Vol.31, No.5 Oct. 1994.

52 Poll, D. Spiral vortex flow over a swept –back wing . Aeronautical Journal. May 1986.

53 Lamar, J. Non-linear lift control at high speed and high angle of attack using vortex flow technology. AGARD Report-740 1986.

54 Panton, R. Effects of a contoured apex on vortex break down. Journal of Aircraft Vol.27, No.3 March 1990.

55 Rao, D. and Campbell, J. Vortical flow management techniques. Progress in Aerospace. Science Vol.24, pp.173- 224.

56 Kerho, M., Hutcherson, S., Blachwelder, R. and Liebeck, R. Vortex generators used to control Laminar separation bubbles. Journal of Aircraft Vol.30, No.3 June 1993.

57 Kern, S. Numerical investigation of vortex flow control through small geometry modifications at the strake/wing juncture of a cropped double-delta wing. AIAA 92-0411.

58 Kern, S. Vortex flow control using fillets on a double delta wing. Journal of Aircraft Vol.30,No.6 Dec.1993.

59 Hebbar, S., Platzer, M. and Khozam, A. Investigation into the effects of juncture fillets on the vortical flow over a cropped double delta wing. AIAA 94-0626.

60 Hebbar, S., Platzer, M. and Khozam, A. Experimental investigation of vortex flow control using juncture fillets on a cropped double delta wing. AIAA 95-0649.

61 Hebbar, S., Platzer, M. and ALKhozam, A. Experimental study of vortex flow control on double delta wing using fillets. Journal of Aircraft Vol.33, No.4 Aug.1996.

62 Huyer, S. Reavis, M. and Luttges, M. A comparative study of differing vortex structures arising in unsteady separated flows. AIAA 88-2582.

63 Hebbar, S. and Platzer, M. Effect of canard oscillations on the vortical flow field of an X-31A –like fighter model in dynamic motion. AIAA 93-3427.

64 Soltani, M. and Bragg, M. Measurements on an oscillating 70 deg. Delta wing in subsonic flow. Journal of Aircraft Vol.27 No.3 March 1990 pp.211.

65 Soltani, M. and Bragg, M. Measured forces and moments on a delta wing during pitch up. Journal of Aircraft Vol.27 No.3 March 1990 pp.262.

66 Wood, N., Roberts, L. and Lee, K. The control of vortical flow on a delta wing at high angle of attack. AIAA 87-2278.

67 Celik, Z. and Roberts, L. Vortical flow control on a delta wing by lateral blowing. AIAA94-0509.

68 Gursul, I., Srinivas, S. and Batta, G. Active control of vortex break down over a delta wing. AIAA Journal. Vol.33 No.9.

69 Ding, Z., Shin, C. and Lourenco, L. Leading edge vortices of a delta wing flow field –a PIV study. AIAA 95-0652.

70 Yang, H. Control of vortex break down on a delta wing by leading edge blowing and suction. AIAA 94-0622.

71 Johari, H. and Moreira, J. Delta wing vortex manipulation using pulsed and steady blowing during ramp-pitching. Journal of Aircraft Vol.33 No.2 April 1996.

72 Williams, S. and Garry, K. An experimental investigation into yaw control at high alpha on a chined fore body using slot blowing. Aeronautical Journal. Oct.1996.

73 Ng, T., Malcolm, G. and Lewis, L. Flow visualisation study of delta wings in wing – rock motion. AIAA 89-2187-CP.

74 Myose, R., Hayashibara, S., Yeong, P. and Miller, L. Effect of canards on delta wing vortex break down during dynamic pitching. Journal of Aircraft Vol.34 No.2 April 1997.

75 Michelsen, W. and Mueller. Low Reynolds number airfoil performance subjected to wake interference from an upstream airfoil. AIAA 87-2351.

76 Hebbar, S. and Platzer, M. Static and dynamics water tunnel flow visualisation studies of a canard configured X-31 like fighter aircraft model. AIAA 91-1629.

77 Hebbar, S. and Platzer, M. Vortex break down studies of a canard configured X-31 like fighter aircraft model. Journal of Aircraft Vol.30 No.3.

78 Alex, K., Hanff, E. and Kind, R. Water tunnel investigation of dynamic manipulation of fore body vortices. AIAA 94-0503.

79 Rao, D. Vortical flow management for improved configuration aerodynamics-recent experiences. AGARD report No.30.

80 Vaughan, J. and Wood, N. Unsteady aerodynamics effects on a half delta wing oscillating in pitch. AIAA 95-1874-CP.

81 Frink, N. and Lamar, J. Water tunnel and analytical investigation of the effect of strake design variables on strake vortex break down characteristics . NASA TP 1676.

82 Debry, B., Komerath, N., Liou, S., Caplin, J. and Lenakos, J. Measurements of the unsteady vortex flow over a wing –body at angle of attack. AIAA 92-2729.

83 Viswanath, P. and Patil, S. Aerodynamic characteristics of delta wing-body combinations at high angles of attack. Aeronautical Journal. May 1994 .

84 Thompson, D. Water tunnel flow visualisation of vortex break down over the F/A-18. ARL-Flight-Mech-R-179.

85 Kramer, B., Suarez, C. and Malcolm, G. Fore body vortex control on an F/A-18 in a rotary flow field. AIAA 94-0619.

86 Hebbar, S. and Platzer, M. A water tunnel investigation of the effects of pitch rate and yaw on LEX generated vortices of an F/A-18 fighter aircraft model. AIAA 91-0280.

87 Klute, S. and Telionis, D. Experimental investigation of three-dimensional vortex interactions over the F/A-18 fore body. AIAA 94-0623.

88 Verhaagen, N., Houtman, E. and Verhelst, J. A study of wall effect on the flow over a delta wing. AIAA 96-2389-CP.

89 Murthy, A. Effects of aspect ratio and side wall boundary layer in airfoil testing. Journal of Aircraft Vol.25 No.3.

90 Katz, J. and Walters, R. Effects of large blockage in wind tunnel testing. Journal of Aircraft Vol.32 No.5.

91 Barnwell, R. Similarity rule for side wall boundary layer effect in two-dimensional wind tunnels. AIAA Journal Vol.18 No.9.

92 Sewall, W. Effects of side wall boundary layers in two-dimensional subsonic and transonic wind tunnels. AIAA 81-1297 R.

93 Murthy, A. Corrections for attached side wall boundary layer effects in two-dimensional airfoil testing. NASA CR 3873.

94 Lawford, J. A. Low-Speed Wind Tunnel Experiments on a Series of Sharp-Edge Delta Wings. Aeronautical Research Council, Tech. Note Aero. 2954, March 1964.

95 Earnshaw, P. and Lawford, J. Low-Speed Wind-Tunnel Experiments on a Series of Sharp-Edged Delta Wings. Aeronautical Research Council R. & M. No. 3424. March 1964.

96 Werle, H. and Solignac, J. Bulbes de Recirculation au Sein D'un Sillage Rech. Aerosp – No. 1977-1, Jan-Feb.

97 Gad-el-Hak, M. and Bandyopadhyay, P. Reynolds number effects in Wall-Bounded Flows. Journal of Fluids Engineering, Vol. 116, March 1994.

98 Kuchemann F.R.S. The Aerodynamic Design of Aircraft. Pergamon Press.1978.

99 Fomison, N. The effects of bluntness and sweep on glancing shock wave turbulent boundary layer interaction. Ph.D. Thesis, Cranfield University, 1986.

100 Schetz, J. Boundary Layer Analysis. Prentice Hall, 1993.

101 Huang, X., Sun, Y. and Hanff, E. Further investigations of leading-edge vortex breakdown over delta wings. AIAA-97-2263.

102 Guglieri, G. and Quagliotti, F. Experimental investigation of vortex dynamics on a 65 delta wing in side-slip. Aircraft Journal March 1997.

103 Yang, H. and Gursul, I. Vortex breakdown over unsteady delta wings and its control. AIAA Journal ,vol.35,no.3.

104 Visser, K. and Nelson, R. A flow visualisation and aerodynamic force data evaluation of spanwise blowing on full and half span delta wings. AIAA-89-0192.

105 Kegelman, J. and Roos, F. Effects of leading-edge shape and vortex burst on the flow field of a 70 degree sweep delta-wing. AIAA-89-0086.

106 Payne, F. and Nelson, R. An experimental investigation of vortex breakdown on a delta wing. AIAA Fluid dynamics, and laser conference 19th ,1987.

107 Cunningham, A. Vortex flow hysteresis. AIAA Fluid dynamics and laser conference 19th, 1987.

108 Weinberg, Z. Effect of tunnel walls on vortex breakdown location over delta wings. AIAA Journal, vol.30, No.6,1992.

109 Bruun, H.H. Hot-film anemometry in liquid flows. Measurement .Science Technology. 7(1996) 1301-1312.

110 Verhaagen, N. Meeder, J. and Verhelst, J. Boundary layer effects on the flow of a leading edge vortex. AIAA-93-3463-cp.

111 Subrahmanyam, K. and Marchman, J. End plate gap effects on a half wing model at low Reynolds number. AIAA-87-2350.

112 Walton, S. Nelson, R. and Batill, S. A comparison of the aerodynamic characteristics of half-span and full-span delta wings. AIAA-89-2161-cp.

113 Murthy, A. Effect of aspect ratio on side wall boundary-layer influence in two-dimensional airfoil testing. AIAA-87-0295.

114 Agui, J. and Andreopoulos, J. Near wall vorticity flux dynamics in a three dimensional boundary layer with separation. AIAA-91-0733.

115 Pass, C.A. Wake blockage correction method for small subsonic wind tunnels. AIAA-87-0294.

116 Fleming, J. and Simpson, R. Experimental investigation of the near wall flow structure of a low Reynolds number 3-d turbulent boundary layer. AIAA-94-0649.

117 Fleming, J. and Simpson, R. Further investigation of the near wall flow structure of a low Reynolds number 3-D turbulent boundary layer. AIAA-95-0788.

118 Hurley, D.G. The downstream effect of a local thickening of the laminar boundary layer. July 1955 A.R.L./A. 146 NOTE.

119 Hopkins, E., Jillie, D. and Sorensen, V. Charts for estimating boundary-layer transition on flat plates. June 1970 NASA TN D-5846.

120 Frink, N. Computational study of wind-tunnel wall effects on flow field around delta wings. AIAA 87-2420.

121 Ashill, P. and Keating, R. Calculation of tunnel wall interference from wall-pressure measurements. Aeronautical Journal. pp36 , Jan 1988.

122 Freestone, M. Vorticity measurement by a pressure probe. Aeronautical Journal. pp 29 ,Jan 1988.

123 Mendelsohn, R. and Polhamus, J. Effect of the tunnel-wall boundary layer on test results of a wing protruding from a tunnel wall. NACA Technical Note No. 1244. April 1947.

124 Gursul, I. and Ho, C. Vortex Breakdown over delta wings in unsteady free stream,AIAA 93-0555.

125 Lowson, M. Visualisation measurements of vortex flow. AIAA 89-0191.

126 Ekaterinaris, J. Numerical Simulation of the effects of variation of angle of attack and sweep angle on vortex breakdown over delta wings. AIAA 90-3000.

127 Kegelman, J. and Roos, F. The flow field of burst vortices over moderately swept wings. AIAA 90-0599.

128 Nelson, R. and Pelletier, A. Factors influencing vortex breakdown over 70 deg. Swept delta wing. AIAA 95-3469.

129 Nelson, R. and Pelletier, A. An Experimental study of static and dynamic vortex breakdown on slender delta wing plan forms. AIAA 94-1879.

130 Thomson, S., Batill, S. and Nelson, R. Delta wing surface pressure for high AoA manoeuvres. AIAA 90-2813.

131 Verhaagen, N and Ransbeeck, P. Experimental and Numerical investigation of the flow in the core of a leading edge vortex. AIAA 90-0384.

132 Karou, A. Separated vortex flow over slender wings between side walls theoretical and experimental investigation. Report LR-300 1980,Delft U.

133 Delery, J. Aspects of vortex breakdown. Progress Aerospace Science Vol.30 pp1-59, 1994.

134 Katz, J. and Walters, R. Investigation of Wind-Tunnel Wall Effects in High Blockage Testing. AIAA 95-0438.

135 Galbraith, R. The aerodynamic characteristics of a GU25-5(11)8 aero-foil for low Reynolds numbers. Experimental in Fluid Vol.3 No.5, 1985.

136 Bray, T. A parametric study of vane and air-jet vortex generators. Ph.D. Thesis, Cranfield University, 1998.

137 Van Dyke, M. An Album of Fluid Motion. The Parabolic Press, 1997.

138 Conger R. and Ramaprian, B. Pressure Measurements on a Pitching Airfoil in a Water Channel. AIAA Journal, Vol.32, No.1, Jan1994.

139 Traub, L. and Rediniotis, O. Low-Reynolds-Number Effects on Delta-Wing Aerodynamics. Journal of Aircraft, Vol.35, No. 4.

140 Gursul, I and Ho, C. Vorticity Dynamics of 2-D and 3-D Wings in Unsteady Free Stream. AIAA 91-0010.

141 Gursul, I. and Yang, H. Further experiments on fluctuations of vortex breakdown location. AIAA 96-0205.

142 Gursul, I. Self-Excited oscillations of vortex breakdown location over delta wings. AIAA 97-0744.

143 Gursul, I. Physics of buffeting flows over delta wings. AIAA 98-0688.

144 Wood, N. and Chesneau, T. Fin buffeting characteristics of a generic single fin aircraft. AIAA95-0439.

145 Wood, N. and Wood, M. Unsteady aerodynamic phenomena on novel wing planforms. ICAS-96-2.11.2.

146 Goldstein, S. Modern development in fluid dynamics, Oxford university press, 1943.

147 Roos, F. and Kegelman, J. An Experimental investigation of sweep-angle influence on delta-wing flows. AIAA-90-0383.

148 Rockwell, D. and Magness, C. Unsteady cross flow on a delta wing using Particle Image Velocimetry Journal of Aircraft Vol.29, No.4, July-Aug.1992.

149 Telionis, D. and Rediniotis, O. 3-D LDV Measurements over a delta wing in pitching motion. AIAA 93-0185.

150 Telionis, D. and Rediniotis, O. Instabilities of vortex breakdown; Their structure and growth. AIAA 95-2308.

151 Traub, L. Prediction of vortex breakdown and longitudinal characteristics of swept slender planforms. Journal of Aircraft Vol.34, No.3,May-june 1997.

152 Verhaagen, N. Tunnel wall effect on the flow around a 76/40 deg. double delta wing. AIAA 98-0312.

153 Evans, R. Freestream turbulence effects on turbulent boundary layers in an adverse pressure gradient. AIAA Journal. Vol.23, No.11 November 1985.

154 Mabey, D. Unsteady vortex flow phenomena on delta wings at high angles of incidence. ICAS-96-1.6.1.

155 Rediniotis, O. and Maines, B. The effects of leading edge suction on delta wing vortex breakdown. AIAA 99-0128.

156 Ho, C. and Lee, M. Response of a delta wing in steady and unsteady flow. ASME Vol.52, 1987 pp.19-24.

157 Gad-el-Hag, M. and Blackwelder, R. The discrete vortices from a delta wing. AIAA Journal. Vol.23, No.6, June 1985.

158 Fage, A. and Johansen, F. The structure of vortex sheets. ARC R&M 1143 ,1928

159 Garry, K. and Broadley, I. Effectiveness of vortex generator position and orientation on highly swept wings. AIAA 97-2319.

160 Traub, L. Prediction of tunnel wall upwash for delta wings including vortex breakdown effects. The Aeronautical Journal March 1999.

161 Hanff, E. and Huang, X. Unsteady behaviour of spiral leading-edge vortex breakdown. AIAA 96-3408.

162 Johari, H. and McManus, K. Visualisation of pulsed vortex generator jets for active control of boundary layer separation. AIAA 97-2021.

163 Johnston, J. and Nishi, M. Vortex generator jets-A means for passive and active control of boundary layer separation. AIAA 89-0564.

164 Shabaka, I. and Bradshaw, P. Longitudinal vortices imbedded in turbulent boundary layers. Part 1. Single vortex. Journal Fluid Mech.Vol.155,1985, pp37-57.

165 Fage, A. and Warsap, J. The effects of turbulence and surface roughness on the drag of a circular cylinder. ARC R&M 1283 October 1929.

166 Ericsson, L. and King, H. Effect of leading edge cross-sectional geometry on slender wing unsteady aerodynamics. AIAA 92-0173.

167 Polhamus, E. A Concept of the vortex lift of sharp-edge delta wings based on a leading edge-suction analogy. NASA TN D-3767.

168 Charnay, G. and Mathieu, J. Development of a turbulent boundary layer on a flat plate in an external turbulent flow. AGARD CP 93, 1972 pp.27.1-27.10.

169 Elle, B. An investigation at low speed of the flow near the apex of thin delta wings with sharp leading edges. ARC F.M.2629, Jan 1958.

170 Preston, J. The interference on a wing spanning a closed tunnel arising from the boundary layers on the side walls, with special reference to the design of two-dimensional tunnels. ARC R&M1924.

171 Greenwell, D. and Wood, N. Some observations on the dynamic response to wing motion of the vortex burst phenomenon. Aeronautical Journal Feb. 1994.

172 Greenwell, D. and Wood, N. Determination of vortex burst location on delta wings from surface pressure measurements. AIAA Journal Vol. 30, No. 11, Nov.1992.

173 Ericsson, L. Critical issues in High-Alpha vehicle dynamics. AIAA 91-3221.

174 Gursul, I. and Menke, M. Nonlinear response of vortex breakdown over a pitching delta wing. Journal of Aircraft Vol.36, No.3, May-June 1999.

175 Chen, J. and Choa, C. Freestream disturbance effects on an airfoil pitching at constant rate. Journal of aircraft Vol.36, No.3, May-June 1999.

176 Ericsson, L. Dynamic stall of pitching airfoils and delta wings, similarities and differences. Journal of aircraft Vol.36, No.3,May-June 1999.

177 Kirkpatrick , D. Analysis of the static pressure distribution on a delta wing in subsonic flow. ARC 30871 August 1968.

178 Pope, A. Wind tunnel calibration techniques. AGARD0graph 54, April 1961.

179 MacMillan, F.A. Viscous effects on flattened pitot tubes at low speeds. 1954 ARC 17106.

180 MacMillan, F.A. Experiments on pitot tubes in shear flow. 1956 ARC 18235.

181 Bergh, H. and Tijdeman, H. 'Theoretical and experimental results for the Dynamic Response of Pressure Measuring Systems'. NLR TRF 238 (1965).

182 Garner, H.C., Roger E.W., Acum, W.E., and Maskell, E.C. ' Subsonic wind tunnel wall corrections'. AGARDograph 109, Oct. 1966.

183 Anderson, J. Fundamentals of Aerodynamics. McGraw-Hill, Inc. Second Edition, 1991

184 Ericsson, L. and Beyers, M. 'Aspects of Ground Facility Interference on Leading-Edge Vortex Breakdown'. AIAA 2000-0978

185 Ericsson, L. 'Further Analysis of Fuselage Effects on Delta Wing Aerodynamics'. AIAA 2000-0981.

186 Shih, C. and Ding, Z. Unsteady structure of leading edge vortex flow over a delta wing. AIAA 96-0664.

187 Gordnier, R. and Visbal, M. Unsteady vortex structure over delta wing. J. of Aircraft Vol.31 No.1 Feb.1994.

188 Verhaagen, N. and Ransbeeck, P. Experimental and Numerical Investigation of the Flow in the Core of a Leading Edge Vortex, AIAA 90-0384.

189 Houghton, E. and Carpenter, P. Aerodynamics for Engineering Student. Edward Arnold, 1998.

190 Kuethe, A. and Chow, C. Foundations of Aerodynamics. John Wiley & Sons. 1986.

191 Baker, C.J. The Turbulent Horseshoe Vortex. Journal of Wind Engineering and Industrial Aerodynamics, Vol.6, 1980, pp9-23.

192 Barber, T.J. An Investigation of Strut-Wall Intersection Losses. Journal of Aircraft, Vol. 15, No.10, October 1978, pp676-681.

193 Kubendran, L.R., McMahon, H.M. and Hubbartt, J.E. Turbulent Flow Around a Wing/Fuselage-Type Juncture. AIAA Journal, Vol.24, No.9, September 1986, pp1447-1452.

194 Shabaka, I.M.M.A. and Bradshaw, P. Turbulent Flow Measurements in an Idealized Wing/Body Junction. AIAA Journal, Vol. 19, No. 2, February 1981, pp131-132.

195 Shizawa, T. and Honami, S. Experimental Study of Horseshoe Vortex at Wing/Body Junction with Attack Angle by Triple Hot-Wire. AIAA 96-0323.

196 Devenport, W.J., Agarwal, N.K., Dewitz, M.B., Simpson, R.L. and Poddar, K. Effects of a Fillet on the Flow Past a Wing-Body Junction. AIAA Journal, Vol.28, No. 12, December 1990, pp. 2017-2024.

197 Briley, W.R. and McDonald, H. Computation of Turbulent Horseshoe Vortex Flow Past Swept and Unswept Leading Edges. Scientific Research Associates, Inc. Report No. R82-920001-F. March 1982.

198 Fleming, J.L., Simpson, R.L. and Devenport, W.J. An Experimental Study of a Turbulent Wing-Body Junction and Wake Flow. AIAA 92-0434.

199 Mehta, R.D. Effect of Wing Nose Shape on the Flow in a Wing/Body Junction. Aeronautical Journal. December 1984, pp. 456-460.

200 Treaster, A.L. and Gurney, G.B. Sidewall Boundary Layer Corrections in Subsonic, Two-Dimensional Airfoil/Hydrofoil Testing. AIAA 84-1366.

201 Hanselman, D. and Littlefield, B. The Student Edition of MATLAB

Version 5. The Math Work Inc., Prentice – Hall,Inc. 1997.

Chapter 12 Appendices

Appendix-A

Water Tunnel

The water tunnel of Cranfield College of Aeronautics is a 'gravity fed ' type facility. The test section is 22cm x 22cm x 108cm long. Maximum flow velocity is approximately 20 cm/sec. with a turbulence intensity < 0.1. (Figure A-2) shows the schematic diagram of the water tunnel. The half-delta wing model is attached to the middle ring of the water tunnel access aluminium alloy door, where the three other sides are made of glass for flow visualisation studies. (Figure A-1).

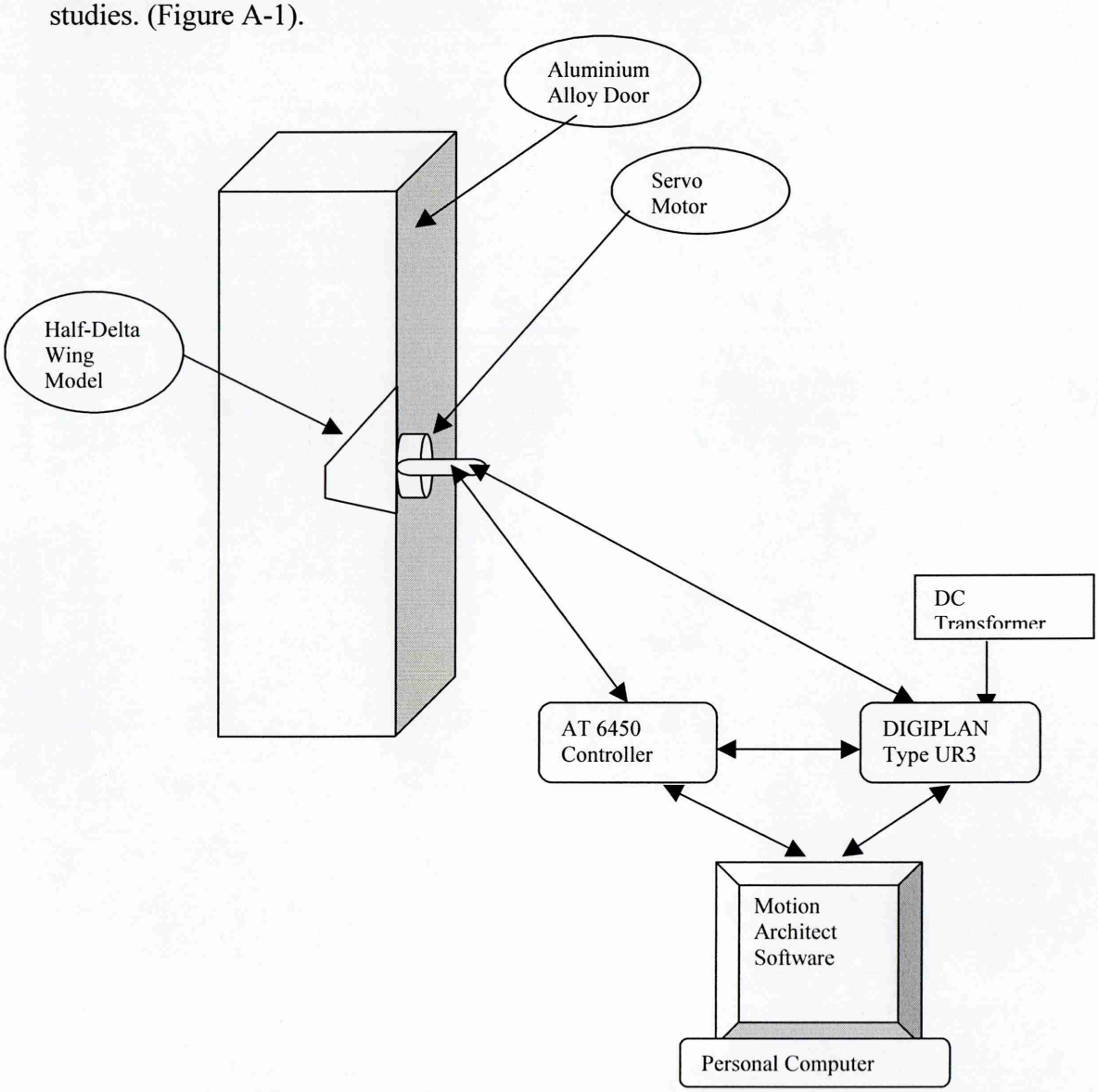

Figure A-1 schematic diagram of Wing Model and The Servo Motor System

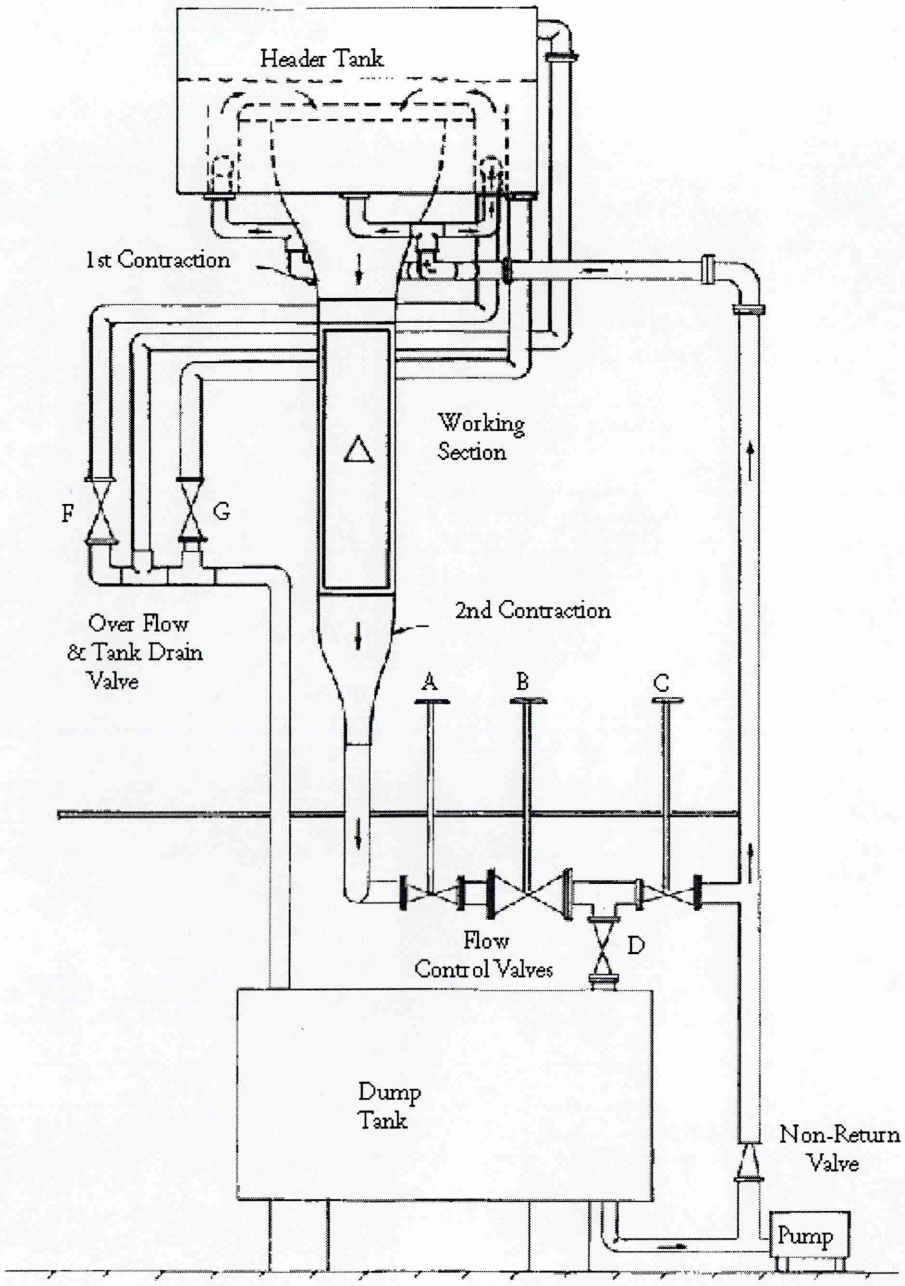

Figure A-2 Water Tunnel Schematic Diagram

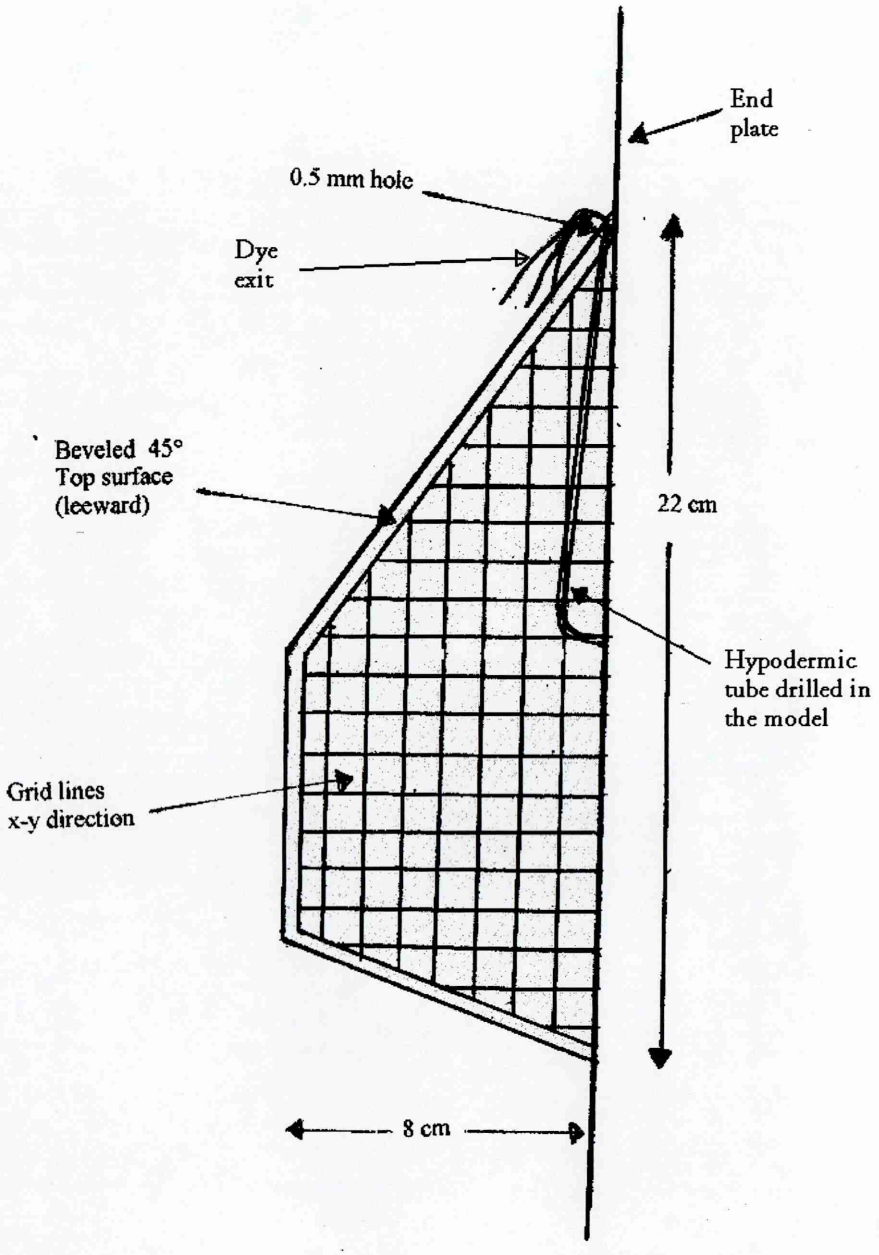

Figure A-3 Dye injection location

Appendix – B

Calibration of the Water Tunnel

An ultrasonic flow meter A500 was used to monitor the flow velocity of the water tunnel (Figure B-1). It is an obstructionless, accurate liquid flow measuring system that can be easily installed into existing piping. There are two interrelated components in the system:

i. **The Sensor**, a factory calibrated flow tube that contains a pair of integrally mounted ultrasonic transducers.
ii. **The Electronic Transmitter**, can be mounted on the sensor or at a remote position up to 30 meters from the sensor.

The Transmitter is enclosed in a weather resistant housing which is fully gasketed – IP65. Operational status indicators (LED's) are located under the enclosure cover. At the end of the Transmitter enclosure are two connectors which accept BNC coaxial cable connectors, one from each Transducer. Power supply and signal connections are achieved by means of flying leads.

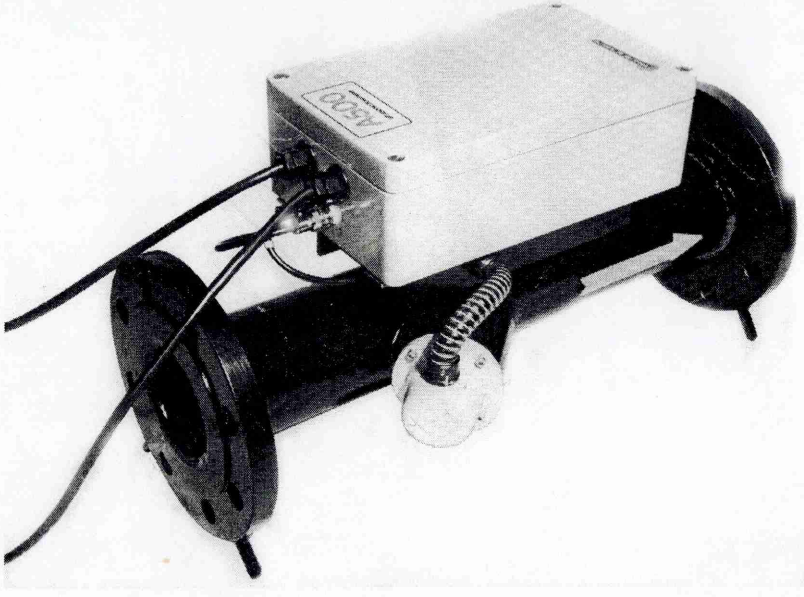

Figure B-1 Ultrasonic Flow Meter A500

The calibration of the water tunnel performed by descending a dye filament over the length of the working test section for different ammeter reading, and by using the linear regression analysis (Fig. B-2), the velocity equation was found :

$$Y = 3.054X - 12.264; \quad Y=\text{flow velocity}, \quad X=\text{Amp. Readout}$$

The water tunnel flow velocity was maintained throughout at a nominal value of 0.077 m/sec. corresponding to a Reynolds number R_e = 17000 based on the model centre line chord. A thermometer was used to monitor the water temperature in the water tank.

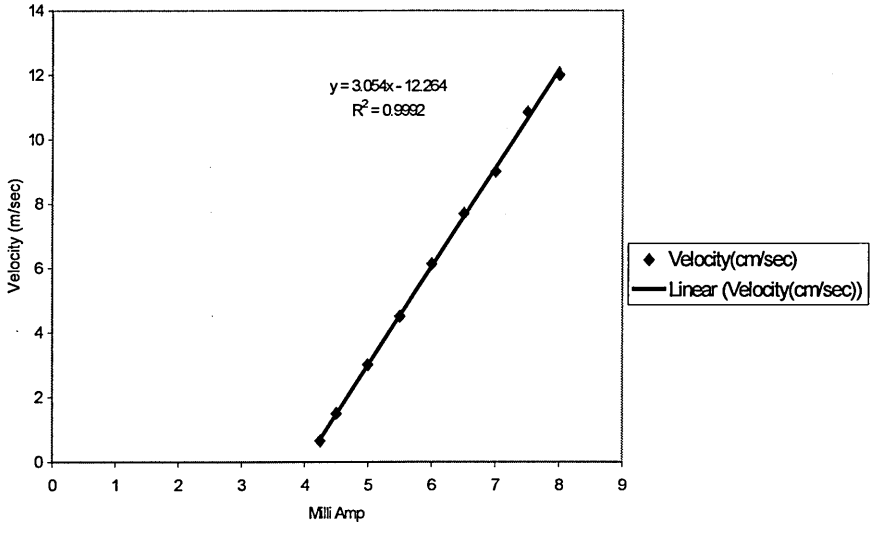

(Figure B-2) Regression Analysis for the velocity at the test section

Appendix – C

Servo Motor

The turn-table that the delta wing model is attached to is controlled by a DC Servo Motor via a PC with a Motion Architect card and Window based application software (Parker Hannifin Corporation), which controls model position. It has an accuracy of 0.01° and a variable speed position (pitch-up and pitch-down), together with the capability of oscillation given the amplitude and frequency of motion. (Figure C-1). The signal from the DC Servo Motor was adjusted and controlled through the DC Servo Drive (DIGIPLAN) and the motor controller AT6450). There were two types of input listed below: mainly one for the static case (Figure C-2) motion and the other is for the dynamic case where programs were written for each reduced pitch rate speed. The program was written in C-Language and input through the Motion Architect Software.

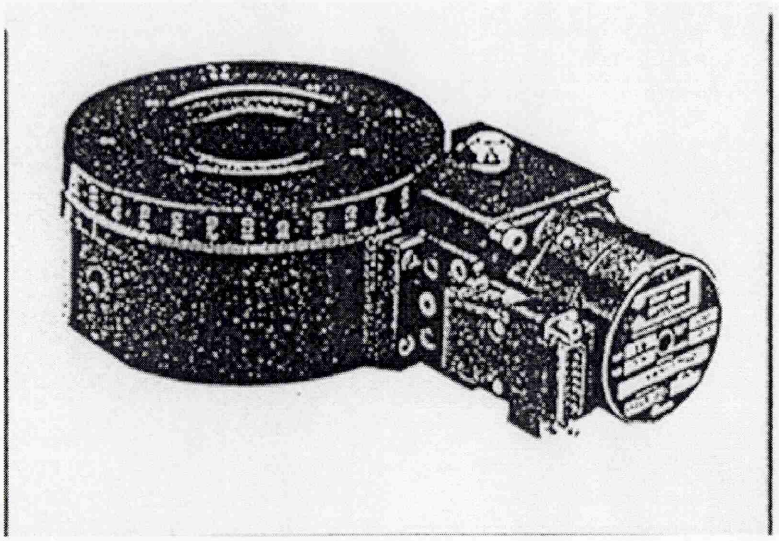

Figure C-1 Servo Motor with turn-table

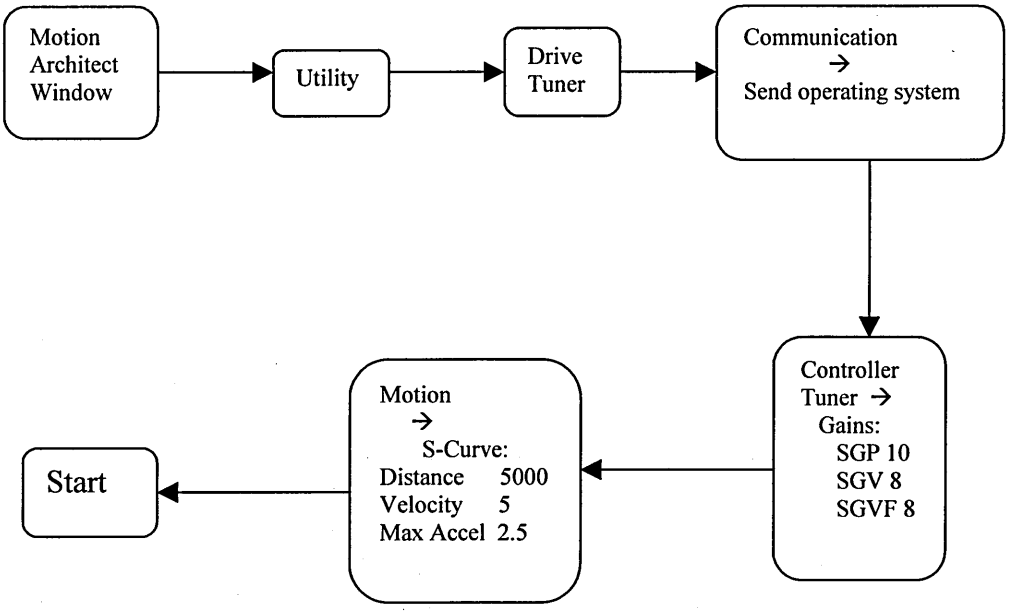

Figure C-2 Block diagram for Static input motion

Dynamic case motion:

Using the same input as for the static motion case, then from the Controller Tuner Window click on Terminal to enter the C-Language programming to write a code that will translate the motion of the Servo Motion for the required amplitude and frequency.

> def dyno1 (it will define a program called dyno1)

> d22500 (it will move the Servo Motor from 0 → 45 deg.)

> v20 (the time required for the motion is 10 sec.)

> l (small letter of L)

> go1

> d~

> t15 (the time will take to rest between pitch-up and down is 15 sec.)

> ln

> end
> run dyno1

Appendix – D

Fibre-Film Probe Anemometer (DANTEC 55R15)

This is a cylindrical quartz fibre thin film sensor which is 70μm in diameter and 3mm long, covered by a nickel thin film approximately 2μm in thickness (Figure D-1). The Probe is mounted by a probe mounting tube (55H136), (Figure D-2).

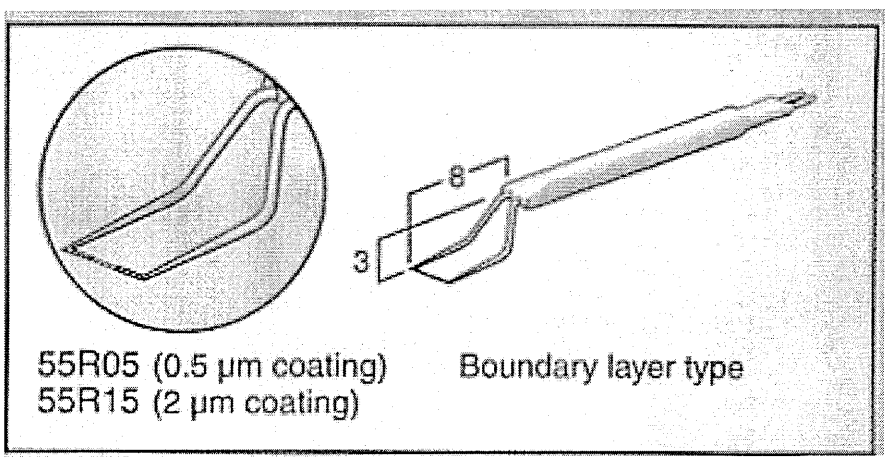

Figure D-1 Fiber-Film Probe (55R15)

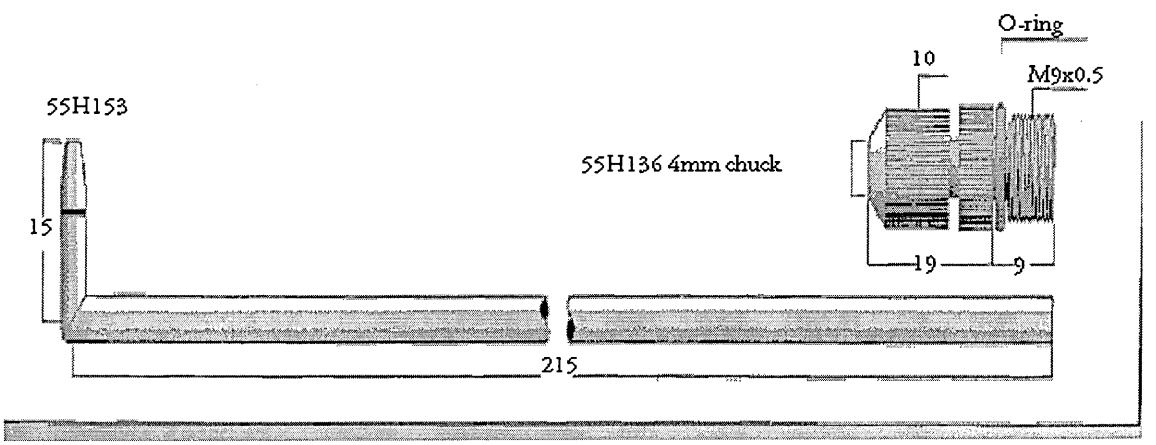

Figure D-2 Fiber-Film Probe Mounting Tube

The Fibre-Film Probe Anemometer measurements are carried out using a digital measurement system which requires a signal conditioning unit (DIGIPLAN), Analogue-to-Digital Converter and a computer system shown in (Fig. D-3).The sampling rate was chosen to be 10,000 in 20 sec for best results.

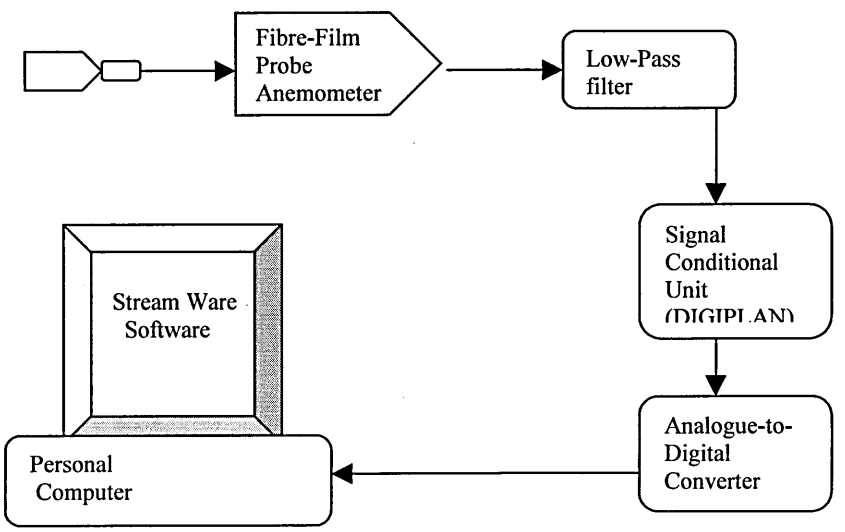

Figure D-3 Schematic diagram of FFPA measurement system

Appendix – E

Wind Tunnel :

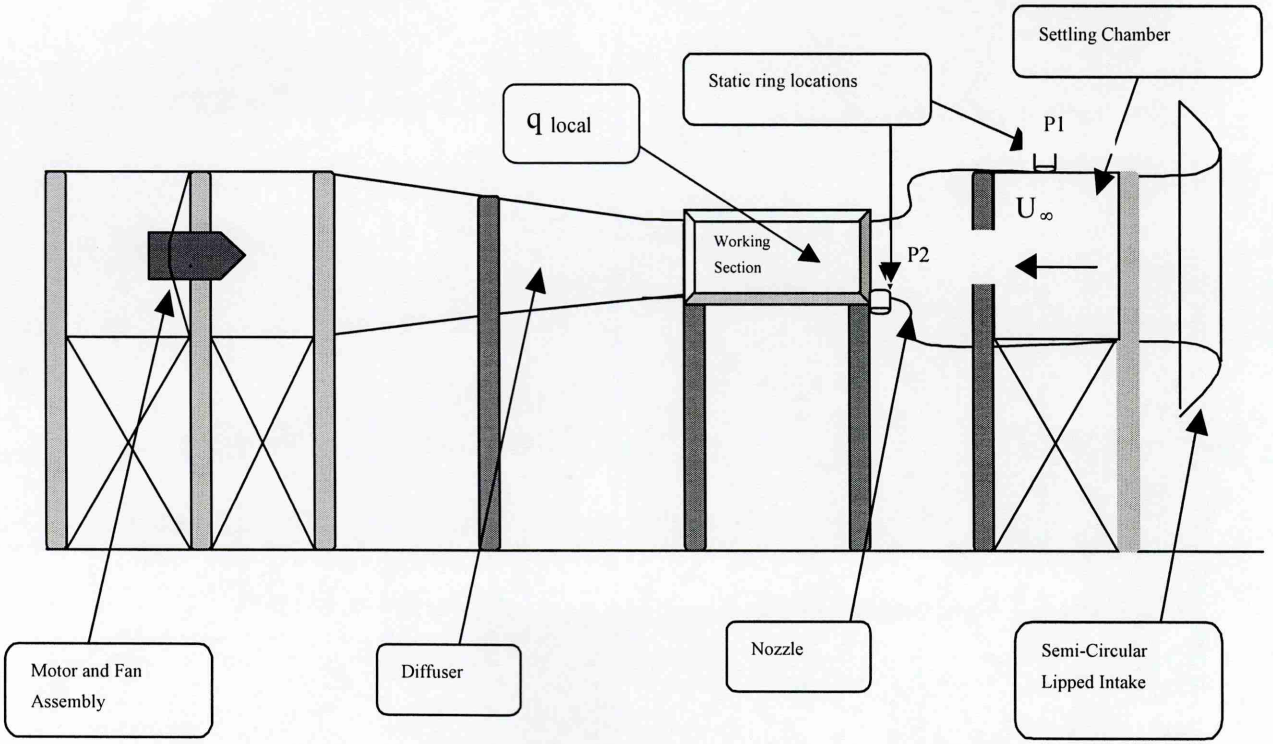

Figure E-1 'Donnington' 3' x 3' Open Return, Closed Working Section, Low Speed Wind Tunnel

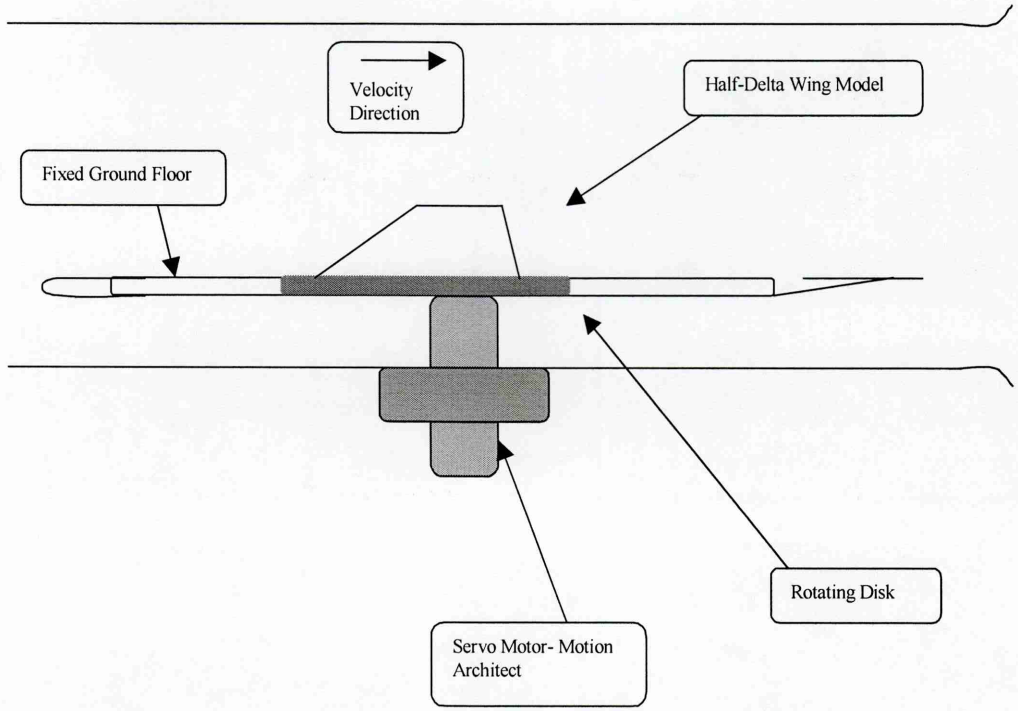

Figure E-2 Working Section and Model Set-Up

Appendix F

Wind Tunnel Calibration

To determine the wind tunnel working section speed, the working section dynamic pressure, q, must be calibrated. This is measured using a pitot tube positioned in the empty working section, where the half-delta wing model is located, calibrated against the difference in pressure, Δp, between the two static pressure rings in the nozzle and settling chamber over a range of speeds, Pope[178]. The calibration factor ' K' was found to be 0.997 (Figure F-1). Two Furness micromanometer transducers FC016 serial no. 9601307 and 9601308 were used to measure the working section dynamic pressure and the pressure difference from the static pressure rings as voltages. The two Furness transducers have been calibrated using a Druck calibrator, where the calibration are 99.8804 mm H_2O/V and 101.480356 mm H_2O/V respectively (Figure F-2).

During the experiment, when the model is placed in the working section, the speed is determined from the difference in pressure between the static pressure rings, measured by transducer serial no. 9601308 as volts, which is multiplied by the calibration constant of the wind tunnel K (0.997) and also by the transducer calibration to give the working section dynamic pressure in mm H_2O, knowing the atmospheric pressure and temperature.

$$q = \rho g h = \tfrac{1}{2} \rho_w v^2$$

;where $\rho_w = p/RT$; $R = 287$ J/kg.k

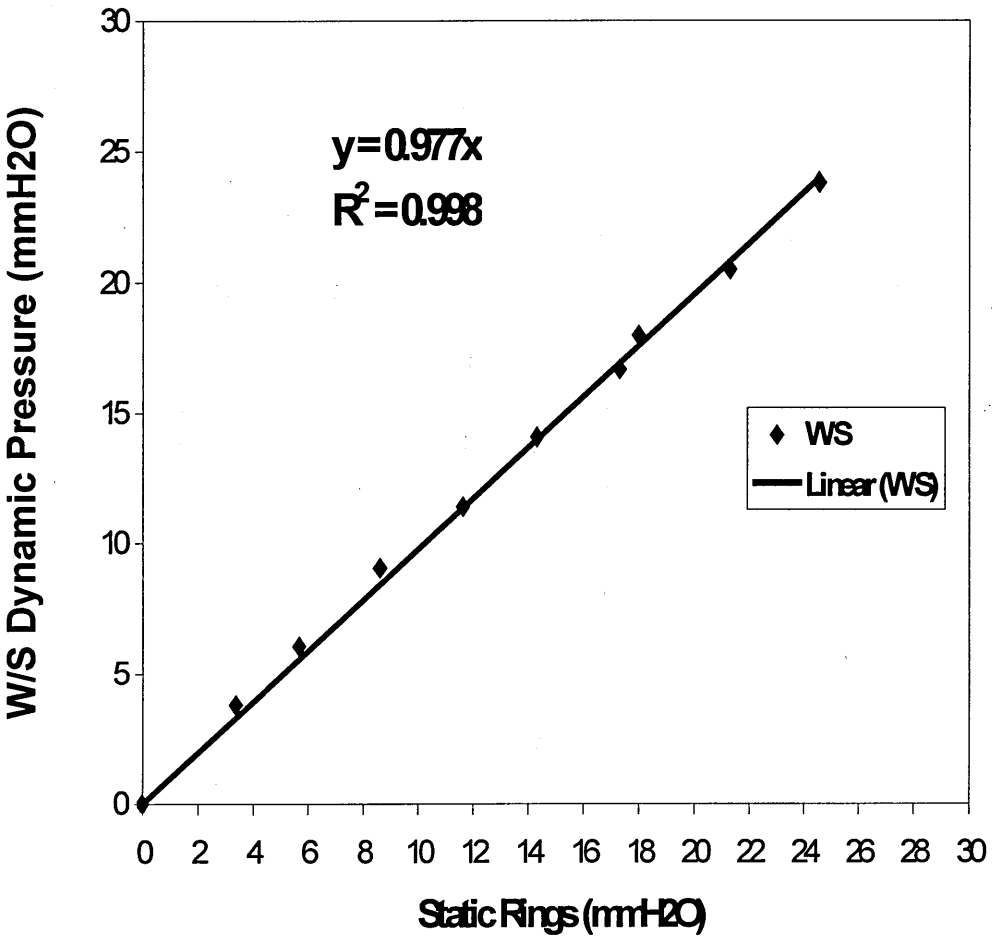

Figure F-1 Wind Tunnel Calibration

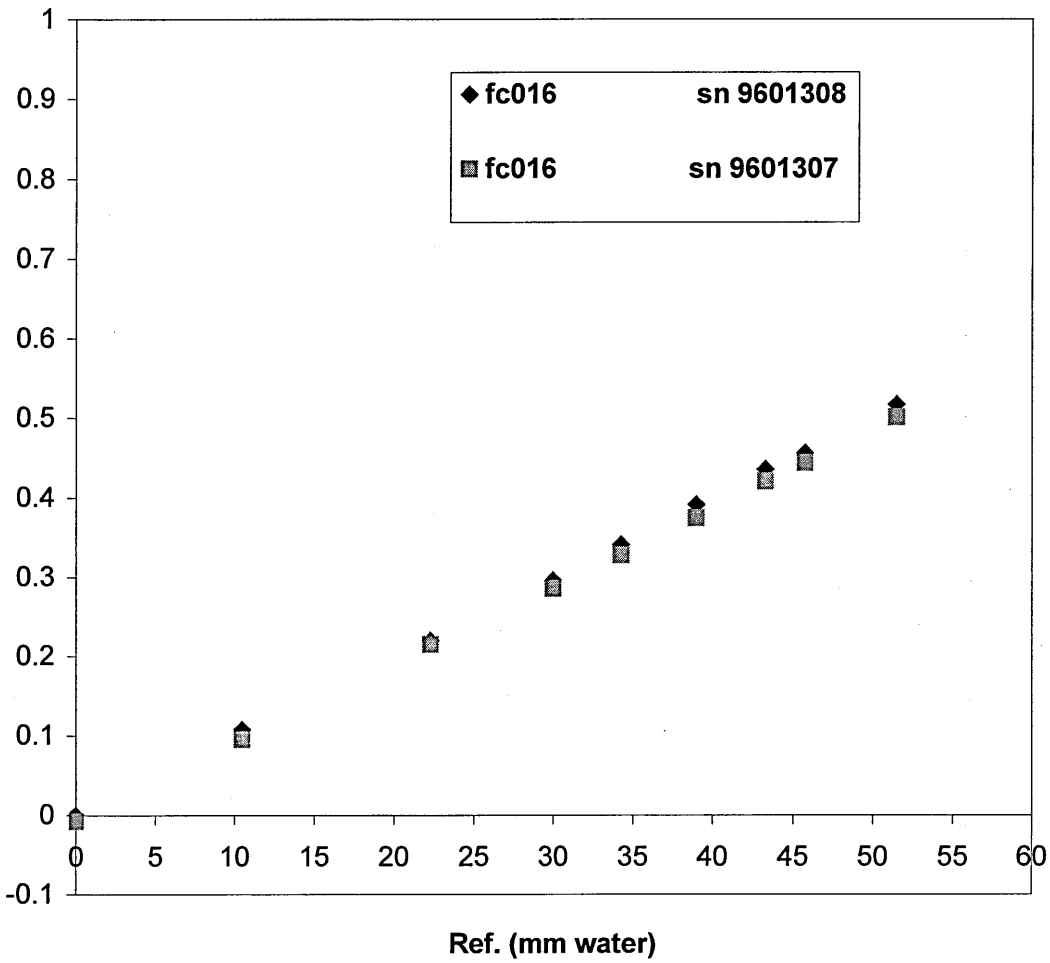

Figure F-2 Furness calibration

Appendix - G

Wind Tunnel Model:

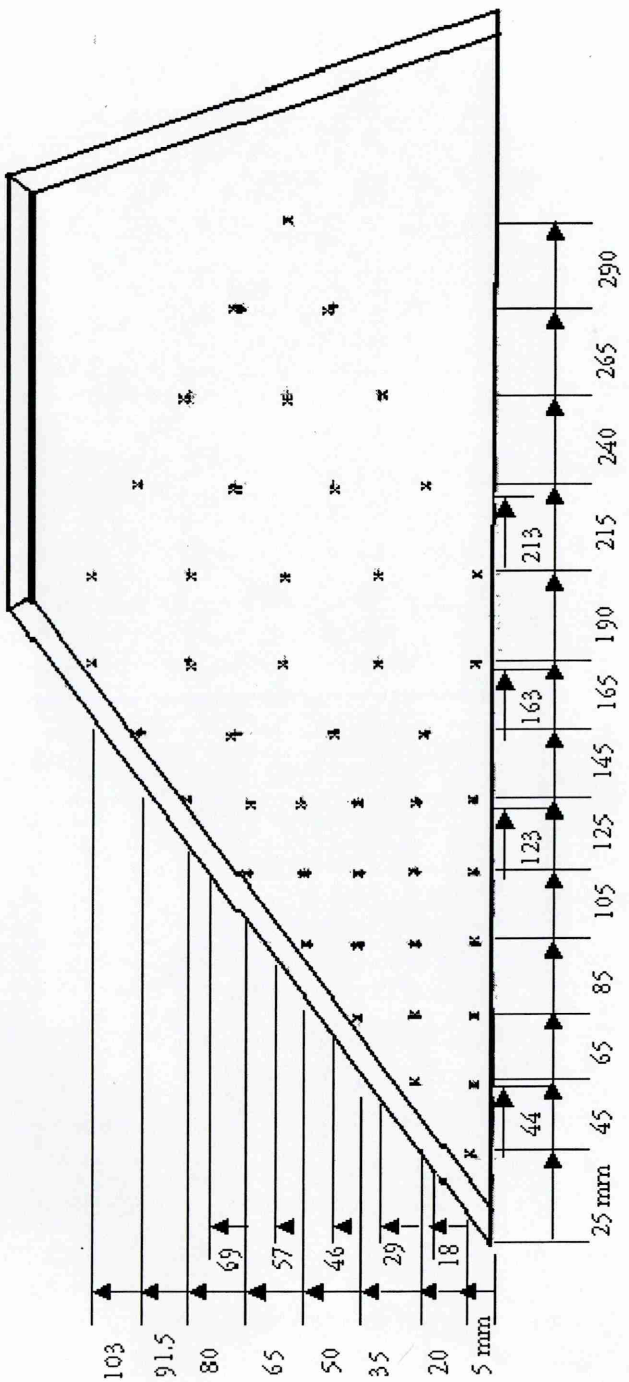

Fig. G-1 Wind Tunnel Half-Delta Wing Model and Pressure Tapping Location

Appendix H:

Water Tunnel Data

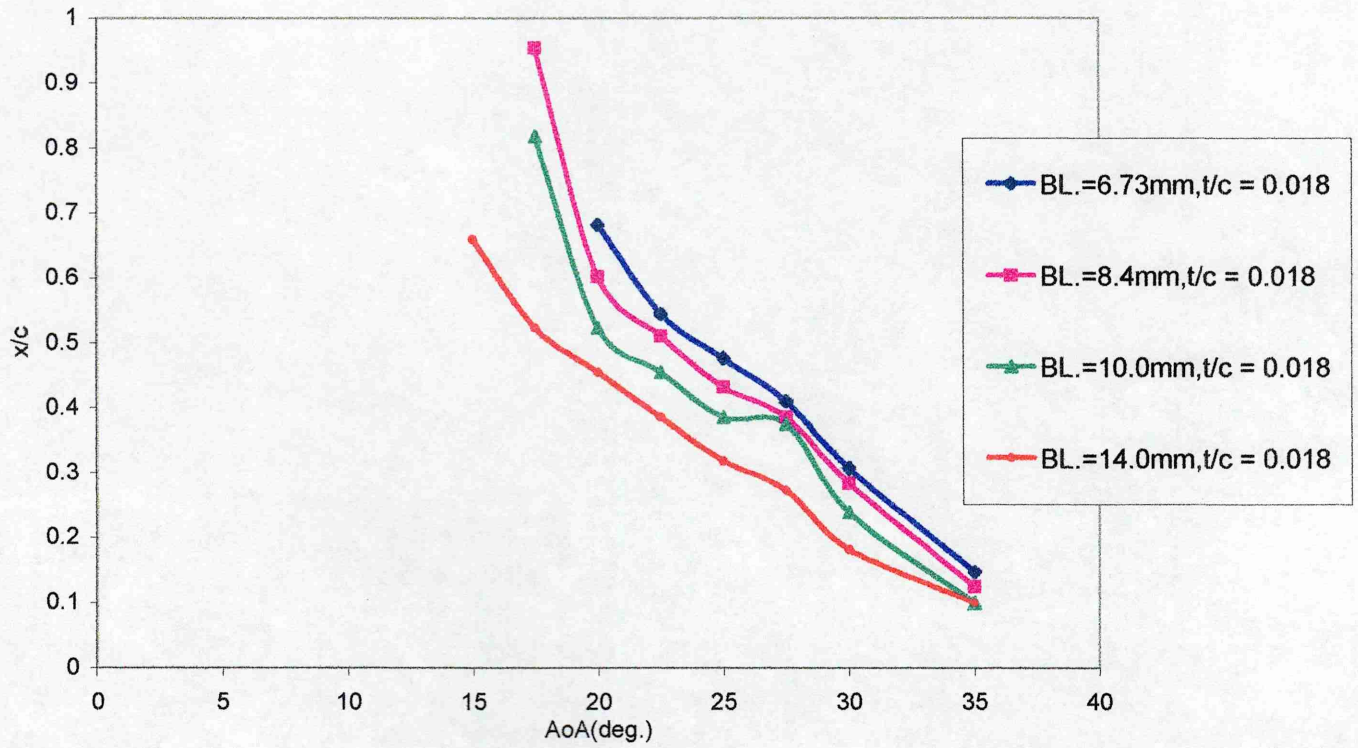

Figure H1 Influence of wall boundary layer thickness on vortex breakdown position for 55 deg. Swept delta wing. (t/c)=0.018

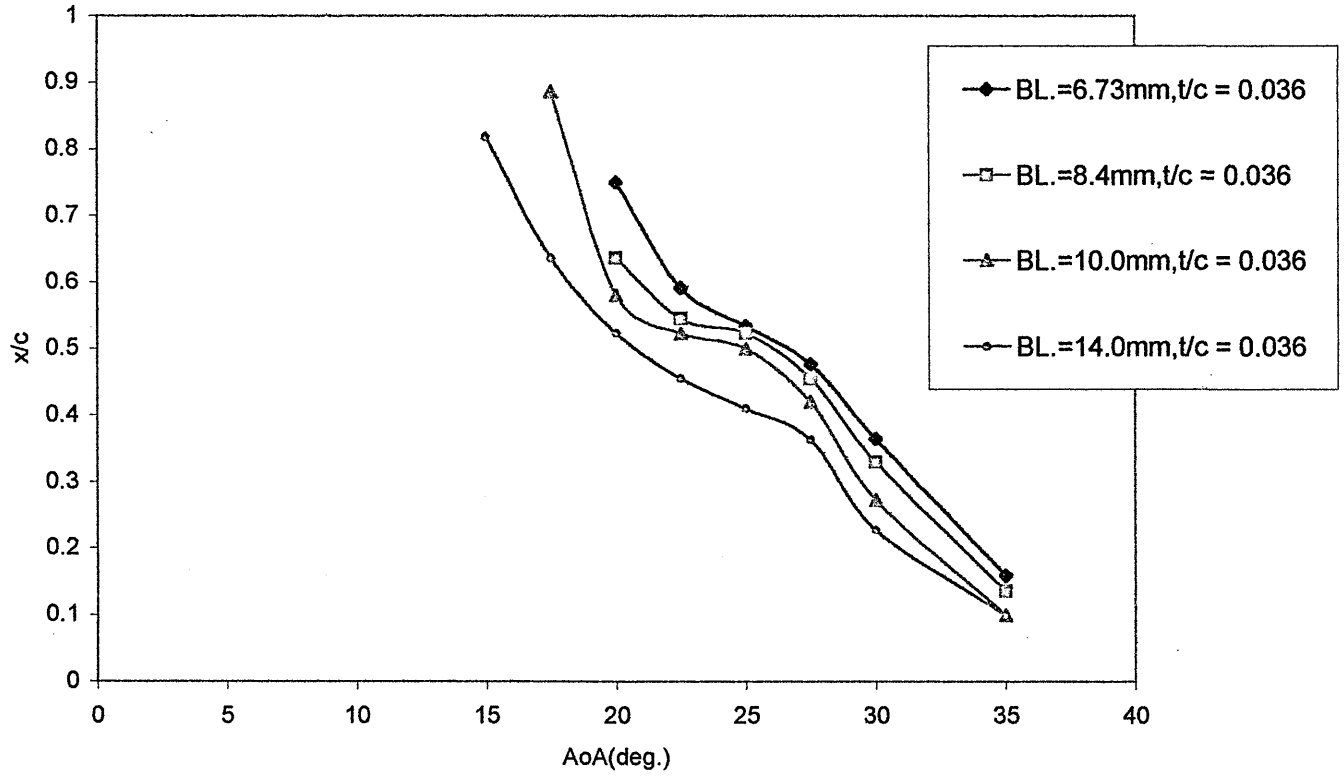

Figure H2 Influence of wall boundary layer thickness on vortex breakdown position for 55 deg. Swept delta wing. (t/c)=0.036

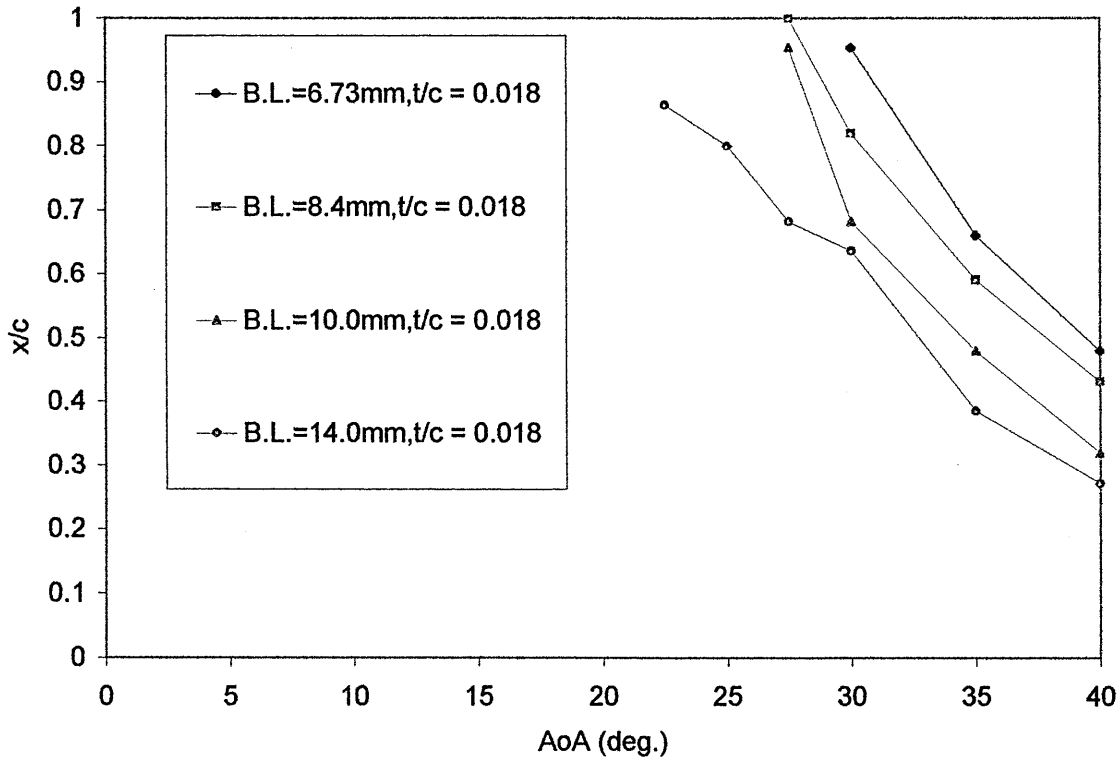

Figure H3 Influence of wall boundary layer thickness on vortex breakdown position for 70 deg. Swept delta wing. (t/c)=0.018

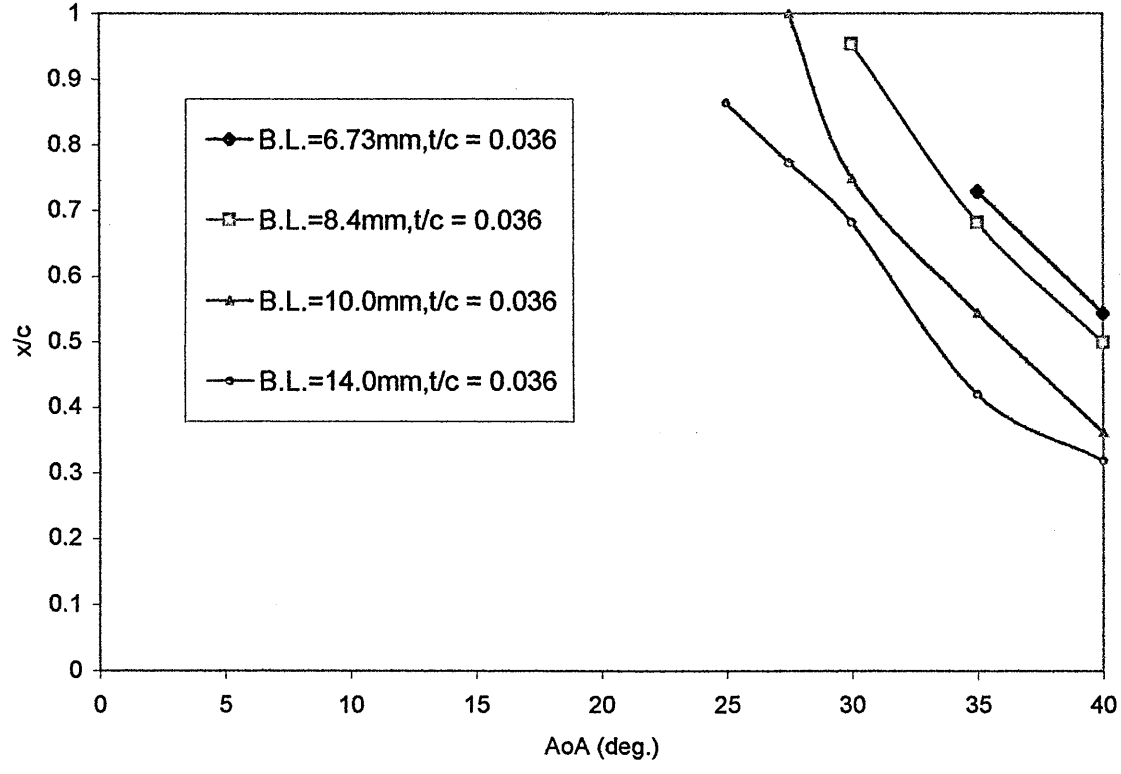

Figure H4 Influence of wall boundary layer thickness on vortex breakdown position for 70 deg. Swept delta wing. (t/c)=0.036

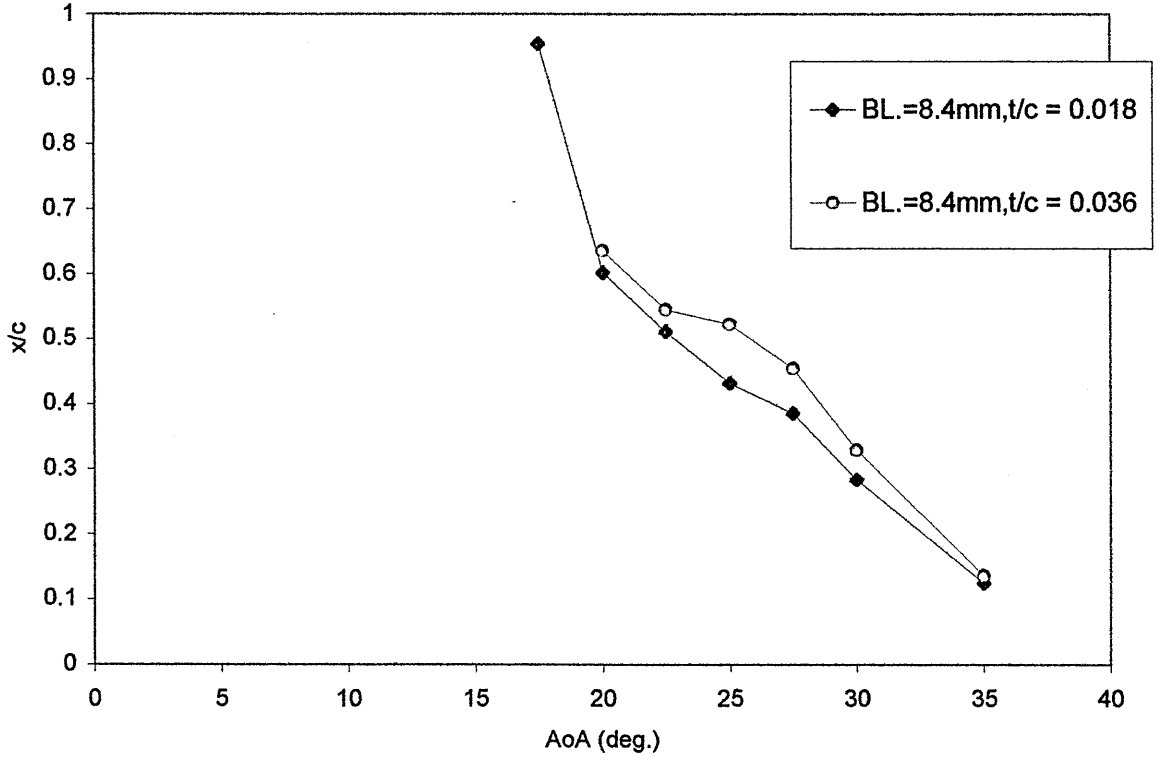

Figure H5 Effect of thickness/chord ratio on vortex breakdown position for 55 deg. swept delta.

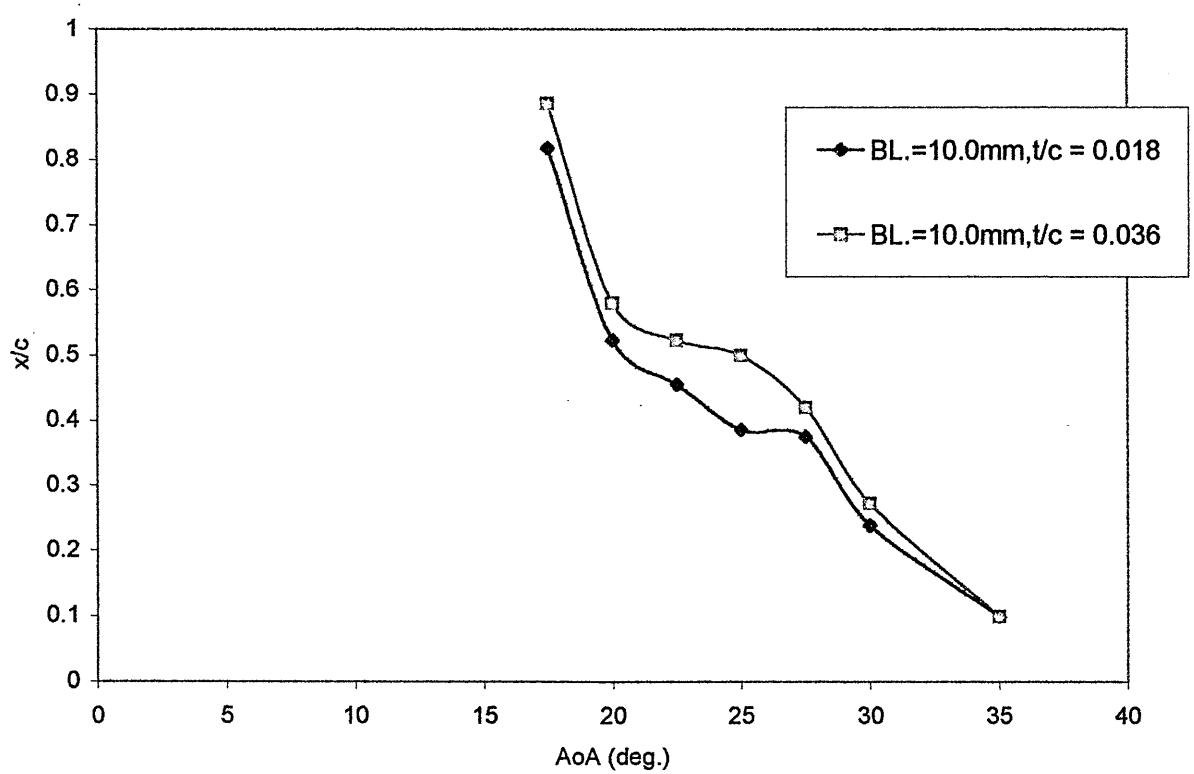

Figure H6 Effect of thickness/chord ratio on vortex breakdown position for 55 deg. swept delta.

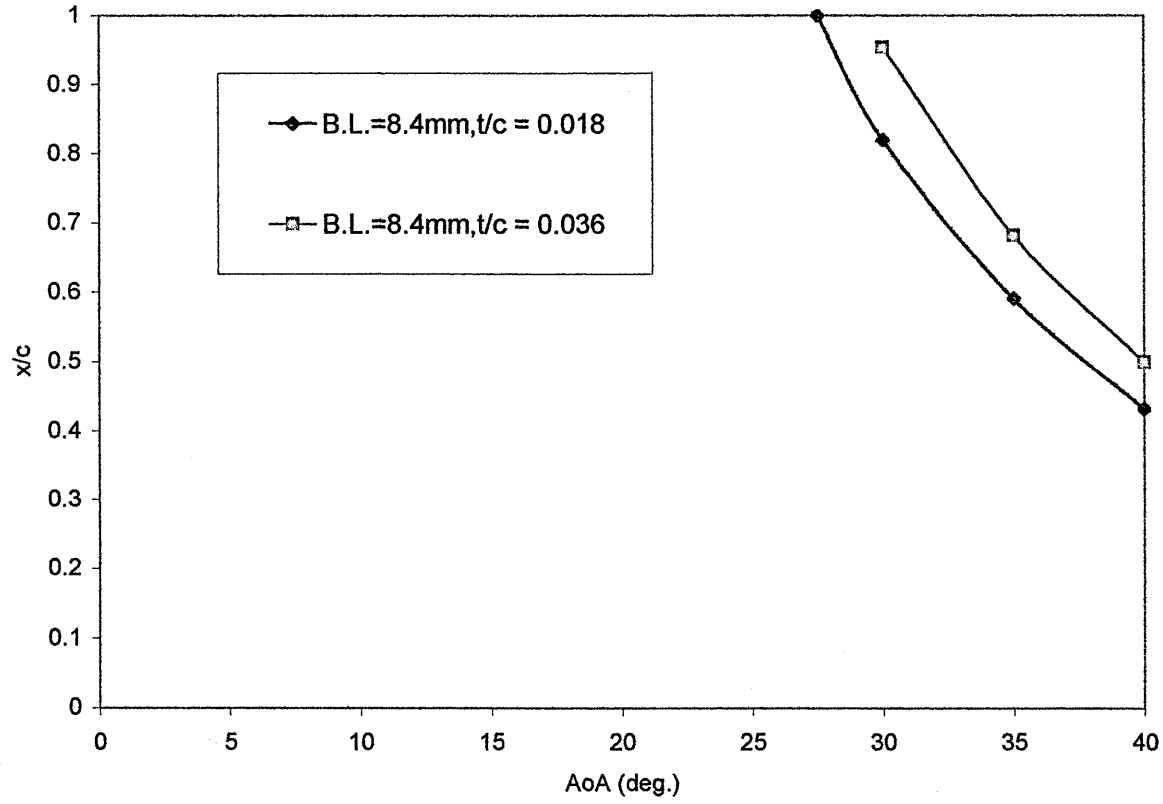

Figure H7 Effect of thickness/chord ratio on vortex breakdown position for 70 deg. swept delta.

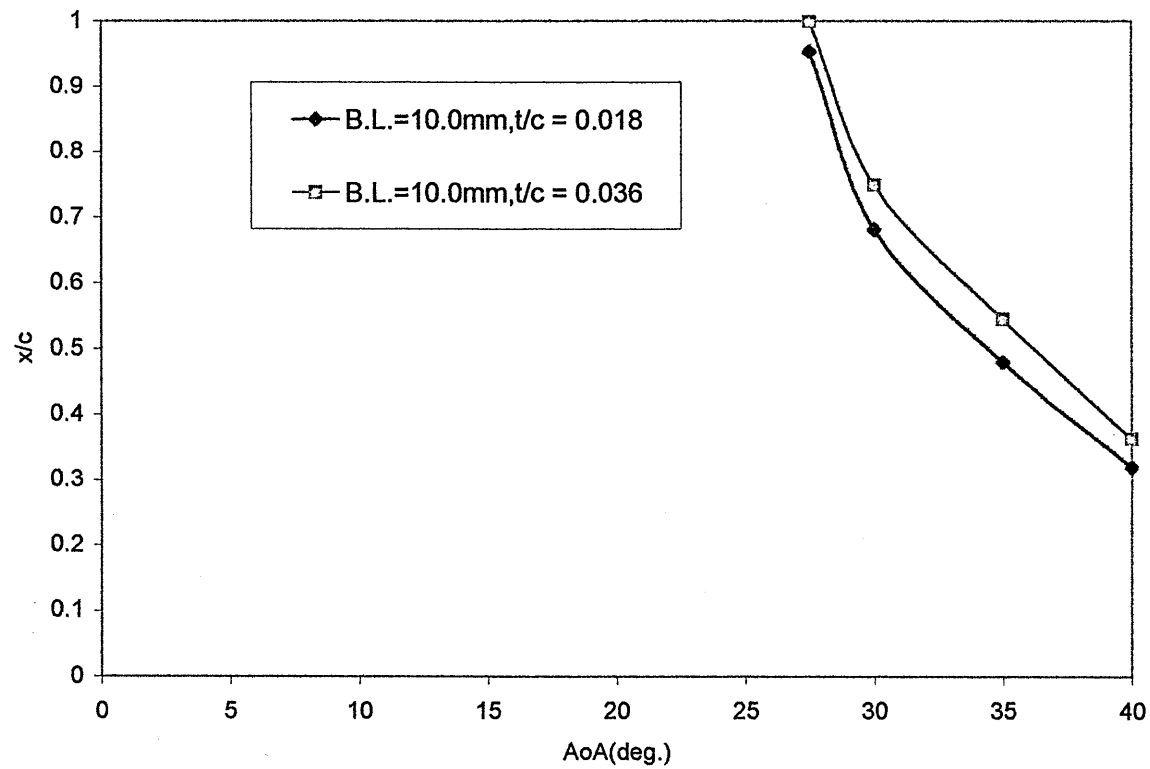

Figure H8 Effect of thickness/chord ratio on vortex breakdown position for 70 deg. swept delta.

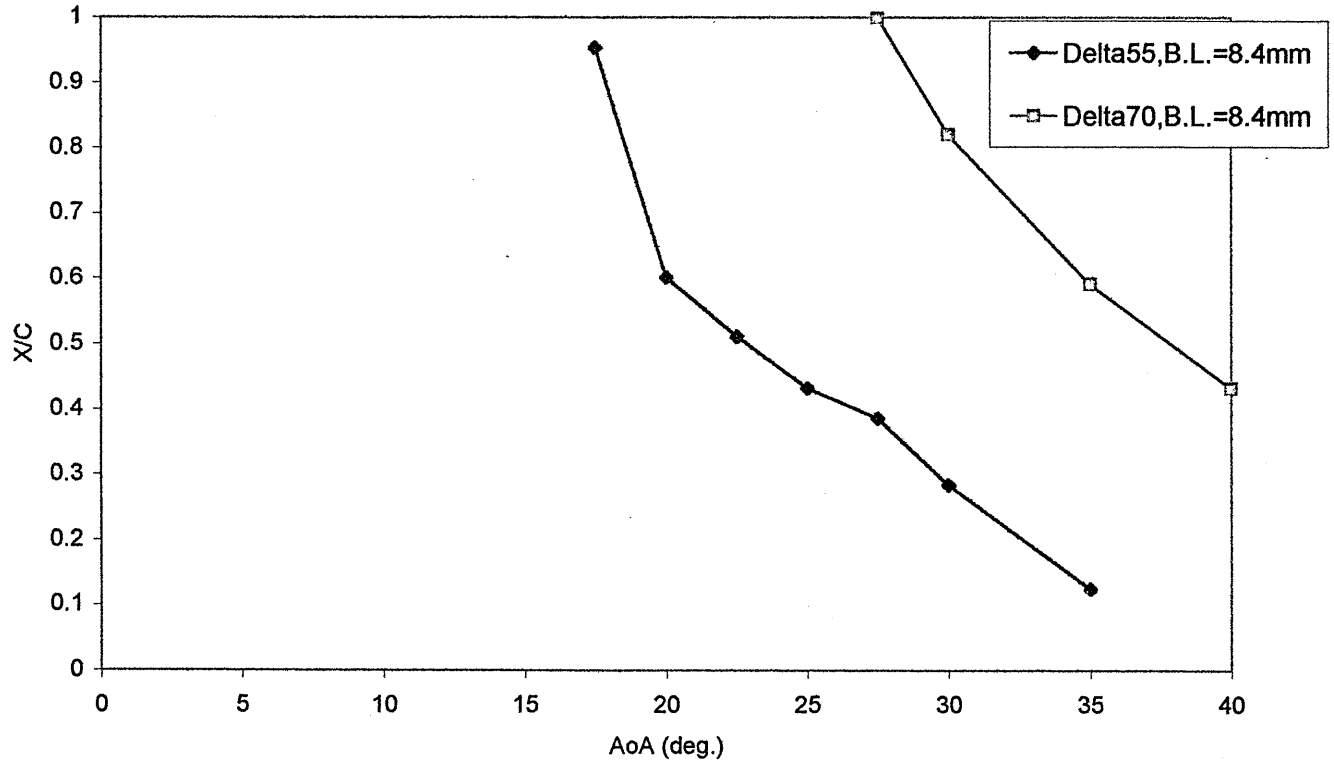

Figure H9 Effect of sweep on vortex breakdown position
t/c = 0.018 for 55 deg. and 70 deg. swept delta

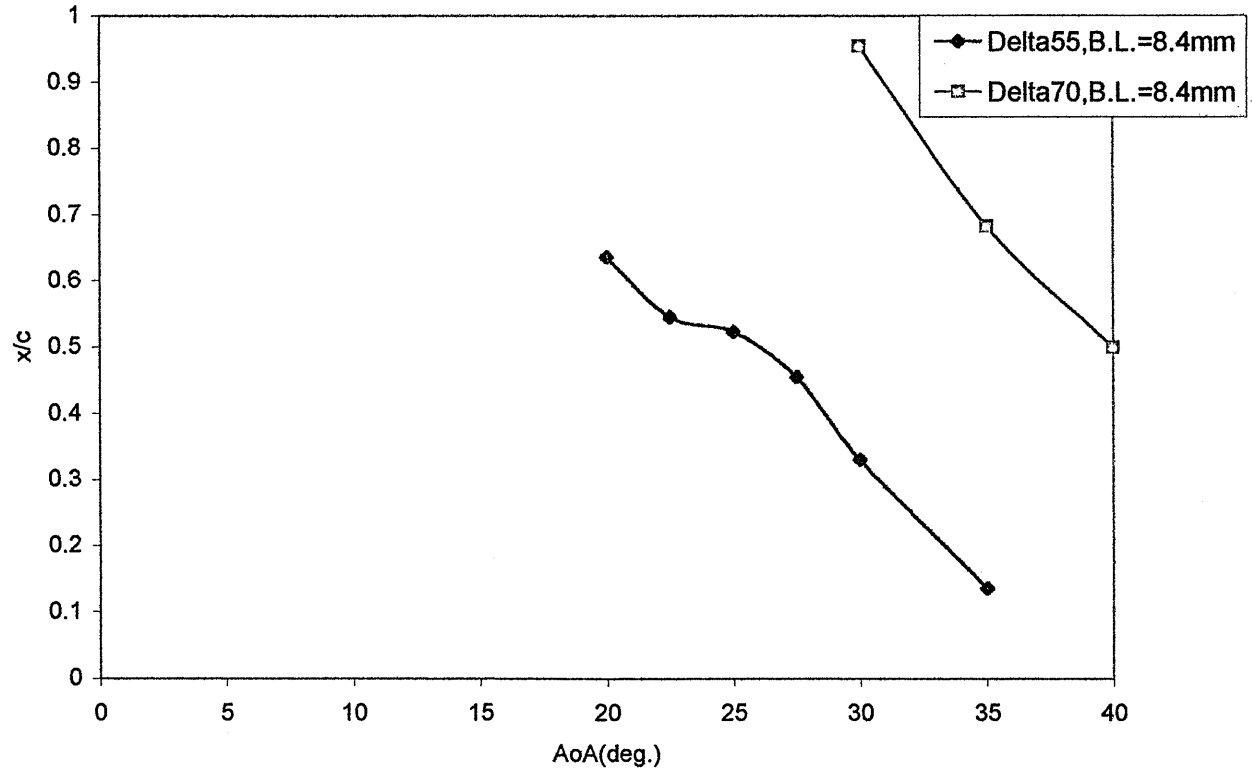

Figure H10 Effect of sweep on vortex breakdown position
t/c = 0.036 for 55 deg. and 70 deg. swept delta

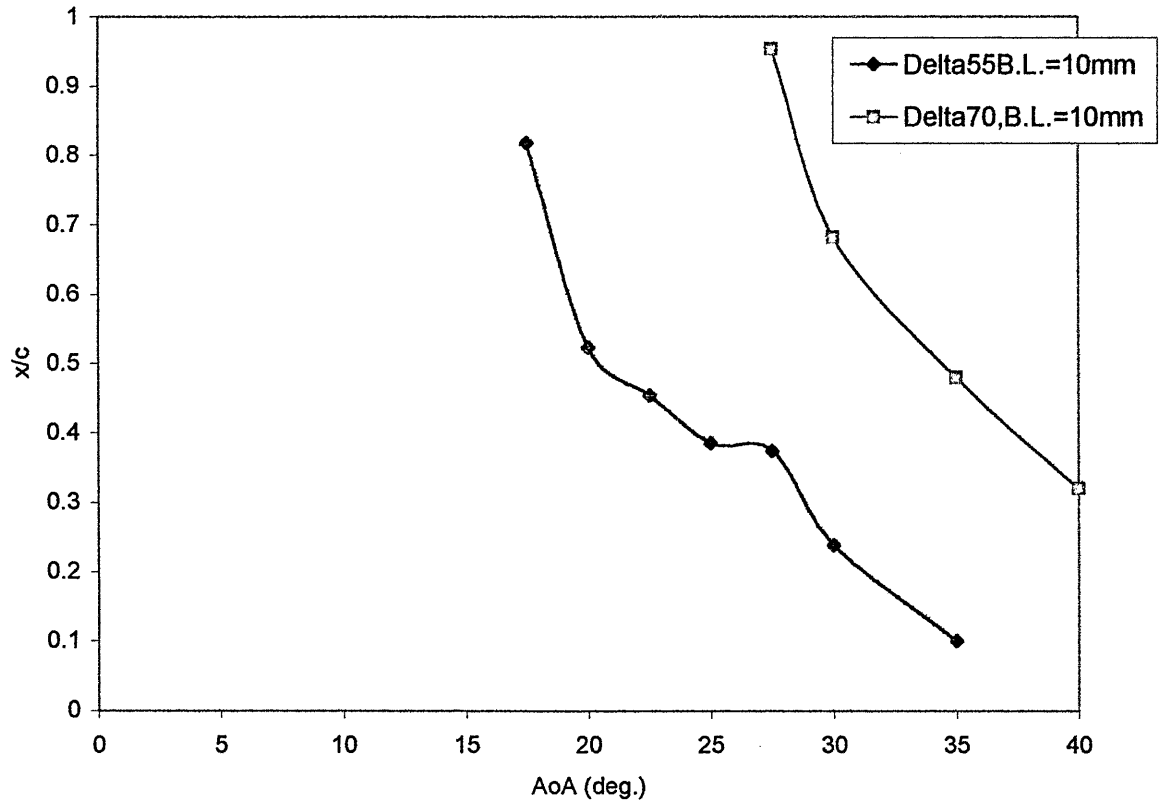

Figure H11 Effect of sweep on vortex breakdown position
t/c = 0.018 for 55 deg. and 70 deg. swept delta

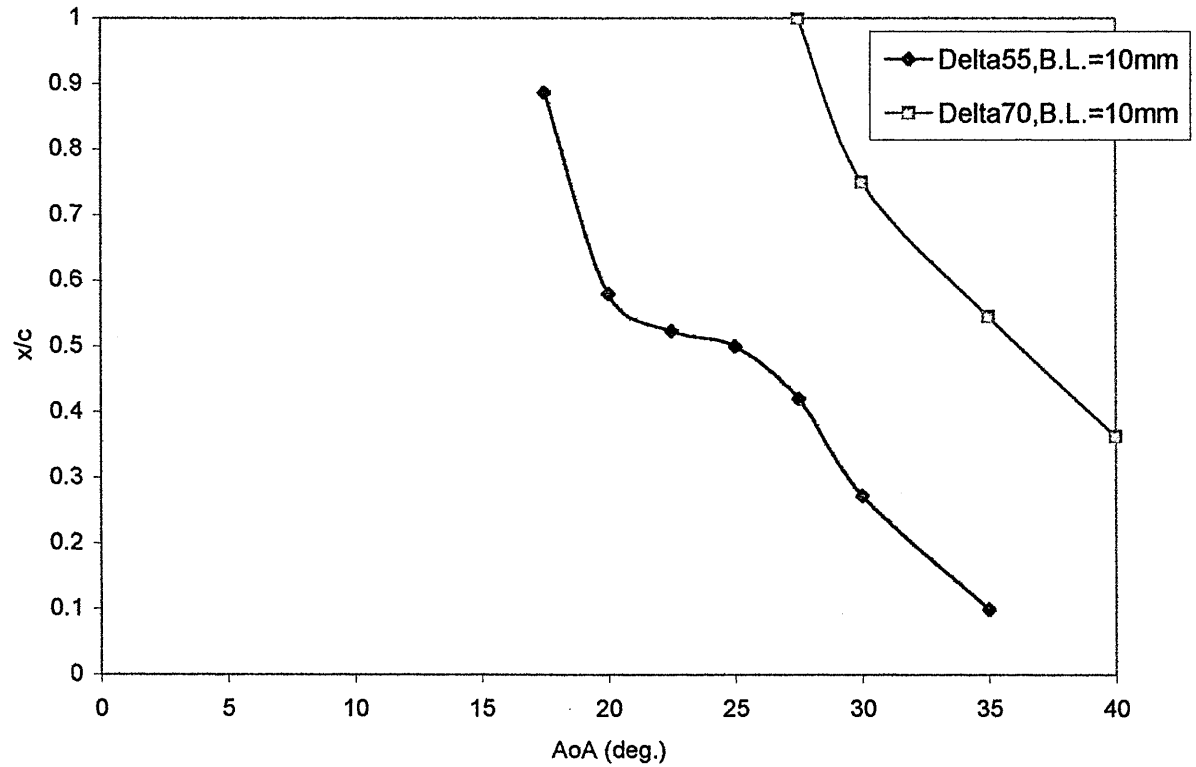

Figure H12 Effect of sweep on vortex breakdown position
t/c = 0.036 for 55 deg. and 70 deg. swept delta

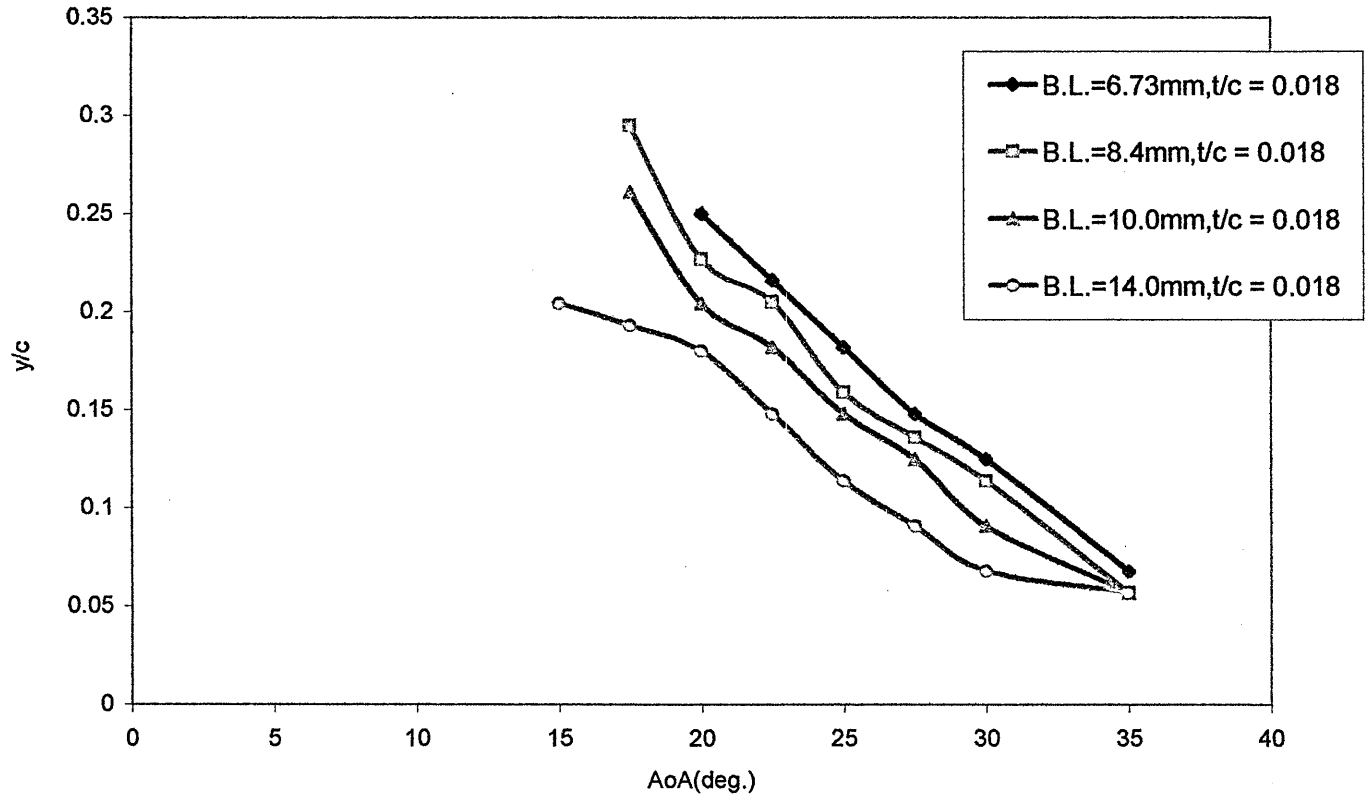

Figure H13 Influence of wall boundary layer thickness on lateral vortex breakdown position vs. AoA for 55 deg. Swept delta,t/c=0.018

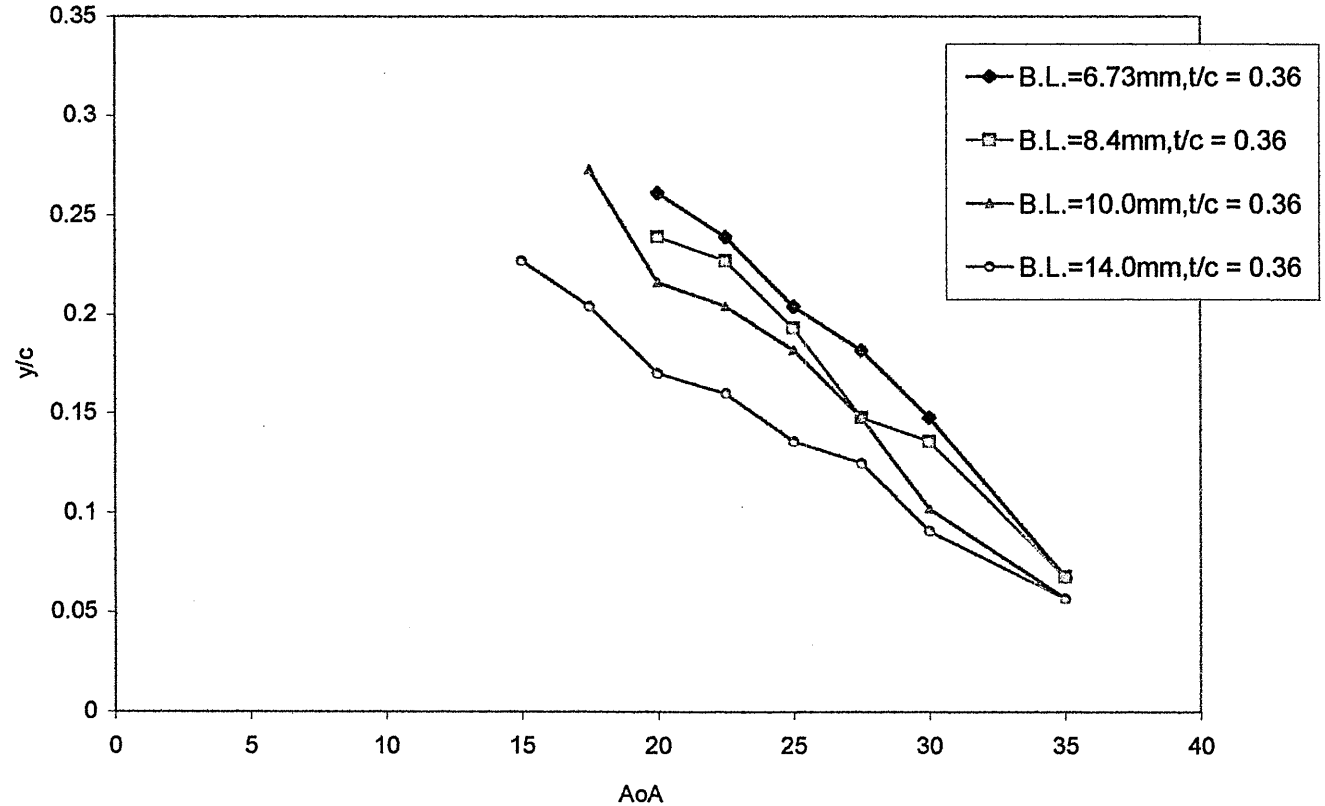

Figure H14 Influence of wall boundary layer thickness on lateral vortex breakdown positionvs. AoA for 55 deg. Swept delta,t/c=0.036

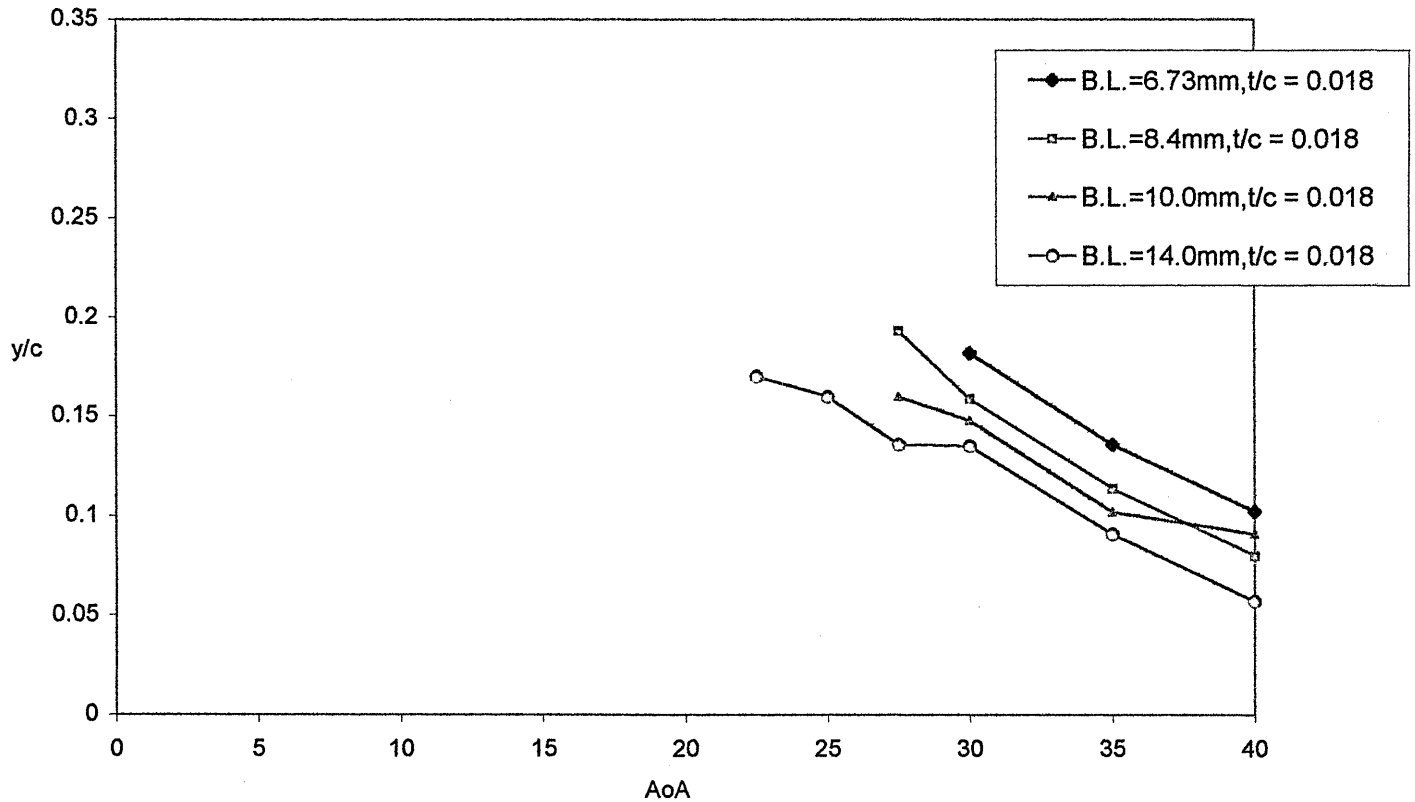

Figure H15 Influence of wall boundary layer thickness on lateral vortex breakdown position vs. AoA for 70 deg. Swept delta,t/c=0.018

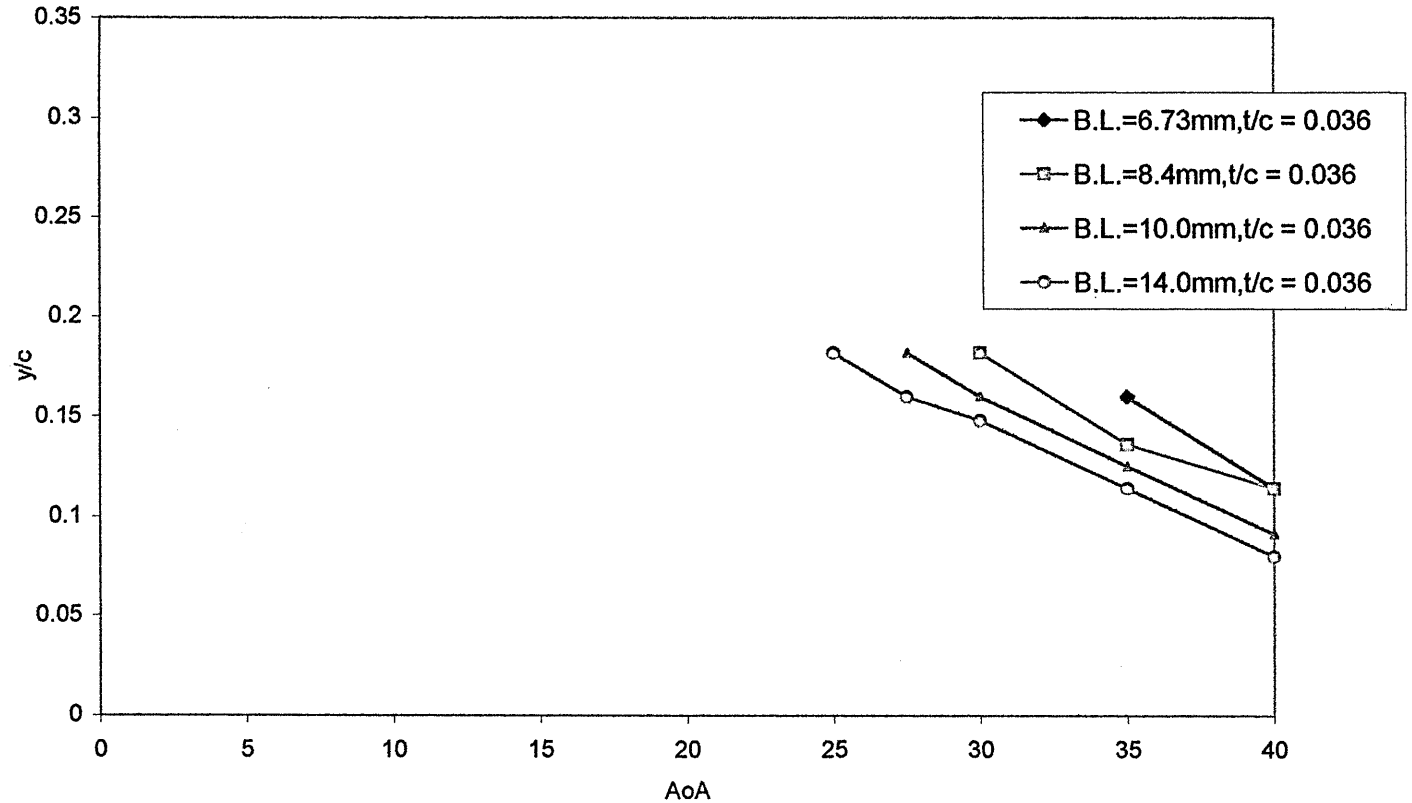

Figure H16 Influence of wall boundary layer thickness on lateral vortex breakdown position vs. AoA for 70 deg. Swept delta,t/c=0.036

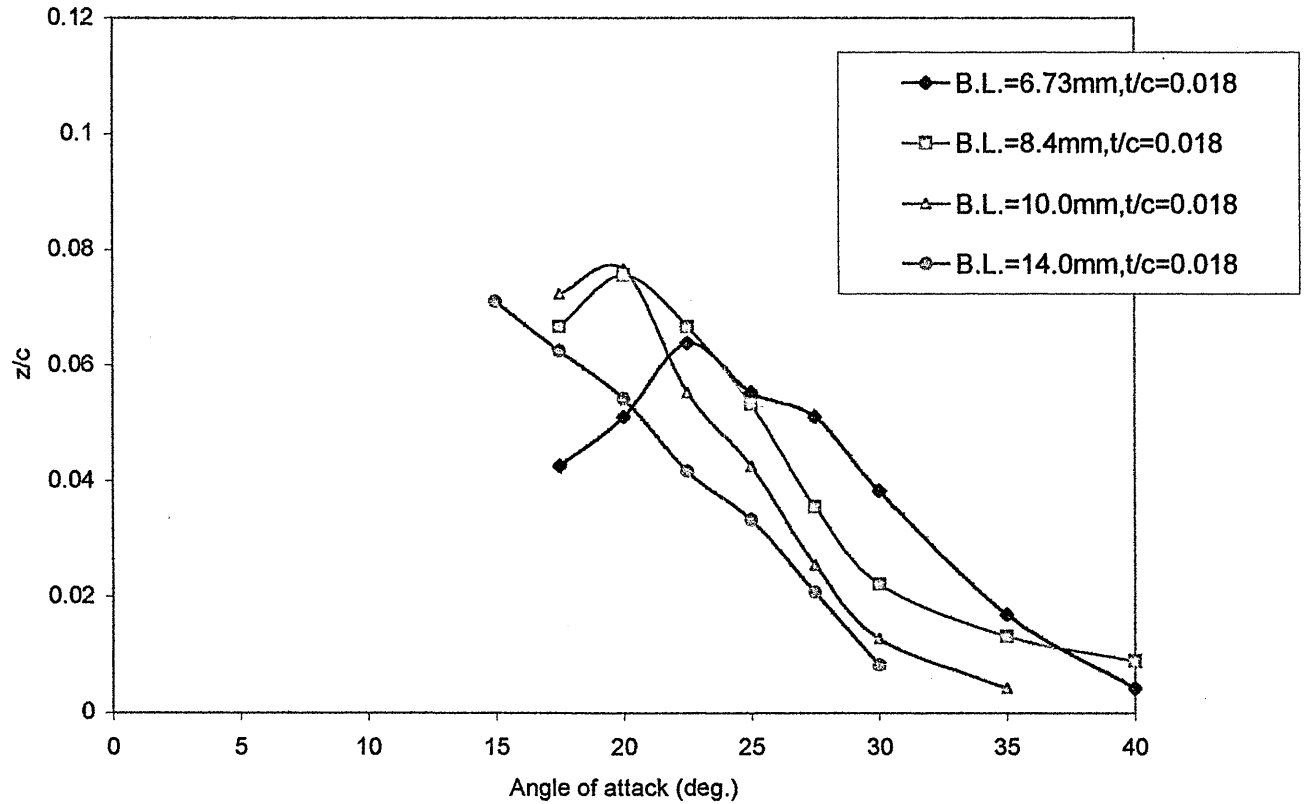

Figure H17 Influence of wall boundary layer thickness on the variation of vertical location of vortex breakdown vs. AoA for 55 deg. Swept delta, t/c = 0.018.

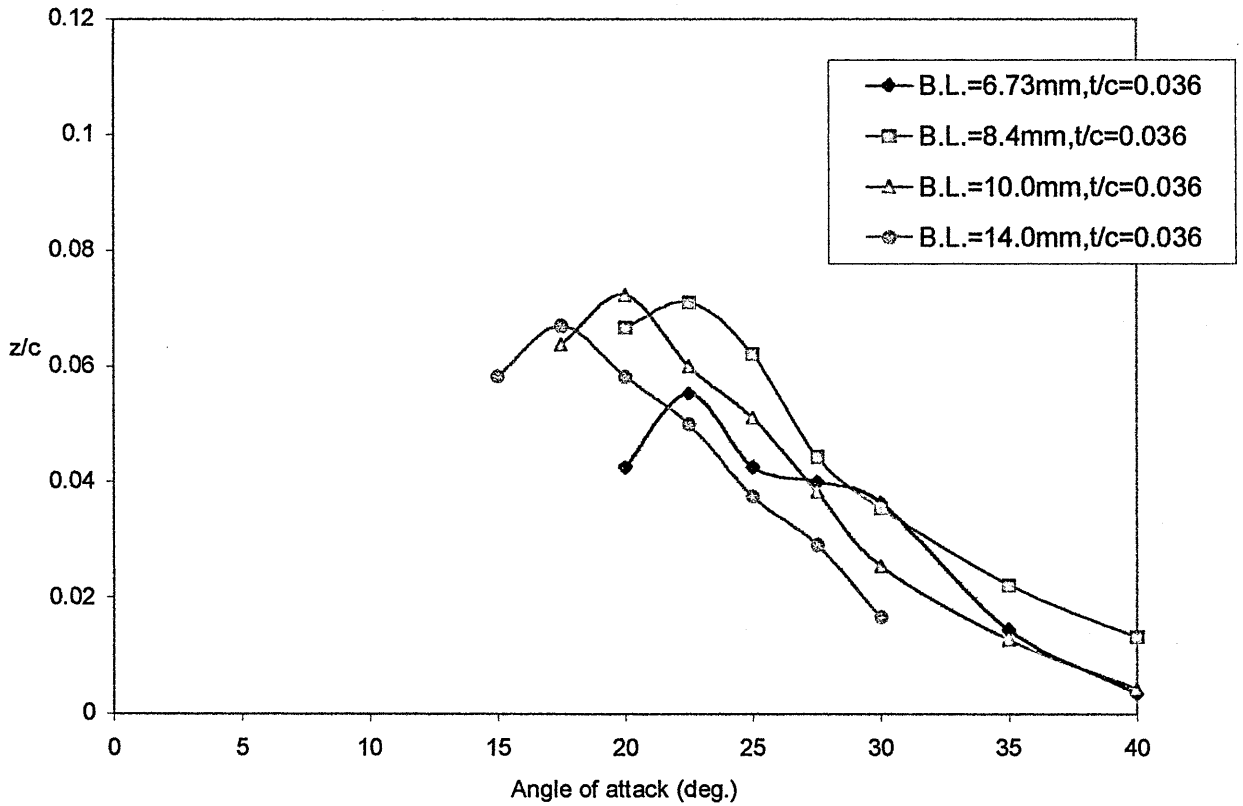

Figure H18 Influence of wall boundary layer thickness on the variation of vertical location of vortex breakdown vs. AoA for 55 deg. Swept delta, t/c = 0.036

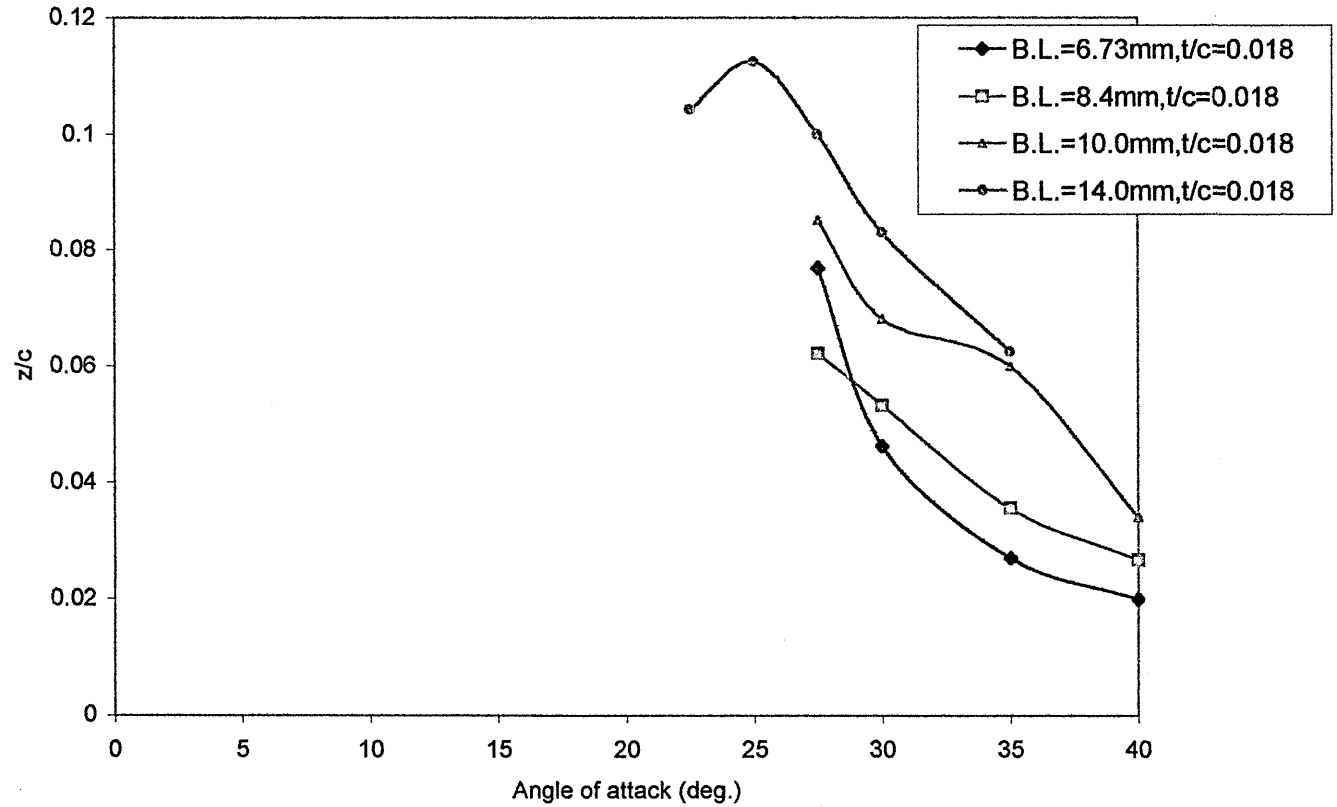

Figure H19 Influence of wall boundary layer thickness on the variation of vertical location of vortex breakdown vs. AoA for 70 deg. Swept delta, t/c = 0.018.

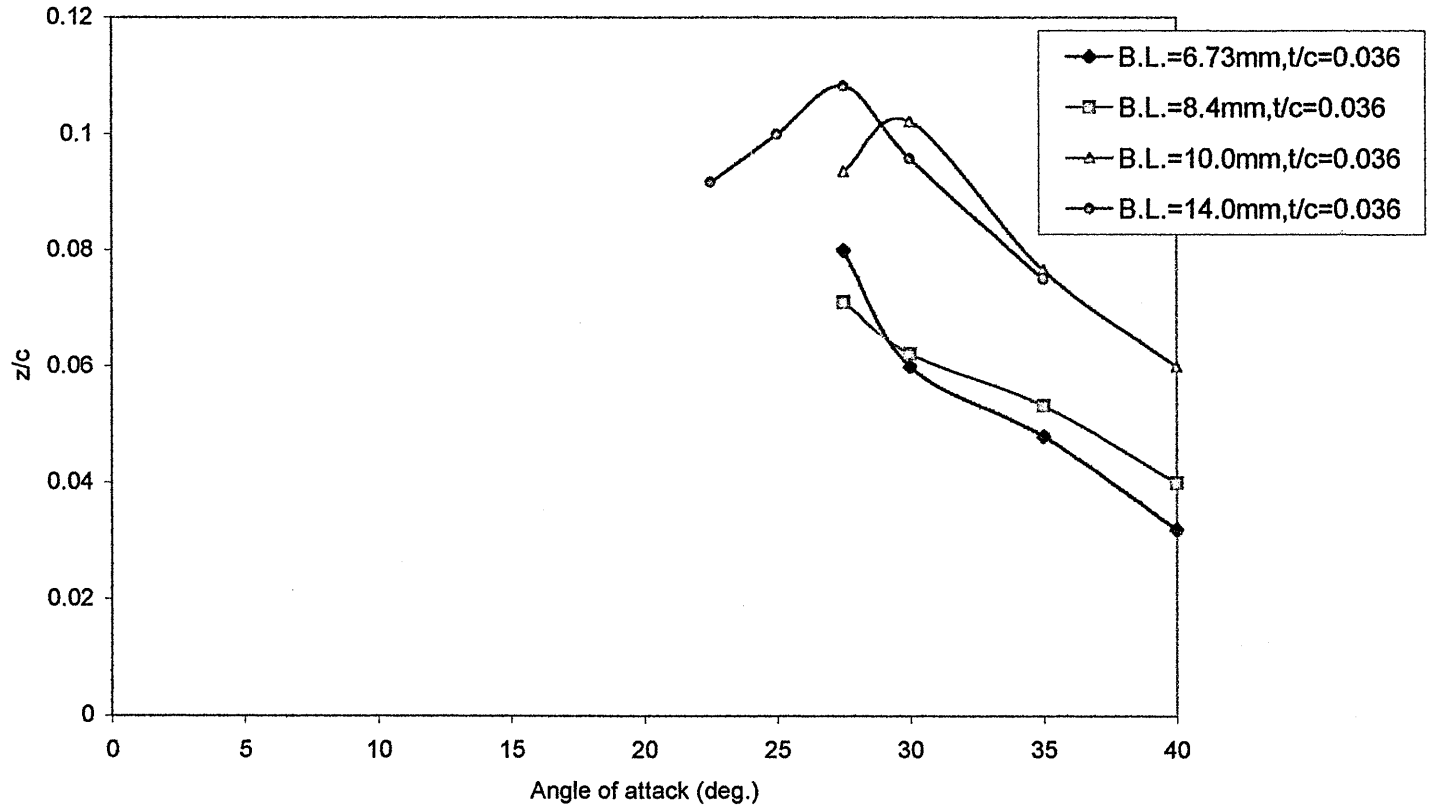

Figure H20 Influence of wall boundary layer thickness on the variation of vertical location of vortex breakdown vs. AoA for 70 deg. Swept delta, t/c = 0.036

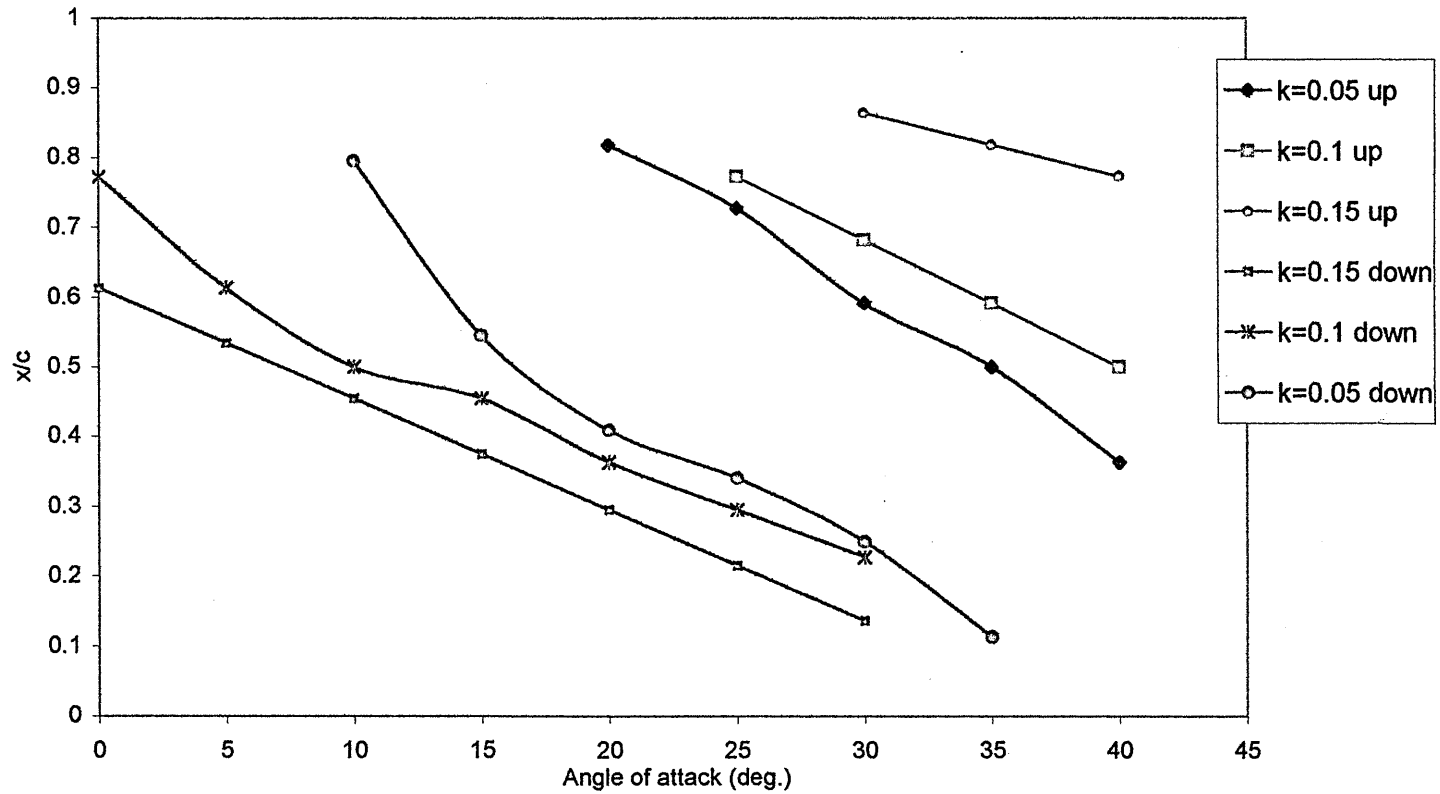

Figure H21 Effect of pitch rate on vortex breakdown position vs. AoA, 55 deg. Swept delta, t/c = 0.018, boundary layer = 6.73 mm, pitch rate k = 0.05, 0.1, 0.15 (up & down)

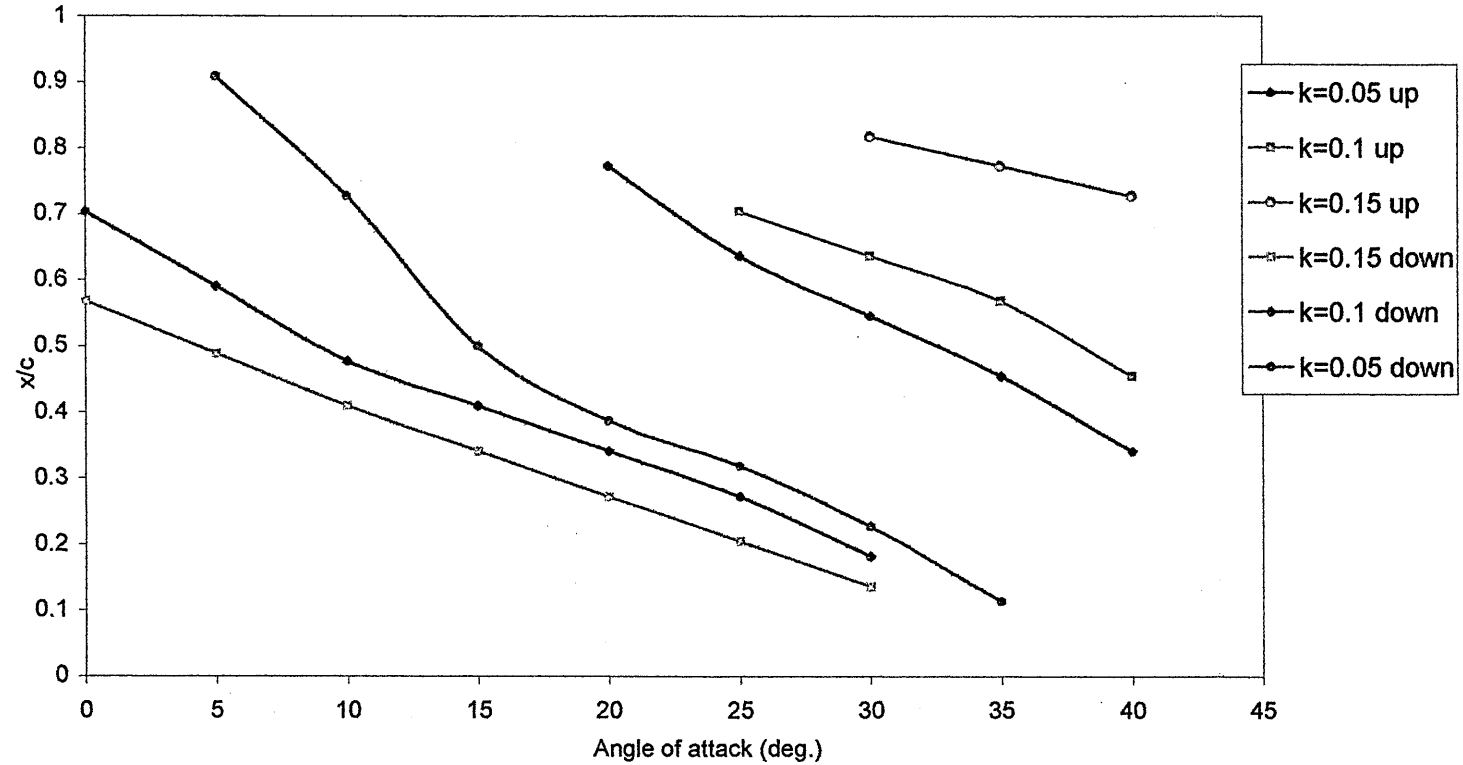

Figure H22 Effect of pitch rate on vortex breakdown position vs. AoA, 55 deg. Swept delta, t/c = 0.018, boundary layer = 8.4 mm, pitch rate k= 0.05, 0.1, 0.15 (up & down)

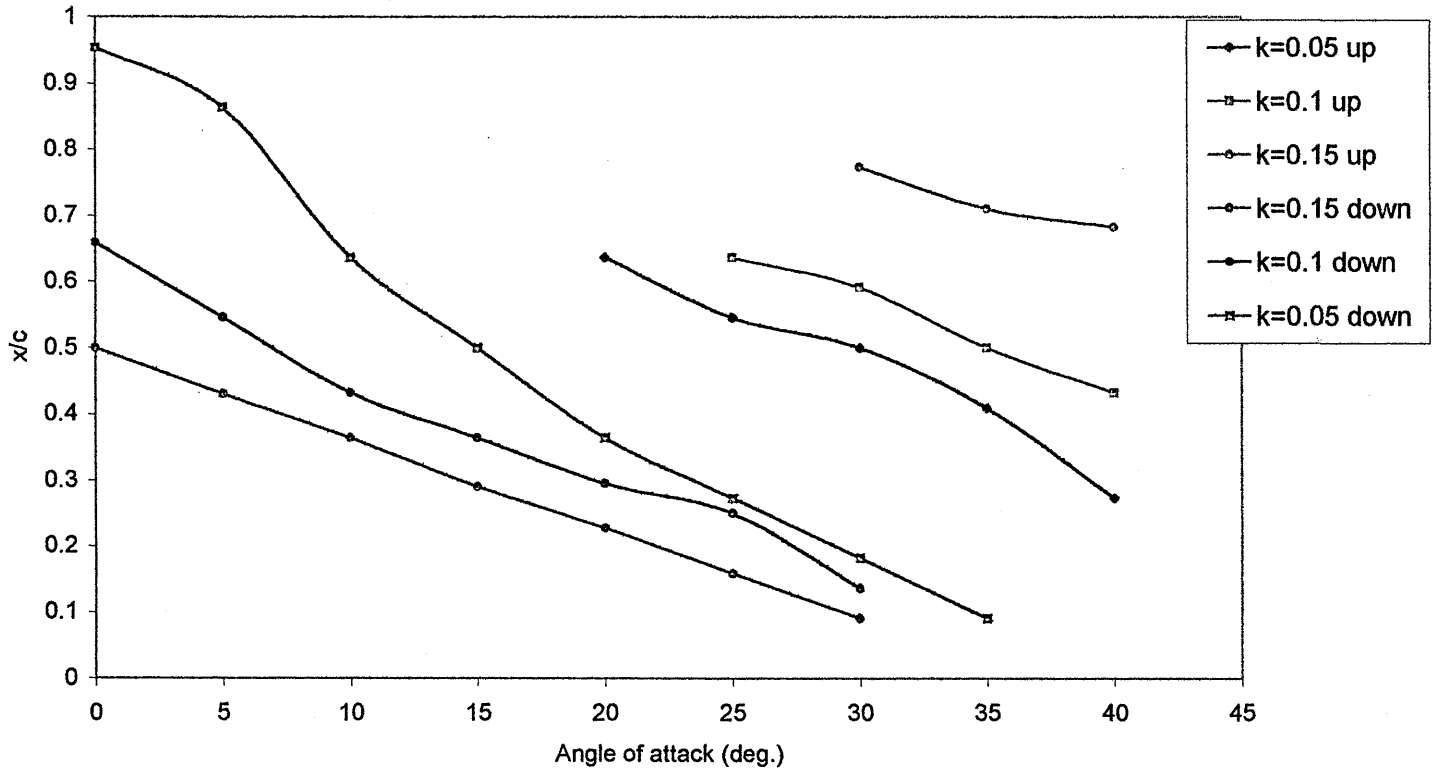

Figure H23 Effect of pitch rate on vortex breakdown position vs. AoA, 55 deg. Swept delta, t/c = 0.018, boundary layer = 10 mm, pitch rate k = 0.05, 0.1, 0.15 (up & down)

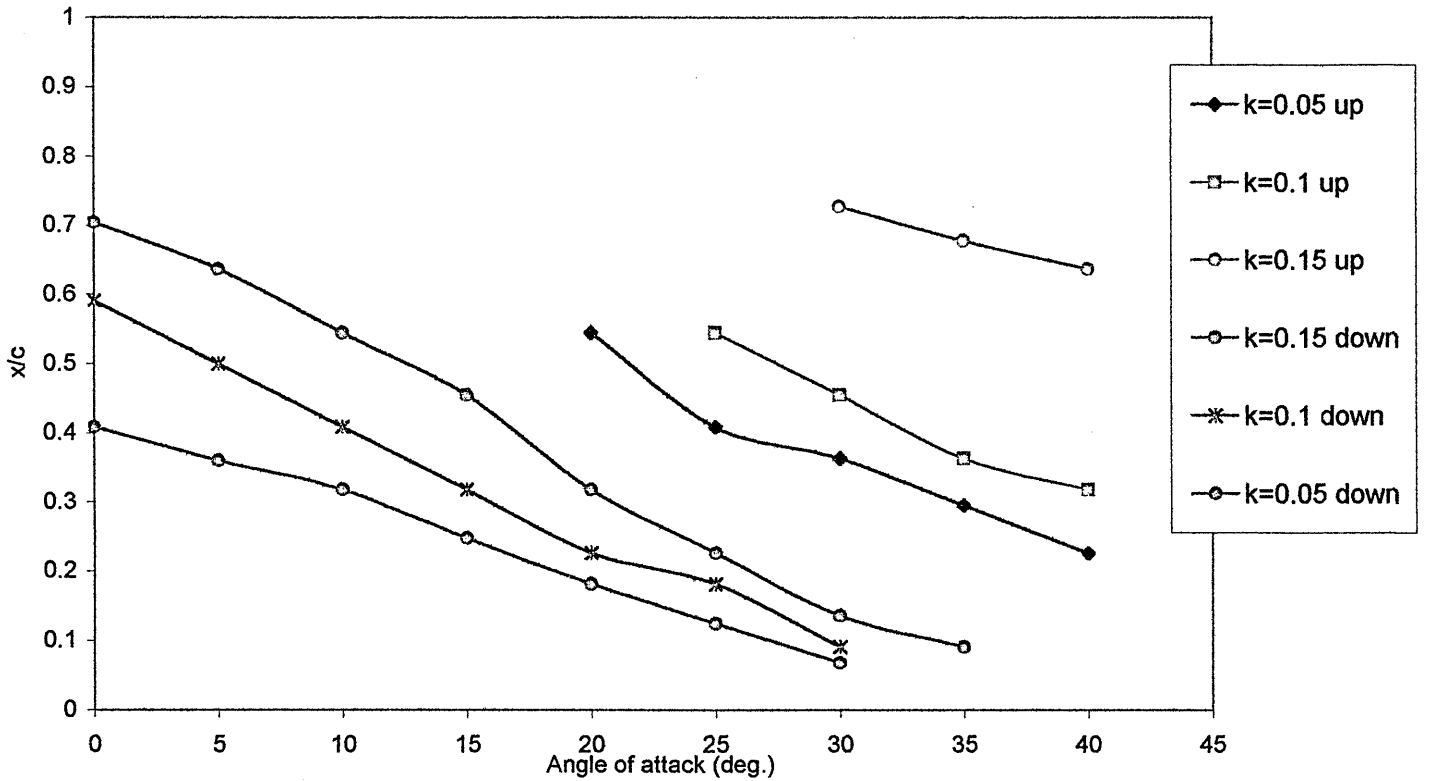

Figure H24 Effect of pitch rate on vortex breakdown position vs. AoA, 55 deg. Swept delta, t/c = 0.018, boundary layer = 14mm, pitch rate k= 0.05, 0.1, 0.15 (up & down)

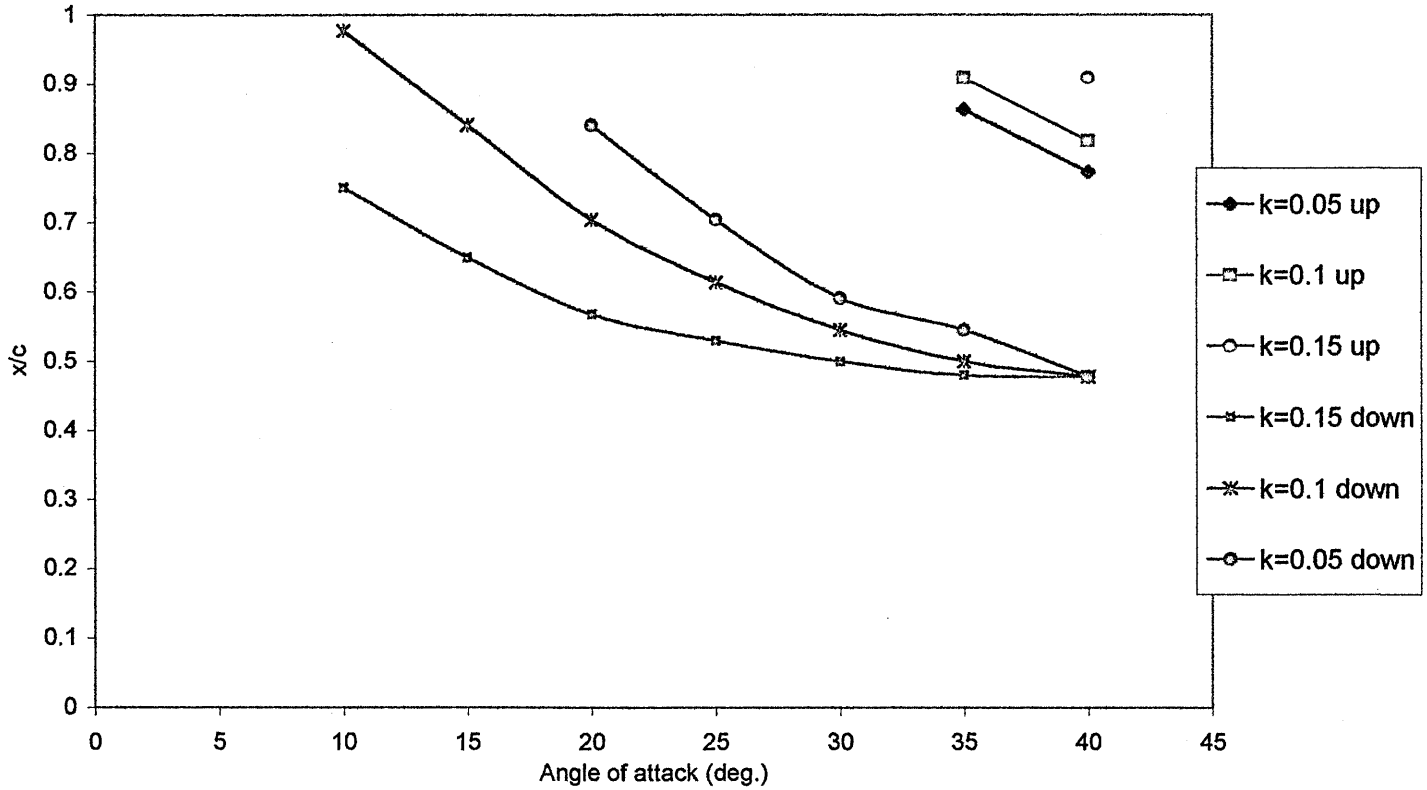

Figure H25 Effect of pitch rate on vortex breakdown position vs. AoA, 70 deg. Swept delta, t/c = 0.018, boundary layer = 6.73 mm, pitch rate k = 0.05, 0.1, 0.15 (up & down)

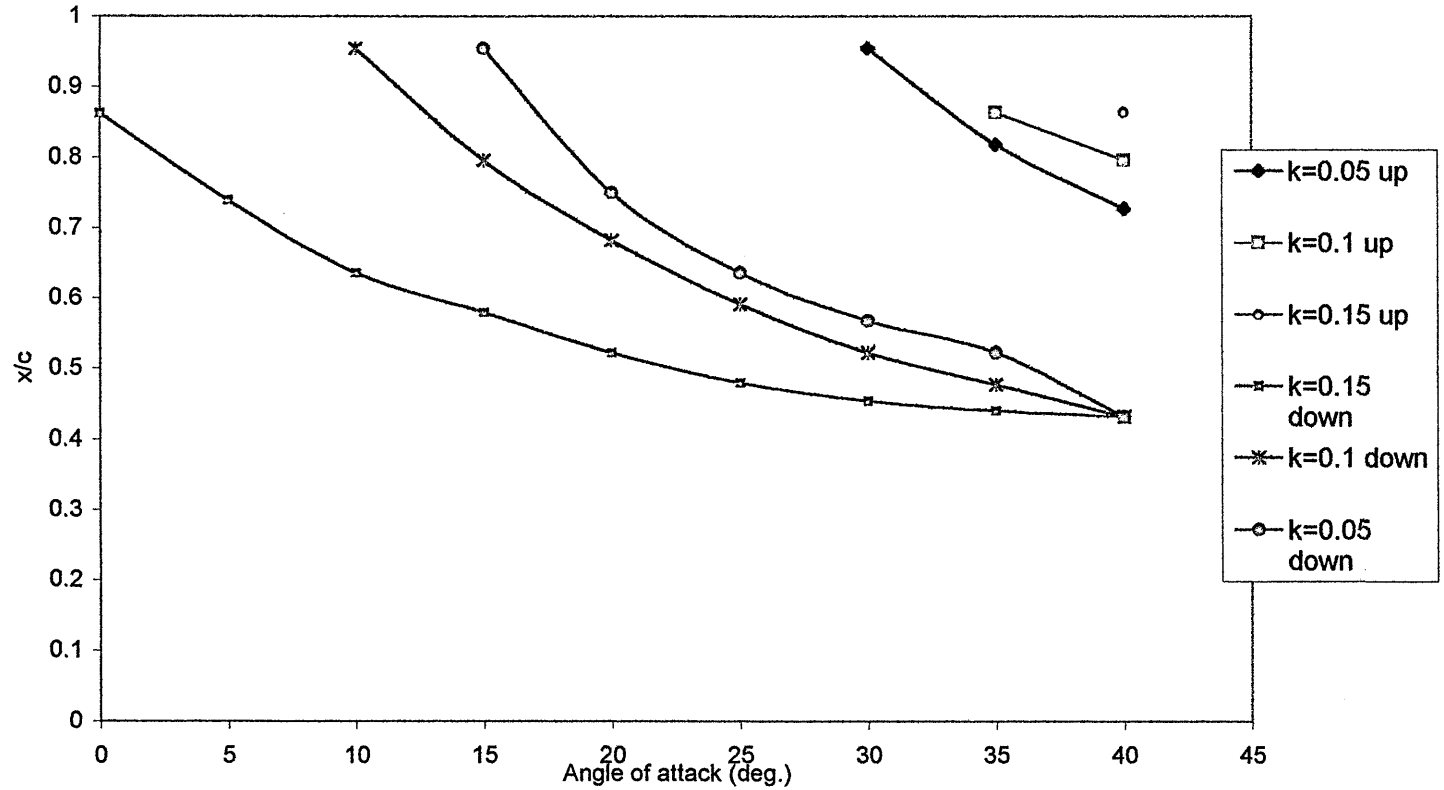

Figure H26 Effect of pitch rate on vortex breakdown position vs. AoA, 70deg. Swept delta, t/c = 0.018, boundary layer = 8.4 mm, pitch rate k= 0.05, 0.1, 0.15 (up & down)

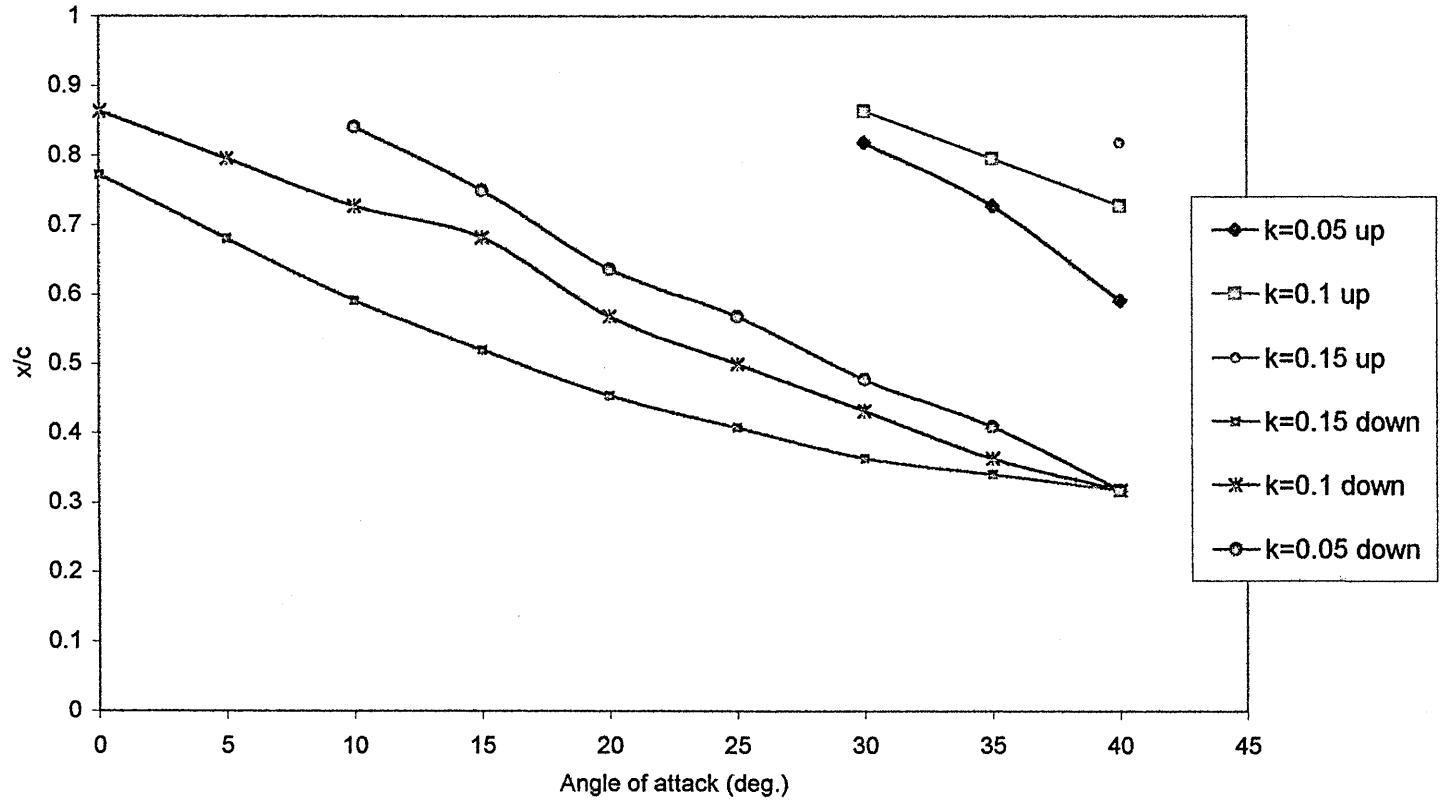

Figure H27 Effect of pitch rate on vortex breakdown position vs. AoA, 70 deg. Swept delta, t/c = 0.018, boundary layer = 10 mm, pitch rate k = 0.05, 0.1, 0.15 (up & down)

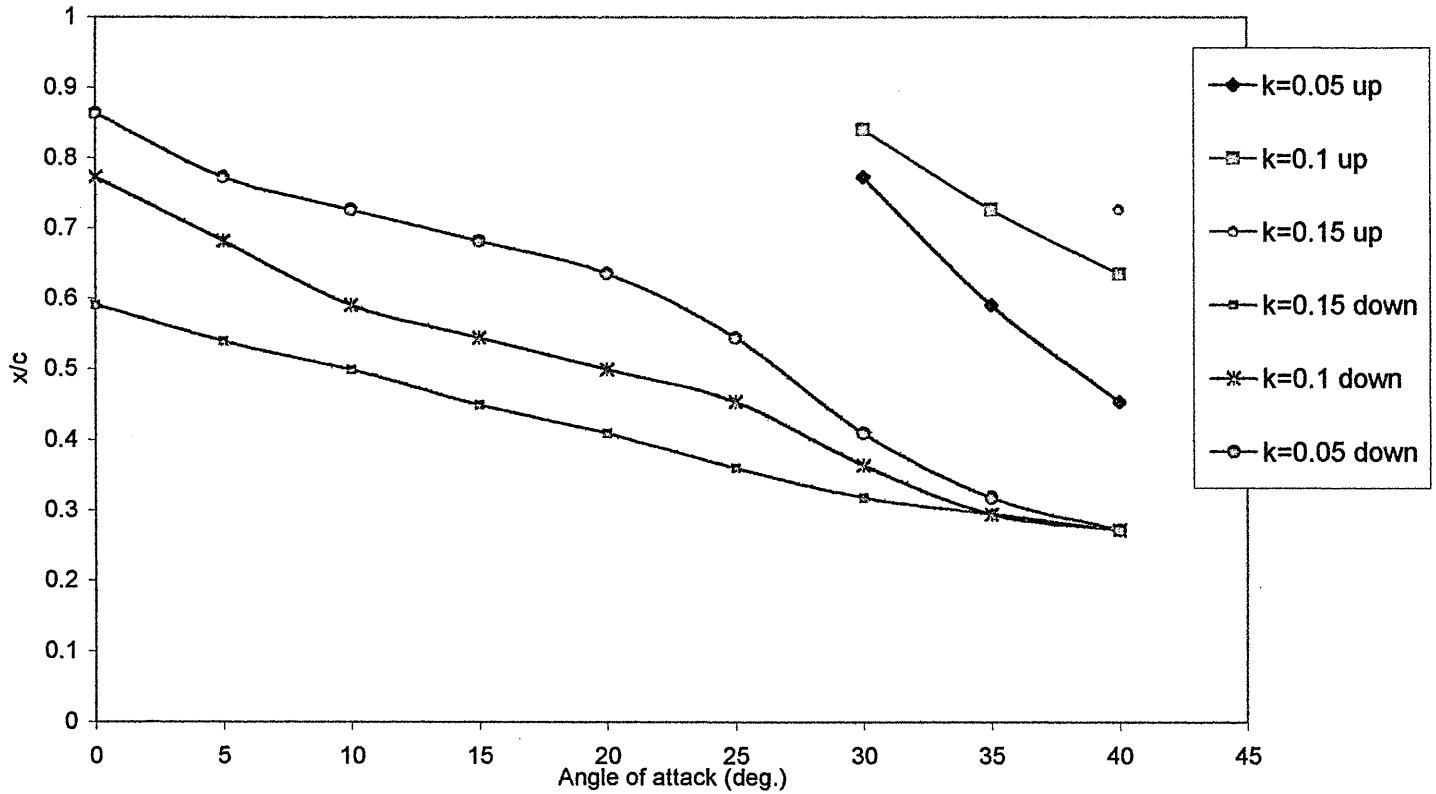

Figure H28 Effect of pitch rate on vortex breakdown position vs. AoA, 70 deg. Swept delta, t/c = 0.018, boundary layer = 14mm, pitch rate k= 0.05, 0.1, 0.15 (up & down)

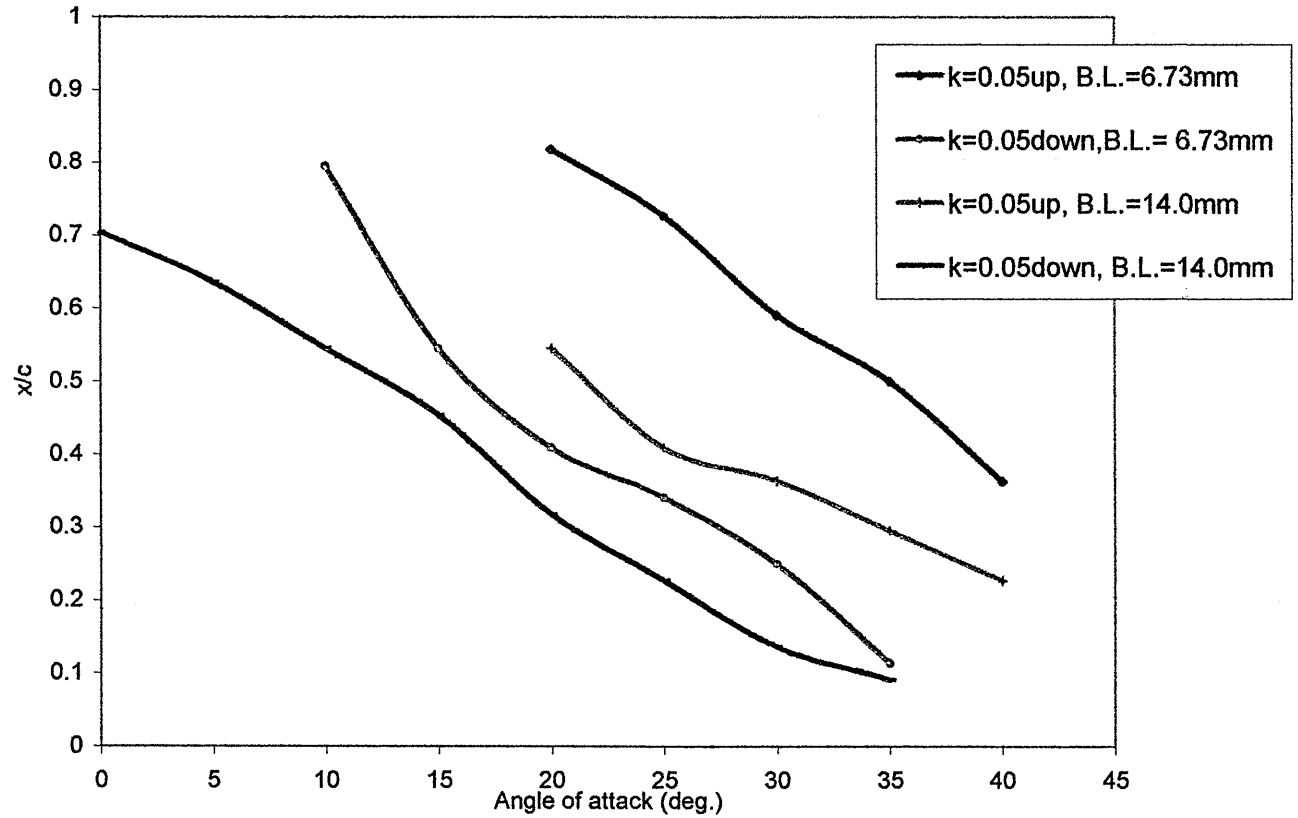

Figure H29 Influence of wall boundary layer thickness on vortex breakdown position x/c vs. AoA, 55 deg. Swept delta, t/c=0.018, k=0.05

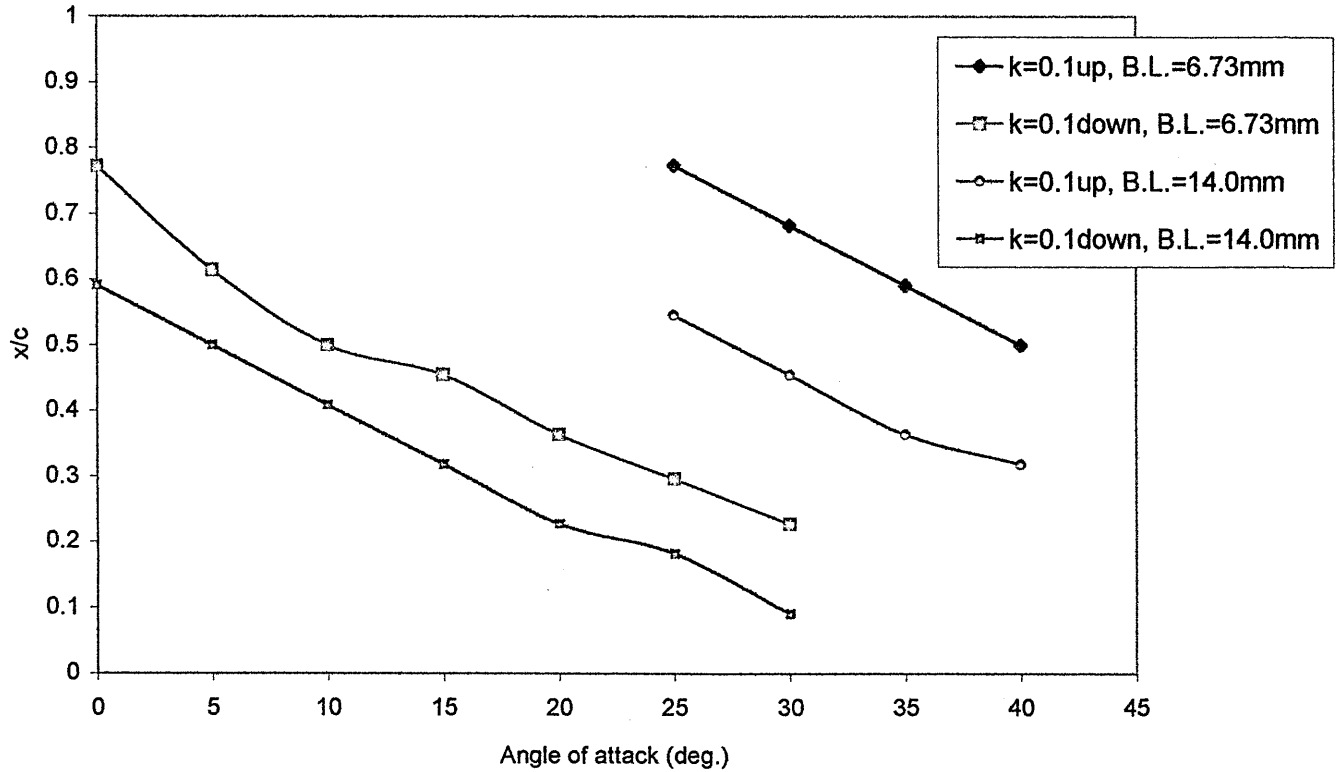

Figure H30 Influence of wall boundary layer thickness on vortex breakdown position x/c vs. AoA, 55 deg. Swept delta, t/c=0.018, k=0.1

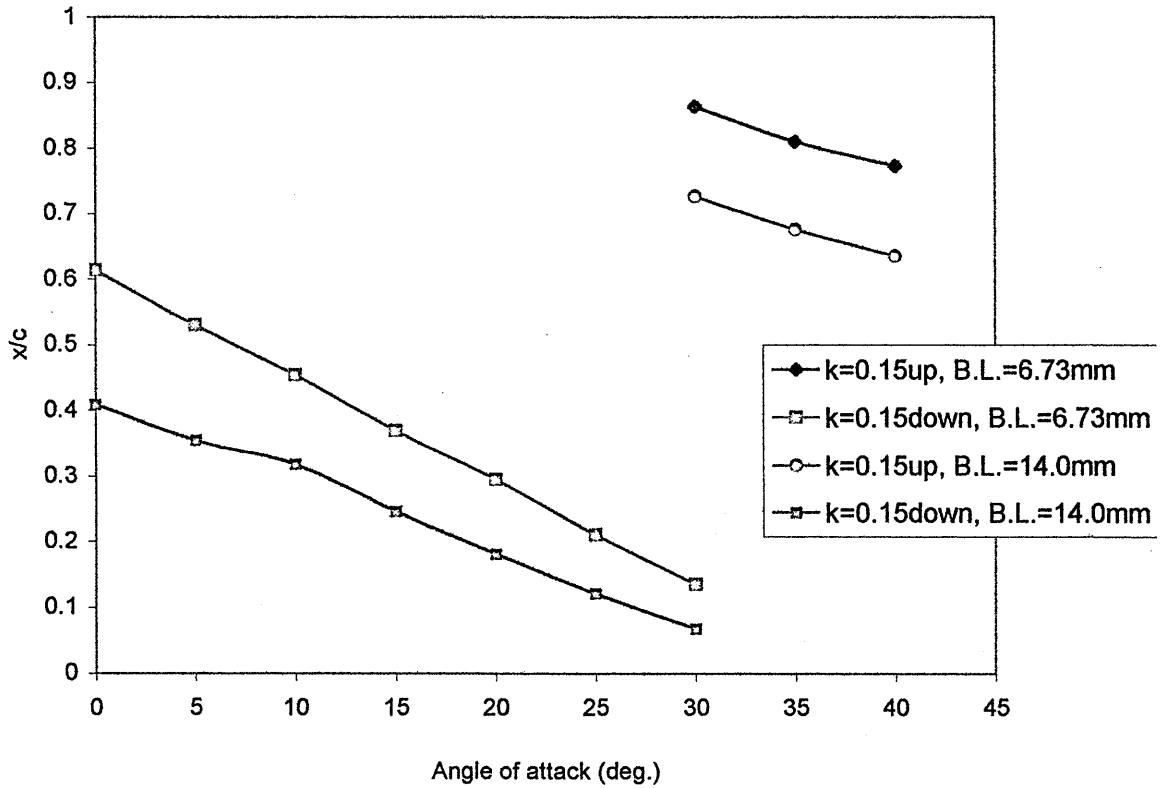

Figure H31 Influence of wall boundary layer thickness on vortex breakdown position x/c vs. AoA, 55 deg. Swept delta, t/c=0.018, k=0.15

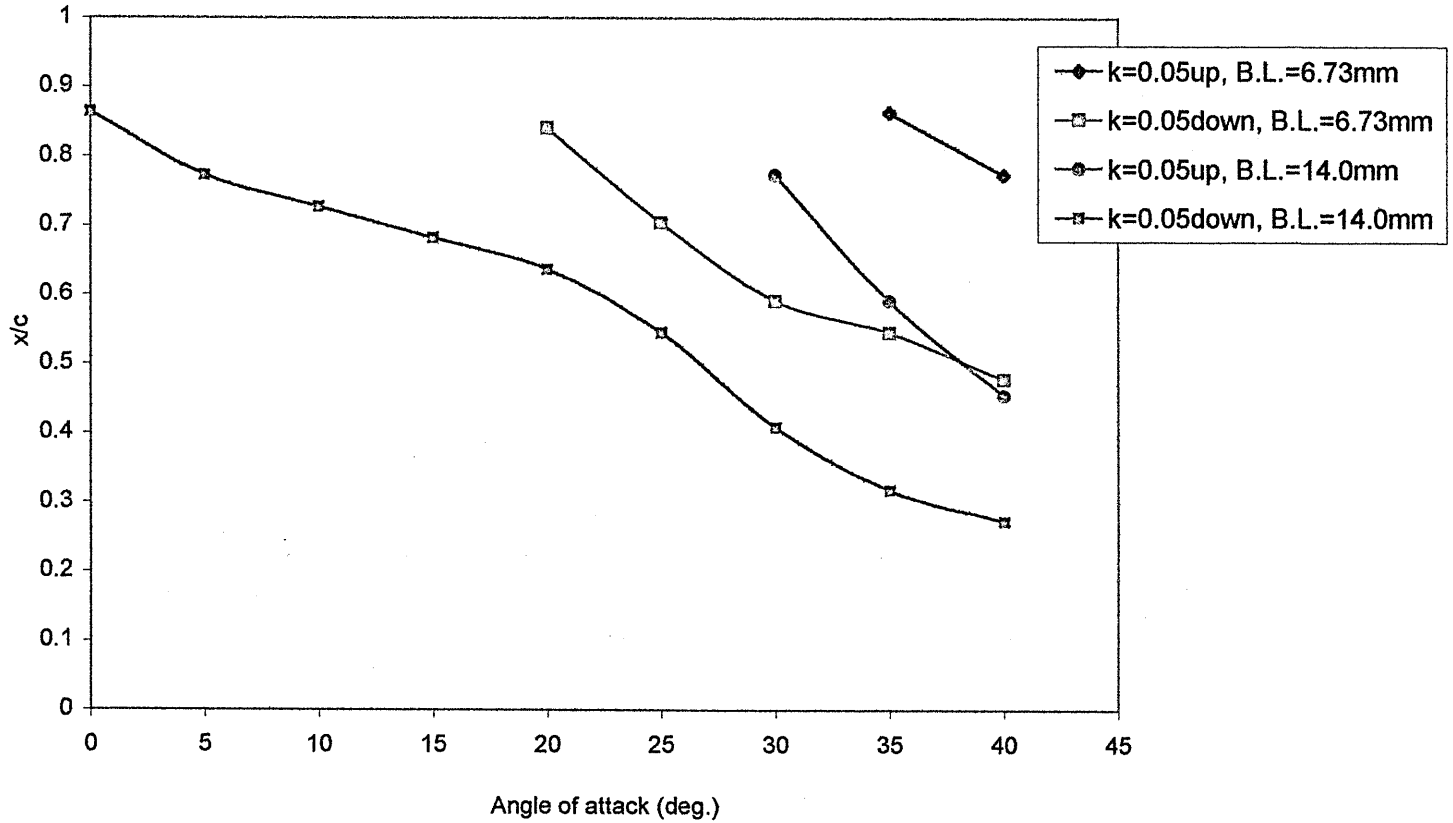

Figure H32 Influence of wall boundary layer thickness on vortex breakdown position x/c vs. AoA, 70 deg. Swept delta, t/c=0.018, k=0.05

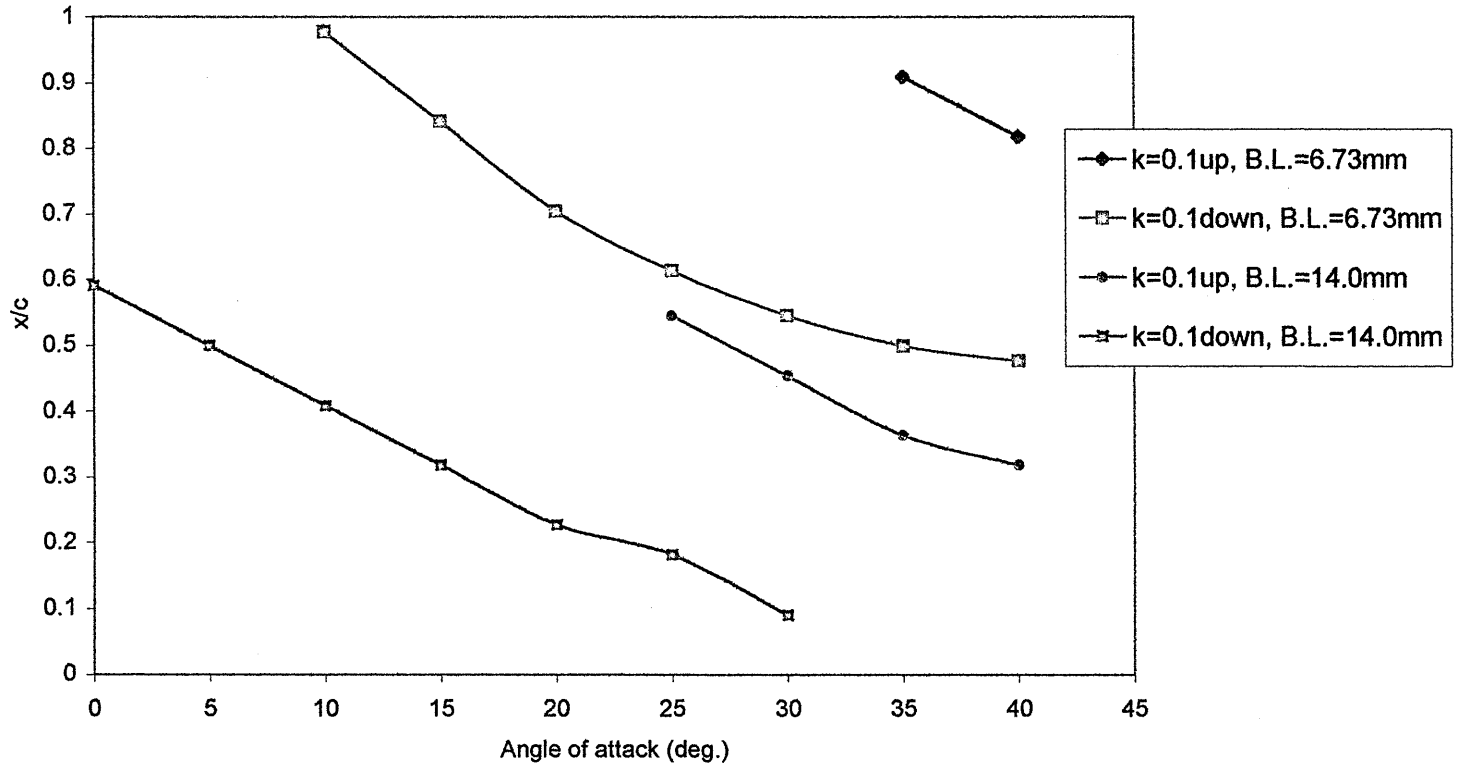

Figure H33 Influence of wall boundary layer thickness on vortex breakdown position x/c vs. AoA, 70 deg. Swept delta, t/c=0.018, k=0.1

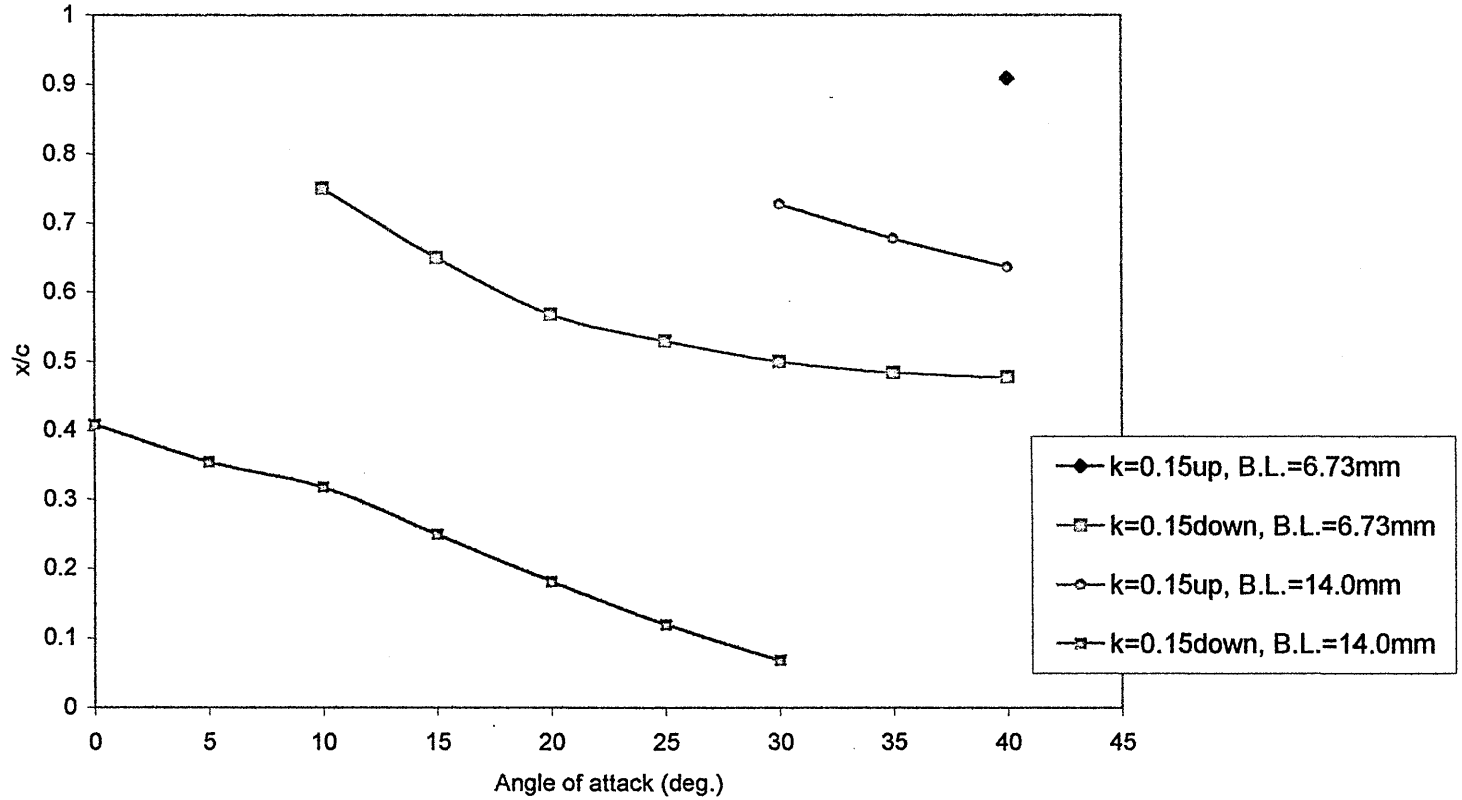

Figure H34 Influence of wall boundary layer thickness on vortex breakdown position x/c vs. AoA, 70 deg. Swept delta, t/c=0.018, k=0.15

Appendix I:

Wind Tunnel Data

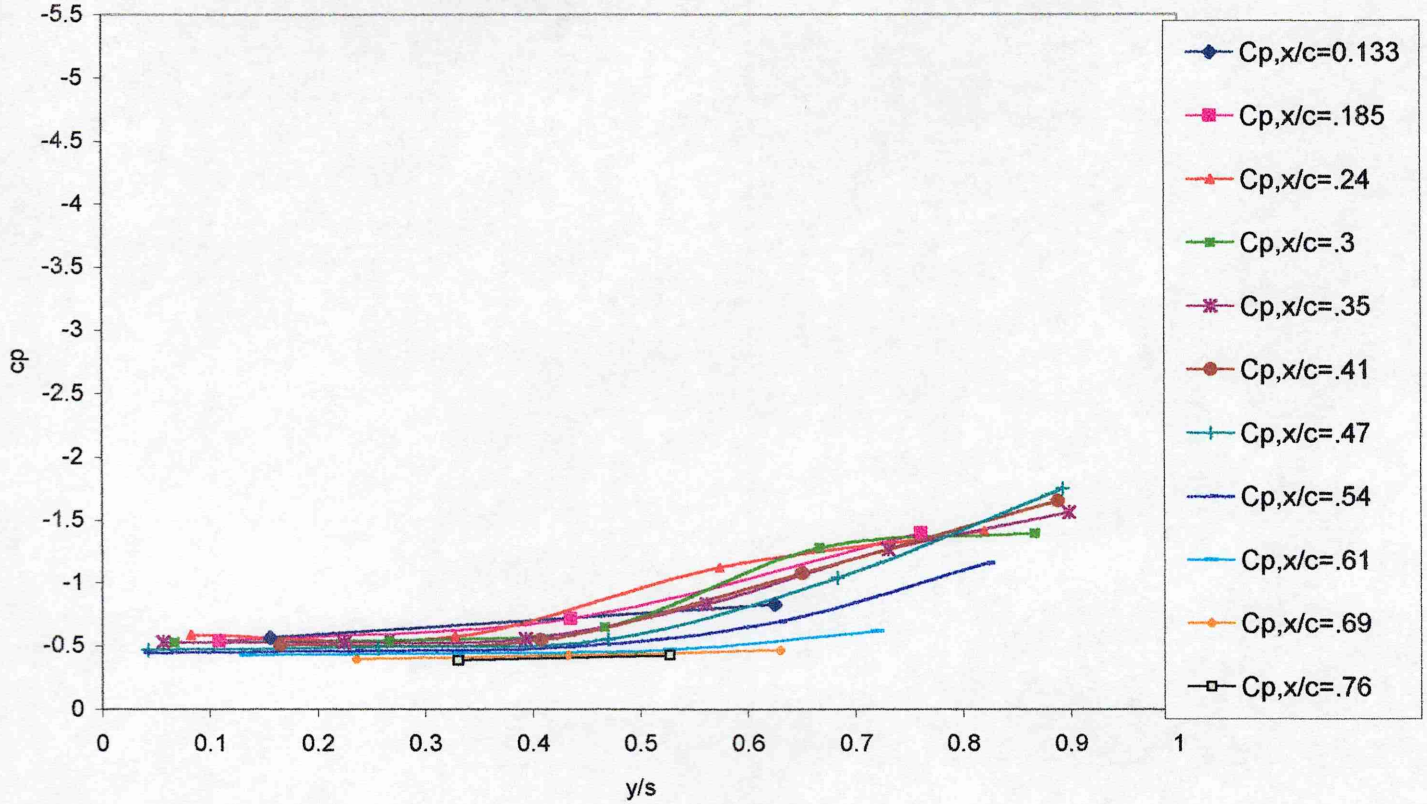

Figure I 1 spanwise Cp distribution , Delta55, AOA=10deg., B.L.=14.0mm

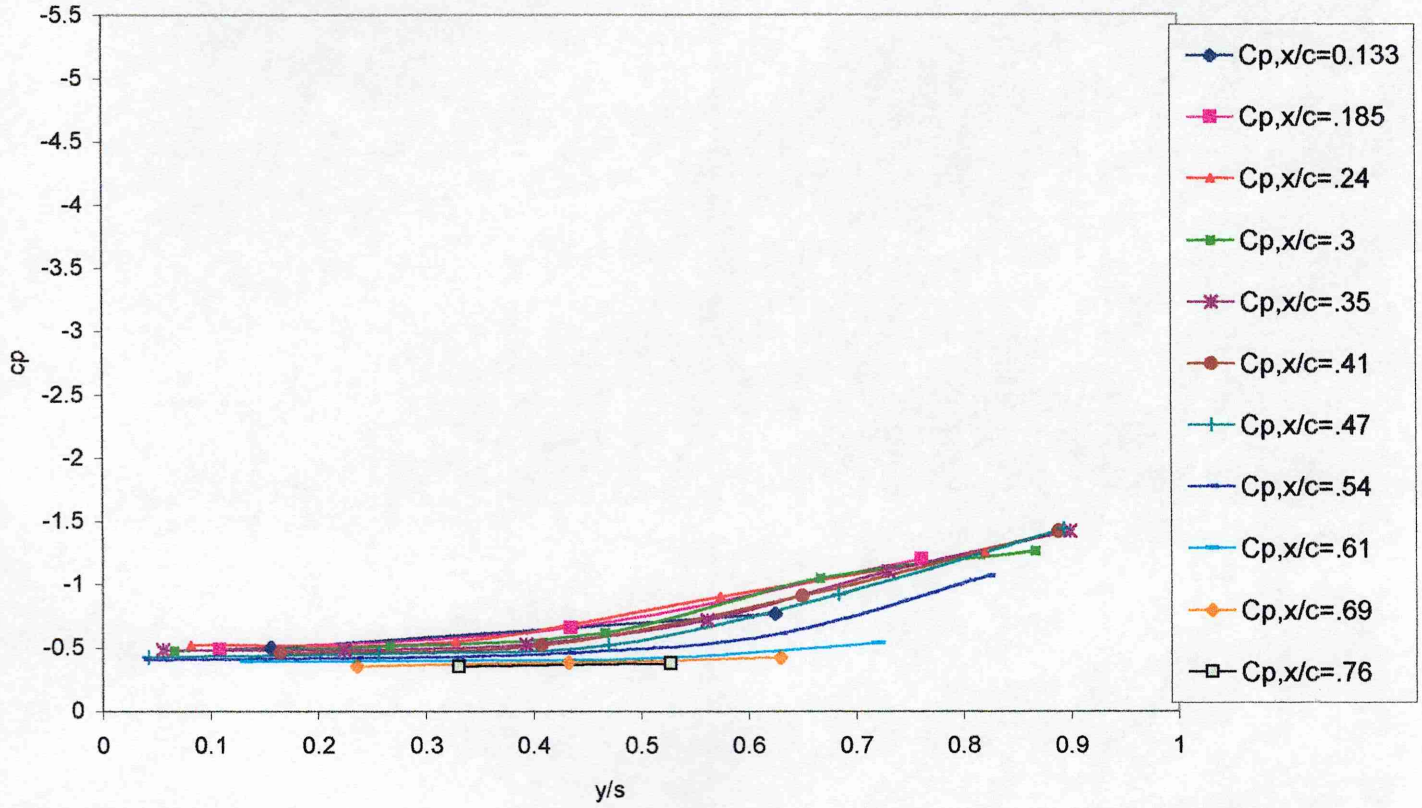

Figure I 2 spanwise Cp distribution , Delta55, AOA=10deg., B.L.=33.0mm

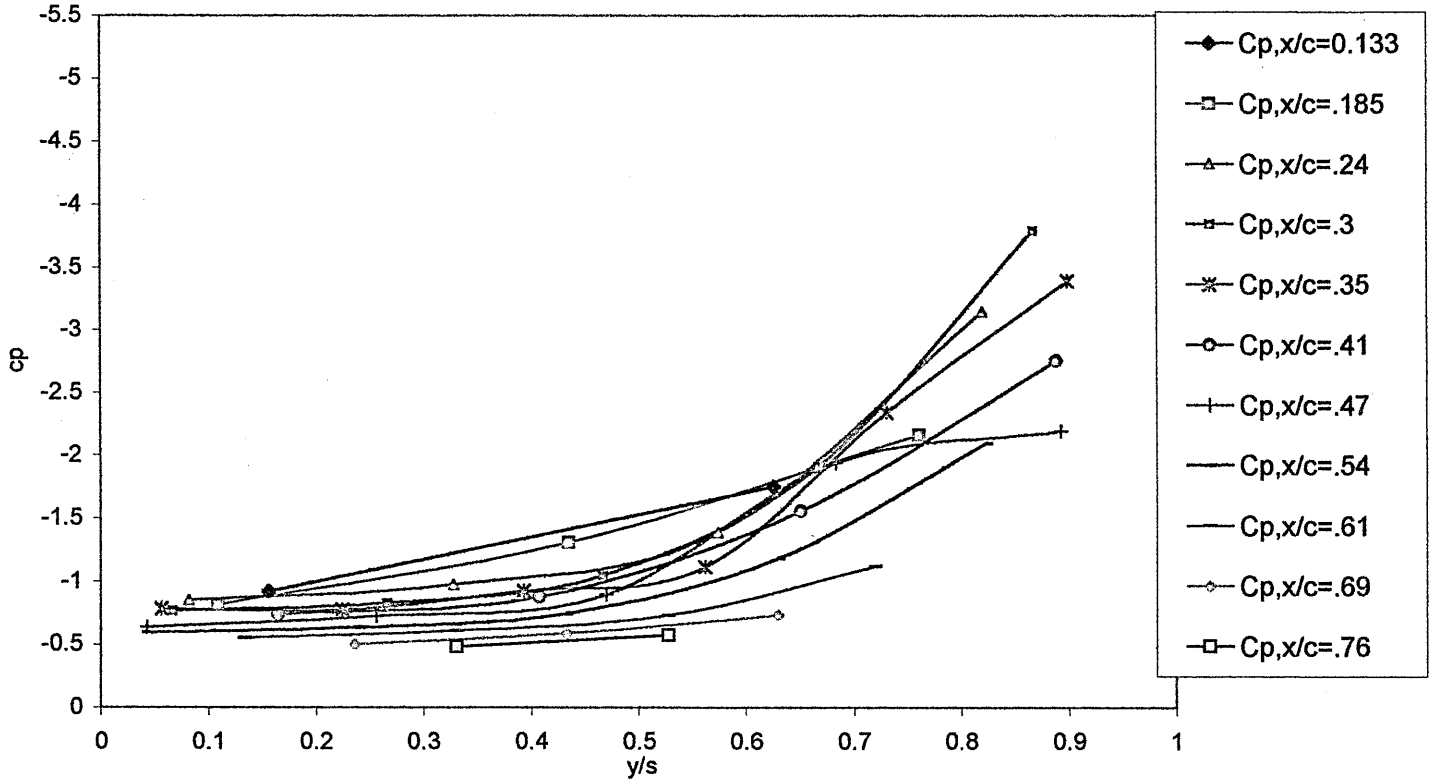

Figure I 3 Spanwise Cp distribution , Delta55, AOA=20deg., B.L.=14.0mm

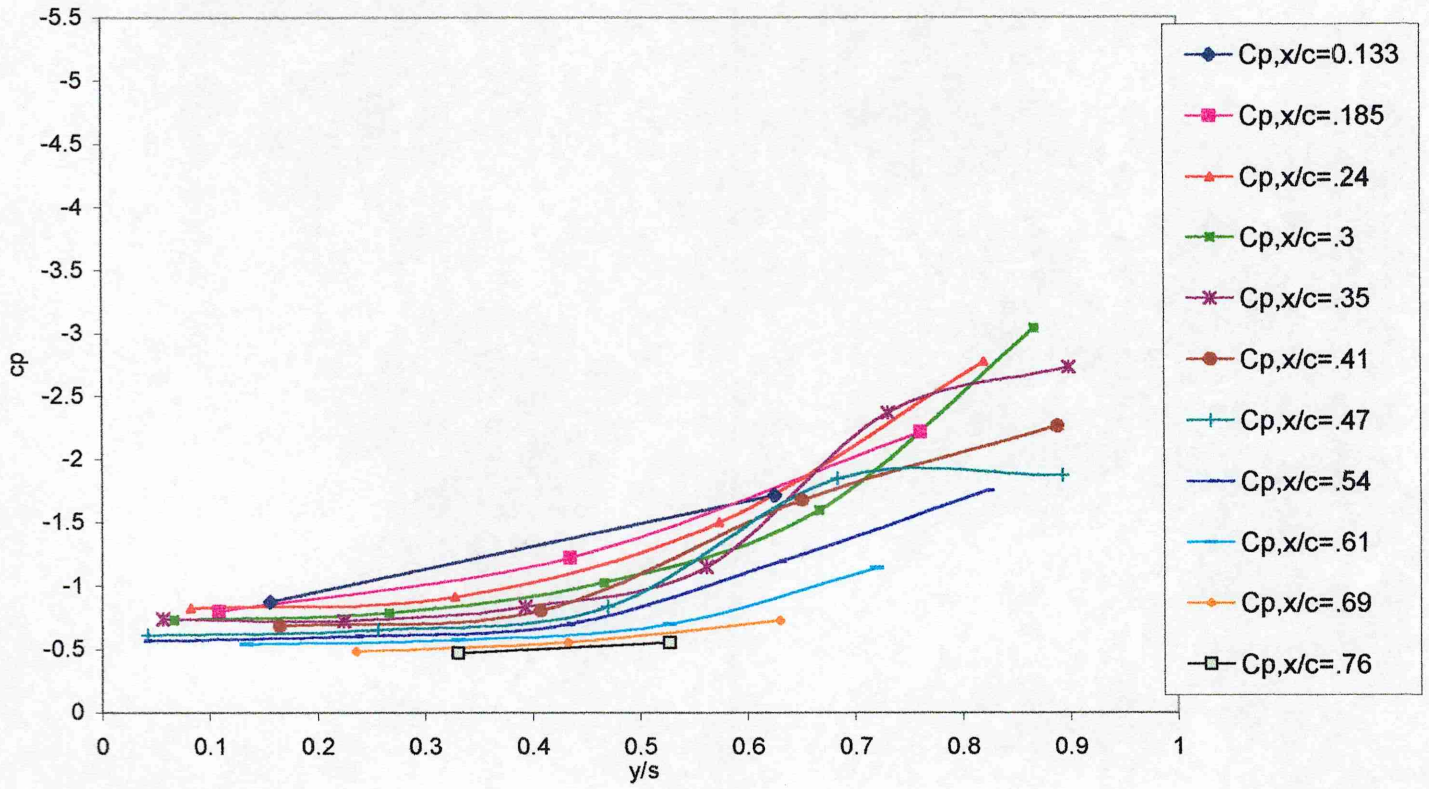

Figure I 4 spanwise Cp distribution , Delta55, AOA=20deg., B.L.=33.0mm

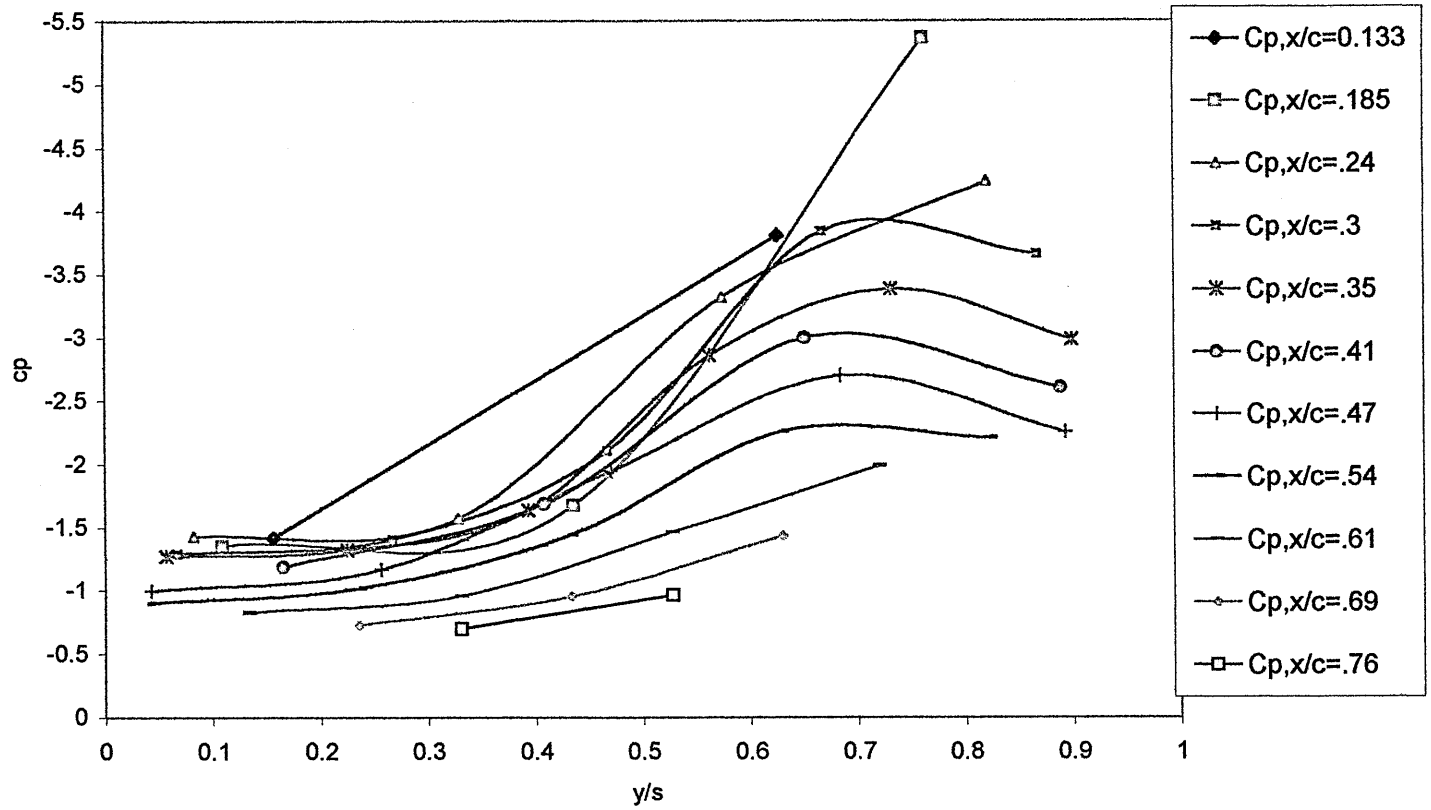

Figure I 5 spanwise Cp distribution , Delta55, AOA=30deg., B.L.=14.0mm

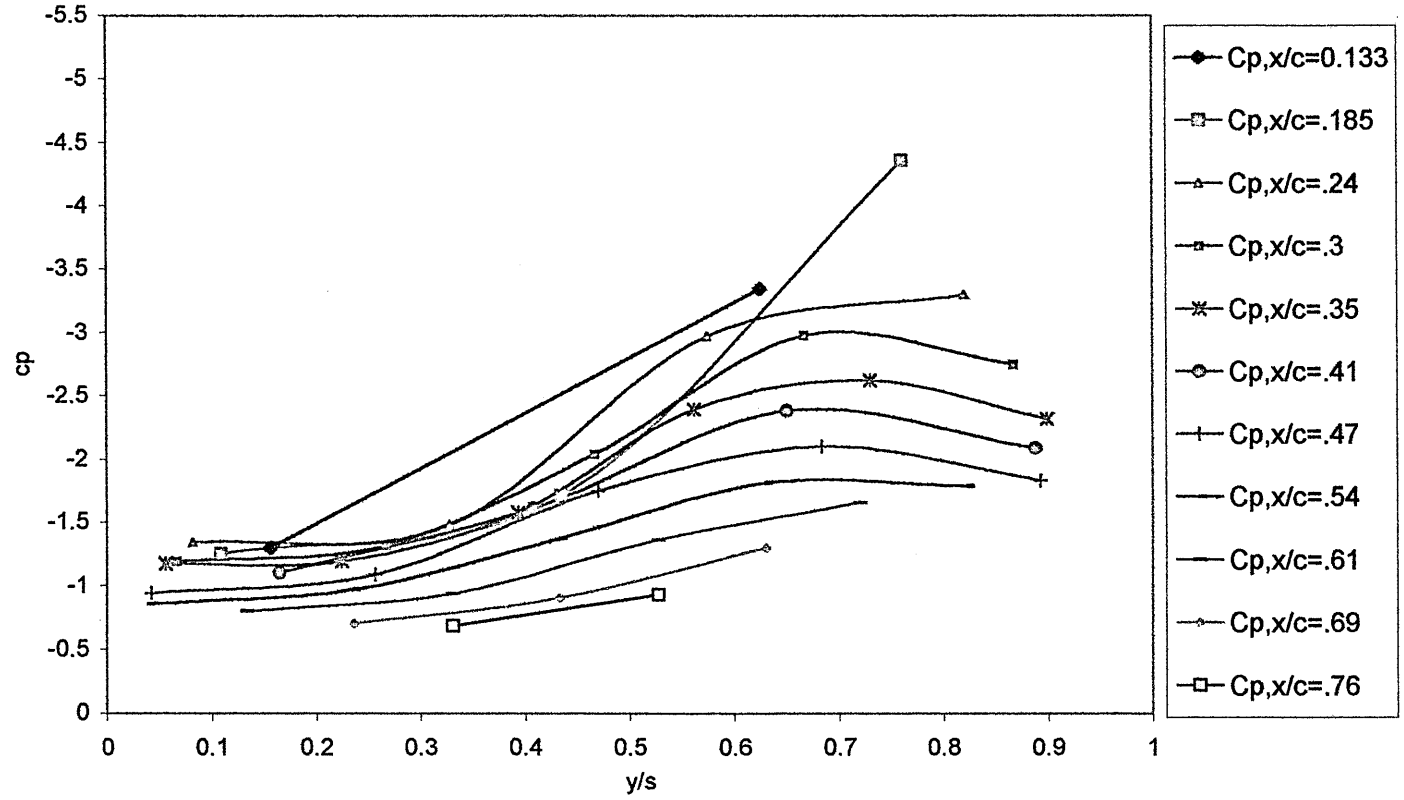

Figure I 6 spanwise Cp distribution , Delta55, AOA=30deg., B.L.=33.0mm

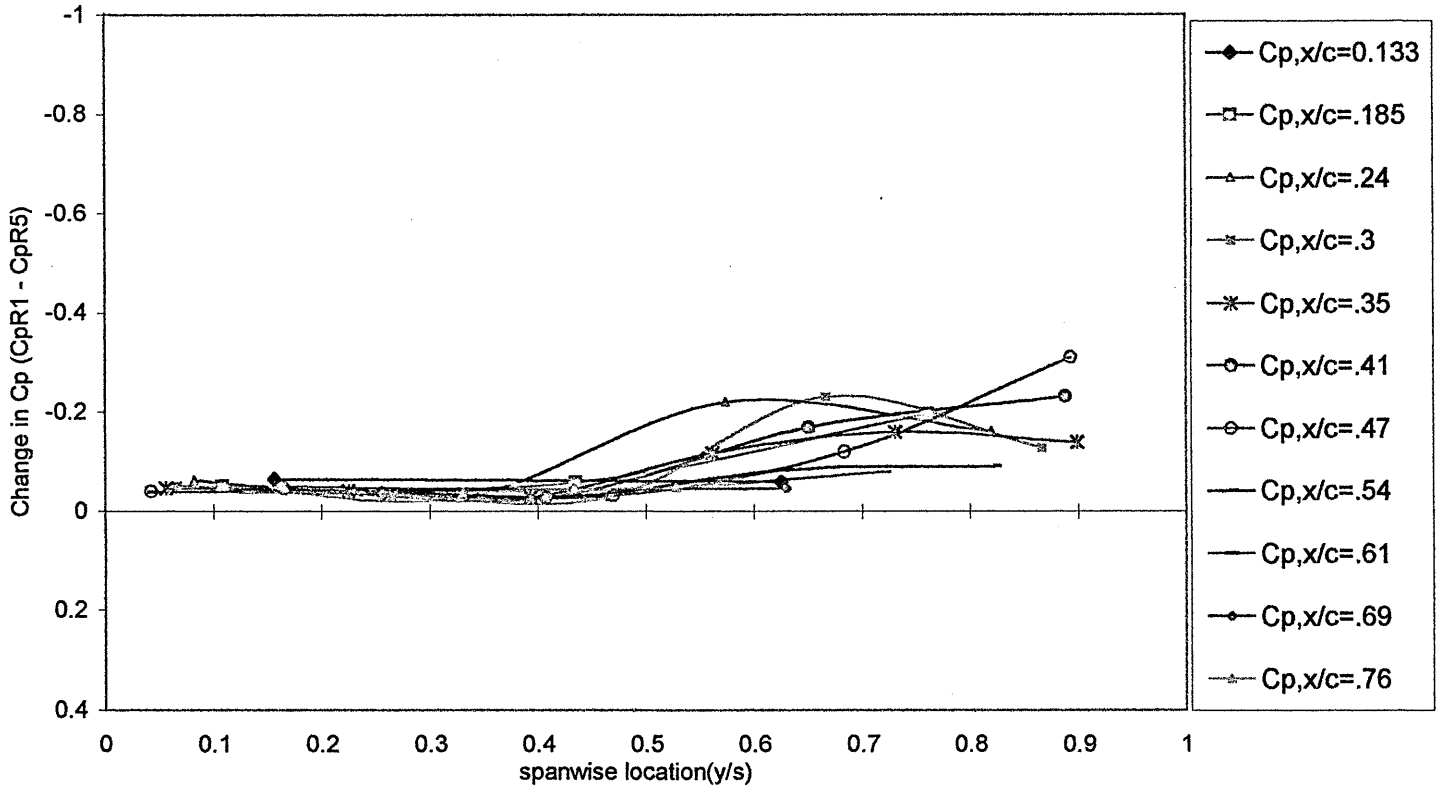

Figure I 7 Change in spanwise Cp distribution vs. local y/s, Delta55, AOA=10deg., for boundary layers R1 &R5

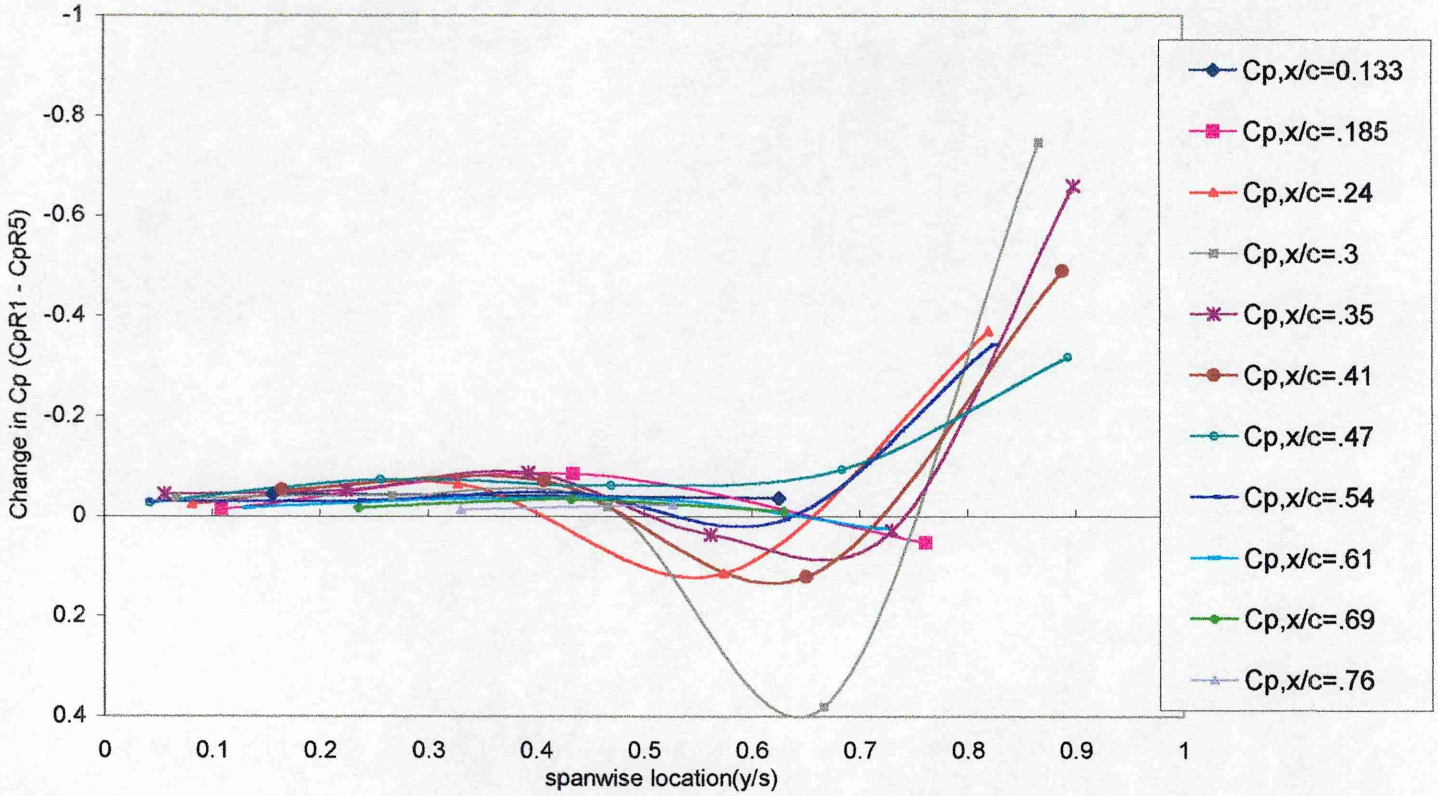

Figure I 8 Change in spanwise Cp distribution vs. local y/s, Delta55, AOA=20deg., for boundary layers R1 &R5

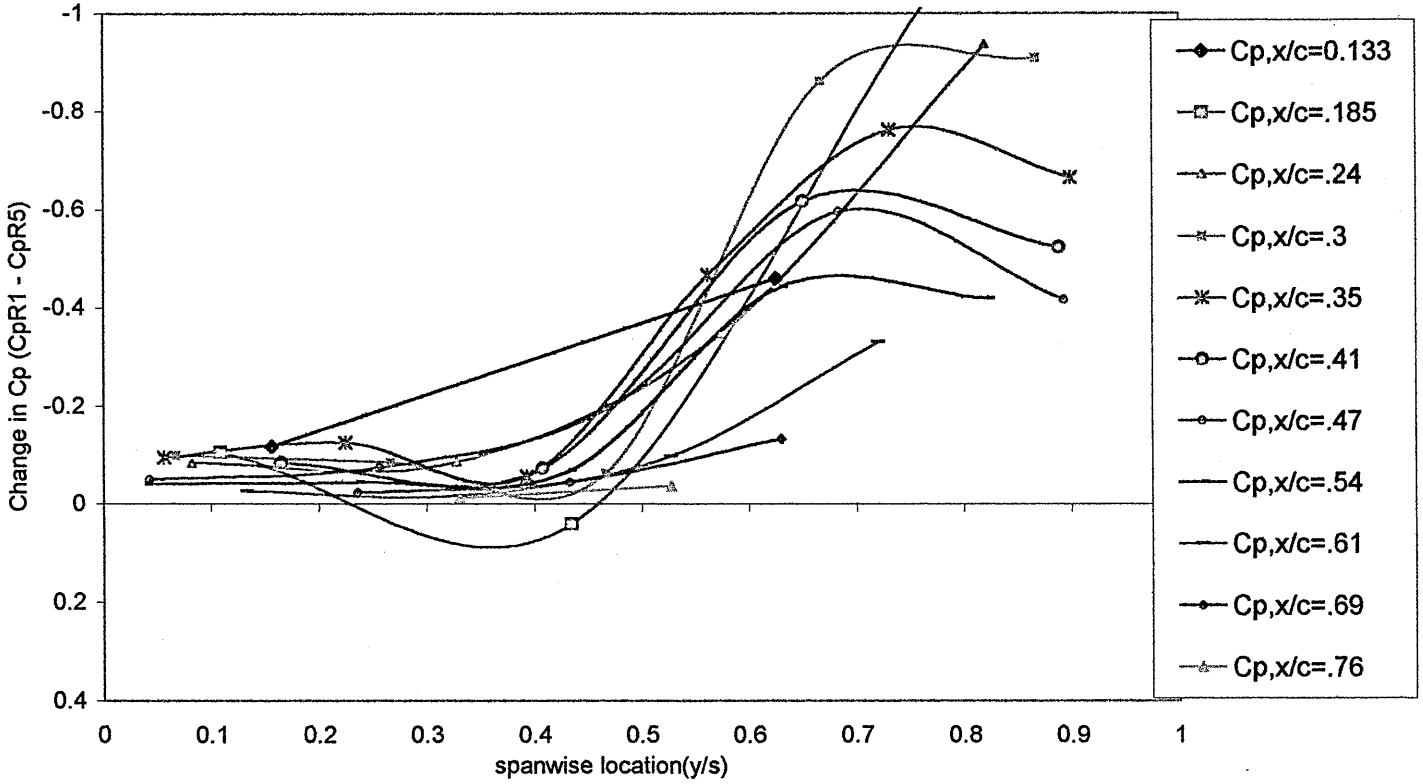

Figure I 9 Change in spanwise Cp distribution vs. local y/s, Delta55, AOA=30deg., for boundary layers R1 &R5

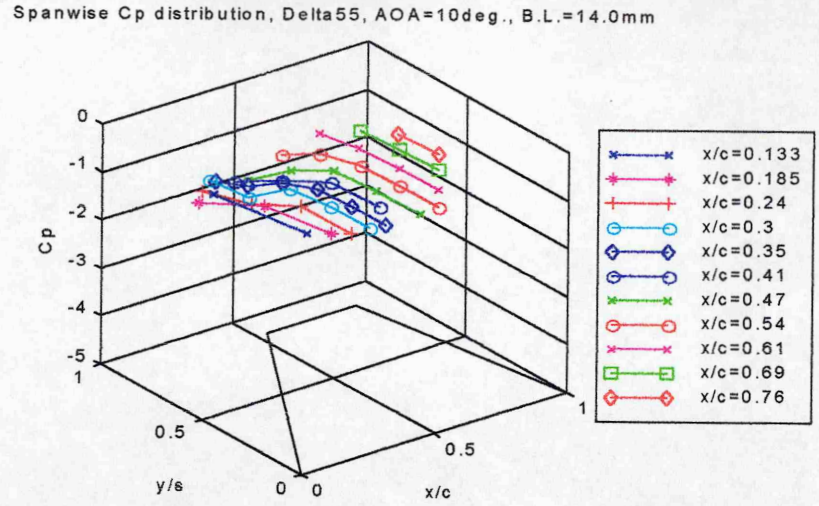

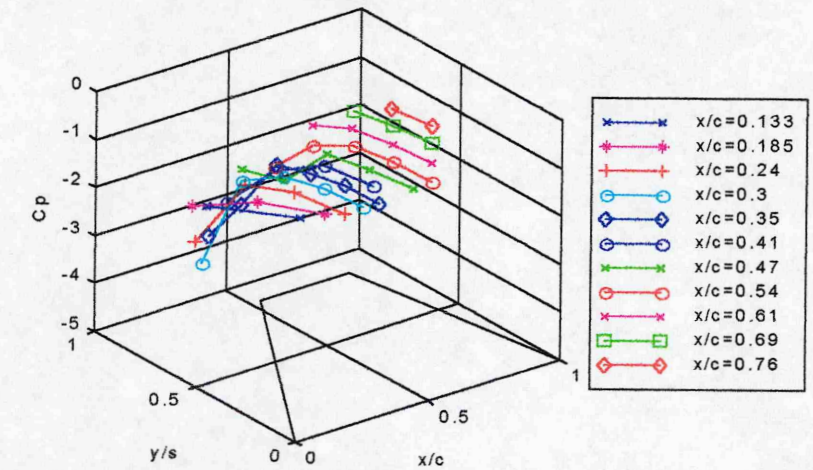

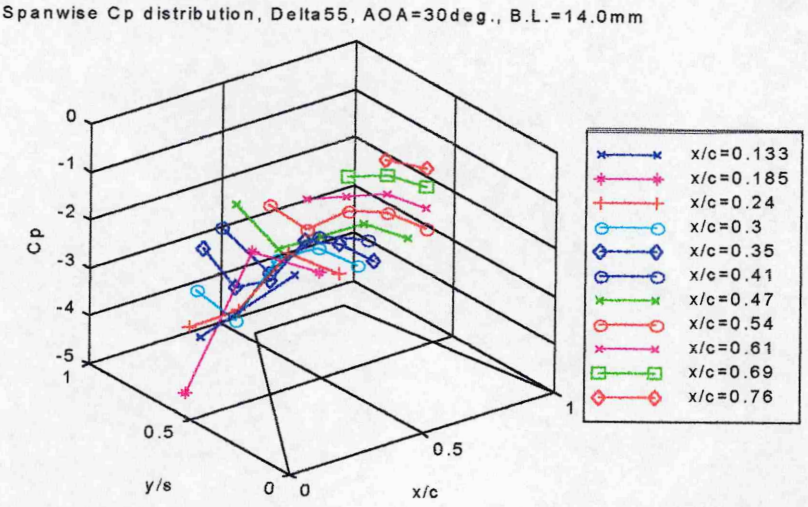

Figure I 10 3D Spanwise Cp distribution, Delta 55 sweep, t/c=0.018, B.L.=14mm

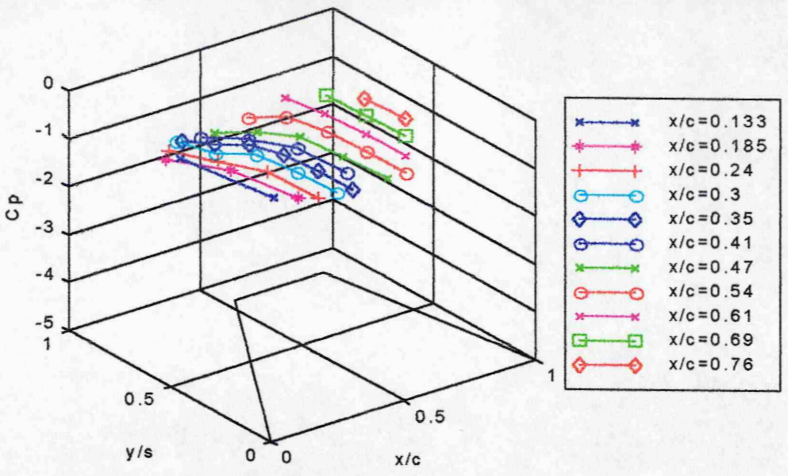

Spanwise Cp distribution, Delta55, AOA=20deg., B.L.=33.0mm

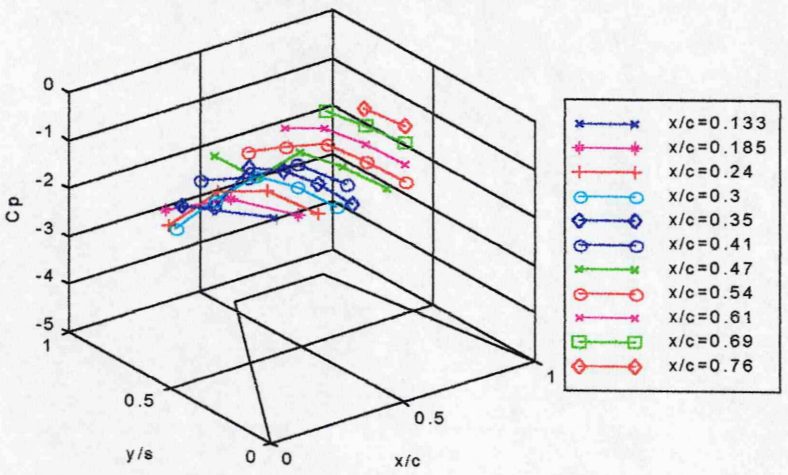

Spanwise Cp distribution, Delta55, AOA=30deg., B.L.=33.0mm

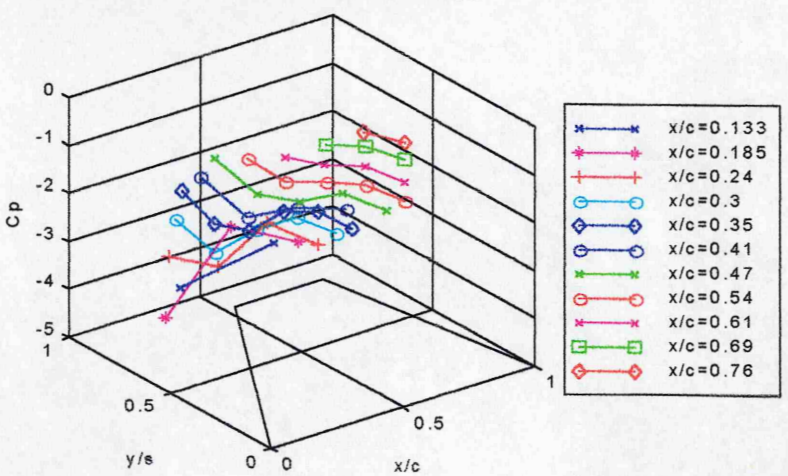

Figure I 11 3D Spanwise Cp distribution, Delta 55 sweep, t/c=0.018, B.L.=33mm

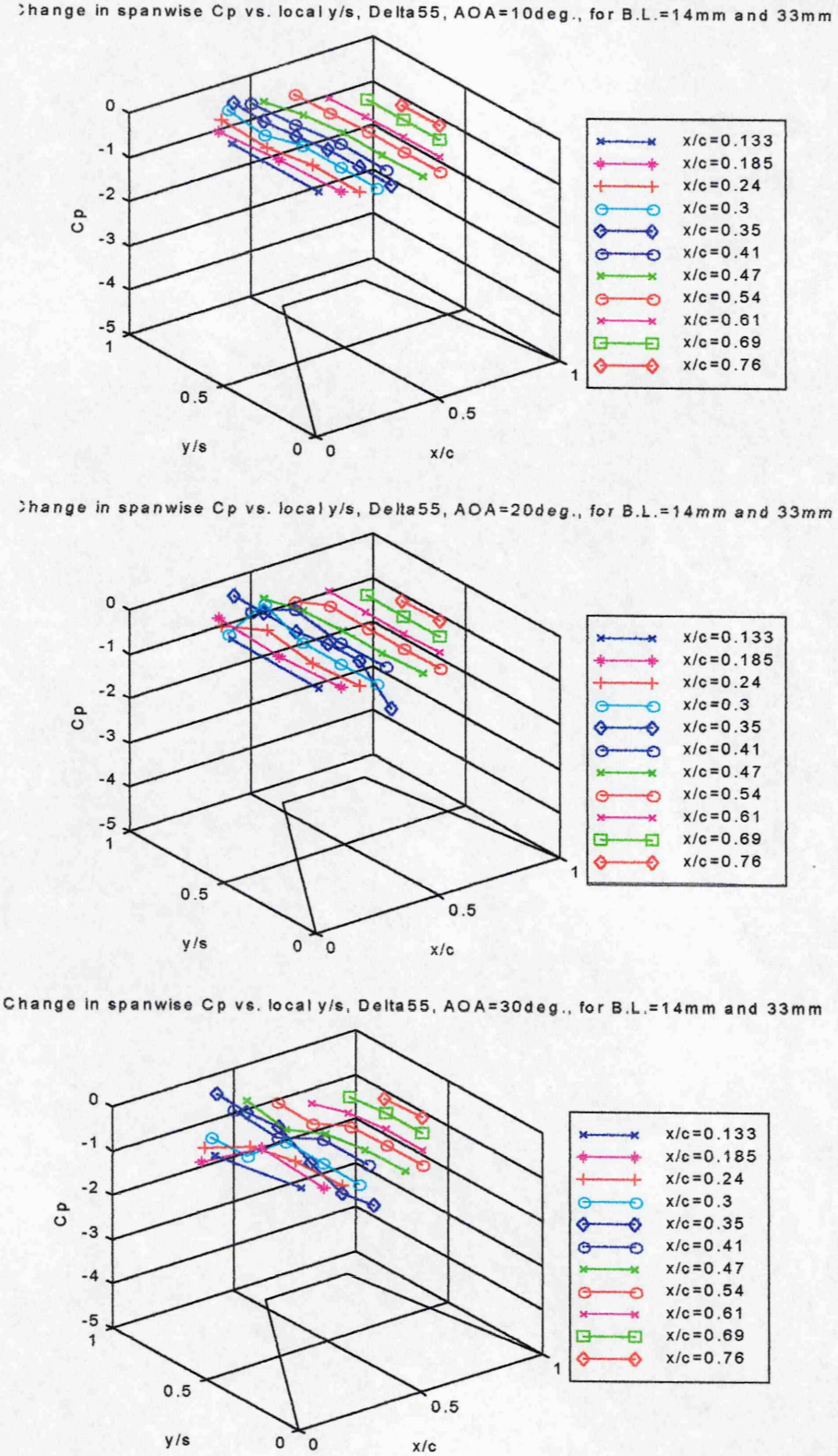

Figure I 12 3D Changes in spanwise Cp distribution, Delta 55 sweep, t/c=0.018, B.L.=14mm, 33mm

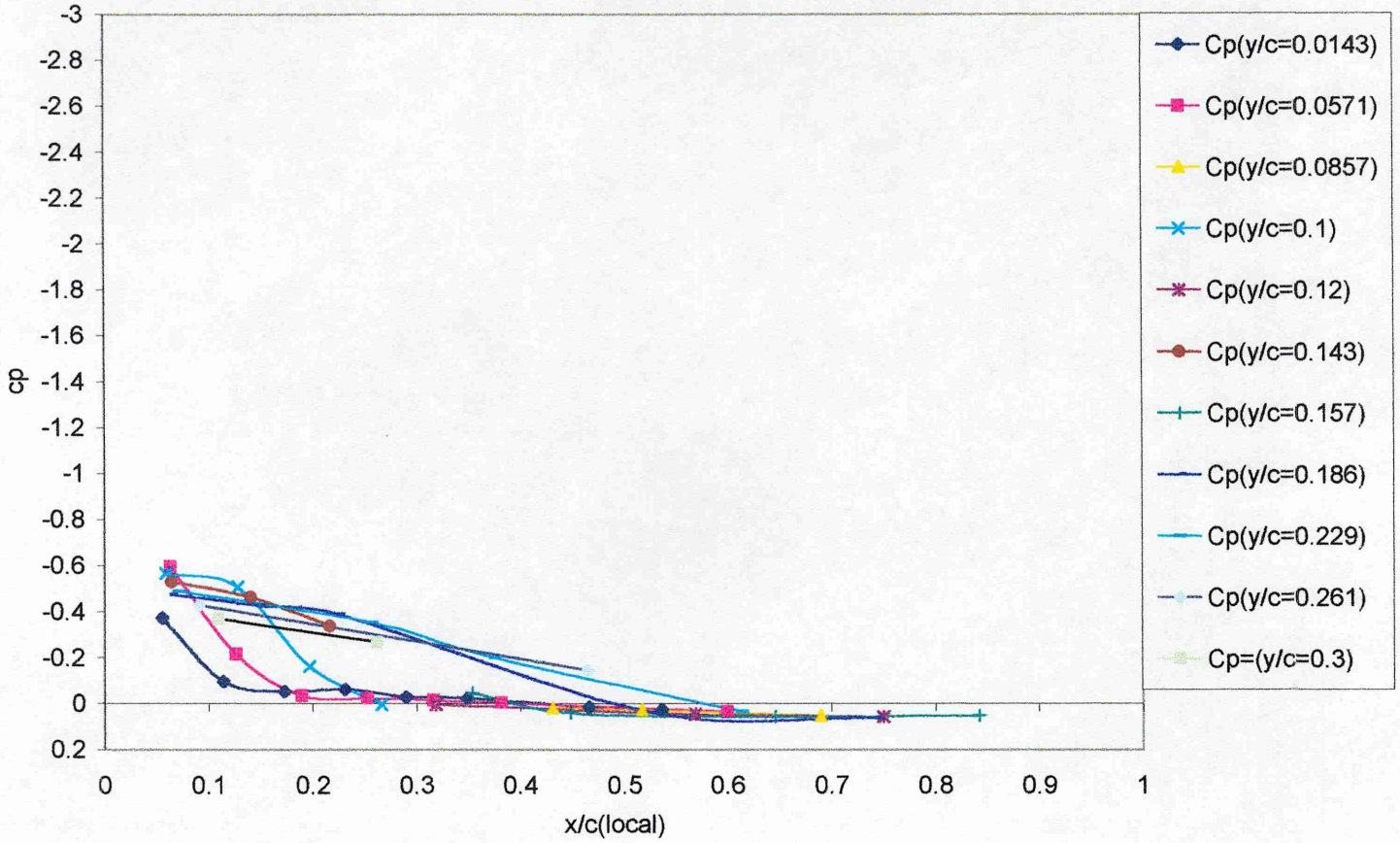

Figure I 13 Axial Cp Distribution, Delta 55, AoA = 10 deg., B.L.=14mm

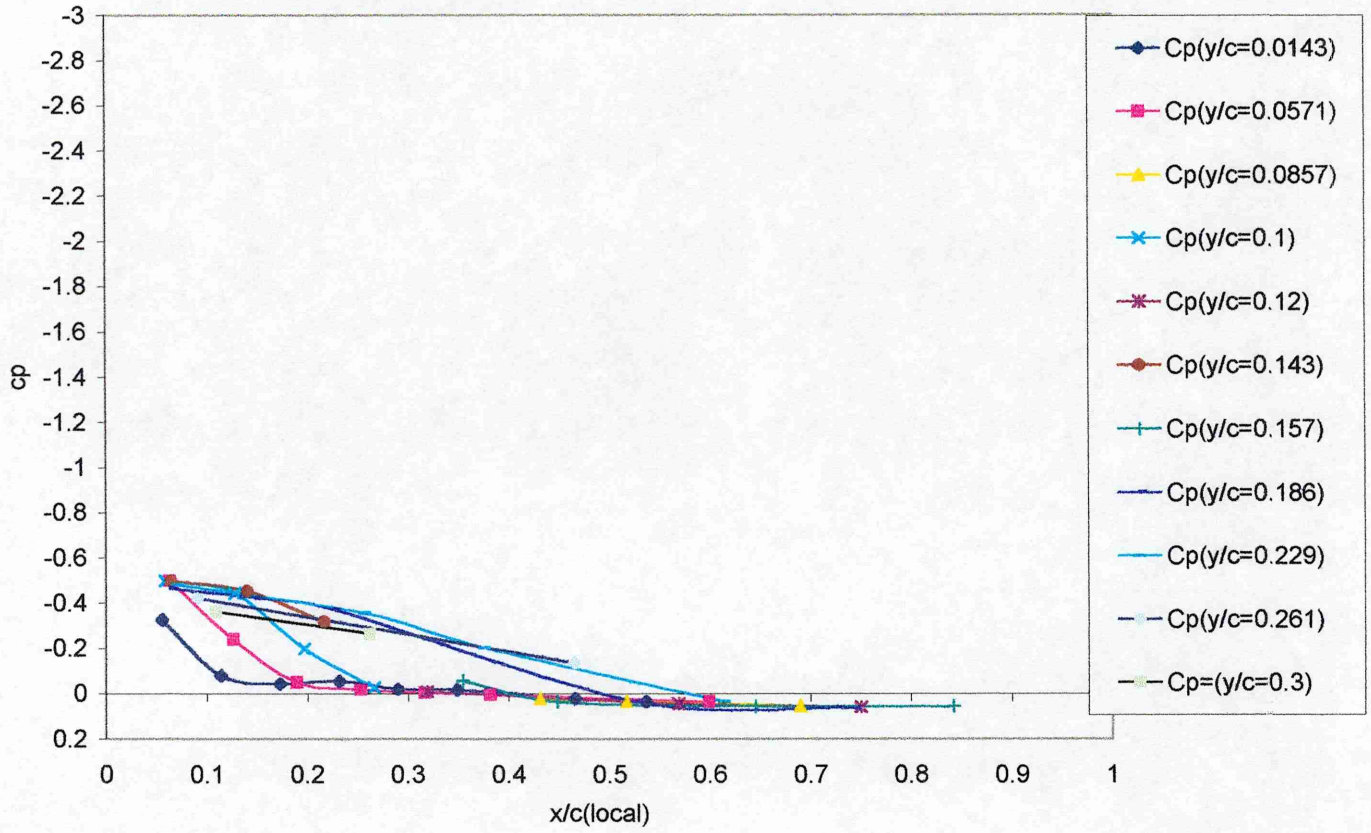

Figure I 14 Axial Cp Distribution, Delta 55, AoA = 10 deg., B.L.=33mm

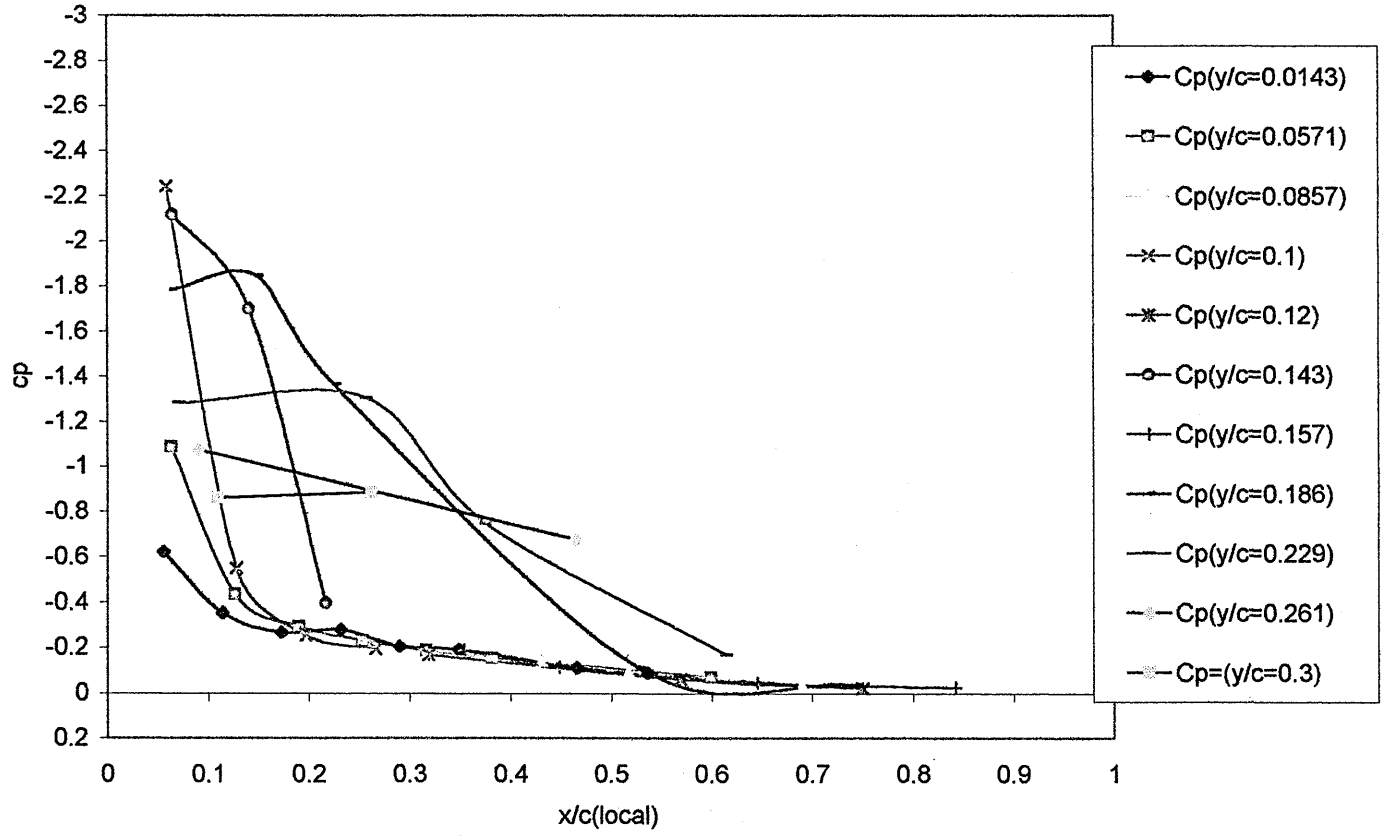

Figure I 15 Axial Cp Distribution, Delta 55, AoA = 20 deg., B.L.=14mm

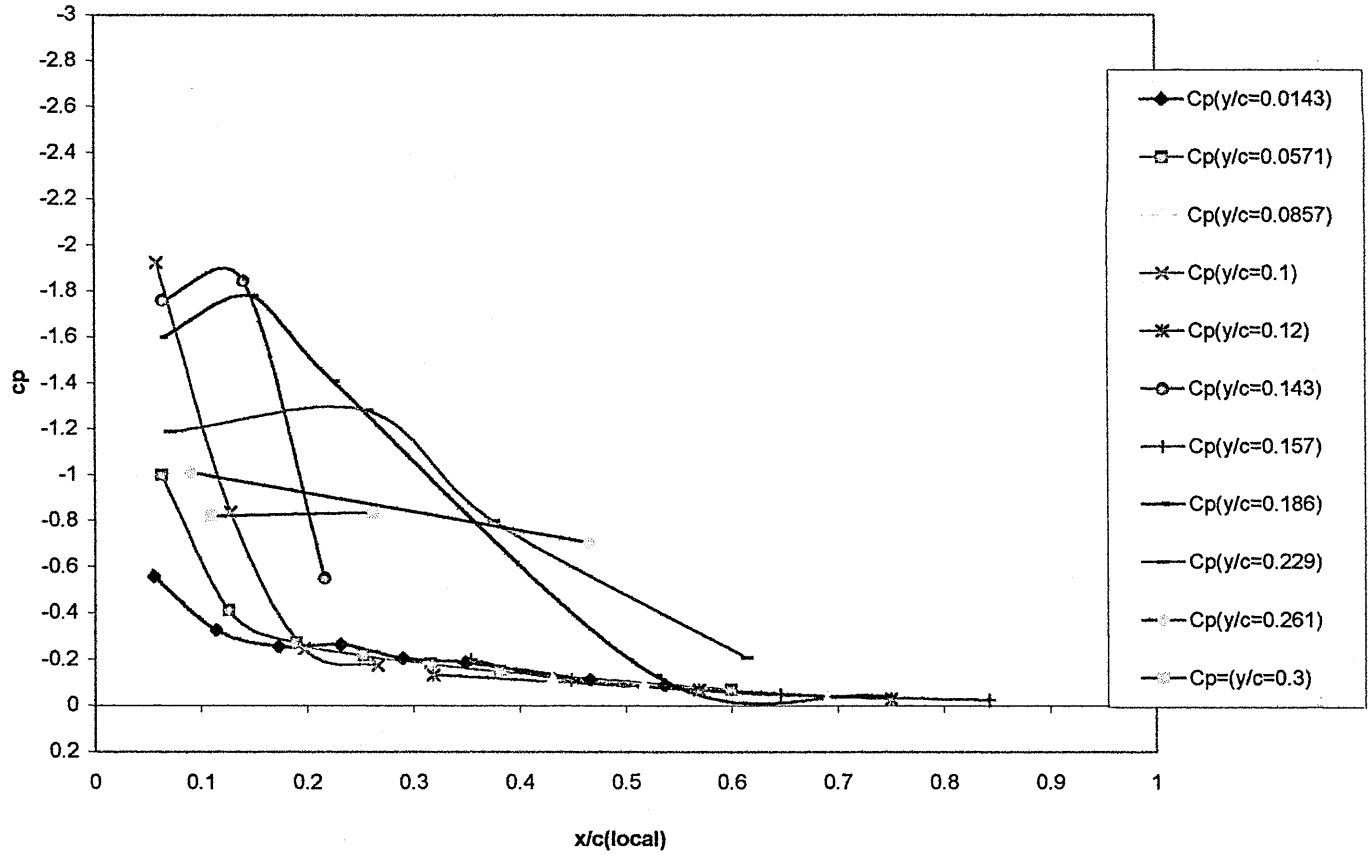

Figure I 16 Axial Cp Distribution, Delta 55, AoA = 20 deg., B.L.=33mm

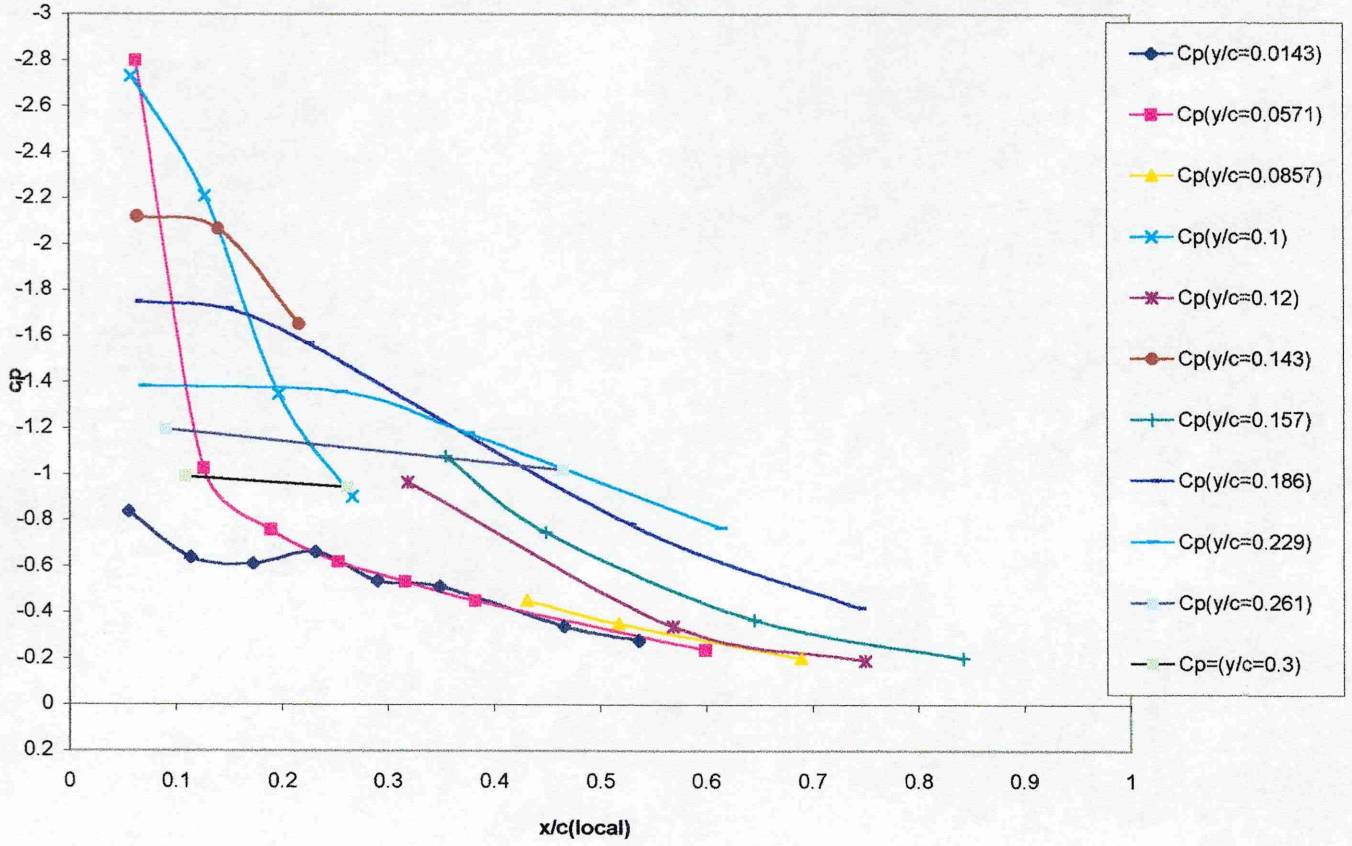

Figure I 17 Axial Cp Distribution, Delta 55, AoA = 30 deg., B.L.=14mm

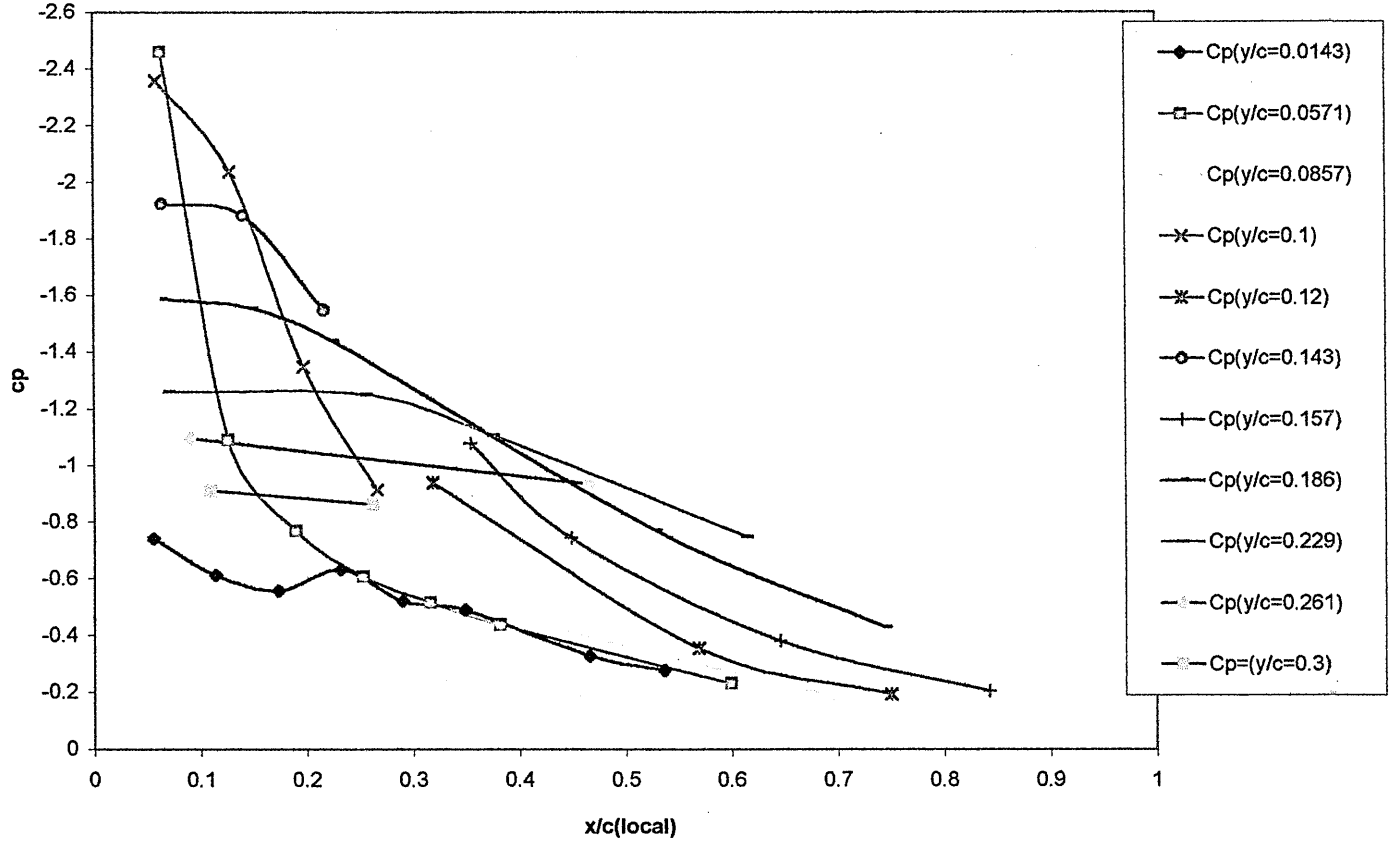

Figure I 18 Axial Cp Distribution, Delta 55, AoA = 30 deg., B.L.=33mm

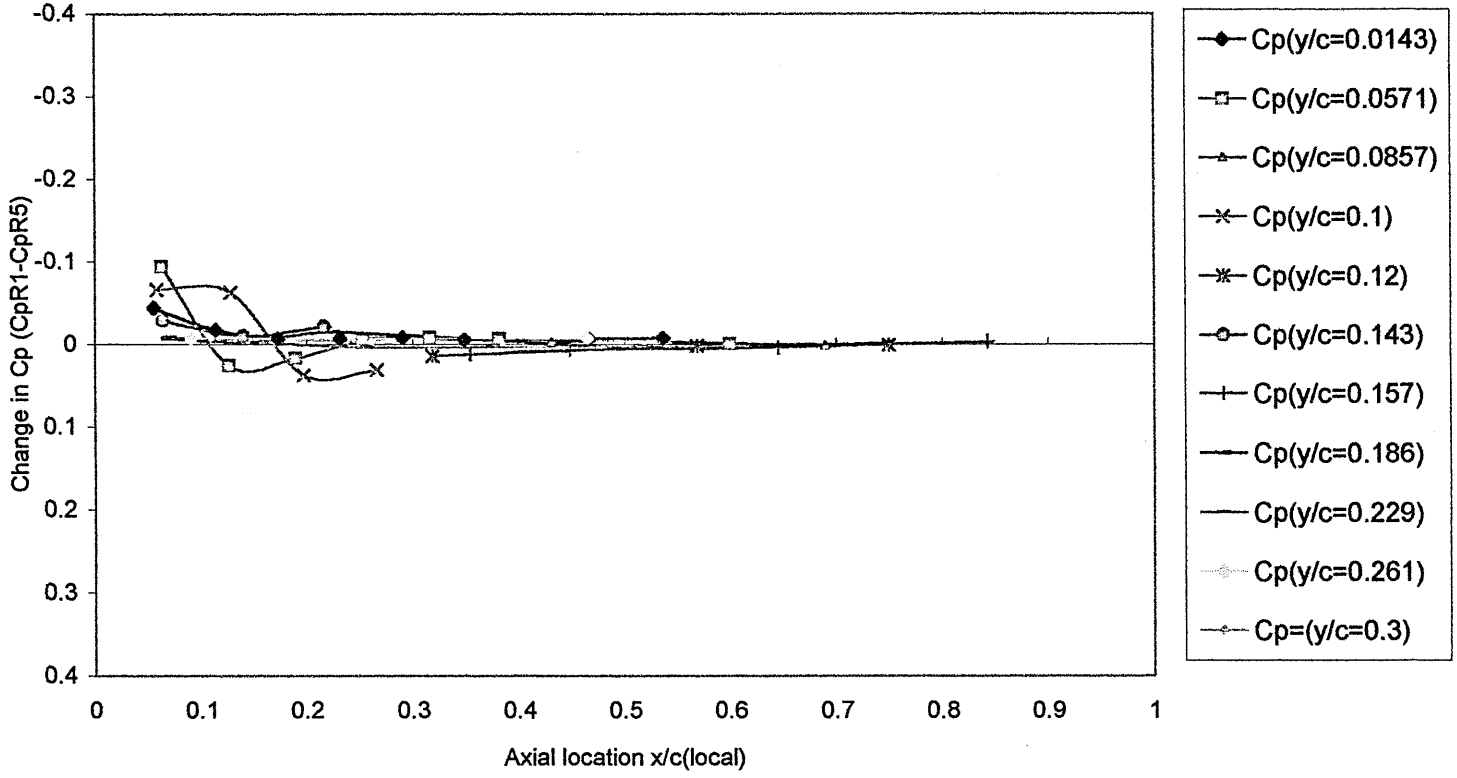

Fig. I 19 Change in axial Cp distribution vs. local y/s, Delta55, AOA=10deg., for boundary layers R1 &R5

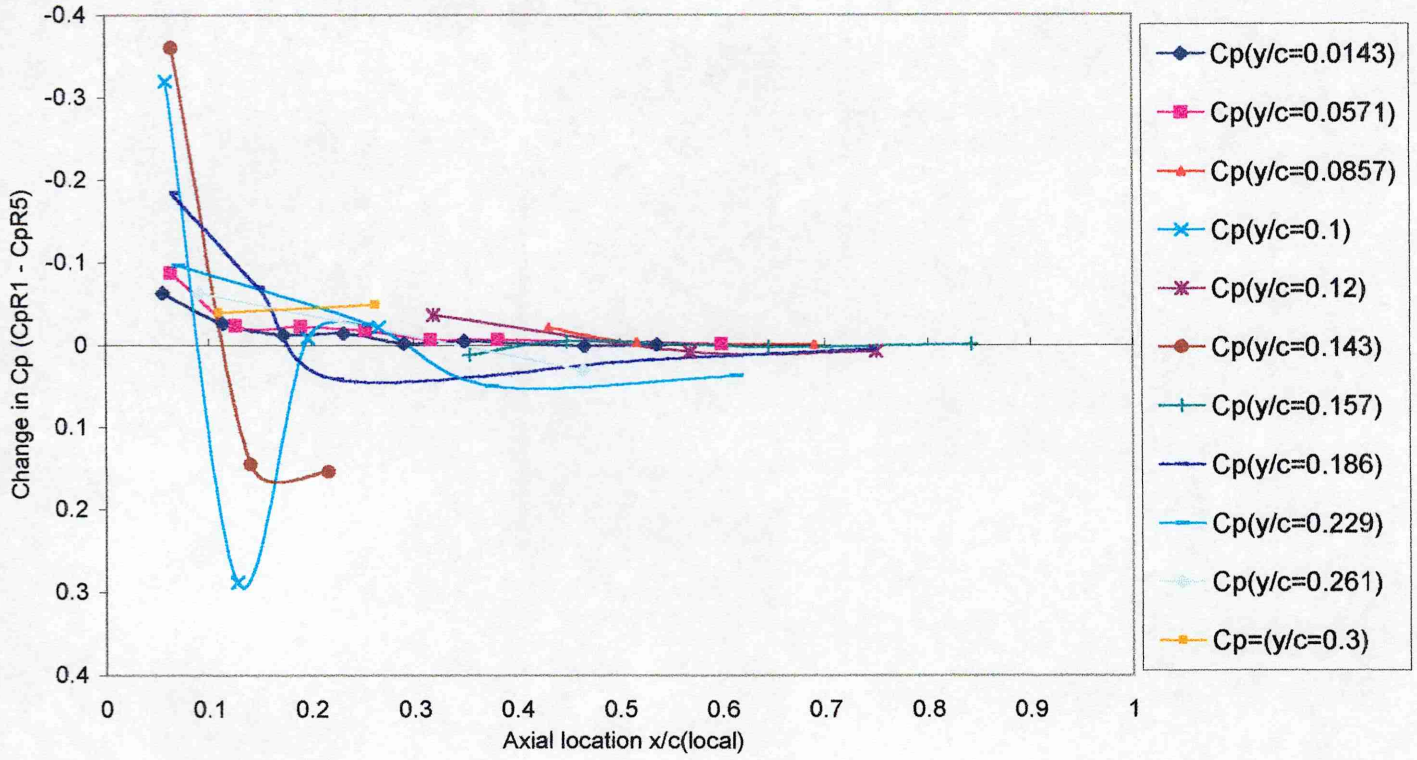

Figure I 20 Change in axial Cp distribution vs. local y/s, Delta55, AOA=20deg., for boundary layers R1 &R5

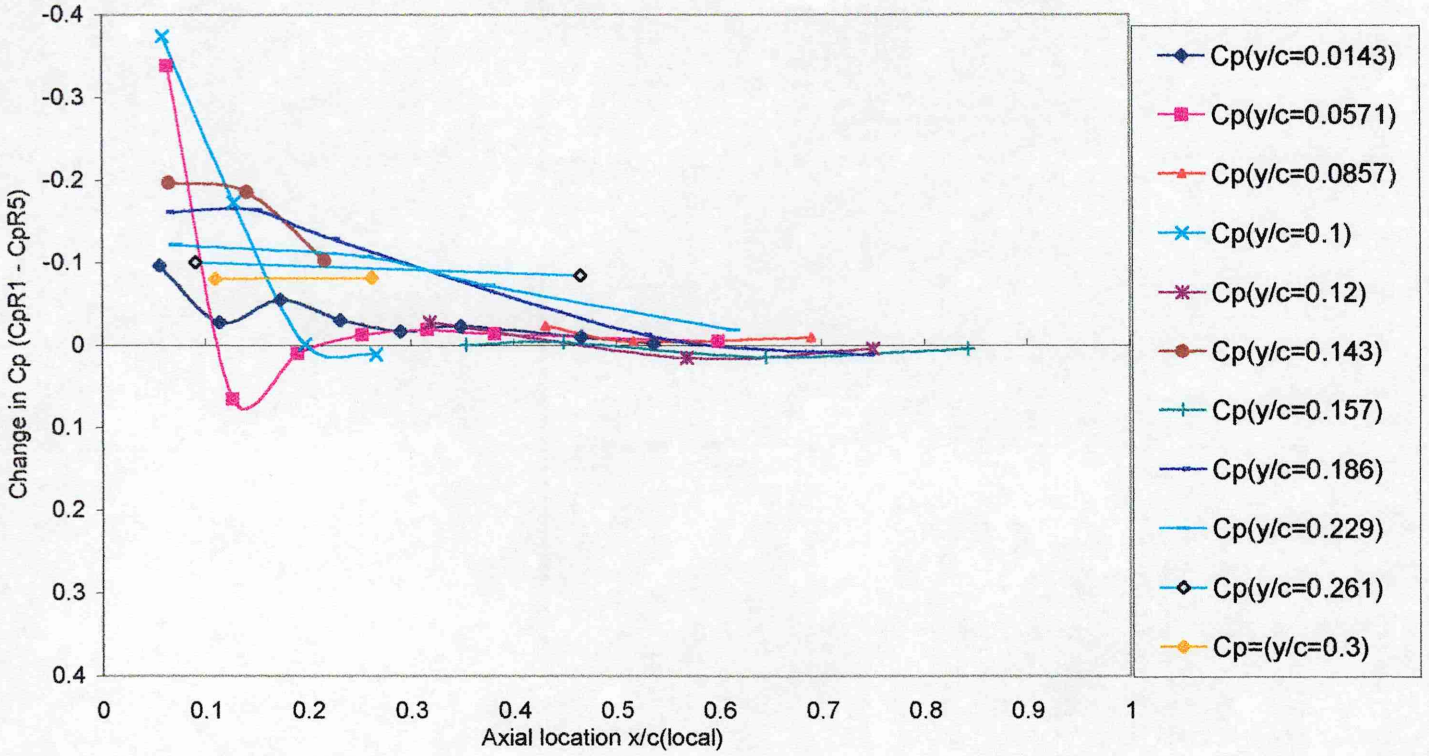

Figure I 21 Change in axial Cp distribution vs. local y/s, Delta55, AOA=30deg., for boundary layers R1 &R5

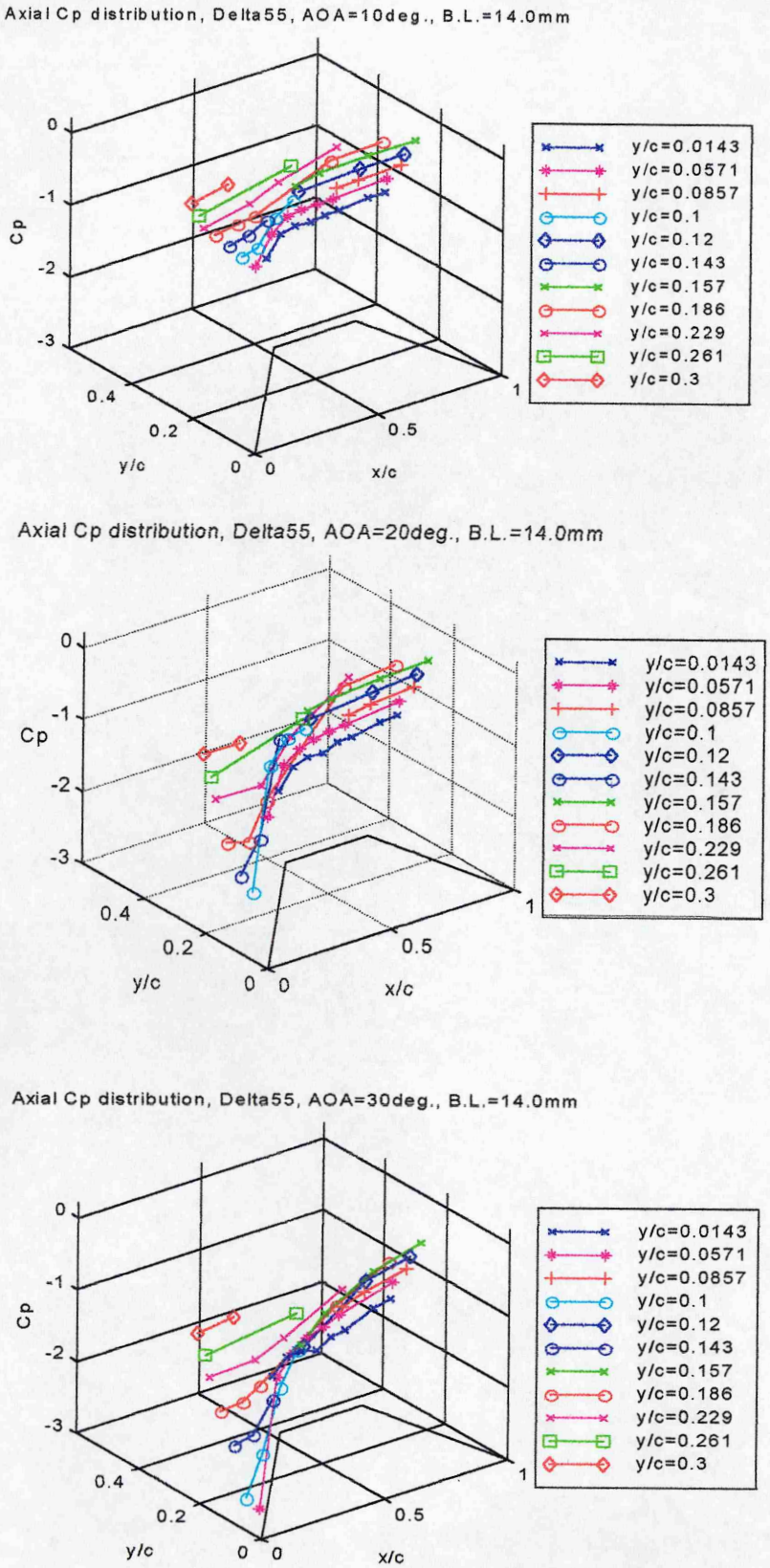

Figure I 22 3 D Axial Cp distribution, Delta 55° sweep, B.L.=14mm

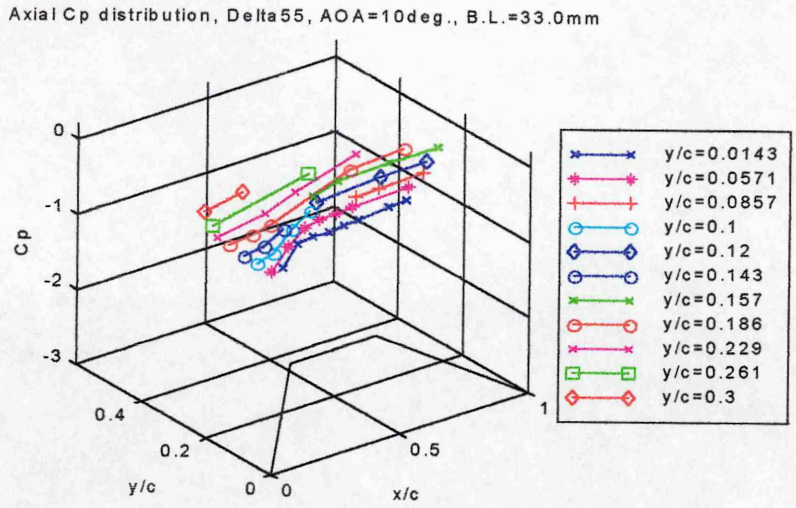

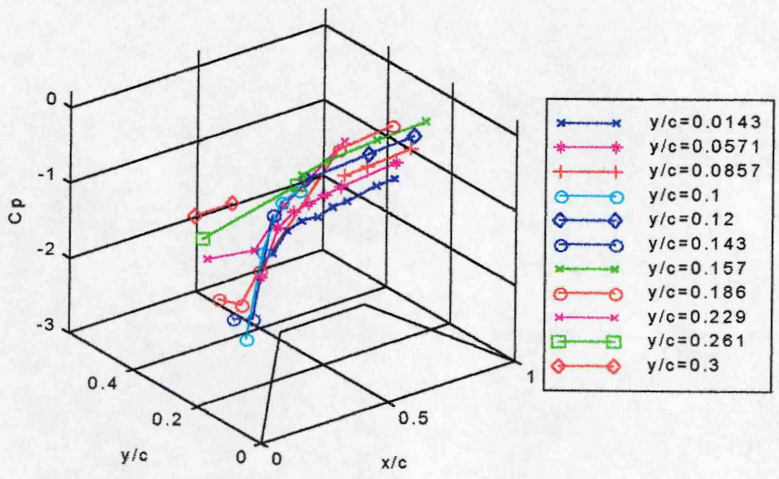

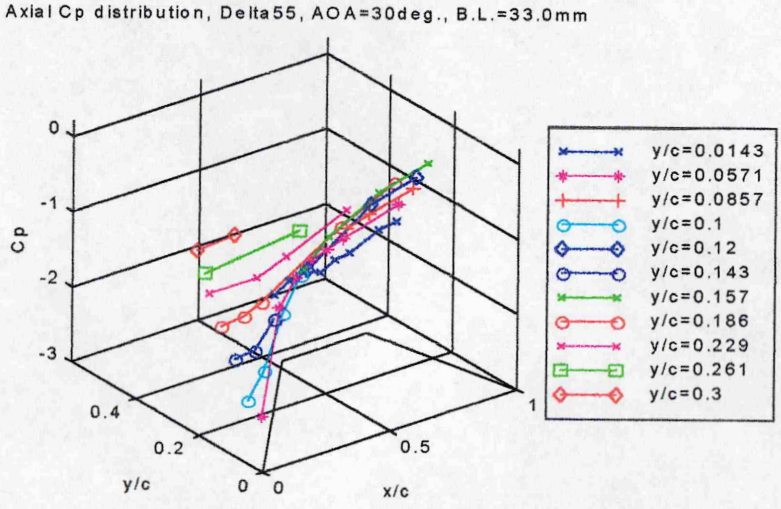

Figure I 23 3 D Axial Cp distribution, Delta 55° sweep, B.L.=33mm

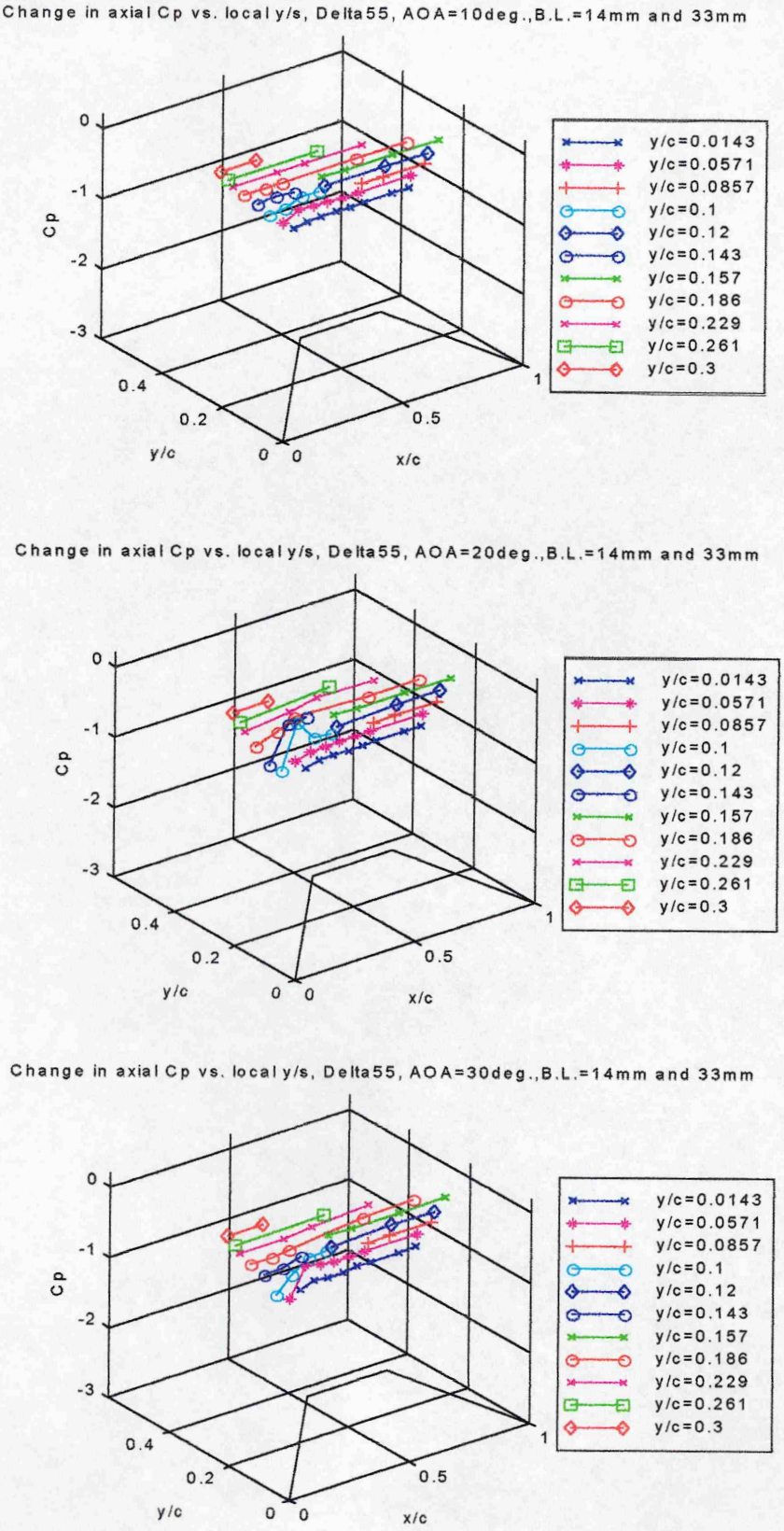

Figure I 24 3 D Change in axial Cp distribution, Delta 55° sweep, B.L.=14mm and 33mm